Universidade de Aveiro Departamento de Física

2019

Ana Rita da Silva Rocha Frias

Concentradores solares luminescentes de elevado desempenho para conversão fotovoltaica baseada em guias de onda flexíveis

High performance luminescent solar concentrators for flexible waveguiding photovoltaics

Universidade de Aveiro Departamento de Física

2019

Ana Rita da Silva Rocha Frias

Concentradores solares luminescentes de elevado desempenho para conversão fotovoltaica baseada em guias de onda flexíveis

High performance luminescent solar concentrators for flexible waveguiding photovoltaics

Ana Rita da Silva Rocha Frias

Concentradores solares luminescentes de elevado desempenho para conversão fotovoltaica baseada em guias de onda flexíveis

High performance luminescent solar concentrators for flexible waveguiding photovoltaics

Tese apresentada à Universidade de Aveiro para cumprimento dos requisitos necessários à obtenção do grau de Doutor em Física, realizada sob a orientação científica da Doutora Maria Rute Amorim de Sá Ferreira André, Professora Associada com Agregação do Departamento de Física da Universidade de Aveiro, do Doutor Luís António Ferreira Martins Dias Carlos, Professor Catedrático do Departamento de Física da Universidade de Aveiro e do Doutor Paulo Sérgio de Brito André, Professor Associado com Agregação do Departamento de Engenharia Eletrotécnica e de Computadores do Instituto Superior Técnico da Universidade de Lisboa.

Trabalho desenvolvido no âmbito do projeto CICECO-Instituto de Materiais de Aveiro, POCI-01-0145-FEDER-007679 (UID/CTM/50011/2013), e Instituto de Telecomunicações (UID/EEA/50008/2013), financiado por fundos nacionais através do FCT/MEC e cofinanciado pelo FEDER sob o acordo PT2020, SusPhotoSolutions - Soluções Fotovoltaicas Sustentáveis, CENTRO-01-0145-FEDER-000005 e Solar-Flex, CENTRO-01-0145-FEDER-030186. A autora agradece o apoio financeiro concedido pela FCT através da bolsa PD/BD/114454/2016.

o júri / the jury

presidente / president

Prof. Doutor Armando da Costa Duarte

Professor Catedrático da Universidade de Aveiro.

vogais / examiners committee

Prof. Doutor Bernardo Gonçalves Almeida

Professor Auxiliar com Agregação da Escola de Ciências da Universidade do Minho.

Prof. Doutor Dawei Liang

Professor Auxiliar da Faculdade de Ciências e Tecnologia da Universidade Nova de Lisboa.

Doutor José Manuel de Nunes Vicente Rebordão

Investigador Coordenador da Faculdade de Ciências da Universidade de Lisboa.

Prof. Doutor João Pedro Esteves de Araújo

Professor Associado da Universidade do Porto.

Prof. Doutora Maria Rute de Amorim e Sá Ferreira André

Professora Associada com Agregação da Universidade de Aveiro.

agradecimentos / acknowledgements

Gostaria de agradecer a todos os que de alguma forma contribuíram para a realização deste trabalho e sem menosprezar as restantes contribuições gostaria de destacar: os meus orientadores, Professora Doutora Maria Rute de Amorim e Sá Ferreira André, Professor Doutor Luís António Ferreira Martins Dias Carlos e ao Professor Doutor Paulo Sérgio de Brito André por toda a ajuda, por todo o conhecimento partilhado, cooperação, incentivo e conselhos dados durante todas estes anos. Para além das competências profissionais, as competências humanas que me transmitiram tornaram-me numa pessoa melhor.

Ao Professor Doutor Sidney Ribeiro e ao Doutor Édison Pecoraro da UNESP - Institudo de Química, Universidade Estadual Paulista, Araraquara-São Paulo, Brasil.

À Professora Doutora Verónica de Zea Bermudez do Departamento de Química da UTAD-Universidade de Trás-os-Montes e Alto Douro.

Ao Doutor Lianshe Fu, pela síntese dos materais (di-ureasils e tri-ureasils).

À Doutora Sandra Correia por todas as discussões científicas, pela ajuda e partilha de conhecimento, pelo acompanhamento e acima de tudo pela amizade.

A todos os meus colegas do Grupo Phantom-G que, de uma forma ou de outra, contribuíram para o desenvolvimento deste trabalho, em particular ao Mestre João Ramalho e Doutora Vânia Freitas e Mestre Marita Cardoso.

À Fundação para a Ciência e Tecnologia pela ajuda financeira.

Ao CICECO Aveiro Institute of Materials, Instituto de Telecomunicações e Departamento de Física agradeço por me terem proporcionado todos os meios físicos para a concretização deste trabalho de doutoramento. Neste contexto, agradeço, também, ao pessoal técnico destas instituições pelo apoio que sempre me disponibilizaram.

Às minhas amigas, que de longe acompanharam sempre o meu percurso, a Catarina, à Gina, à Rita e à Valentina por serem as amigas de sempre e pelo constante incentivo e motivação. A todos os amigos da universidade, por todas as horas de almoço bem passadas, pela boa disposição constante e por me terem acompanhado durante todos estes anos, Carlos Rosário, Maria Relvas, Renato Pereira, Tiago Paixão, Roberto Costa e Jennifer Teixeira.
Um agradecimento muito especial ao Edgar Wright, por ser a melhor pessoa que podia ter ao meu lado, por ser o melhor amigo e companheiro de todas as aventuras e, em especial, por estar sempre presente quando mais precisei.
O agradecimento mais importante é dirigido à família, em especial aos meus pais, irmãos e avós pela presença e apoio.
A todos, muito obrigada!

Palavras-chave

Híbrido orgânico-inorgânico, camada luminescente por desvio descendente de energia, concentradore solare luminescente, fibra ótica de plástico, corantes orgânicos, iões lantanídeos, eficiência ótica de conversão, eficiência quântica externa, sustentabilidade.

Resumo

O desfasamento entre o espetro AM1.5G e o espetro de absorção das células fotovoltaicas é um fator crítico que limita o desempenho das mesmas. De forma a ultrapassar isto, diversas aproximações têm sido propostas. Entre elas, têm sido enfatizadas as camadas luminescentes por desvio descendente de energia, dispositivos capazes de melhorar o desempenho em condições de operação específicas, e os concentradores solares luminescentes, considerados uma tecnologia complementar à das células fotovoltaicas para utilização em ambientes urbanos.

As camadas luminescentes por desvio descendente de energia são revestimentos diretamente depositados no topo de células fotovoltaicas capazes de absorver a radiação incidente complementar à que as células fotovoltaicas absorvem e subsequentemente reemitem-na com um comprimento de onda específico que é refratado/refletido até à célula fotovoltaica. Os concentradores solares são dispositivos compostos por uma matriz transparente incorporando centros óticos ativos que absorbem a radiação incidente, que é posteriormente reemitida com um comprimento de onda específico e transportada por reflexão interna total até à célula fotovoltaica localizada nas extremidades da matriz. Esta configuração permite a produção de dispositivos fotovoltaicos embebidos em fachadas de edifícios e janelas, permitindo que estes sejam transformados em unidades de produção de energia, contribuindo para o desenvolvimento de edifícios de energia zero.

O principal objetivo deste trabalho consiste no fabrico e caracterização de híbridos orgânicos-inorgânicos com espessura e índice de refração controlados utilizando polimetil-metacrilato, di- e tri-ureasil incorporando diferentes iões lantanídeos, nomeadamente Tb^{3+}, Eu^{3+}, Yb^{3+} and Nd^{3+}, e corantes orgânicos como Rodamina 6G, Rodamina 800, Silício 2,3-naftalocianina bis(trietil siloxano), clorofila e R-ficoeritrina cuja emissão varia entre o visível e o infravermelho próximo. Concentradores solares luminescentes com geometria planares e cilíndrica foram estudados. A geometria cilíndrica permite que o efeito de concentração seja superior, quando comparado com a geometria planar, uma vez que a razão entre a área exposta e a área das extremidades aumenta. A geometria cilíndrica é explorada, através da produção de concentradores solares luminescentes em fibra ótica de plástico onde a camada ótica ativa se encontra no interior da fibra, como um preenchimento do núcleo oco. A possibilidade de aumentar a área exposta foi, também, abordada através do fabrico de uma matriz de concentradores solares luminescentes colocados lado a lado com diferentes geometrias da bainha. Para além disso, as propriedades óticas dos corantes orgânicos naturais, que têm sido pouco exploradas na literatura, foram alvo de estudo através da incorporação de moléculas de clorofila e de R-ficoeritrina como centros óticos em concentradores solares luminescentes. Os resultados experimentais mais relevantes foram validados através de simulações baseadas no método de Monte-Carlo.

Key-words

Organic-inorganic hybrid, luminescent down-shifting layer, luminescent solar concentrator, plastic optical fibre, organic dyes, lanthanide ions, optical conversion efficiency, external quantum efficiency, sustainability.

Abstract

The mismatch between the AM1.5G spectrum and photovoltaic cell absorption is one of the critical factors limiting their performance. To overcome it, several approaches have been proposed. Among them, emphasis is given to luminescent down-shifting layers, additive devices that are able to enhance performance under typical operation conditions, and to luminescent solar concentrators, a complementary technology to PV cells for use in urban environments.

Luminescent down-shifting layers are coatings that are directly deposited on the surface of photovoltaic cells, and absorb the incident radiation that is not absorbed by photovoltaic cells, subsequently re-emitting it at a specific wavelength and refracting/reflecting it towards the photovoltaic cell. Luminescent solar concentrators are devices comprising a transparent matrix incorporating optically active centres that absorb the incident radiation, which is then re-emitted at a specific wavelength and transferred by total internal reflection to photovoltaic cells located at the edges of the matrix. This configuration enables photovoltaic devices to be embedded in building facades or windows, allowing them to be transformed into energy harvesting units, contributing for the development of zero-energy buildings.

This thesis aimed to produce and characterize transparent organic-inorganic hybrids with controlled thickness and refractive index using poly(methyl methacrylate), di- and tri-ureasils incorporating different lanthanide ions, namely Tb^{3+}, Eu^{3+}, Yb^{3+} and Nd^{3+}, and the following organic dyes: Rhodamine 6G and Rhodamine 800, silicon 2,3-naphthalocyaninebis(trihexylsilyloxide), chlorophyll and R- phycoerythrin molecules with emission tuned from the visible to NIR spectral regions. LSCs with planar and cylindrical geometry are studied. The use of the cylindrical geometry allows the effect of concentration to be higher when compared with the planar geometry, since the ratio between the exposed area and the area of the edges is increased. The cylindrical geometry concentrators are produced from plastic optical fibres with hollow cores, where the optically active layer was injected. The exposed area was further optimised through the production of bundles of LSCs, in which optical fibres with different cladding geometries were placed side by side. Finally, the attractive properties of natural-based dye molecules for the production of luminescent solar concentrators, which have been poorly explored, are also studied through the incorporation of chlorophyll and R- phycoerythrin as optically active centres. Key experimental results were also validated using Monte-Carlo ray-tracing simulations.

Contents

List of Figures

List of Tables

Chapter 1

Introduction

We are currently experiencing a growing demand for comfort and higher mobility which has caused a huge increase in worldwide energy consumption. This trend has been observed over the last 150 years, Figure 1.1A, and midterm exhaustion of fossil fuels is likely [1]. In light of these facts, solving the global energy crisis is undoubtedly one of the major scientific challenges facing mankind. It is thus imperative that alternative forms of energy are developed, particularly those that can also reduce CO_2 emissions [2].

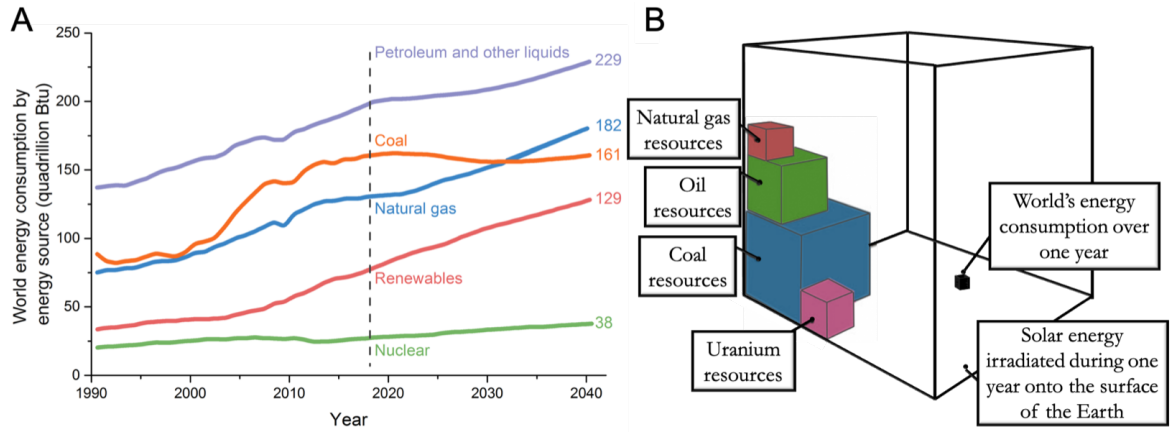

Figure 1.1: (A) Historic and projected of the worldwide energy consumption by energy source (in quadrillion Btu $= 1.05505585 \times 10^{18}$ *joules*). Adapted from [1]. (B) Solar energy potential relative to the world's energy consumption and existing fossil fuel resources. Adapted from [2].

New technologies that efficiently harness renewable energy sources, such as the Sun, wind, and tides are ackowledged to be the most viable solution. Solar energy seems to have great potential to fulfill worldwide energy needs because solar irradiation on Earth is $\sim$ 14000 times

larger than the world's energy consumption. Accumulated over one year, the energy of solar irradiance on Earth is much greater than that which can be produced by all known fossil fuel resources. Figure 1.1B compares the energy potential of existing fossil fuel resources and solar energy. The Sun is an abundant, environmentally friendly, inexhaustible source of energy, which is available in every country particularly in those countries which are expected to experience high economic and population growth in the coming decades [3]. One of the major advantages of solar energy is that it can be captured and converted into electricity by photovoltaic (PV) cells.

Although fossil fuels will continue to dominate the energy production landscape in the coming years, it is expected that solar panel capacity will overtake that of nuclear energy. An illustrative example of this tendency toward the use of renewable energy sources, Portugal was in news reports across the world in May 2016, when it ran entirely on renewable energy for 107 consecutive hours, Figure 1.2. Additionally, in March 2018, the electricity produced from renewable sources in Portugal was 4812 Gigawatts per hour (GWh), exceeding consumption needs by approximately 165 GWh.

Figure 1.2: Headlines of different newspaper reporting that Portugal was able to run for four and a half days only on renewable energy.

However, despite the development of photovoltaic systems over the last few decades, the conversion of solar energy into electricity remains a daunting task because it is not efficient enough and market competitive yet [4].

Currently, the most efficient PV cells are based on III-V semiconductors [5], such as GaAs (gallium arsenide) with a power conversion efficiency (PCE, defined as the ratio between the output electrical power and the input optical power) of $\sim 29\,\%$ [6], and multilayered structures such as GaAs, GaInP (indium gallium phosphide), InGaAs (indium gallium arsenide), GaInNAs (indium gallium arsenide nitride) and Ge (with PCE values as large as $\sim 46\,\%$). However, these cells are too expensive to be competitive [6]. Although presenting lower efficiencies, the most common PV cells are based on crystalline Si (c-Si), polycrystalline Si (p-Si) and amorphous Si (a-Si) with PCE values of ~ 28, ~ 21 and $\sim 10\,\%$, respectively [5, 6]. Si-based PV cells represent about $80\,\%$ of the market, and will remain dominant until more efficient and cost effective PV technology is developed [7]. All-organic and dye-sensitized PV cells are emerging as potential competitors to Si-based as they work under diffuse radiation conditions, which is a significant advantage for integration into urban buildings because Si-based PV cells do not work under such conditions [8]. However, these cells still have low PCEs (maximum of $\sim 12\,\%$) and high fabrication cost, when compared to Si-based cells. Among the efforts to improve PV conversion efficiency, we highlight the emerging field of perovskite-based PV cells, which has gained visibility in recent years due to unprecedented increases in efficiency in a short period of time (~ 6 years) [9, 10]. Recently, a record efficiency of $23.6\,\%$ was reported for a tandem PV cell composed by perovskite and silicon [11]. Despite such promising advances, efficiency is still low, especially in the UV spectral region, and their stability remains an issue since they degrade in ambient conditions, when exposed to air, moisture and UV radiation [12, 13].

The major problem limiting the conversion efficiency in PV cells is the mismatch between material-related absorption and the solar spectrum. The spectral distribution of sunlight at Air Mass 1.5 global (AM 1.5G) consists of photons with wavelengths ranging from the ultraviolet (UV) to the infrared (IR) (280-2500 nm, 0.5-4.4 eV). Both c-Si and perovskite PV cells display large external quantum efficiency (EQE) in the red/NIR spectral region (700 nm to 1100 nm) because they are only able to use a relatively small fraction of solar photons, Figure 1.3. This is due to the fact that each PV material responds to a narrow range of solar photons, limited by the characteristic bandgap energy (E_g) of the material. Focusing on the most used PV cell, which is made of single-junction c-Si and has a E_g of 1.1 eV, the Shockley-Queisser limit imposes a conversion efficiency limit of $\sim 33\,\%$ (approximating the

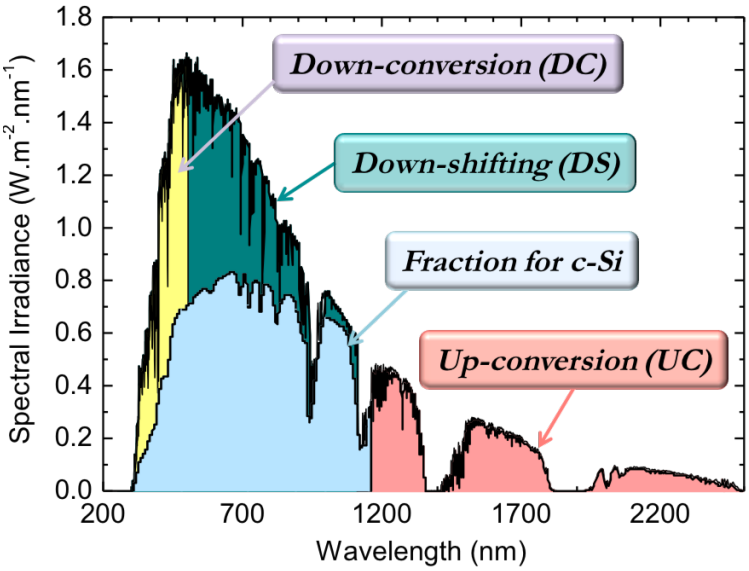

Figure 1.3: AM1.5G solar spectral irradiance spectrum. The shadowed areas represent the fraction available for down-conversion (26 %, up to 550 nm), down-shifting (81 %, up to 1100 nm) and up-conversion (16 % in the 1200-2500 nm range) processes for a c-Si wafer. The absorption curve of Si is also indicated [14].

cell to a black body, at 300 K, and the temperature of the Sun 6000 K) [15]. Photogeneration of charge carriers occurs when the device absorbs photons with energies that are greater or equal to E_g. All photons with energy lower than E_g which reach the PV cell will be transmitted through the device and lost. However, the absorption of photons with energy higher than E_g is also inefficient, since the excess energy is lost as heat through non-radiative recombination of photoexcited charge carriers [16]. The thermalization of photons with energies exceeding E_g and the non-absorption of photons with energy below E_g means that a loss of approximately 50 % of the solar energy reaching Si-based PV cells is lost when converted into electricity. Another problem limiting the conversion efficiency of the PV cells is related with the inefficiency of the PV cells under diffuse radiation conditions.

Different energy ranges in the solar spectrum can be used for PV conversion, as pictured in figure 1.3. In the case of down-conversion, an incident high energy photon is converted into two photons with lower energy, which can lead to an absolute emission quantum yield (q) up to $q \leq 2$. In up-conversion, two low energy photons are converted into one high energy photon, $q \leq 0.5$. Down-shifting is similar to down-conversion but in this case only one photon is emitted, $q \leq 1$.

Down-converters or -shifters are placed on top of PV cells to absorb part of the solar spectrum and re-emit at specific wavelengths, shifting the wavelength of UV and visible photons toward the spectral region that is converted by the PV cell with high efficiency. Up-converters absorb photons that are not used by the PV cell, shifting transmitted photons from the IR to the near-infrared (NIR) or visible part of the spectrum: transmitted photons are usually reflected back into the PV cell by a back reflector [17].

Inherent thermalization and non-absorption losses can be minimized using luminescent materials as spectral converters [4]. This approach, termed third-generation solar photon conversion, involves the incorporation of spectral converters [18–22] onto PV cells. It is expected that spectral converters will help overcome the above-mentioned limitations of PV cells, reducing the mismatch between the absorption and solar spectra, and increasing the absorption of diffuse radiation. Spectral converters can be applied to existing PV cells in the form of an active photoluminescent layer, whose purpose is to absorb radiation and convert it to wavelengths that are more efficiently converted. Spectral converters do not require modifications to the standard solar cell architecture or intrinsic device materials and, can be easily optimized for specific types of solar cells through a wise selection of the incorporated luminophore.

All spectral converters exploit the photoluminescence processes to capture low- or high-energy photons that cannot be used by the bare PV cell and convert them to photons with a useful wavelength. In this thesis, two types of spectral converters are studied: luminescent down-shifting (LDS) layers and luminescent solar concentrators (LSCs), Figure 1.4.

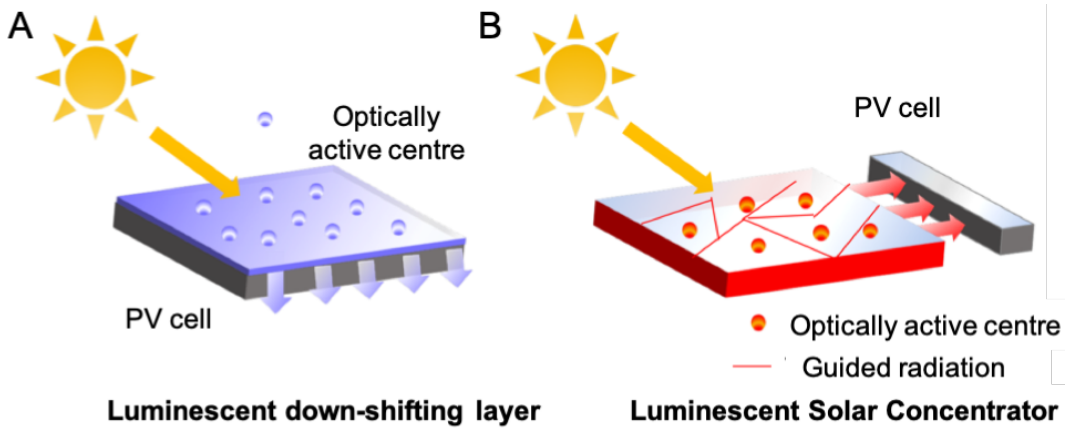

Figure 1.4: Schematic representation of a solar cell with a (A) down-shifting layer and (B) a luminescent solar concentrator.

These two approaches are in very different stages of development. While for LDS layers the main research strategy is to increase the performance of PV cells, LSCs should be seen as complementary devices for PV cells in some specific niche markets. The ability of LSCs to concentrate sunlight onto small areas can contribute to reduce the size and cost of PV cells [23]. Also, the coupling of PV cells to the edges of LSCs is a very interesting strategy to PV urban integration, presenting solutions to different challenges. From the point of view of EU policy, buildings are a strategic focus in the bid to achieve a sustainable and competitive low-carbon economy by 2020. The European Commission encourages Member States to decrease energy consumption in buildings and convert national building stocks from energy consumers to energy producers through retrofit measures and renewable energy sources [24]. The main goal is the construction of zero-energy buildings, with zero net energy consumption, meaning the total amount of energy used by the building on an annual basis is roughly equal to the amount of renewable energy created on-site or by renewable energy sources elsewhere [25]. For instance, the company AVANCIS CNBM is implementing new market solutions like rooftop systems, Figure 1.5A and solar facades for architects, engineers and planners 1.5B. This is driving down the costs of solar technology to a level below that of conventional energy, and thus speeding up the changeover to a global energy supply based on renewable energy sources.

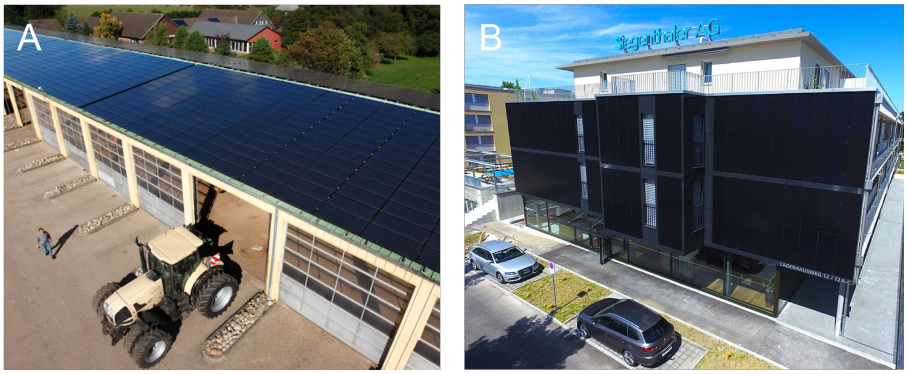

Figure 1.5: (A) Photo of a rooftop systems with solar modules [26] and (B) a solar facade in Bern, Switzerland [27].

While rooftop PV systems pose no implementation challenges, PV cells on facades reduce the amount of sunlight inside buildings and design options are limited: PV panels are typically black and nontransparent. Aesthetic concerns make solar panels a less desirable option in public areas. In order to overcome some of these limitations, LSCs could be embedded in facades, windows, walls as well as on rooftops, and coupled to efficient and small PV

cells, allowing everyday buildings to be transformed into harvesting machines [16]. From an aesthetic point of view, LSCs may be appealing because they can be produced in almost any color and shape, and can either be translucent or opaque [28]. Some examples of existing buildings with coloured facades where such technology could be implemented are presented in Figure 1.6.

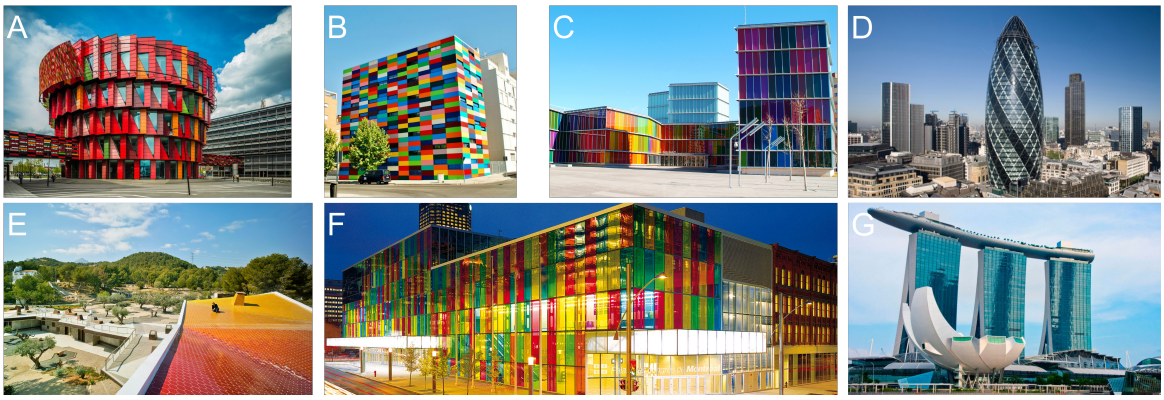

Figure 1.6: Photos of colourful buildings around the world. (A) The Kuggen in Gothenburg, Sweden [29], (B) Carabanchel 24 building in Madrid, Spain [30], (C) MUSAC (Museo de Arte Contemporáneo de Castilla y León) in León, Spain [31], (D) The Gherkin building in London, United Kingdom [32], (E) El Captivador in Alicante, Spain [33], (F) The Palais des congrès de Montréal in Montréal, Québec, Canada [34] and (G) Marina Bay Sands building in Singapore [35].

Beyond policy and aesthetic considerations, the integration of PV panels into the built environment has proven difficult because PV panels operate optimally under direct irradiation. In the built environment, sunlight is diffuse and non-uniform, as it is scattered and reflected by buildings, trees, and clouds, reducing the performance of solar cells [36]. LSCs operate similarly in direct and indirect sunlight [37]. Despite having modest electrical generation efficiency, LSCs are cheap, can be applied over large areas, and incorporated into construction elements [38].

LSCs can also be implemented in wearable fabrics and mobile energy devices [39]. In particular, target delivered power values up to $10\,W$ may be feasible with LSCs, which is sufficient to charge low-voltage devices such as mobiles phones, sensors and wi-fi routers. There are some examples of PV cells being applied to fabrics like backpacks and coats, but the exposed area tends to be small, and design is limited by the aesthetics of PV cells. Using LSCs, it would be possible to have devices with larger exposed area without compromising

aesthetics and reducing the amount of PV material needed, reducing the cost of the device. LSCs can also be used in urban furniture to complement the performance of existing PV devices, increasing the available area for PV conversion and allowing electronic devices to be charged. Examples of existing wearable PV devices and urban furniture are presented in Figure 1.7.

Figure 1.7: Wearable PV devices and PV urban furniture. (A) Tommy Hilfiger Solar Clothing [40], (B) Solar Backpack from EPFL [41], (C) Solaires Solar-Powered Backpacks Charge Gadgets on the Go [42], (D) Lux Solar-Panel Necklace Lights Up Any Outfit [43], (E) Soofa 'smart bench' [44], (F) eTree, Tree-like street furniture [45] and (G) Solar-Powered Soldiers to Revolutionize Australian Combat [46].

A third possible application for LSCs in every day life is noise barriers along highways. A group of researchers in The Netherlands has been developing this idea in the framework of a program called SONOB - Solar Noise Barriers. The main goal of this program is to tackle the issues related to the production of larger-scale LSC devices, and monitor their performance under the harsh conditions experienced in The Netherlands over the course of a year.This project resulted in three publications [38, 47, 48], and the main results are summarized below. Two $12\,mm$ thick noise barrier modules with an area of $4 \times 5\,m^2$ each were constructed, one placed facing East/West and the other North/South, Figure 1.8A [38]. In turn, each module was made up of 4 individual $1 \times 5\,m^2$ panels. Two were $8\,mm$ thick clear glass plates with embedded Si PV cells, and the other two dye-embedded LSC devices, one containing the fluorescent dye Lumogen Orange240 and the other Lumogen Red305 (both dyes provided by BASF). In the first work, the relative performance of the largest LSC constructed to date is

described. Comparisons are made between the performance of North/South and East/West facing panels during a sunny day. It is shown that the performance of the East/West panels varies much more over the course of the day, as the structural elements of the barrier interfere with solar illumination and cause shading, but perform similarly for both front and back illumination conditions. Results obtained over a period of 200 days mirror the results over a single sunny day. This work also demonstrates the importance of frame design to minimize self-shading of the LSC panels [38].

In the second work, the relative performance of the large area LSC noise barrier is tested before and after the application of street art, Figure 1.8B [47]. Performance is compared with that of East/West facing panels on a sunny day. It is shown that the edge mounted PV cells that are further away from the artwork perform at about 80 % of their original performance level, while cells mounted nearby show a greater drop in performance, suggesting that the effect of street art is primarily a localized effect. Furthermore, it is demonstrated that illumination by sunlight from the rear side of the panel, opposite to the artwork shows less of a performance drop. In summary, the overall performance of a large-scale prototype LSC device is affected by the application of street art, which blocks out solar radiation, but the effect is mostly confined to areas in the immediate vicinity of the blocked areas, and the remaining area of the panel continues to operate at a reasonable level [47].

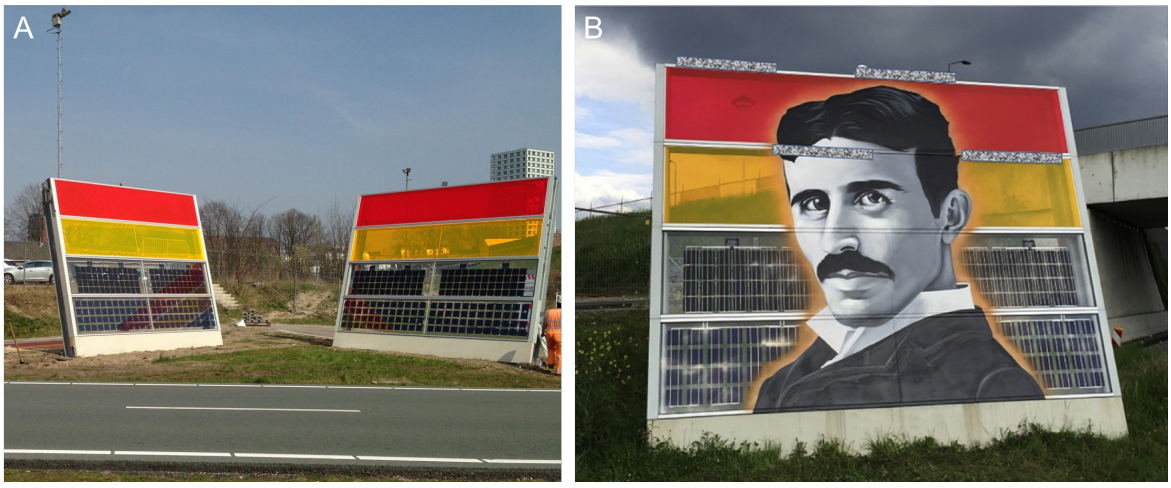

Figure 1.8: (A) Photograph of the LSC noise barrier site. The barrier on the left faces North/South, and the barrier on the right faces East/ West [49]. (B) Photograph showing street art design on the surface of the LSC panel. Adapted from [46].

In the third work [48] comparisons are made for the performance of a number of attached

photovoltaic cells with changing spectral illumination, cloud cover conditions and other seasonal variations, and the temperatures of the cells. Differences in performance are attributed to the positioning of the panels whether facing North/South or East/West. In general, the panels facing East/West run cooler than those facing North/South. The LSCs in both orientations appear to perform more efficiently in cloudy conditions: one factor contributing to this increased performance is that the solar spectrum matches the absorption spectrum of the embedded dye better under cloudy conditions. This work is a step forward in the characterization of large-scale LSC devices, and suggests that the performance of devices can be predicted for any location given sufficient knowledge of the illumination conditions, and is an important step towards the commercialization of these alternative solar energy generators for use in urban settings [48].

In the aforementioned paragraphs LSCs have already been produced at large-scale and implemented in real-life applications showing that the first step towards the transference between laboratory prototypes to real-life solar-energy harvesting units has already started and has potential to be continued and implemented in other real-life applications.

1.1 Luminescent down-shifting layers

In its simple form, luminescent downshifting layers are coatings deposited on the top surface of PV cells, Figure 1.4. As such, LDS layers do not depend on geometric concentration to improve PV devices efficiency, but are instead used to tune the absorption spectral window [14] and reduce the amount of reflected radiation at the PV cells surface. The down-shifting materials absorb the short-wavelength radiation, typically in the 300-500 nm range, and re-emit it at a longer wavelength where the external quantum efficiency of the PV device is high. The lower energy photons emitted by the luminophores after absorption are subsequently absorbed by the PV cell, producing more electron-hole pairs and thus generating higher short-circuit current (I_{SC}) [50]. This should lead to an increase in the EQE of the device in the absorption window of the LDS layer, although experimentally this is not always observed [51].The open-circuit voltage (V_{OC}) and fill factor (FF) typical of each PV cell should not change significantly upon incorporation of an LDS layer since they depend primarily on the intrinsic materials of the PV cell itself [52]. LDS layers can be utilized in many PV devices that exhibit poor spectral absorption to short-wavelength solar radiation. While luminescent

down-shifting could potentially enhance the PV efficiency, it is important to note that the design will not be able to overcome the Shockley-Queisser efficiency limit, as the absorption of a high energy photons by the down-shifting materials can only result in the generation of one electron-hole pair in the solar cell [23, 53].

The luminophores choice for LDS layers fall into the same categories as those used for LSCs, being the most common ones the organic dyes [54–56], quantum dots (QDs) [52, 57–59] and lanthanice (Ln^{3+}) metal ions/complexes [60–63]. Typical host material include polymers [64–67], silica hybrids [68–70], or glasses [62, 63, 71] although there are also numerous examples of luminophores coated directly onto device surface [72, 73]. When a host material is used, the thickness must be optimized to minimize edge emission and reflectance [50, 74].

Recent research has focused on the optimization of host-luminophore combinations, with the goal of improving the stability, efficiency and ease fabrication of the devices. LDS layers should be tailored to the PV cell in use, and as such, there is no one size fits all [16]. In Table 1.1 figures of merit for a variety of LDS layers using different PV devices are listed.

Currently, Si-based PVs correspond to 90 % of the global market [16] and thus, significant research has been dedicated to the design of LDS layers for these cells. Theoretical studies to determine the maximum efficiency gains possible by applying LDS layers to Si PV cells predict an increase of 0.6-1 % [87]. Jin *et al.* showed that the maximal electrical outputs of commercial c-Si and a-Si PV cells are effectively enhanced by surface coating of the ORMOSIL (organically modified silicate) composite phosphor films doped with $[Eu(phen)_2]Cl_3$ (phen=phenanthroline) or $[Tb(bpy)_2]Cl_3$ (bpy=2,2'-bipyridine), which can convert UV into visible radiation. The relative radiation-to-electricity conversion efficiencies around 118 % and 108 % for the hybrid c-Si and a-Si PV cells devices, respectively, could be increased by optimizing the incorporation of the Ln^{3+}-based complexes. Since the enhanced outputs for c-Si and a-Si PV cells are strongly dependent on the coating conditions of ORMOSIL:$[Eu(phen)_2]^{3+}$ and ORMOSIL:$[Tb(bpy)_2]^{3+}$ films, greater enhancement of these outputs are expected to be made by improving the coating process and film quality [88]. Some studies used isolated Eu^{3+} or Eu^{2+} ions doped in polymer hosts as the LDS layer; however the low absorption coefficients associated with Ln^{3+} ions limited the efficiency [18, 89]. However, the use of Eu^{3+} or Eu^{2+} phosphors or complexes has delivered improved performance. Chen *et al.* reported a Ba_2SiO_4:Eu^{2+} LDS layer coated directly onto a Si PV cell, in which the addi-

Table 1.1: Figures of merit for LDS layers applied on different PV cell types, where the absolute power conversion efficiency (PCE (%)) achieved and the percentage increase in PCE (ΔPCE (%)) compared to the bare cell is also presented.

Cell type	Luminophore	λ_{abs} (nm)	λ_{em} (nm)	PCE	ΔPCE	Ref.
Si	Ba_2SiO_4:Eu^{2+}	350	510	17.7	4	[75]
c-Si	Gd_2O_2:Eu^{3+}	350	625, 700	12.97	24	[60]
c-Si	Si QDs	400-1000	850	3.8	23	[76]
c-Si	$[EuL_3](Et_3NH)_3$	325	615	9.51	6	[61]
c-Si	$[TbL_3](Et_3NH)_3$	325	540	9.42	5	[61]
c-Si	CdTe/CdS/ZnS QDs	350	600	16.14	5	[70]
c-Si	$CuInS_2$/ ZnS QDs	400	600-700	16.21	4	[58]
c-Si	Mn^{2+}, $Zn_xCd_{1-x}S$/ZnS	350	600	14.3	4	[72]
CIGS	Lumogen Violet/Yellow	350-475	475-600	-	2.93	[54]
GaAs	CdSe/ZnS QDs	350	540	18.05	25	[73]
GaAs	CdZnS/ZnS QDs	300	450	28.7	3	[57]
InGaP	CdS_xSe_{1-x}/ZnS QDs	350	580	15.6	15	[77]
CdS/CdTe	Eu^{3+}, Mn^{2+} doped glasses	400	615	17.53	7.14	[78]
DSSC	CdSe/ZnS QDs	350	500	2.98	5	[79]
DSSC	Lumogen Violet	370	430	4.5	68	[64]
DSSC	EuD_4TEA	350	620	3.41	62	[80]
DSSC	$CaAlSiN_3$:Eu^{2+}	460	625	5.0	40	[81]
OPV	C545T:Alq_3	300-500	575	3.82	15	[82]
OPV	C QDs	350	550	3.18	12	[83]
PSC	YVO_4/Eu^{3+}	295	610	7.93	7	[84]
PSC	$ZnGa_2O_4$:Eu^{3+}	400	610	13.8	29	[85]
PSC	Lumogen Violet	370	450	18.7	8	[86]

CIGS = copper indium gallium selenide, CdS/CdTe = cadmium sulfide/cadmium telluride, DSSC = dye-sensitized solar cell, OPV = organic photovoltaic, PSC = perovskite solar cell, C545T= 10-(2-benzothiazolyl)-2,3,6,7-tetrahydro-1,1,7,7-tetramethyl-1H,5H,11H-(1)benzopyropyrano(6,7,8-i,j)quinolizin-11-one; Alq_3 = tris(8-quinolinolato) aluminium; EuD_4TEA = europium(III) tetrakisdibenzoylmethide triethyl ammonium.

tion of Ag nanoparticles and a SiO_2 spacer increased the PCE of the cell from 17.1 % to 17.7 % [75]. A LDS layer comprised of Gd_2O_2S:Eu^{3+} with an absolute emission quantum yield of 0.27-0.33, doped in poly(vinylpyrrolidone) and spin-coated onto a polycrystalline Si

cell (PCE=10.44 %) was also reported. The $Gd_2O_2S{:}Eu^{3+}$ phosphors formed spherical particles and improved both the antireflection properties and I_{sc} of the cell, increasing the PCE to 12.97 % [60]. Although the majority of studies have been focused on Eu^{3+} or Eu^{2+} as the luminophore, other Ln^{3+} ions have also been investigated with comparable performance. For example, Fix *et al.* showed that LDS layers prepared from $[LnL_3](Et_3NH)_3$ (Ln = Eu, Tb) (L = triazole-pyridine-bis-tetrazolate antenna) doped in ethylene vinyl acetate (EVA) by spin-coating delivered a moderate increase in the PCE from 9 % to 9.51 % and 9.42 % for Eu^{3+} and Tb^{3+} analogues, respectively. A $[Eu(tta)_3phen]$ complex was also incorpoated in EVA but despite the increase of EQE observed in the UV, the I_{SC} and PCE of the solar cell decrease after eposition of the modified EVA, Figure 1.9. This can be explained by the small loss of EQE observed in the visible part of the spectrum, which can originated from a parasitic absorption in the same region [61].

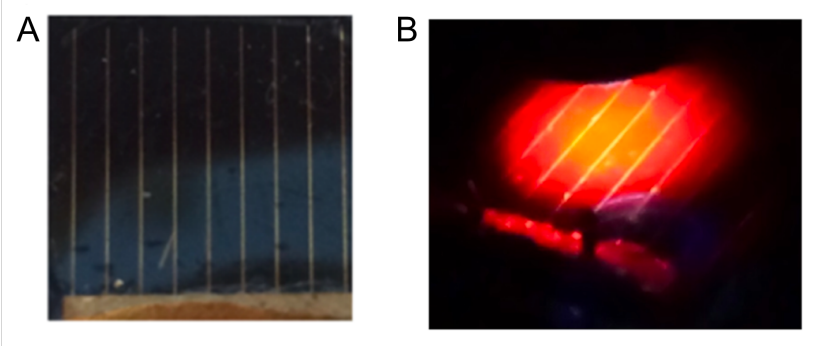

Figure 1.9: c-Si cell fabricated and coated with ethylene-vinyl acetate including [Eu(tta)3phen]. Top view (A) without illumination and (B) illuminated at a wavelength of 350 nm. Adapted from [61].

Chung *et al.* reported down-shifting phosphors composed of $Y_2O_3 : Eu^{3+}$ or $Y_2O_2S : Eu^{3+}$ dispersed in either polyvinyl alcohol (PVA) or Poly(methyl methacrylate) (PMMA) on top of multi-crystalline Si PV cell: fourteen-fold increase in PCE was found under UV irradiation for which the absorption of c-Si is low [90]. McIntosh *et al.* presented results on c-Si PV cells where the PMMA encapsulant contained down-shifting molecules like Lumogen dyes. These results indicate a 40 % increase in EQE for operating wavelengths up to 400 nm [91]. Stupca *et al.* demonstrated the integration of ultra thin films (23-10 nm) of monodisperse luminescent Si nanoparticles on polycrystalline Si PV cells, 1 nm sized blue emitting and 2.85 nm red emitting particles enhance the conversion efficiency by 60 % in the UV and 3-10 % in the

visible for the red and blue emitting particles, respectively [92].

Recent attention has shifted to the use of QDs as luminophores for LDS layers. Draaisma *et al.* addressed the aggregation of QDs in host materials by exchanging capping ligands on $CuInS_2$/ZnS QDs with thiol-functionalized oligocaprolactone to increase solubility within a UV-curable acrylate resin host, Figure 1.10. The LDS layers yielded an overall decrease in PCE when applied to the Si PV cell. This study demonstrates that careful control of absorption and the quantum yield of the QDs, as well as the adhesion of the layer to the PV cell are crucial to obtain working LDS layers [51].

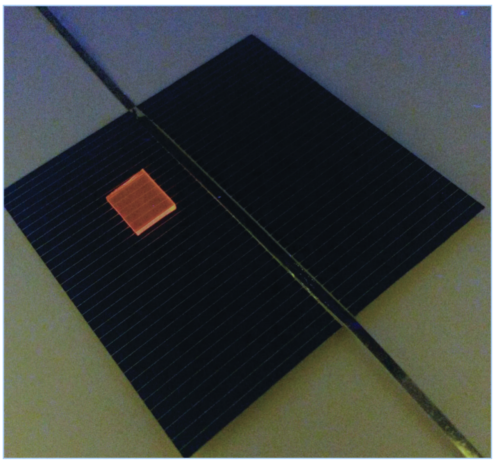

Figure 1.10: Photograph of the polymer-QD composite placed on top of a c-Si solar cell. The photo has been taken under 366 nm UV illumination. Adapted from [51].

Xuan *et al.* produced red-emitting CdSe/CdS/ZnS QDs though microwave synthesis, which led to highly reproducible products. Although the QDs displayed a moderate absolute emission quantum yield of 0.25 when doped into a silica matrix and coated on a Si PV cell, an increase in the PCE of 0.8 % from 15.34 % to 16.14 % was observed [70]. The same group reported an air-exposed, one-pot, microwave synthesis of $CuInS_2$/ ZnS QDs, which showed high absorption below 400 nm, high absolute emission quantum yield of 0.56 and emission in the red/NIR region. Upon incorporation into a PMMA host and coating on a Si PV cell (PCE=15.6 %), a PCE increase to 16.21 % was observed [58]. These QDs had the additional advantage of low toxicity compared with Cd-based alternatives. Levchuk *et al.* demonstrated an easily scalable one-pot synthetic route to fabricate Mn^{2+} doped $Zn_xCd_{1-x}S$/ZnS nanocrystals. The QDs showed absolute emission quantum yields up to 0.70 and the synthesis gave consistent results when scaled up to 40 times the initial volumes. The QDs were applied

directly to Si PV cells using the doctor blading method and an increase from 13.8 % to 14.3 % in the PCE was observed [72].

LDS layers are often applied to cells in conjunction with other surface modifications to minimize reflectance and maximize luminophore absorption. Xu *et al.* patterned the Si substrate by nanosphere lithography to lower the reflectance of the surface and also applied a Si-QD/SiO_2 composite layer. A PCE increase from 3.1 % to 3.8 % was observed, demonstrating that LDS layers can be used effectively in conjunction with other radiation management techniques to improve the overall efficiency [76]. Long afterglow $SrAl_2O_4$:Eu^{2+},Dy^{3+} phosphors were successfully synthesized by sol-gel process. Under UV excitation, the emission of $SrAl_2O_4$:Eu^{2+},Dy^{3+} matches to the spectral response of the Si PV cells. When it was embedded in SiO_2 film and applied as luminescent downshifter on the front side of Si PV cell, the conversion efficiency of the cell under one Sun illumination is improved 4.6 % maximum as compared to the one with pure glass. After 100 mW/cm^2 illumination for 1 min, the light source was turned off. The PV cell still shows an efficiency of 1.16 % in the dark due to the long after-glow properties of $SrAl_2O_4$:Eu^{2+},Dy^{3+} phosphors [93].

Thin film chalcogenide solar cells are potentially well suited for LDS applications as they typically exhibit narrower EQE ranges than Si cells [50]. Parel *et al.* combined LSC and LDS properties in a so-called concentrating LDS layer. This layer consisted of Lumogen dyes (Violet 570, Yellow 083 and Orange 240) doped in a PMMA plate placed on a CdTe cell. The geometric concentration occurs by placing a large area LDS plate on a smaller area PV cell in a planar architecture. An increase of up to 20 % in the I_{sc} of the cell was obtained, demonstrating the potential of the architecture [56]. Thick LDS films prepared from combinations of Lumogen dyes (Violet 570 and Yellow 083) in polyvinyl butyral (PVB), Figure 1.11, were also applied to CIGS cells. An absolute emission quantum yield of 0.96 was obtained and a 2.93 % relative increase in PCE was observed, which was in good agreement with simulated predictions [54].

Quantum dots luminophores have also been attracting significant attention in LDS layers for thin film cells. Han *et al.* used CdS and CdSe/ZnS QDs of different sizes to tune the emission colour in LDS layers applied to GaAs-based PV cells. These cells have a better short-wavelength response than other thin film technologies, their integration with LDS systems is often overlooked. A PCE increase from 14.48 % to 18.05 % was achieved for green-emitting

Figure 1.11: Photo of layers with combined dyes, V570, and Y083 (from left to right) under UV radiation (300-420 nm). Adapted from [54].

CdSe/ZnS QDs applied directly to the cell surface [73]. Hodgson *et al.* characterized the performance of CdS_xSe_{1x}/ZnS QDs (absolute emission quantum yield of 0.51), doped in PMMA as a function of concentration. A maximum PCE increase of 1.7 % was observed at optimum concentration [52]. Commercial QDs Trilite 585 and Trilite 665 (absolute emission quantum yield of 0.41), were deposited onto an InGaP solar cell and subsequently coated with a semiconductor passivation layer. Resonance energy transfer occurred from the passivation layer to the QDs, enabling a two mechanism LDS process, from both direct illumination and resonance energy transfer. This resulted in an improvement in PCE of 2 % giving a maximum PCE of 15.6 % compared to the bare cells (PCE=13.6 %) and illustrates how LDS can be used in conjunction with surface passivation to minimize charge carrier recombination [77]. Polydimethylsiloxane films were doped with CdZnS/ZnS core-shell QDs (absolute emission quantum yield up to 0.50), and nanopatterned using a Si-based mold to imprint the moth eyed pattern on the polydimethylsiloxane. This moth eyed coating decreased surface reflection. A PCE increase of 0.9 %, from 27.8 % to 28.7 %, was observed giving another example of how contemporary LDS layers are viewed as complimentary to other surface treatments [57].

There are some examples in the literature reporting the application of LDS layers incorporating more than one luminophore. Steudel *et al.* reported borate glasses doped with Sm^{3+}, Eu^{3+} and Tb^{3+}. These glasses were co-doped with two of the rare-earth ions for an absorption broad-band. The gain in the I_{sc} density of the CdTe solar cells were measured. Although the single-doped glasses revealed a slight increase in the I_{sc} density, the doubled-doped glasses allowed higher efficiency gains since a significant broader spectral range is covered for absorption. For a Tb^{3+}/Eu^{3+} doped glass, an efficiency increase of 1.23 %was achieved [94]. Song *et al.* codoped phosphate glasses with Mn^{2+} and Eu^{3+} ions, Figure 1.12, to investigate their potential as bi-functional superstrate glass for CdS/CdTe soalr cells and experimental performances of LDS layers were obtained. As a result, the codoped glasses were effectively

improve the photoelectric conversion efficiency by 7.140 % compared to bare CdS/CdTe solar cells [78].

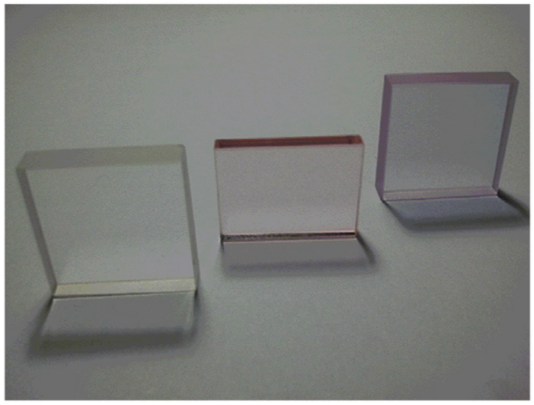

Figure 1.12: Photograph of Eu^{3+}-doped, Mn^{2+}-doped and Eu^{3+}-Mn^{2+} codoped samples, from the left to right, respectively. Adapted from [78].

LDS layers are not limited to applications in the surface of the devices. Liao *et al.* deposited CdSe/ZnS QD aggregates (absolute emission quantum yield = 0.40) between the transparent conducting oxide (TCO) anode and a CdS/CIGS p-n junction via pulsed spray deposition. A PCE increase of 0.92 %, from 8.42 % to 9.34 % was measured [95]. Also, the use of internal LDS layers is not limited to QD-based systems. Bouras *et al.* used Nd-doped SnO_2 films as a luminescent TCO layer in CIGS cells. The layers showed efficient energy transfer from the SnO_2 host matrix to the Nd^{3+} dopants, leading to an enhancement of the I_{sc} of the cell [96]. The glass cover slide can also be transformed into an LDS layer by doping with metal ions. Silicate glass slides doped with Ag^+ or Cu^+ by ion exchange were tested as cover slips for GaAs-based cells. Cu^+ performed better than the Ag^+ doped glass, with a 2 % increase in maximum power output observed, despite the low absolute emission quantum yield (0.004) [63].

LDS layers can be applied to DSSCs to improve both the spectral response and stability, by inhibiting UV-induced degradation of the dye. Griffini *et al.* have demonstrated LDS layers for DSSC based on Eu^{3+} complexes [80] and Lumogen Violet 570 [64], doped in fluoropolymeric hosts Figure 1.13, which generated an 1.82 % (2.68-4.50 %) and 1.31 % (2.1-3.41 %) increase in the PCE, respectively. Long term outdoor stability tests were performed over 2000 h and the LDS-coated devices showed only 2-7 % decrease in PCE with time, whereas uncoated devices decreased almost 30 % of the initial value. Ahmed *et al.* used plasmonic LDS layers, based

on PMMA doped with CdSe/ZnS QDS (absolute emission quantum yield = 0.71 in solution), to improve the efficiencies of both DSSCs and Si cells. Coupling of the LDS layers to the cells increased the PCE by 2.85-2.98 % and 8.4-8.9 %, respectively [79]. Hosseini *et al.* applied a dual function LDS-reflective layer onto the bottom of a DSSC. $CaAlSiN_3{:}Eu^{2+}$ was used as the luminophore (absolute emission quantum yield = 0.51) and through a combination of LDS and back reflection, an increase in PCE of 3.3 % to 4.8 % was observed [81]. However, despite the potential benefits of LDS layers to DSSCs, there are still few examples.

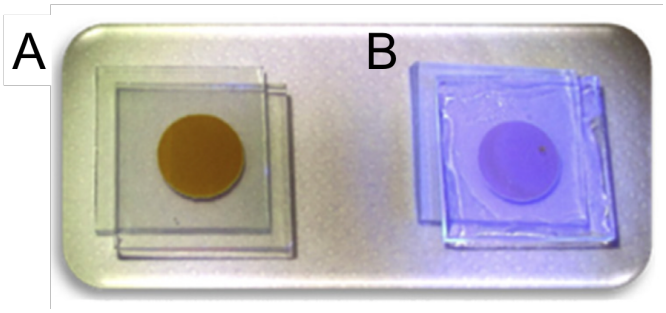

Figure 1.13: Photo the coating-free and a V570-doped LS-DSSC when irradiated with UV radiation. Adapted from [64].

LDS layers are also an attractive method for improving both the efficiency and stability of OPV. The organic materials used in the photoactive and charge extraction layers can show poor stability to prolonged UV-radiaton exposure, which has limited their commercialization to date [97]. Recently, the use of nanopatterned LDS layers by direct nanoimprinting of spin-coated Eu^{3+} and Tb^{3+} doped perhydropolysilazane polymer ceramics was repoted to give red and green emission respectively. Soft imprint lithography was used to form regular nanocone and nanocylinder patterns on the film surface, that act as scattering centers to increase the photoluminescence intensity compared with the non-patterned ones. The emission could also be tuned by varying the cone diameter with a red-shift observed with increasing diameter. The nanopatterned films showed both high transparency and water resistance, with a maximum PCE increase from 4.1 % to 4.6 % observed, along with improved stability [95]. Krebs *et al.* applied commercial tris(hexafluoroacetylacetonate) mono(1,10-phenanthroline)-europium (Eu(hfac)(phen)) PMMA inks as LDS layers to OPV cells (PCE=2.79 %) by doctor-blading and screen-printing. The bifunctional layers increased the device half-life by 850 % for indoor light stability testing and a PCE increase of $\sim$ 0.25 % up to 3.04 % was observed [98]. Transition metal complexes such as $Ag(POP)(Bphen)(BF_4)$ (POP=bisphosphinophenyl

ether, Bphen=bathophenanthroline) have also been used as direct LDS coatings on OPVs, Figure 1.14, leading to improved stability over 150 h continuous illumination at 1 Sun and a PCE increase from 3.66 to 3.76 % [99].

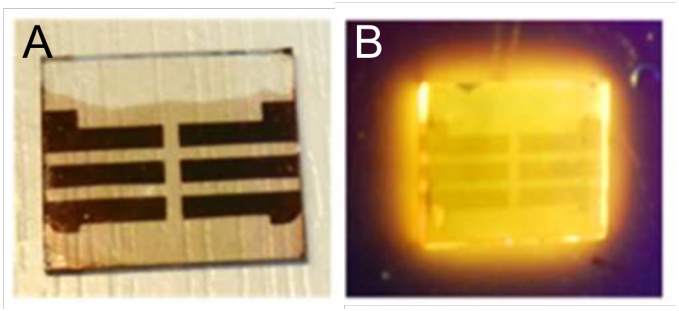

Figure 1.14: Photo of the OPV with an Ag(POP) LDS applied on the radiation incident surface under (A) white light and (B) UV illimunation. Adapted from [99].

Contemporary LDS coatings for OPV using more unusual luminophore or host materials have also been reported. Zhang's group synthesized fluorescent carbon dots (CD) from L-ascorbic acid using (N-(2-aminoethyl)-3- aminopropyl)tris-(2-ethoxy) silane as a stabilization and passivation agent, and also as a host material for the CDs. The CD-silane hybrid was converted to a solid through hydrolytic condensation of the silica network due to solvent loss when applied to the cell surface by spin-coating. Upon incorporation into the silane host an increase in the absolute emission quantum yield from 0.04 to 0.09 and in the PCE from 2.85 to 3.18 % were observed [83]. A 10-(2-benzothiazolyl)-2,3,6,7-tetrahydro-1,1,7,7-tetramethyl-1 H,5H,11 H-(1) benzopyropyrano(6,7,8-i,j)quinolizin-11-one (C545T) fluorescent molecule doped tris(8-quinolinolato) aluminum (C545T:Alq_3) LDS layer (absolute emission quantum yield = 0.95) was applied to an OPV cell, yielding a PCE increase of 0.5 % to 3.82 %, due to favorable overlap between the C545T emission and the OPV absorption window [82]. Prosa *et al*. deposited OPV cells over silk fibroin doped with a stilbene luminophore as a LDS layer. The cells with the silk fibroin showed improved stability ($\sim$ 15 % PCE decrease compared with $\sim$ 35 % for reference device) over 70 days in a glove box and afforded an indium tin oxide free flexible device [100].

In PSCs long term stability is hindered by a susceptibility to thermal and UV degradation [101]. The first example of LDS applied to PSCs was by Chander *et al*. who applied a YVO_4/Eu^{3+} nanophosphor by spray deposition to the device surface, Figure 1.15. The coated PSCs showed higher efficiencies after continuous radiation soaking, with a PCE increase

from 7.42 % to 7.93 % and improved stability compared to uncoated devices [84]. Hou *et al.* demonstrated a method of LDS incorporation into PSCs by doping $ZnGa_2O_4$:Eu^{3+} into the mesoporous TiO_2 layer. This resulted in a PCE increase of over 3 %, from 10.67 % to 13.80 %, and presents an interesting method of spectral conversion with minimal loss mechanisms [85]. Very recently, Bella *et al.* demonstrated a PSC coated with a Lumogen Violet-fluoropolymer LDS layer on the top side, and an undoped polymer encapsulation coating on the back side of the cell. The coated PSCs showed improved stability over six months compared to the bare devices under continuous UV illumination, with a PCE increase from 17.31 % to 18.67 % [86]. PSCs with only the Lumogen Violet LDS layer and without the back polymer coating also showed improved stability compared to the bare cells, with efficiency losses only occurring after 75 days continuous illumination in an inert atmosphere. This result indicates that the role of the LDS layer in reducing UV degradation is critical. Although examples of LDS for PSCs are limited, the field is highly dynamic, and will certainly change in the near future.

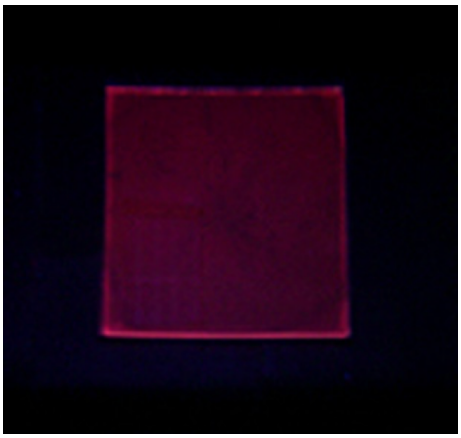

Figure 1.15: Photo of a YVO_4:Eu^{3+} phosphor layer coated on quartz substrate recorded under UV (300 nm) illumination. Adapted from [84].

1.2 Luminescent solar concentrators

Luminescent solar concentrators, Figure 1.16, are complementary devices comprising a transparent substrate (flat sheet of glass or plastic) that can be either doped or coated with optically active centres. Solar radiation reaching the surface of the concentrator is partially refracted into the photoluminescent material and after absorption by the active centres, photons are re-emitted isotropically at a lower energy [102].

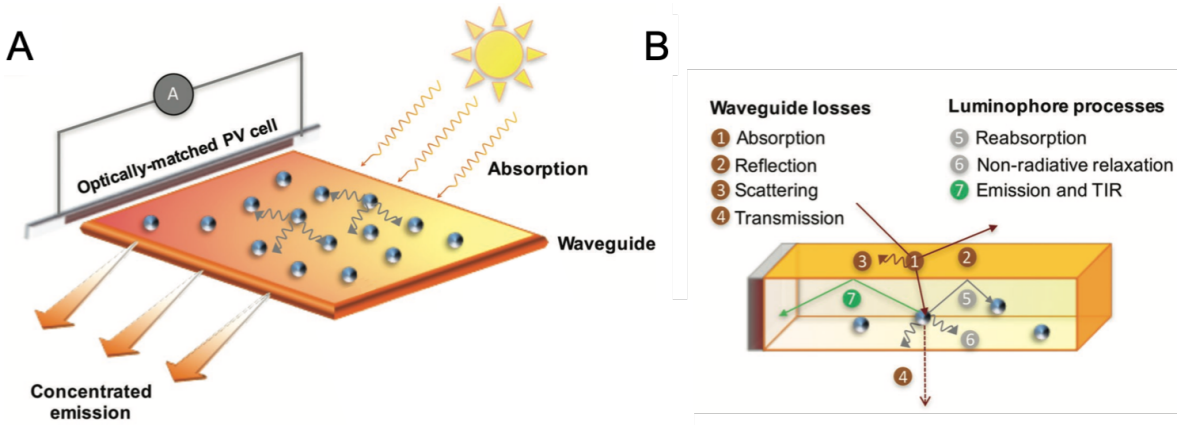

Figure 1.16: Operating principle of a LSC. (A) Radiation incident on the LSC is absorbed by the luminophores and re-emitted at longer wavelengths. The emitted photons are propagated through the waveguide by total internal reflection, resulting in concentration of the emission at the slab edges. The concentrated emission can be used to sensitize an optically matched PV cell, placed at one, some or all of the edges. (B) Primary processes and losses occurring in a planar LSC. Waveguide losses include absorption, reflection and scattering of the incident sunlight at the surface or internal defects, or complete transmission. Luminophore losses include low absorption or emission efficiencies (e.g., due to non-radiative relaxation), reabsorption of emitted photons by neighboring molecules or emission of photons within the escape cone of the waveguide. Adapted from [16].

Although the LSC toolbox is fairly simplistic, in practice the optical conversion efficiency (η_{opt}) of any LSC is limited by intrinsic loss mechanisms, Figure 1.16, many of which are related to the materials choice. Luminophore-associated losses include: incomplete harvesting of the solar spectrum, a low absorption efficiency and/or low absolute emission quantum yield, photodegradation of the luminophore, and reabsorption losses due to the absorption of emitted photons by neighboring luminophores. The luminophores should exhibit:

- Broad absorption spectrum with a high molar absorption coefficient ($> 10^3\, M^{-1} \cdot cm^{-1}$);
- Large Stokes shift (energy difference between absorption and emission spectra) to minimize reabsorption losses;
- High absolute emission quantum yield (> 0.5);
- Emission energy resonant with the PV cell absorption (input-output gain) to minimize thermalization losses;
- Photo and thermal stability.

The waveguide losses include: escape cone losses leading to the non-capture of emitted photons, surface reflections and radiation scattering at internal and external defects and parasitic absorption. The ideal waveguide should thus have a high refractive index (for instance, for a waveguide with a refractive index of 1.5-1.6, 75 %-78 % of all emitted photons will be reflected internally), be free of defects and exhibit a high transmittance outside the absorption region. As such, while the basic LSC design comprises just two components, the demands placed on the materials used are extremely high and there is considerable scope for innovation in this area.

A wide variety of luminophores have been studied in an effort to meet all the desired requirements and thus, an overview of the most used ones 1) organic dyes, 2) transition metals and Ln^{3+}, and 3) quantum dots will be presented followed by a state-of-the-art review on LSCs since its appearance until nowadays.

Since the first studies on LSCs, π-conjugated organic dyes have been investigated extensively as potential luminophores of choice due to their high solubility, high absolute emission quantum yields, high absorption coefficient and good photostability. The most investigated dyes for application in LSCs belong to the following classes of molecules: bipyridines [103], coumarins [104–111], dicarbocyanine iodides [112], dicyano methylenes [108, 113], lactones [109], naphtalimides [109, 111, 114], oxazines [105], perylenes and perylenebisimides [104, 109–111, 114–122], perylenebisimidazoles [116], phtalocyanines [123], phycobilisomes [124–126], porphyrins [123, 127–129], pyrromethenes [109], rhodamines [106–109, 129–131], sulforhodamines [105, 120], tertiary amine derivates of tetra-cyano-p-quinodimethane [132], thioxanthenes [109], (iso)violanthrones [118], and some unspecified dyes including BASF K1 [120, 131, 133], BASK K27 [133] and BASF Lpero [133].

The most commonly used dyes in LSCs have been the rhodamines, coumarins and perylene(bisimides) derivatives. Rhodamines are known for their high absolute emission quantum yield and high molar extinction coefficient but also for their small Stokes shift. As a result, photons can be reabsorbed by neighoring luminophores as they are transported by total internal reflection (TIR) through the waveguide. While this does not necessarily translate into intrinsic loss in itself, if the reabsorbed photons are not subsequently re-emitted or the emitted photons are directed within the escape cone of the waveguide, reabsorption will contribute significantly to optical losses in the LSC. Moreover, organic luminophores show a strong ten-

dency to aggregate via intermolecular π-π stacking interaction between the aromatic rings and the neighboring molecules. Aggregation may lead to either partial or complete quanching due to preferential relaxation via non-radiative channels [134]. In order to overcome reabsorption in molecular luminophores, an alternative approach is to use a multichromophoric system in which efficient energy transfer cascades occur from energy donors to covalently linked acceptors. In this approach, chromophores employing different highest occupied molecular orbital (HOMO)- lowest unoccupied molecular orbital (LUMO) gaps are employed to create an energy gradient through which excitation energy can be shuttled. Such systems are designed to mimic the role of radiation-harvesting chromophoric scaffolds found in plants and photoactive bacteria [125, 128, 135], Figure 1.17.

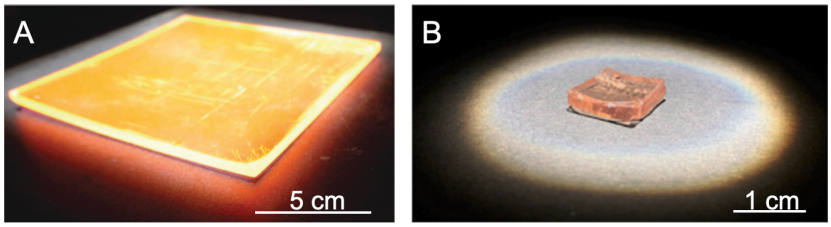

Figure 1.17: Photohraphs of LSCs containing (A) three oligofluorene-BODIPY donoracceptor systems photoexcited at 365 nm, adapted from [125], and (B) chlorophyll molecules under AM1.5 illumination, adapted from [128].

Rare earth ions (sometimes complexed with ligands) are investigated as luminophores for usage in LSCs primarily because of their promise of high photostability and their large Stokes shift, although the presence of organic ligands may compromise the lifetime of the molecules [23]. Large Stokes shift can be achieved by designing luminophores in which the absorption and emission processes occur from different energy states, localized on either the same or different chemical species. Ln^{3+} have been vastly studied as phosphors for LSCs due to their large Stokes shift [5, 136]. However the low molar absorption coefficient associated with f-f transitions [137] prevent the practical application of isolated Ln^{3+} species in solar energy harvesting. But this can be overcomed by taking advantage of the antenna effect, in which coordinated organic ligands absorb radiation and the energy is transferred to the Ln^{3+} centre, from which emission occurs. This solution successfully harness the high molar absorption coefficient of the organic dyes.

Quantum dots are nanostructures from semiconducting materials with dimensions in the order of 10-100 nm. The size of the QDs is in the order of the de Broglie wavelength of

the electron. As a consequence of their restrictive size, excited electrons are confined in the semiconductor, which exhibits optical and electrical properties similar to those of atoms. QDs are also good candidates to be used as luminophores in LSCs due to the possibility of engineering the photophysical properties thought a wise selection of the material/architecture combination employed (*e.g.*, by forming core-shell [138], alloyed [139] or doped QD structures) [140]. This structural versatility provides a way of tuning the E_g in such a way that QDs can absorb and emit across the entire spectral region [141]. One of the main issues concerning the application of QDs in LSC is the toxicity of the metals used (*e.g.* Cd, Pb) [142]. While an argument can be made that in LSCs the QDs are embedded in a host matrix and thus exposure to environment is limited, recyclability and correct disposal measures remain an issue. Researchers may look towards new classes of QDs based on more friendly materials like carbon [143] or silicon [144].

The use of liquid crystalline host materials to control the orientation of luminophores has also been investigated for radiation management in LSCs [145–148]. Planar luminophores typically orient parallel to the alignment direction of the liquid crystalline, such that their primary absorption and emission transition dipole moments are also parallel aligned. This configuration can lead to improved radiation concentration at the corresponding waveguide edges [145–149]. Alternatively, luminophores can be aligned perpendicular to the waveguide surface, which can reduce surface losses to $< 10\,\%$ [149]; however this configuration leads to low absorption and correspondingly low efficiencies due to misalignment of the absorption dipole moment with the incident radiation. This problem can be offset to some extent through the use of a two dye system, in which the absorption axes of each dye are aligned parallel and perpendicular to the host LC matrix, respectively [147].

Despite the potential for generating low-cost solar power, LDS layers and LSC development faces various challenges, most of which related to the materials used in their design [150]. The key requirements for the waveguide are a high radiation-trapping efficiency and optical transparency across the visible spectral range. Furthermore, as the waveguide acts as a host or support material for the luminophore, processability and stability are also important. The waveguide materials choice has received significantly less attention than the luminophores and transparent in visivle and cheap polymers such as PMMA and poly(carbonate) are the most commonly used [23]. Degradation of the luminophore and of the polymer waveguide under

continuous illumination severely affects the device stability. Although PMMA is considered the gold standard waveguide material for LSCs, it is susceptible to photo- and thermal oxidation [151] after prolonged radiation exposure, which gives rise to the formation of photon trap sites which reduce the transport efficiency [152]. The stability question raised by organic polymer waveguides has led to the investigation of inorganic glasses (*e.g.*, silica-zirconia and silica-titania) [153] and organic-inorganic hybrids [136] as potential alternatives as waveguides. While pure glass waveguides have high refractive index, their weight and fragility limit their useful application in building integrated photovoltaics [23]. In contrast, organic-inorganic hybrids offer the best of both worlds, combining processability and chemical functionality from the organic component, with optical transparency and high stability from the inorganic one [154]. Organic-inorganic hybrid waveguides from the ureasil family have also been doped or coated with organic dyes [155–158] and Eu^{3+} β-diketonate complexes [159, 160] to produce LSCs. Ureasils are comprised of a siliceous skeleton that is chemically grafted to poly(ethylene oxide) (PEO)/poly(propylene oxide) (PPO) chains through urea cross-linkages. The huge variety of organic precursors available both commercially and through custom synthesis introduces the possibility of tuning the functional and mechanical properties (*e.g.*, strength, flexibility, porosity) of the hybrid. Moreover, the use of mixed metal oxide sol-gel precursors (*e.g.*, silica-titania, silica-zirconia) provides a means of tuning the refractive index [153]. Organic-inorganic waveguides thus offer the potential to deliver tailored properties for LSCs in a single material.

In the following paragraphs an overview of the current state-of-the-art of LSCs is presented in order to give a global perspective of the field as well as of the current strategies and drawbacks.

Flat plate LSCs were first developed in the late 1970s [107, 130, 161, 162]. The first LSC, at the time termed a fluorescent/luminescent collectors, was reported by Weber and Lambe in 1976. They described a planar LSC using Nd^{3+} and Rhodamine 6G (Rh6G) doped glasses. with an estimated energy conversion efficiency of $\sim 10\,\%$, a value that may be limited by gaps in the absorption spectra of the active media under consideration. While increasing the concentration of the active media in a glass matrix probably improves absorption, a better approach is to mix together dopants that have a common emission region but non-overlapping absorption spectra, *e.g.* dyes, which can also be used for coating [130]. This work was followed

by the theoretical study by Goetzberger and Greubel. The geometry of their desired LSC was determined by the fact that the radiation is collected at one of the edges of the plate. The remaining edges should be coated with highly reflective films in order to increase the reflection efficiency. Such considerations lead them to a triangular shape, as can be seen in Figure 1.18, where it also shown how such concentrators can be arranged to continuously cover large areas. Using this configuration they were able to obtain concentration factors of approximately 100. The advantage of the proposed geometry lies in the fact that different portions of the solar spectrum can be separated and converted by PV cells with different energy gaps. Absorption losses in a triangular plastic LSC were found to be relatively low [161].

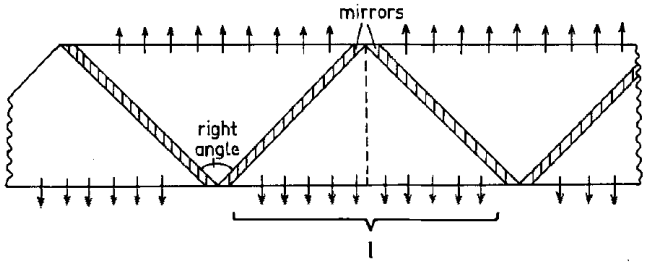

Figure 1.18: The optimum shape of a LSC is a triangle with a right angle at the apex. Two sides are mirror coated. The concentrated energy is obtained at the hypotenuse with length l. Adapted from [161].

In the next year, the group of A. H. Zewail published a series of experiments described to illustrate enhanced photon trapping and efficient energy transfer in mixed-dye planar solar concentrators containing, for example, Rh6G and Coumarin 6. These concentrators are able to absorb more solar radiation to give an enhanced photon-flux gain that exceeds the single-dye concentrator. It is also shown that the energy absorbed by the donor dye is transferred efficiently into the emitting acceptor by two competing processes [107].

In the following years, Reisfeld and Neuman announced the fabrication of LSCs made of uranyl-doped glass [163] whose performance was later improved by Reisfeld and Kalisky in 1980 through the incorporation of Nd^{3+} and Ho^{3+} ions [164]. The presence of the Ln^{3+} ions induced an increase in the conversion efficiency with respect to that observed in LSCs based solely on uranyl-doped glass [163] because the energy absorbed by the uranyl group could be efficiently transferred to the Nd^{3+} and Ho^{3+} ions that emit in the NIR spectral range, closer to the maximum sensitivity of the c-Si PV cells [164]. Transition metal utilization was

reviewed by Reisfeld and Jorgensen in the 1980 decade [165, 166].

A substantial increase in LSC research has occurred over the past three decades, where the major advances in the field have been highlighted in several reviews published in the last ten years. Some figures of merit recently reported in the literature are presented in Table 1.2, and it should be noted that the PCE values calculated for LSCs cannot be compared with those calculated for LDS layers as the relative position of PV cells regarding illumination is different. Key concepts related to loss sources (*e.g.* re-absorption and escape cone) and the role of long term photostability, a critical issue common to distinct optical species, were discussed by Rowan *et al.*[150] Another approach which has been pointed out is the use of NIR emitting QDs, despite the low intrinsic absolute emission quantum yields which are still a severe drawback. According to the authors, challenges for organic-inorganic hybrids are envisaged, because it is unlikely that a single organic or inorganic material can overcome the loss issues, the integration of the positive characteristics of each one into a hybrid material is considerably more attractive [150]. In fact, the properties of organic-inorganic hybrid materials are not just the sum of individual contributions from organic and inorganic phases but the role of their interfaces are dominant [89].

The optical losses associated with LSCs were further reviewed in more recent studies. For instance, Reisfeld reported the use of an organic-inorganic hybrid ormocer matrix to incorporate luminescent dyes in order to enhance their optical properties, by reducing re-absorption and increasing photostability [167]. Other studies discussed the possibility of maximising the radiation trapped inside the substrate through the application of selective mirrors that reflect the emitted radiation back inside the substrate [23]. Photonic structures constructed at the surface of the LSC were also employed to increase the trapping efficiency, as one will notice later in this section [167]. The increase of the absolute emission quantum yield by using plasmonic structures was also discussed [23].

Several studies focused on emitting species have been published. A review on the role of QDs as emitting species for LSC applications emphasized that the low absolute emission quantum yields measured in organic matrices, large emission-absorption overlaps, unknown photostability and toxicity are still relevant issues to be addressed [141]. The incorporation of multiple stacks where organic (dyes) and inorganic (QDs) species are combined may result in an enlargement of the absorption range leading to efficiencies well above 10 % [168].

Table 1.2: Figures of merit for LSCs with different architectures.

Architecture	Cell type	λ_{abs} (nm)	η_{opt} (%)	PCE (%)	Ref.
Perylimide-GLYMO, Thin Film, Glass	c-Si	420-620	18.8	-	[119]
DCJTB, Pt(TPBP), Thin Film, Glass	c-Si	300-1400	4.7	6.8	[127]
$M_6(II)X_{12}$, Thin Film, Glass	c-Si	300-1400	-	0.44	[169]
CdSe/CdS QDs, Doped, PMMA	-	300-1400	10.2	-	[170]
PbS/CdS QDs, Doped, Acrylate	-	300-1400	6.1	-	[171]
$CuInSe_xS_{2-x}$/ZnS QDs, Doped, poly(lauryl methacrylate)	-	300-1400	3.27	-	[172]
TPE/PMMA, Thin Film, Glass	-	320	13.2	-	[173]
gem-pyrene ethene/PMMA, Thin Film, Glass	c-Si	300-1400	-	0.32	[174]
LR305/Urethane matrix (LT), Thin Film, Glass	mc-Si	300-1400	2.48	0.49	[175]
F4Eu/F4Tb, Thin Film, Glass	-	290	1.2/1.7	-	[176]
Eu^{3+} bridged silsesquioxane, Thin Film, Glass	-	300-380	12.3	-	[177]
LR305, Doped, Di-ureasil	c-Si	300-800	14.5	0.54	[155]
EVA, LR305/PMMA, Thin Film, EVA	CIGS	300-1400	-	8.14	[178]
Ureasil, PMMA, Eu, hollow core cylinder	-	300-380	72.4	-	[158]
Red LSC	DSSC	300-1400	-	0.1	[179]
PbS QDs doped PMMA, hollow cylinder	c-Si	600-950	6.5	-	[180]

M

= Mo, W, X = Cl, Br, I; F4=silsesquioxane, DCJTB = 4-(dicyano-mthylene)-2-tert-butyl-6-(1,1,7,7-tetramethyljulolidyl-9-enyl-4H-pyran; TPBP = tetraphenyltetraben- zoporphyrin; TPE = tetraphenylethene; LR305 = Lumogen Red 305; EVA = ethylene vinyl acetate.

Bunzli and Chauvin reviewed the work done on the role of Ln^{3+} ions in PV systems. The energy conversion mechanisms are explained and their role in improving the solar energy conversion efficiency is described and proven. A quantitative general assessment is made predicting improvements on the order of 5 % in conversion yield are feasible taking into account both the specific properties of the rare-earth materials and the effective features and needs of the photovoltaic devices [5].

Despite the potential for generating low-cost solar power, LSC development faces various challenges, most of which related to the materials used in their design [150], and various authors (even since the very beginning of the field [165]) concluded that the complementary combination of organic and inorganic compounds into single hybrid materials should play a key role in design optimization [5, 150, 164, 166]. Moreover, despite the quite limited use of hybrid materials in the fabrication of LSCs, their efficiency values, which can be seen in table 1.2 are of the same order of magnitude as those of pure organic LSCs [112, 181, 182]. Besides the influence of materials design, the manuscript gives particular attention to how geometry and emission mechanisms (energy conversion) can be used to enhance the LSC performance. Although the three distinct mechanisms DS, DC and UC can be involved in solar energy conversion, to the best of our knowledge, only LSCs based on DS hybrid materials have been reported until now.

Goldschmidt *et al.* demonstrate that the EQE of a stack of two plates with different dyes, in which four GaInP-based PV cells were placed, is 6.7 %. They argued that the conversion efficiency was limited by the spectral range of the organic dyes used, and if similar EQEs obtained in the 450-600 nm range were obtained for the 650-1050 nm range an overall system efficiency of 13.5 % could be achieved [183]. Slooff *et al.* presented results for $50 \times 50 \times 5\, mm^3$ PMMA plates where both CRS040 and Red305 dyes were dispersed at 0.003 and 0.01 $wt\%$, respectively. The plates were attached to multi-crystalline-Si, GaAs- and InGaP- based cells, and a diffuse reflector (97 % reflection) was used at the rear side of the plate. The highest measured efficiency was 7.1 % for 4 GaAs-based cells connected in parallel (7% in series) [112].

More recently, Yoon *et al.* proposed a luminescent concentrator PV system that embeds large scale interconnected arrays of micro scale Si-based PV cells in thin matrix layers doped with luminophores as an alternative to the conventional LSC planar geometry. The dimensions

and design of the micro-cells allow radiation to be captured not only through the top surfaces, but also through their side walls and bottom surfaces, further increasing their power output by more than 300 %. This unusual LSC design offers improved performance compared to conventional layouts, and a variety of engineering options with particular value in ultra-thin, light-weight and bendable systems [113].

Kate *et al.* presented divalent thulium (Tm^{2+}) doped halide materials that can absorb almost 63 % of the solar power due to absorption bands up to 900 nm and emit and have negligible self-absorption. This resulted in LSCs with power efficiencies around 15 %, arinsing from the absorption over the entire visible spectrum. This material can be applied in high efficiency electricity generating windows as depicted in figure 1.19 [184].

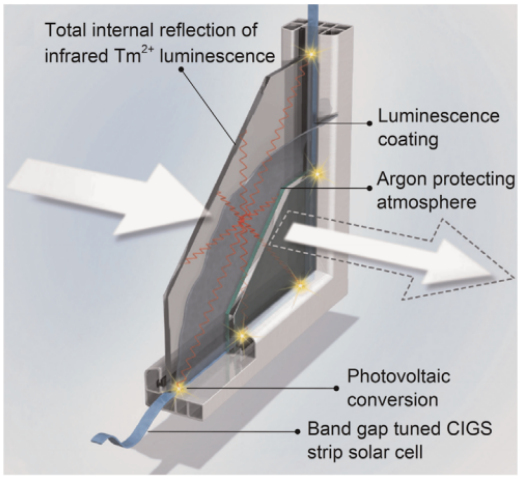

Figure 1.19: Schematic representation of the operating principle of a semi-transparent, colourless luminescent solar concentrator in which the coating re-emits absorbed sunlight that is waveguided by total internal reflection to the edges of the coated glass where PV cells convert the radiation to electric power. Adapted from [184]

Banal *et al.* have reported a transparent planar concentrator using H-aggregates of gem-pyrene ethenes, which display excimer-like emission with Stokes shifts greater than 1 eV. Planar LSCs were prepared by casting a thin film of the gem-pyrene ethane in PMMA (50 % w/w)) onto a glass substrate (absolute emission quantum yield of 0.52), which was subsequently adhered to silicon PV cells, electrically coupled in parallel, delivering a PCE of 0.32 % [174].

Meinardi *et al.* developed a rectangular planar LSC using 'Stokes-shift-engineered' CdSe/CdS QDs with shells to create LSCs without reabsorption losses for device dimensions up

to tens of centimetres, Figure 1.20. Monte Carlo simulations show a 100-fold increase in efficiency using core-shell structures compared to the core-only analogues due to minimized re-absorption losses. With their LSC they measured optical power conversion efficiencies (defined as the ratio between the luminous power collected by the photodiode and the solar power incident onto the LSC) of up to 10 % and an effective concentration factor of 4.4. To experimentally validate the concept of Stokes-shift engineering for the suppression of reabsorption losses, they fabricated a large-area prototype device ($21.5 \times 1.3 \times 0.5\,cm^3$), as shown in Figure 1.20 [170] under room and UV illumination. The same group showed that the decrease in the absolute emission quantum yield caused by interactions between the surface of the QD and the host medium can be somewhat mitigated through surface passivation [172]. Colourless LSCs prepared from alloyed $CuInSe_xS_{2-x}$ QDs coated with a ZnS passivating layer incorporated in a poly(laurylmethacrylate) waveguide exhibited an optical power conversion efficiencies of 3.27 % for $G = 10$ and maintained an absolute emission quantum yield of 0.40.

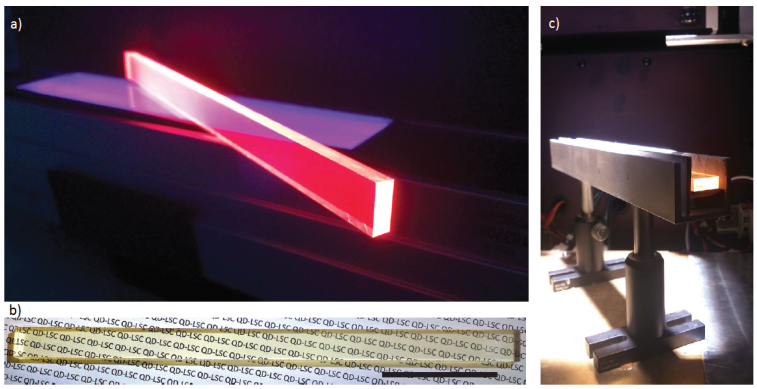

Figure 1.20: (A) Photograph of a QD-PMMA based LSC comprising CdSe/CdS QDs illuminated ate 365 nm, (B) under ambient illumination and (C) the same LSC during measurements of the concentration factor with illumination from a solar simulator(AM1.5G). Adapted from [170]

Due to the fact that CdSe/CdS QDs provide a potentially low-cost and high-performance alternative to photovoltaic devices, Bronstein *et al.* coupled a photonic mirror to a luminescent waveguide to form an optical cavity where emitted luminescence is trapped omnidirectionally, Figure 1.21. By mitigating escape cone and scattering losses, 82 % of the emitted photons travel through the waveguide, creating a concentration ratio of 30.3 for the photons in the 350-450 nm range, in a waveguide with a geometric gain of 61. They also studied the photon transport inside the luminescent waveguide, and they found that unimpeded photon collection

can be achieved across the entire length of the waveguide. In Figure 1.21, the black rectangle is a photovoltaic cell, the blue lines represent solar photons which are then converted to radiation in the red spectral region by the QDs and either collected by the solar cell os lost to the escape cone. In this new design, a wavelength-selective mirror traps the luminescence inside the cavity, increasing the intensity of the red emission inside the cavity. The desired absorption, emission, and reflectance spectra are also sketched. The result is an improvement in the collection efficiency of red photons, which cannot escape, and the improvement of the power output from the solar cell [185].

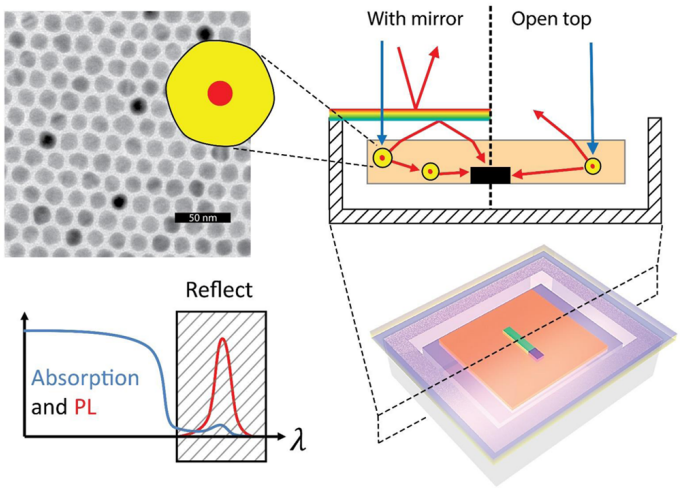

Figure 1.21: Graphic showing a typical transmission electron micrograph of giant CdSe/CdS QDs, incorporated into a traditional luminescent concentrator (on top) and the luminescent concentrator cavity (with mirror). Adapted from [185]

Bradshaw *et al.* introduce and analyse CdSe nanocrystals doped with copper ions ($Cd_{0.999}Cu_{0.001}Se$) which, despite having a fluorescence yield of less than 40 %, exhibit broad absorption of incident radiation and large Stokes shift that exceeds that of the current leading luminophores in LSCs. Their results suggests that broad-spectrum incident-radiation absorption and large Stokes shifts are more important than fluorescence yields for obtaining high-output emission in metre-scale LSCs [186]. If these new materials can be produced in bulk quantities and incorporated uniformly into solid polymeric waveguides, and have long-term stability in sunlight, a major step forward in LSC performance may soon be a reality [187].

Zhou *et al.* designed a rectangular LSC based on NIR-emitting PbS/CdS core-shell QDs encapsulated in a poly(butyl methacrylate-co- methacrylate)/poly(ethylmethacrylate) (pLMA-

co-EGDM) waveguide which exhibited absolute emission quantum yield of 0.40-0.50 and $\eta_{opt} = 6.1$ ($G = 10$) for the champion device, considering single edge emission and with the remaining three edges covered with reflective mirrors [171]. The size of the Stokes shift was shown to depend on both the core size and shell thickness. The addition of transition metal dopants in the form of substitutional defects can also be used to isolate the absorbing centre from the emissive state.

The phosphorescent platinum tetraphenyltetrabenzoporphyrin [Pt(TPBP)] was successfully implemented as the emitter molecule in tandem LSCs by Currie *et al.*, resulting in power conversions efficiencies (PCEs) of 6.8 %, 11.9 % and 14.5 % for c-Si, CdTe and CIGS cells, respectively [127]. Excitation of the singlet state of Pt(TPBP), coupled with the low absorption coefficient of the emissive triplet state produced a large Stokes' shift and minimizes re-absorption in this LSC configuration.

Circular arrangements (prepared by the rub-alignment method) of a coumarin dye embedded in a photopolymerisable LC host coated on a waveguide were shown to effectively concentrate the emitted radiation to the waveguide centre, Figure 1.22 [148]. A cone shape-void was drilled into the centre of the waveguide to enhance out-coupling of radiation and a solar cell was placed on its surface for photosensitization. Selective irradiation of the aligned LSC resulted in a constant open circuit voltage (V_{OC}), but increased the short-circuit current (I_{SC}) by ~ 33 % for silicon and III-V PV cells.

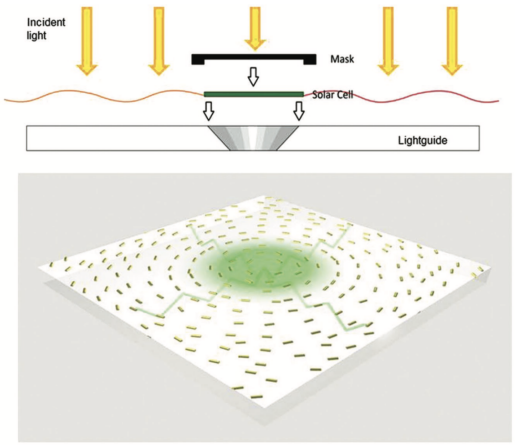

Figure 1.22: Graphic showing a typical transmission electron micrograph of giant CdSe/CdS QDs, incorporated into a traditional luminescent concentrator (on top) and the luminescent concentrator cavity (with mirror). Adapted from [185]

Graffion *et al.* first introduced the use of luminescent bridged-silsesquioxane thin films doped with Ln^{3+} ions as LSC materials [176, 188]. Single wavelength excitation (290 nm)η_{opt} values of 1.2 % and 1.7 % were obtained for Eu^{3+}- and Tb^{3+} containing films, respectively [176]. More recently, a superior silsesquioxane system based on an ethane tetracarboxamide-based organosilane doped with Eu^{3+} ions were also reported [177]. Thin films ($\sim$ 200-400 nm) spin-coated on glass substrates led to highly luminescent coatings with an absolute emission quantum yield of 0.60 and an optical conversion efficiency of 12.3 % (excitation: 300-380 nm). Organic-inorganic hybrid waveguides from the ureasil family have also been doped or coated with organic dyes [155] and Eu^{3+} β-diketonate complexes [159, 189] to produce LSCs. A planar, doped LSC based on LR305 doped in a di-ureasil (two urea bridges) waveguide exhibited an $\eta_{opt} = 14.5$ % (emission: 300-800 nm, $G = 3.3$) for the optimized device, Figure 1.23 [155]. A power conversion efficiency of 0.54 % was obtained for the champion LSC coupled to a c-Si PV cell using the di-ureasil precursor as an optical glue to minimize interfacial losses. Despite the limited use of hybrid materials in LSCs to date, their efficiency values are already comparable to those of pure organic LSCs [155, 176].

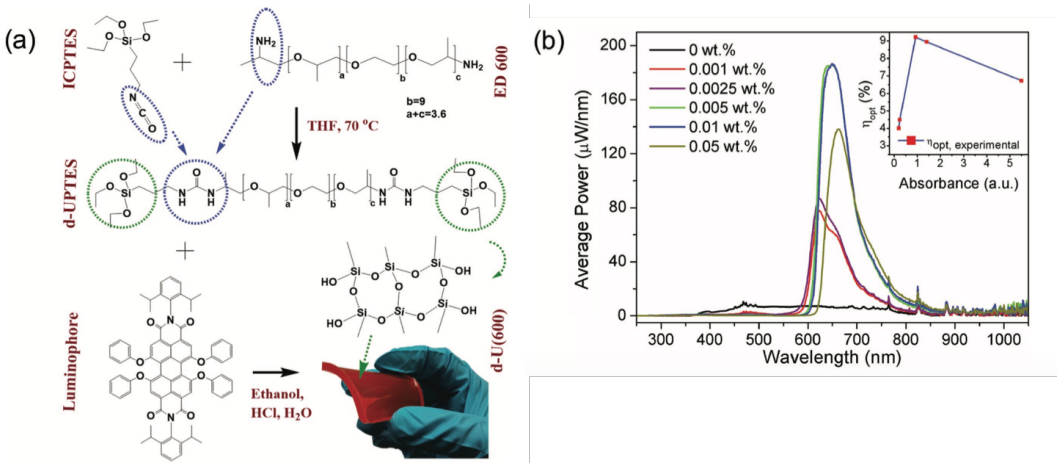

Figure 1.23: Synthesis and characterization of LR305-di-ureasil planar waveguides. (A) Schematic representation of the LSC fabrication. In the first step, the precursors Jeffamine ED-600 and ICPTES are reacted to obtain di-ureapropyltriethoxysilane (d-UPTES). Following the dissolution of the luminophore, LR305, in d-UPTES, acid-catalyzed hydrolysis and condensation of the siliceous network is initiated to obtain the LR305-d-U(600) LSC. (B) Optical power spectra of doped LR305-d-U(600) LSCs with a dark absorbing background, averaged over all four edges. (Inset) Variation of the experimental optical (red squares) efficiencies of the LSCs with a dark background, determined over the 300-800 nm spectral range, with respect to the LSC absorbance. Adapted from [155].

McIntosh *et al*. made a theoretical comparison between square-planar cylindrical LSCs, proposing a new geometry composed of a sequence of attached cylinders. They found that when luminescence occurs close to the surface the optical concentration of a cylindrical LSC can be 1.0 to 1.9 times higher than that of the square-planar LSC of equivalent collection area and volume, depending on the absorption coefficient of the host material. When this multi-cylindrical geometry is considered, a small increase in optical concentration is obtained for all angles of incidence, due to the multiple reflections between neighbour cylinders aligned side by side [190].

The longer and thinner a cylinder, the larger the ratio between the area of its illuminated surface and its edges. Thus, a LSC with a fibre geometry should have a large concentrating potential. As optical and polymer fibres are already produced on large scales, manufacturing processes for these fibres are well known. The production steps are optimized, resulting in low host material losses and low manufacturing cost. At the same time fibres have the advantages of being light-weight and flexible. By analysing the interaction of the solar photons with the fibre, and investigating different configurations, a better understanding of the working mechanism of this type of LSC can be achieved [3], showing the importance of such studies when applied to new LSC geometries.

Inman *et al*. fabricated both solid and hollow cylindrical LSCs using NIR PbS QDs as the active medium in PMMA matrices as can be seen in Figure 1.24. Their experimental results were in good agreement with theoretical calculations showing that the hollow structures can lead to higher absorption of the incident radiation and less self-absorption compared to the solid cylindrical and planar geometries, yielding higher optical efficiencies [180].

Van Sark *et el*. analysed the effect of varying the device geometry on LSC performance using ray-tracing modelling. Hexagonal, square and a right-angle triangle QD doped LSCs of increasing top surface were studied. Their results indicate that all geometries can attain the same minimum relative cost per unit power, thus, varying the geometry type does not offer any significant relative cost reduction. However, the results do show that the selection of the device size is critical for achieving the lowest possible cost per unit power output. So, there is no substantial gain between the three different shapes of LSCs [104].

Taking advantage of the cylinder shape of PMMA-derived plastic optical fibres (POFs), Wu *et al*. fabricated a zero self-absorption hybrid solar concentrator by doping the fibre with

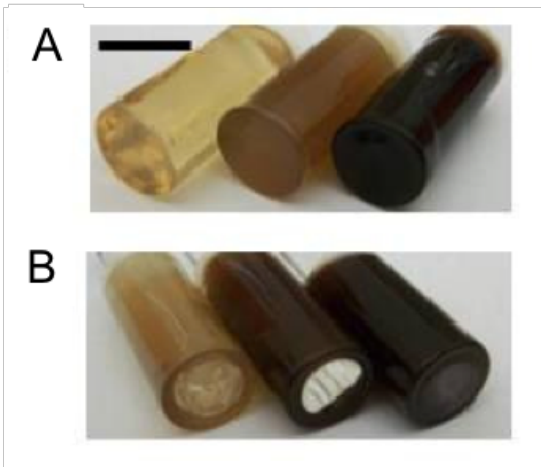

Figure 1.24: Photographs of (A) solid and (B) hollow cylindrical LSCs using NIR PbS QDs with different sizes. The scale represents 1.0 cm. Adapted from [180].

a rare earth complex $Eu(tta)_3phen$. The cylindrical geometry provides a geometric gain of up to $\sim$ 1500 (for a typical diameter of 1 mm and a length of 1 m). To study the re-absorption processes they also measured the emission spectra of the organic solar concentrator doped with the organic complex. These complexes have a long Stokes shift because the energy levels and sub-levels of the ligands and ions belong to two electron systems, Figure 1.25, and compared it to other dyes such as rhodamine 6G [191].

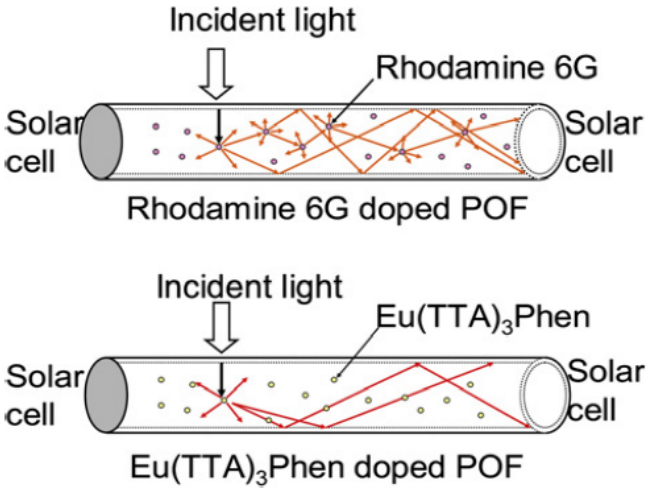

Figure 1.25: Schematic models for two fibre luminescent solar concentrators: Rhodamine 6G doped POF and $Eu(tta)_3phen$ doped POF. In the first one, there is an energy transfer between the luminescent dyes, resulting in a serious self-absorption loss. In the second one, no such energy transfer occurs. Adapted from [191]

Edelenbosch *et al.* used a ray tracing approach to increase the understanding of the working mechanisms in the fibre and optimize the effective concentration potential. A significant result obtained with this approach was that, when comparing homogeneous and coated fibres that absorb an equal number of photons, the coated fibre is indeed more efficient than the homogeneous fibre in the regime of low photon absorption. When the absorption coefficient is high, maximum re-absorption takes place within a relatively short length of fibre. This means that increasing the length of the fibre does not induce more re-absorption but it does increase the geometric concentration. Furthermore, the increase in the geometric concentration is larger than the loss due to the host absorption and scattering, thus increasing the length of the fibre has the potential to increase the effective photon concentration well beyond that achieved by flat plate LSCs. Using fibres will induce high re-absorption losses as the photons have to travel a relatively long way to the end of the fibre. This is compensated by the high geometrical concentration made possible by this configuration. Maximizing the absorption and geometrical concentration can be achieved tuning the length and radius and reducing the escape cone losses by placing the dye close to the surface making these important parameters for a fibre LSC, Figure 1.26 [3].

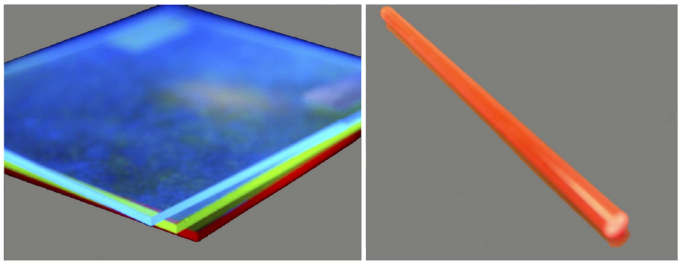

Figure 1.26: Luminescent solar concentrators with flat plate and cylindrical geometries. Adapted from [3].

Colantuono *et al.* have performed a set of numerical experiments in order to evaluate the efficiency of the concentrator when the thickness and material properties of the outer layer are changed, and to compare the performance of the rectangular and cylindrical devices under various conditions. Qualitatively they found that a bilayer device has greater optical efficiency than a comparable homogeneous version. For the cylindrical geometry improval over the homogeneous device is more strongly dependent on both the thickness and the attenuation of the luminescent layer compared to the rectangular geometry [192].

Correia *et al.* proposed a new concept on light-weight and mechanically flexible high-performance waveguiding photovoltaics through the fabrication of cylindrical LSCs of commercial PMMA-based plastic optical fibres coated with Eu^{3+} doped with organic-inorganic hybrid layer, Figure 1.27. The proposed approach may create new opportunities for cost-effective sunlight collection and wearable solar harvesting fabrics for mobile energy with negligible self-absorption and transport losses [159].

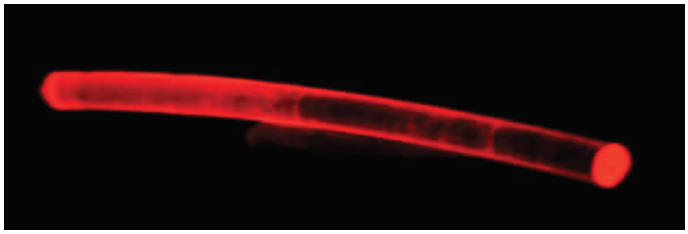

Figure 1.27: Photograph of the fibre LSC under UV illumination. Adapted from [159].

The same group reported the fabrication of large area LSCs (length up to $2.5\,m$) in which bulk and hollow-core, cylindrical optical fibres were coated or filled with an active layer comprised of either Rh6G or $Eu(tta)_3{\cdot}2H_2O$ doped in a ureasil hybrid matrix, Figure 1.28. For the bulk-coated LSC, radiation propagation along the entire fibre length was observed, with a maximum η_{opt} of 0.6 % ($F = 6.5$). In contrast, for hollow-core LSCs radiation propagation was restricted to shorter distances (6-9 $\times\, 10^{-2}\,m$) due to attenuation by the ureasil matrix. Optimized hollow-core devices displayed a maximum η_{opt} of 72.4 % ($F = 12.3$), demonstrating the considerable potential afforded by fibre optic LSCs for commercial scale-up [158].

Optical fibres also provide a suitable means of integrating LSCs with emerging PV technologies such as DSSCs, which cannot easily be fabricated as thin, robust strips. Peng *et al.* reported the combination of fibre DSSCs with commercially available LSCs using a connective envelope or groove made from aluminium foil. A maximum power of $10\,mW$ (PCE=0.1 %) was reported for a red solar module ($70.56\,cm^2$) coupled with four optical fibre DSSCs on each edge ($5.50\,cm$) [179].

Vishwanathan *et al.* inspired by the cylindrical geometry, evaluated the performance of luminescent solar concentrator photovoltaic (LSC-PV) elements with narrow PV cells strips that could be integrated in an outdoor lighting pole. Si PV cells were attached to the back of both flat and cylindrically bent PMMA radiation-guide sheets containing the dye Lumogen Red 305, as were mirrors to non-covered edges of the radiation guides, as can be seen in

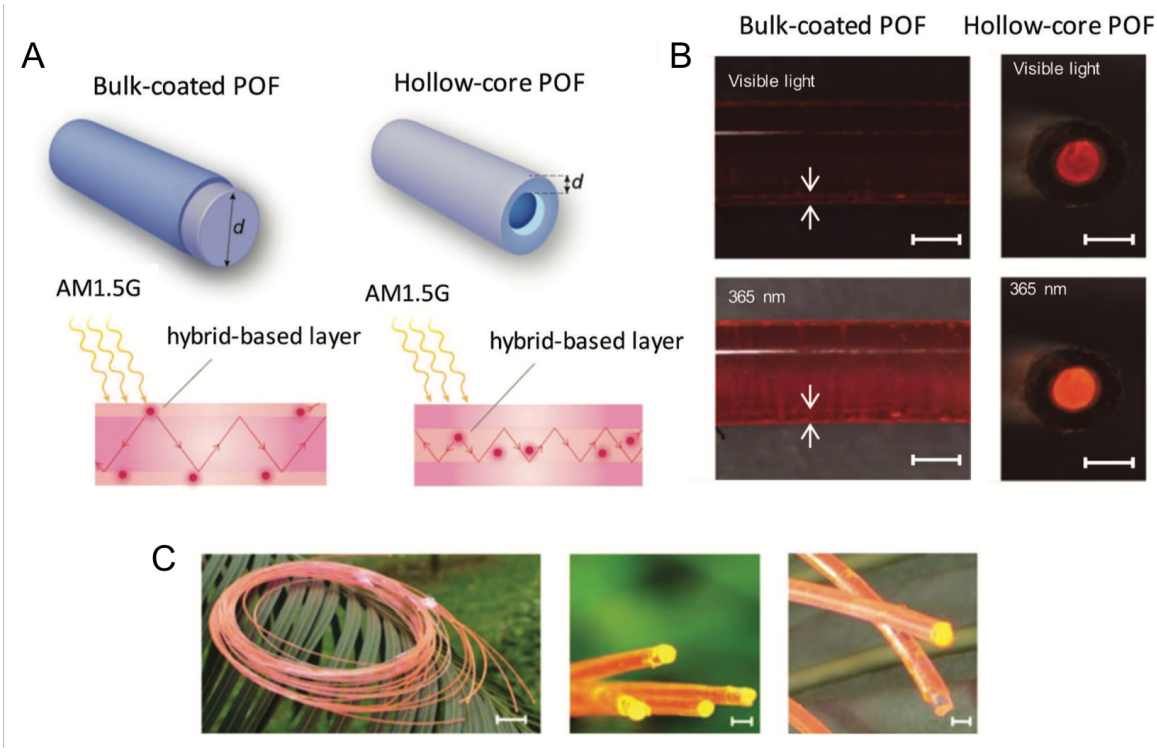

Figure 1.28: Bulk-coated and hollow-core PMMA-based optical fibres (POFs). (A) Schematic representation of POF structure. The LSC layer is a Rh6G (red circle) doped ureasil hybrid coated at the surface of the POFs or embedded into its hollow core. (B) Photographs of bulk-coated and hollow-core POFs under illumination with white light and at 365 nm. The arrows indicate the active layer; scale bars of $5 \times 10^{-4}\,m$. (C) Outdoor photographs of bulk-coated POFs. Scale bars of $10^{-3}\,m$. Adapted from [158].

Figure 1.29. The energy performance of these two elements was measured and the flat and bent LSC-PV elements were also simulated using optical modeling and the resulting performance parameters from the simulations and experiments were compared, and found to be in good agreement. From the simulations for a flat LSC-PV, the optical collection efficiency, concentration and electrical conversion efficiencies were found to be 18 %, 1.8 % and 2.8 %, respectively, for a geometric gain of 10. For a bent LSC-PV shape, the corresponding values are 21 %, 1.4 % and 3.4 % for a geometric gain of 6.7. Due to reduced sensitivity to the angular dependence of the incoming signal these bent LSC-PV elements are expected to perform well on both sunny and cloudy days [193].

Jimenez-Solano *et al*. developed a PV module that combined an LSC (LR 305 in PMMA, 2 μm thick) sandwiched between ethylene vinyl alcohol-coated glass covers, with two CIGS cells placed in-plane with the LSC, separated by an air gap. The performance of the LSC was

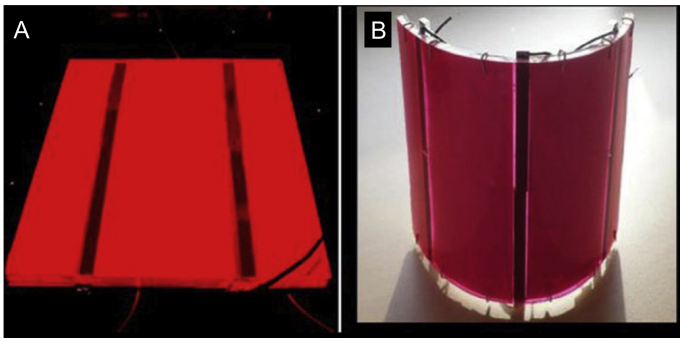

Figure 1.29: Photographs of (A) flat $100 \times 100\ mm^2$ LSC prototype with four PV cells (each strip consists of c-Si PV cells with two PV cells) and (B) bent $157 \times 100\ mm^2$ LSC prototype with six PV cells. Adapted from [193]

enhanced by coupling the luminescent film to nano-structured photonic crystals made of a periodic structure of alternating porous titania and silica nanoparticle layers, that simultaneously enhanced radiation absorption at shorter wavelengths and radiation-guiding at longer ones. Optimized modules showed incident to guided photon efficiencies around 28 % higher than those containing no photonic crystal layer (PCE=8.14 %) [178].

Complementary radiation management techniques, such as surface plasmon resonance (SPR) and Bragg reflectors can also be integrated with LSCs to enhance their performance. Chen *et al.* recently reported the fabrication of electrospun organic nanofibres comprised of poly[2,7-(9,9- dihexylfluorene)-alt-4,7-(2,1,3-benzothiadiazole)] nanoparticles as the LSC and Ag nano-particles for the SPR effect. The nanofibres were integrated into OPV cells as an aligned, check-patterned network, leading to a PCE of up to 7.12 %, an 18 % enhancement compared to the parent device [194].

Photonic nanostructures such as 3D opals have also been integrated into LSCs to modify the angular emission profile of the luminophore, such that the emitted photons are coupled more effectively into the TIR of the waveguide [195]. Photonic nano-spheres have been used to extend the spectral range of collection of LSCs. Bozzola *et al.* coated an LSC with a monolayer of self-assembled polystyrene nanospheres, whose role was to promote forward diffraction into the waveguide slab at wavelengths not absorbed by the luminophore. The wavelengths of the diffracted radiation were tuned by changing the diameter of the nanospheres, with an optimum diameter of 700-800 nm found to effectively diffract NIR photons into the waveguide [196].

1.3 Objectives of the thesis

From the survey of the state-of-the-art presented above, it is clear that the global need to improve the efficiency of PV devices is still a pressing issue, one that can potentially be achieved through the coupling of luminescent layers and/or luminescent solar concentrators to PV cells. Despite several recent works on the subject (presented in Tables 1.1 and 1.2), there are several challenges to be addressed regarding both optically active materials and device characteristics. Ideally, materials must have high absolute emission quantum yield, and broad absorption and emission bands that overlap with the solar spectral irradiance and PV cells absorption, respectively. Organic-inorganic hybrid materials doped with highly efficient optical active centres are prime candidates as they meet all the desired requirements. Concerning the optimisation of device characteristics, improvements in efficiency can be obtained by increasing the ratio between the exposed and collection areas (geometrical gain) of LSCs. This ratio is dependent on the geometry of the LSC, and the cylindrical geometry is potentially more advantageous than the planar geometry. Following the results reported in the literature the objectives of this thesis are described hereinafter.

One of the objectives of this thesis was to produce and characterize transparent organic-inorganic hybrids with controlled thickness and refractive index using PMMA, di- and tri-ureasils incorporating Ln^{3+} and organic dyes. These materials were used to fabricate LDS layers and LSCs.

In what concerns LDS layers, the main goal of this thesis is to address the issue of the mismatch between the AM1.5G spectrum and the PV cells absorption curve, as well as the impact of the reflectance on the performance of the devices. To this end, vis-NIR Ln^{3+} based ionogels were studied.

One of the challenges to improving LSCs perfomance is related to increasing the geometrical gain and, consequently, the concentration factor that quantifies the overall performance of LSCs. To that, both planar and cylindrical LSCs were fabricated. LSCs based on a novel flexible cylindrical geometry were processed by filling PMMA plastic optical fibres with the optically active hybrids. This all-polymer fibre-LSCs benefit from large-area and lightweight. This innovative approach presents an advantage over coated optical fibres, protecting the active medium from environmental conditions, and opens the door to further studies on LSC architectures based on hollow-core fibres. One further goal of this thesis is to modify the outer

geometry of LSCs to allow easier coupling between them, forming an LSC matrix (bundle), to maximize the coverage area of a square PV cell. All aforementioned LSCs configurations will likely have distinct geometrical gain factors, and it is thus also an aim of this thesis to study the impact of these factors on performance.

The response of Si PV cells is maximal in the NIR wavelength range, so that LSCs optimised for coupling with Si PV cells can benefit from optically active centres that emit in the NIR range. In this thesis, both visible and NIR-emitting organic dyes were tested, in planar and cylindrical hollow-core LSCs.

A further challenge to the production of luminescent layers is the use of abundant and sustainable molecules. With sustainable LSCs design in mind, we may draw inspiration from photosynthesis, and view PV solar energy conversion as artificial photosynthesis stopped short. Chlorophyll is key to photosynthesis, as it is responsible for sunlight harvesting, and its emission properties in the red-NIR spectral region are resonant with the main absorption region of the most common Si PV cells. R-phycoerythrin (R-PE), a phycobiliprotein extracted from *Gracilaria sp.* algae was also studied in different LSC geometries. Despite their attractive properties, the use of natural-based dye molecules in LSCs is poorly explored, an issue this thesis also seeks to address.

Finally, this thesis addresses the quantification of LSC performance. Several measures of LSC performance are reported in the literature, which often makes comparison hard or impossible. This issue is addressed in detail later on, and complemented by Monte Carlo ray-tracing simulations of LDS layers and LSCs performance as a function of geometrical and material properties (absorption and emitting spectral range, absolute emission quantum yield and dispersion curve).

1.4 Organization of the thesis

This thesis is divided in 8 chapters, as follows:

In Chapter 1, the state of the art and the context of the present work are described, as well as the main motivations and goals.

In Chapter 2, the background information of LSCs and LDS layers in what concerns to working principles and performance quantification, in the absence and in the presence of PV cells. Here, concepts like optical conversion efficiency, power conversion efficiency, radiation

trapping, integral overlap and external quantum efficiency are addressed.

In Chapter 3, a historical background and introduction to Monte-Carlo ray-tracing algorithms are described as well as its implementation in the scope of the present work.

In chapter 4, the synthesis and preparation of the used materials, including the organic-inorganic hybrids, polymers and dopants are described.

In chapter 5, the fabrication and characterization of transparent LDS layers and planar LSCs made of PMMA doped with Ln^{3+} based ionogels are described. As well as the fabrication and characterization of NIR emitting LSCs based on SiNc.

In chapter 6, the fabrication and characterization of hollow-core triangular shaped POFs filled with organic-inorganic hybrids doped with Eu^{3+} complex, and organic dyes like rhodamine 6G and rhodamine 800 were addressed. Also, due to the triangular shaped POFs, a LSC based on a bundle structure was optimized to cover the PV cell.

In chapter 7, sustainable LSCs were developed. Here, planar LSCs based on chlorophyll were fabricated and characterized as well as cyllindical and bundle liquid-LSCs produced based on R-PE.

Finally, in chapter 8, the general conclusions and future prospectives are described. In Appendix A, the description of some devices and experimental techniques is detailed and a list of publications resulting from this work is presented in Appendix B.

Chapter 2

Fundaments and background

2.1 Working principle of down-shifting layers

Luminescent down-shifting (LDS) is a purely optical approach to increase a solar cell's ultra-violet/blue response by shifting short wavelength radiation to longer wavelengths where the external quantum efficiency (EQE) of the solar cell is higher [18, 50, 91, 197, 198]. The down-shifted photons have energy that better match with the photosensitivity spectral response of the solar cell as illustrated in Figure 1.3 for different types of PV cells. In the device, LDS layers, the luminescent material convert the high energy photons to lower energy photons before the interaction with the solar cell occurs.

2.1.1 Performance quantification

The LDS layers performance is quantified by relative changes in the EQE and in the I-V curves of a PV cell measured with and without the layer [51, 54, 72]. The EQE, particularly, measures the wavelength dependency of the PV cell response and thus allows the direct quantification of the role of the LDS layers. The material of the matrix used in LDS layers does not have the need for long range TIR as geometric concentration is not involved; but a refractive index between 1.4 and 2.4 is still advantageous to minimize both surface reflection and scape cone losses [161]. If a host material is used, its thickness must be optimized in order to minimize edge emission [50, 74].

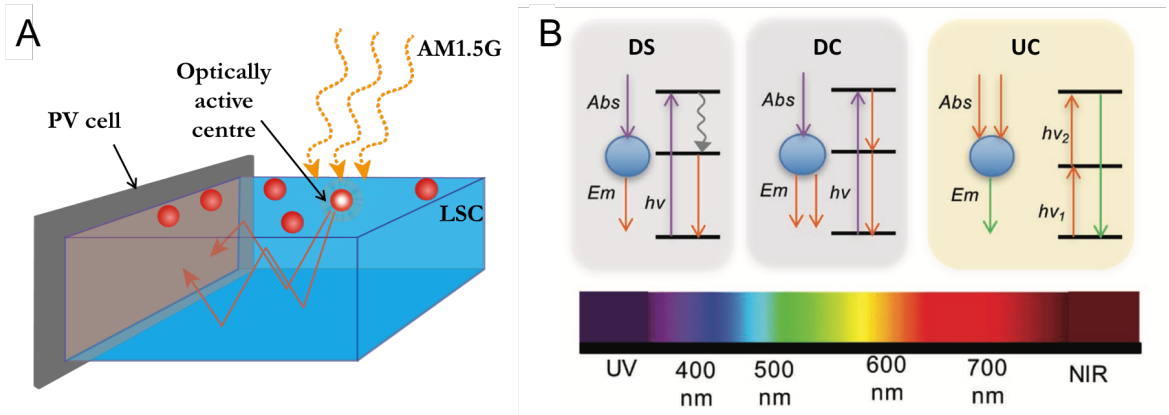

Figure 2.1: (A) Schematic representation of the working principle of a LSC. (B) Photoluminescence processes employed in spectral converters and their integration with PV cells to form luminescent solar devices. Simplified energy level diagrams for down-shifting (DS), down-conversion (DC) and up-conversion (UC). DS converters absorb a single high energy UV/blue photon and convert it to an emitted photon of lower energy. In DC, a single high energy photon is downconverter into two (or more) lower energy photons. Conversely, UC materials absorb two (or more) low energy photons and convert them to one emitted high energy photon. Adapted from [16].

2.2 Working principle of luminescent solar concentrators

A LSC may be represented as a transparent substrate doped with optically active ions. The principle of operation of a LSC is illustrated on Figure 2.2. The sunlight is incident on the top of the transparent substrate, with a refractive index n. Since there are optically active centres in the substrate, they will absorb the sunlight and re-emit it at a specific wavelength. The emitted radiation is transported to the edge, until it reaches the PV cell attached, by TIR, if the emission angle is greater than the critical angle (θ_c). The other edges of the LSC should be covered with a reflective coating (or PV cells) to trap photons inside the transparent substrate avoiding to escape.

The principle of TIR is based on the refraction and reflection phenomena resulting from radiation propagation mediums with distinct refractive indexes (Figure 2.3) [199]. An incident ray on a medium with a refractive index n_i reaches the interface with an angle θ_1 and can be either refracted to another medium with refractive index n_j or reflected with an angle θ_2. There is a limit situation in which the incident beam with an angle smaller than 90°, θ_c, originates a refracted beam that propagates parallel to the interface between the dielectrics. Any incident beam with an angle greater than θ_c will not be refracted, but totally reflected

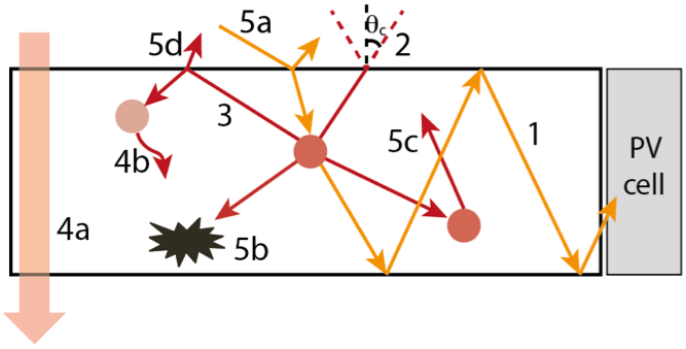

Figure 2.2: Schematic representation of the working principle of a LSC and of the main loss mechanisms: 1) total internal reflection; 2) radiation emitted through the escape cone; 3) re-absorption of the emitted radiation by an optical active centre (solid sphere); 4a) non-absorbed radiation; 4b) non-radiative deactivations; 5a) surface reflection; 5b) internal waveguide scattering; 5c) self-absorption; 5d) surface scattering. Although not represented for simplicity, the photostability of the emitting centres could also be a loss source in LSCs. Adapted from [23].

instead.

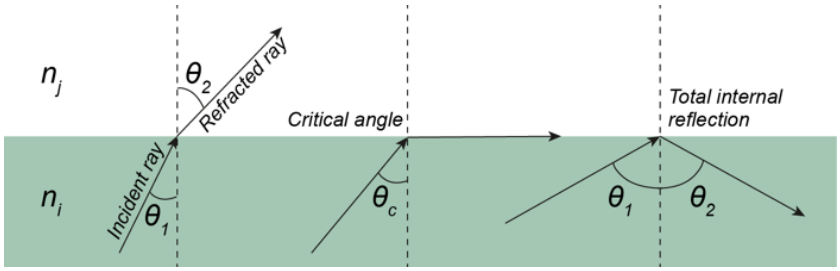

Figure 2.3: Schematic representation of total internal reflection principle.

Nevertheless, part of the emission is lost through the escape cone at the surface. The escape cone is determined by θ_c, (through Snells law) [168]:

$$\theta_c = sin^{-1}\left(\frac{n_j}{n_i}\right) \tag{2.1}$$

Several loss mechanisms may be present in LSCs which reduce the amount of radiation reaching the PV cells [23]. The main ones are represented in Figure 2.2. As mentioned above, the emitted radiation is only trapped inside the waveguide if the angle of incidence is greater than θ_c. If it is less than θ_c, the radiation leaves the waveguide through the called escape cone and is lost (2). Also, if the absorption spectrum overlaps the emission one, re-absorption of the emitted radiation may occur (3). The absorption range of the optically active centre

is important because, in the case of optically active centres with limited absorption range, some non-absorbed incident radiation can pass through the waveguide (4a). Moreover, if the optically active centre has a non-unity q, emission may not occur and the absorbed photon is lost (4b). A small fraction ($\sim 4\,\%$, assuming a typical $n_i \sim 1.5$) of incident radiation is reflected from the surface of the waveguide (5a) through the so-called Fresnel reflection. The emitted radiation may also be scattered (5b) or absorbed (5c) by the waveguide material and lost. Also, some surface scattering may occur (5d).

2.3 Radiation trapping

In a LSC in which the optically active layer is deposited on top of a transparent substrate, radiation trapping may occur only in the optically active layer or in the combined system of the optically active layer and the substrate, according to the refractive index contrast, $\Delta n_{i,j} = n_i - n_j$ with $i, j = 1, 2, 3$, between the (1) air, (2) optically active layer and (3) substrate (Figure 2.4) [152].

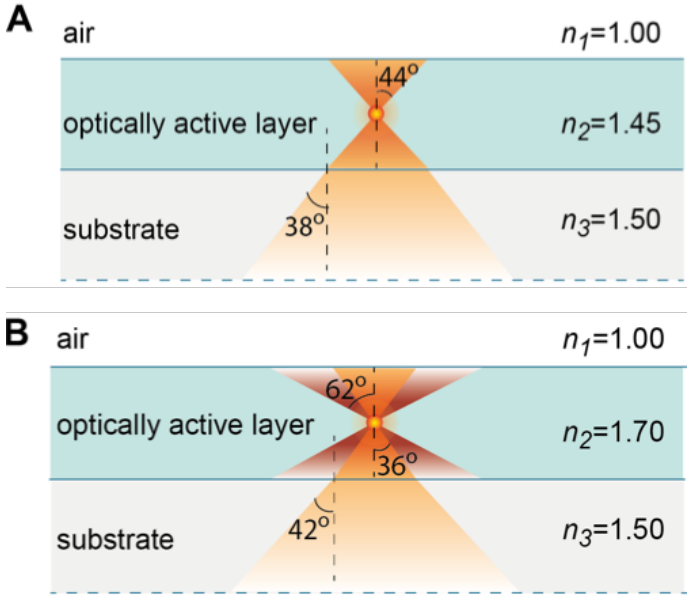

Figure 2.4: Schematic representation of the cross-section of example LSCs with (A) $\Delta n_{2,3} < 0$ and (B) $\Delta n_{2,3} > 0$, with the escape cones and radiation trapped in the substrate and in the optically active layer (orange) and only in the hybrid (brown). The critical angles θ_c are also indicated.

In the cases where $\Delta n_{2,3} < 0$ (Figure 2.4a), radiation propagation of converted radiation

would occur mostly in the substrate than in the optically active layer. If $\Delta n_{2,3} > 0$ (Figure 2.4b), trapping will occur within the external interface with air and also in the optically active layer-substrate interface, with most of the propagation occurring in the optically active layer.

For planar LSCs where an optically active layer is deposited on top of a substrate, the trapping efficiency is defined as follows [200]:

$$\eta_{trap} = \left(1 - \frac{1}{n_p^2}\right)^{1/2} \tag{2.2}$$

where n_p is the refractive index of the emitting medium at λ_p. It is defined as the fraction of photons confined within the substrate, i.e., the fraction of photons emitted from the edge versus the photons emitted from the face and edge combined. This term accounts for the emission losses at the surface through a so-called escape cone (Figure 2.2).

Considering a cylindrical substrate (hollow-core filled optical fibres or coated optical fibres) the trapping efficiency is defined by the optical energy trapped (or guided) by the fibre divided by the total energy emitted within it by the fluorophores of the optical active layer [201]. Trapping efficiency can be derived as function of the cladding-to-core refractive index ratio as follows [201]:

$$n_t = 1 - \left(\frac{n_{core}}{n_{clad}}\right)^2 \tag{2.3}$$

where n_{core} and n_{clad} are the refractive index of the core and the cladding, receptively.

Another parameter that contributes to n_t is the distance r from the fibre centre at which the emission occurs which, for a POF with external diameter R, is given by [202]:

$$n_t = 1 - \frac{1}{\pi}\int_0^{\pi} \frac{\sqrt{\left(n_{clad}^{-2} - \left(\frac{r}{R}\right)^2 sin^2\beta\right)}}{1 - \left(\frac{r}{R}\right)^2 sin^2\beta} d\beta \tag{2.4}$$

where r is the radial distance of the cylinder with radius R.

The influence of how reflectance affects the absorption ability of the PV device, can be determined by the Haze factor. It refers to the degree of incident radiation scattered forward towards the absorber layer. It can be described by the ratio between the diffuse reflectance

($R_{diffuse}$) and total reflectance (R_{total}), [203, 204].

$$Haze = \frac{R_{diffuse}}{R_{total}} \tag{2.5}$$

2.4 Performance quantification

The LSCs performance quantification has been reported in several distinct ways in the literature. Here, we revise the different approaches.

2.4.1 Planar and cylindrical geometries

The performance of a LSC is quantified by the optical conversion efficiency (η_{opt}) which is a measure of the ratio between the output power at the LSC edges (P_{out}) and the incident optical power (P_{in}) [110, 141, 181, 200, 205]:

$$\eta_{opt} = \frac{P_{out}}{P_{in}} \tag{2.6}$$

The η_{opt} can be described by weighting all the losses (Figure 2.2) in the LSC, given by the product of several terms [200]:

$$\eta_{opt} = (1 - R)\eta_{abs}\eta_{SA}\eta_{yield}\eta_{Stokes}\eta_{trap}\eta_{tr} \tag{2.7}$$

in which:

- $R = (n_j - n_i)^2/(n_j + n_i)^2$ is the Fresnel reflection coefficient for perpendicular incidence, in which n_i represents the refractive index of the optically active layer at the incident wavelength (λ_i).

- $\eta_{abs} = 1 - 10^{-A}$ is the ratio of photons absorbed by the emitting layer to the number of photons falling on it, with A representing the absorbance value at λ_i. For LSCs with a non-planar geometry, η_{abs} is not constant along the device surface and, then, the thickness must be estimated accordingly. For instance, for cylindrical geometry, and perpendicular incidence of Sun radiation, the optical absorption path increases from the middle to the surface along the radial direction.

- η_{SA} is the self-absorption efficiency, arising from self-absorption of the emitting centres. When the spectral overlap between the excitation and emission spectra of the emitting centres is null, $\eta_{SA} = 1$, as in the case of Ln^{3+}. If this overlap is not null, $\eta_{SA} < 1$, as typically observed for dyes and QDs.

- η_{yield} is the absolute emission quantum yield of the optically active centre at λ_i.

- $\eta_{Stokes} = \lambda_i/\lambda_p$ is the Stokes efficiency calculated by the energetic ratio between the average energy of the emitted photons (the emission peak position, λ_p, in energy units) and the incident energy (corresponding to λ_i).

- η_{trap} = as defined in Eq. 2.2

- η_{tr} takes into account the transport losses due to matrix absorption and scattering, frequently it is considered that $\eta_{tr} = 1$, as the transport and scattering losses are neglected. Nevertheless, Graffion *et al.* reported that scattering plays an important role, which readily contributes to decrease η_{tr} [188]. In particular, the emission ratio C, defined as the ratio between the intensity at the surface and at the edges, was modelled by:

$$C = \frac{\eta_{opt} A_t}{\frac{\eta_{sf}}{2} A_e} = \frac{2\eta_{trap}}{(1 - \eta_{trap})} \frac{A_s}{A_e} \tag{2.8}$$

where

$$\eta_{sf} = (1 - R)\eta_{abs}\eta_{yield}\eta_{Stokes}\eta_{trap}(1 - \eta_{tr})\eta_{SA} \tag{2.9}$$

is the conversion efficiency of the signal emitted at the surface of the film (in which the trapping efficiency is replaced by its complementary value, $(1 - \eta_{trap})$, A_s and A_e are the top surface and edge surface area of the LSC (assuming all of the other faces with reflective coatings and a white diffuser on the rear side [172]), respectively, and the factor 1/2 takes into account the emission regards only one film surface. The C factor predicted by Eq. 2.8 should be compared with that measured experimentally [188]. It was demonstrated in the literature that, for LSCs based on bridged silsesquioxane hybrids doped with Eu^{3+}, the value estimated by Eq. 2.8 was substantially higher

($C = 57$) than the experimental value ($C = 6$). Such discrepancy was explained by considering that the signal trapped in the waveguide will lose part of its intensity due to scattering effects along the propagation in the film, in a similar way that was performed in the estimation of the losses incurred by self-absorption in LSCs of liquid solutions of PbS QDs [206]. Therefore, Eq. 2.8 was rewritten as follows:

$$C_{eff} = \frac{2\eta_{tr}\eta_{trap}}{(1-\eta_{trap})+(1-\eta_{tr})}\frac{A_s}{A_e}. \tag{2.10}$$

Although not usually mentioned in the literature, notice that η_{opt} is dependent on the excitation wavelength. Therefore, the calculus of the overall η_{opt} through Eq. 2.7 requires integration over the excitation spectrum limits (λ_1 and λ_2):

$$\eta_{opt} = \eta_{trap}(\lambda_p)\frac{1}{(\lambda_2-\lambda_1)} \times \int_{\lambda_1}^{\lambda_2}(1-R(\lambda_i))\eta_{abs}(\lambda_i)\eta_{yield}(\lambda_i)\eta_{Stokes}(\lambda_i,\lambda_p)d\lambda_i \tag{2.11}$$

with $\eta_{SA} = \eta_{tr} = 1$ [188, 200]. Obviously, integration limits that lie outside the AM1.5G spectral range are not useful for PV conversion. In this sense, an effective η_{opt} can be calculated replacing the limits in Eq. 2.11 by those of the overlap integral between the excitation and the AM1.5G spectra, given by [156]:

$$O = \int_{\lambda_1}^{\lambda_2}\Phi_{AM1.5G}(\lambda) \times (1-10^{-A(\lambda)})d\lambda \tag{2.12}$$

where λ_1 and λ_2 are the limits of the spectral overlap between the excitation spectrum of the optical active layer and the AM1.5G spectrum, $\Phi_{AM1.5G}$ is the photon flux of AM1.5G and A is the absorbance of the active layer [207].

The variation of the percentages of the AM1.5G solar irradiance (Figure 2.5) points out that for excitation wavelengths between 280 and 320 nm only 0.15 % is available for down-shifting conversion and that between 280 and 400 nm that percentage increases to 4.6 % [5]. The η_{opt} values calculated through Eq. 2.11 can be directly compared with those estimated by Eq. 2.6 and represent a valuable tool to describe the performance of a LSC in the absence of a solar simulator.

The predictable maximum limit for η_{opt} was theoretically studied [119, 130, 161, 208, 209]

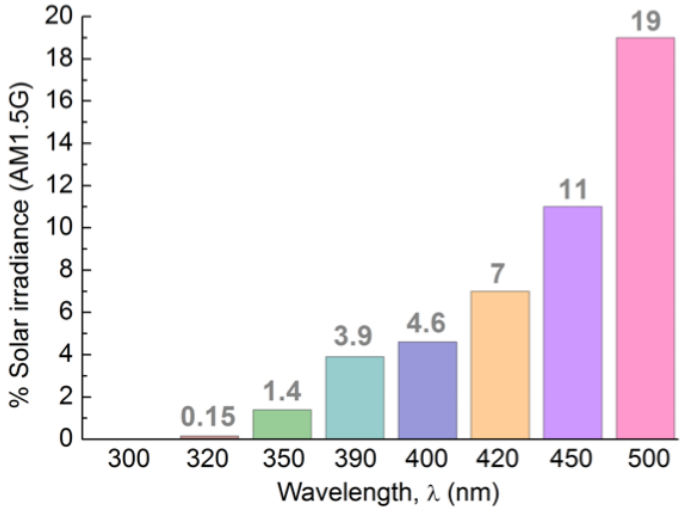

Figure 2.5: Calculated percentages of the AM1.5G solar spectrum emitted between 300 nm and 500 nm. Adapted from [5].

not taking into account the wavelength dependence. For instance, efficiency calculations with conventional PV cell theory applied to LSCs in a stack of transparent sheets involving dyes and semiconductors (Ge, Si, GaAs) yield a theoretical maximum conversion efficiency of 30 %, although more realistic values around 20 % have been mentioned under optimum conditions [161]. Monte-Carlo studies (taking into account the absorption and emission probabilities) on LSCs based on perylimide dyes embedded in GLYMO ((3-Glycidoxypropyl)trimethoxysilane) [119], liquid solutions of Rhodamine B and Red305 encapsulated in glass tubes [208], and commercial CdSe-CdTe QDs [209] were also performed. Moreover, a mathematical assessment of LSCs accounting for all the intrinsic (size, shape, design and materials) and extrinsic (geographical, seasonal and spectral distribution of solar radiation) factors that influence the performance of such devices was also reported [165]. In all these works, the main limiting factor is the high spectral overlap between emission and absorption spectra that yield maximum values of η_{opt} within 20-30 %.

The maximum limit for η_{opt} can be also inferred through a simpler analysis of Eq. 2.7, considering that all the involved parameters can be near the unit, except η_{opt} and η_{Stokes}. For typical values of the refractive index around 1.5, $\eta_{trap} \sim 75\,\%$ and for a wavelength shift from the UV/blue to the red spectral region around 690 nm (wavelengths at which the a-Si PV cells are more efficient) [5] $\eta_{Stokes} \sim 50\,\%$, the maximum predictable value for η_{opt} is $\sim 40\,\%$. Besides η_{opt}, another parameter that is also often used to quantify the performance of a LSC

is the concentration factor [141]:

$$F = G \times \eta_{opt} \tag{2.13}$$

in which G is the geometrical gain factor $G = A_s/A_e$.

2.4.2 Prototype coupled to photovoltaic cells

When the LSCs are coupled to a PV device, the η_{opt} can be calculated by [119]:

$$\eta_{opt} = \frac{P_{out}}{P_{in}} = \frac{I_{SC}^L V_0^L}{I_{SC} V_0} \frac{A_e}{A_s} \frac{\eta_{solar}}{\eta_{LSC}} \frac{\int I_{AM1.5G}(\lambda) d\lambda}{\int_{\lambda_1}^{\lambda_2} I_{AM1.5G}(\lambda) d\lambda} \tag{2.14}$$

where η_{LSC} is the PV device efficiency at λ_p and η_{solar} is the average efficiency value of the cell with respect to the total solar spectrum [119]. The parameters I_{SC}^L and V_0^L stand for the short-circuit current and the open-circuit voltage, respectively, when the PV device is coupled to the LSC under AM1.5G illumination. I_{SC} and V_0 represent the short-circuit current and the open-circuit voltage, respectively, when the PV device is directly exposed to AM1.5G illumination (in the absence of the LSC). The associated error $\Delta\eta_{opt}$ is given by:

$$\begin{aligned}
(\Delta\eta_{opt})^2 = &\left(\frac{\delta\eta_{opt}}{\delta I_{SC}^L}\Delta I_{SC}^L\right)^2 + \left(\frac{\delta\eta_{opt}}{\delta V_0^L}\Delta V_0^L\right)^2 + \left(\frac{\delta\eta_{opt}}{\delta A_e}\Delta A_e\right)^2 + \left(\frac{\delta\eta_{opt}}{\delta\eta_{solar}}\Delta\eta_{solar}\right)^2 \\
&+ \left(\frac{\delta\eta_{opt}}{\delta I_{SC}}\Delta I_{SC}\right)^2 + \left(\frac{\delta\eta_{opt}}{\delta V_0}\Delta V_0\right)^2 + \left(\frac{\delta\eta_{opt}}{\delta A_s}\Delta A_s\right)^2 + \left(\frac{\delta\eta_{opt}}{\delta\eta_{LSC}}\Delta\eta_{LSC}\right)^2 \\
\Leftrightarrow (\Delta\eta_{opt})^2 = &\left(\frac{V_0^L A_e \eta_{solar}}{I_{SC} V_0 A_s \eta_{LSC}}\Delta I_{SC}^L\right)^2 + \left(\frac{I_{SC}^L A_e \eta_{solar}}{I_{SC} V_0 A_s \eta_{LSC}}\Delta V_0^L\right)^2 + \left(\frac{L_{SC}^L V_0^L \eta_{solar}}{I_{SC} V_0 A_s \eta_{LSC}}\Delta A_e\right)^2 \\
&+ \left(\frac{L_{SC}^L V_0^L A_e}{I_{SC} V_0 A_s \eta_{LSC}}\Delta\eta_{solar}\right)^2 + \left(-\frac{I_{SC}^L V_0^L A_e \eta_{solar}}{(I_{SC})^2 V_0 A_s \eta_{LSC}}\Delta I_{SC}\right)^2 + \left(-\frac{I_{SC}^L V_0^L A_e \eta_{solar}}{I_{SC} (V_0)^2 A_s \eta_{LSC}}\Delta V_0\right)^2 \\
&+ \left(-\frac{I_{SC}^L V_0^L A_e \eta_{solar}}{I_{SC} V_0 (A_s)^2 \eta_{LSC}}\Delta A_s\right)^2 + \left(-\frac{I_{SC}^L V_0^L A_e \eta_{solar}}{I_{SC} V_0 A_s (\eta_{LSC})^2}\Delta\eta_{LSC}\right)^2
\end{aligned} \tag{2.15}$$

The ratio:

$$\frac{\eta_{solar}}{\eta_{LSC}} = \frac{\int EQE_{PV}(\lambda) I_{AM1.5G}(\lambda) d\lambda}{\int EQE_{PV}(\lambda) I_{em}(\lambda) d\lambda} \tag{2.16}$$

where EQE_{PV} is the external quantum efficiency of the PV device coupled to the LSC and

I_{em} is the LSC active layer emission spectrum intensity.

In the literature, Eq. 2.14 is often presented in simplified formulations given by Eq. 2.17, Eq. 2.18 [110, 141, 180, 181, 205, 206, 208] and Eq. 2.19 [175, 180, 206, 210, 211], that are not considered to be comparable to the ones previously described, since they will only take into account the current delivered by the PV device, instead of the total electrical power, despising the voltage and, thus, overestimating the η_{opt} values:

$$\eta_{opt} = \frac{I_{SC}^{L}}{I_{SC}} \frac{R_{PV}}{R_{solar}} \frac{A_e}{A_s} \tag{2.17}$$

in which R_{PV} is the spectral response of the PV device to λ_p and R_{solar} is the average responsivity value of the cell with respect to the total solar spectrum,

$$\eta_{opt} = \frac{I_{SC}^{L}}{R_{PV}} \frac{1}{\int I_{AM1.5G}(\lambda) d\lambda} \frac{A_e}{A_s} \tag{2.18}$$

and,

$$\eta_{opt} = \frac{I_{SC}^{L}}{I_{SC}} \frac{A_e}{A_s} \tag{2.19}$$

Also, the following expression can be found in the literature, which does not account for the mismatch between the emission of the active layer and the spectral response of the PV device in use, and thus is not comparable to Eq. 2.14 [212]:

$$\eta_{opt} = \frac{P_{out}}{A_s \int I_{AM1.5G}(\lambda) d\lambda} \tag{2.20}$$

When the LSC coupled to a PV device is put under simulated solar illumination, the overall PCE is defined as the ratio between the output electrical power and the input optical power, given by:

$$PCE = \frac{P_{out}^{el}}{P_{in}} \frac{I_{SC}^{L} V_0^{L}}{A_s \int_{\lambda_1}^{\lambda_2} I_{AM1.5G}(\lambda) d\lambda} \times FF \tag{2.21}$$

where P_{out}^{el} and FF are the PV device output electrical power and the fill factor of the PV device.

The performance of a LSC when coupled to a PV device may also be quantified in terms of EQE [168, 175, 210, 213–218]. The EQE can be defined as the ratio of the number of

generated charge carriers that actually contribute to the generated current to the number of incident photons. The EQE of a PV device can then be expressed in terms of the incident optical power and the current generated as [219]:

$$EQE = \frac{I_{SC}\, h\, c}{P_{in}\, e\, \lambda} \tag{2.22}$$

where e is the charge of the electron, h is the Planck's constant and c is the speed of light.

In cylindrical geometries, we should note that the dependence of the optical path on the geometry is weighted through the G parameter, by considering in the calculus of A_s the effective length (L_c) that is the equivalent length for a fibre without attenuation, given by:

$$L_c = \lim_{L\to\infty} \frac{\left(1 - e^{-\alpha L}\right)}{\alpha}. \tag{2.23}$$

Experimental characterization

During the course of this thesis, different LSCs geometries were tested an thus, different experimental set-ups were implemented. In this section a description of all schemes is presented.

The η_{opt} definition that was used is the one written in Eq. 2.14 The relative error ($\Delta\eta_{opt}/\eta_{opt}$) is below 0.1 %. However, to enable a comparison with the literature, in some cases an alternative definition was also considered, Eq. 2.19. The PCE definition that was used is the one written in Eq. 2.21.

The experimental η_{opt} values were determined by illuminating the top surface of the LSCs with simulated AM1.5G illumination. In section 5.2 and 7.3 for the planar and cylindrical LSCs with bundle structure, the optical power at the LSC output was estimated using a c-Si PV cell (KXOB22-12X1L, IXYS) coated by the manufacturer with an EVA film with a mask matching A_e dimensions, according to the coupling scheme in Figure 2.7A. Whereas no reflective devices were used on the cylindrical LSCs with bundle structure, for the case of planar LSCs, a reflective tape (reflectance curve in Figure 2.6) was used on all the edges of the cuvette, in the backside and in the area which is not illuminated by uniform solar simulator radiation.

In section 5.3, 7.2 and in section 7.3 for the single-based cylindrical LSCs, the optical power at the LSCs output was estimated using a commercial photodiode (IF D91, Industrial

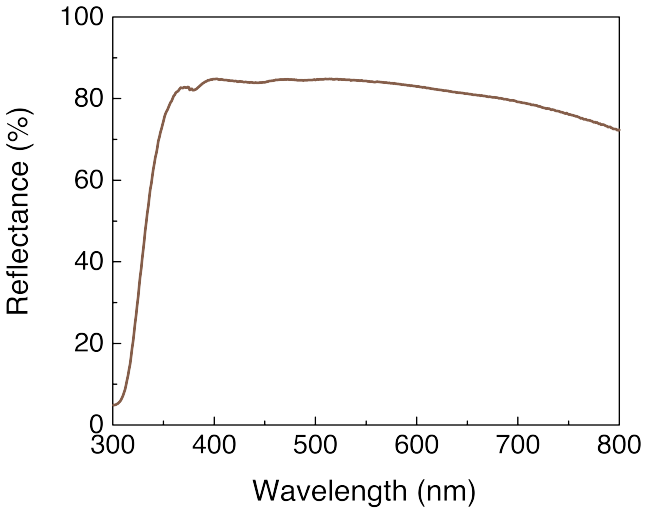

Figure 2.6: Reflectance curve of the reflective tape used on the p-LSC.

Fiber Optics, Inc.) with wall-plug efficiency to the AM1.5G solar spectrum distribution of 4 %. The photodiode was coupled to one edge of the LSC while kept inside a black cap to prevent influence of direct illumination from the solar simulator, according to the coupling scheme in Figure 2.7B. Despite the fact that the diameter value ($10^{-3}\,m$) of the collection area of the photodiode (A_{PD}) is analogous to that of the LSC thickness edge where the radiation is concentrated, the geometric difference between the LSC edges area (A_e) and A_{PD} was taken into account through a geometrical correction factor (A_e/A_{PD}) applied in the calculus of η_{opt}.

In section 6, the η_{opt} values were determined under natural daylight illumination ($\sim 944\,W \cdot m^{-2}$).

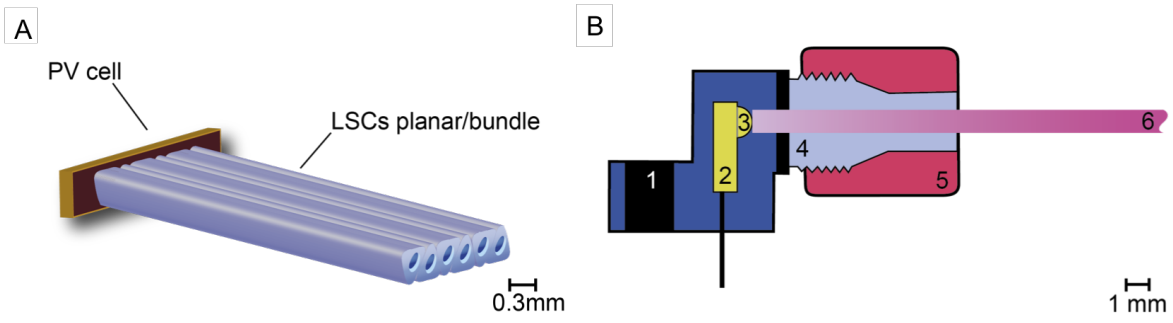

Figure 2.7: Diagram of (A) PV cell coupling to the LSC-based bundle and (B) photodiode coupling to the LSC where the numbers stand for 1) mounting hole, 2) PV detector, 3) lens, 4) housing, 5) locking nut and 6) cylindrical LSC. The scale refers to the device dimensions.

The I_{sc} and V_0 values were measured using a source meter device (2400 Source Meter®

SMU Instruments, Keithley). Measurements were performed under AM1.5G illumination ($1000\,W \cdot m^{-2}$) using a $150\,W$ xenon arc lamp, class A, solar simulator (Model 10500, Abet Technologies). The mismatch in the UV spectral region between the AM1.5G solar spectral irradiance and that of the Xe lamp in the solar simulator was taken into consideration following a methodology reported in detail elsewhere [159].

The EQE was calculated using Eq. 2.22. The solar simulator was coupled to a monochromator (Triax 180, Horiba Scientific). The I_{sc} andP_{in} values were measured using the source meter and the PV devices (photodiode or PV cell, depending on the case) above mentioned.

Chapter 3

Monte-Carlo ray-tracing simulations

Monte Carlo simulations (also called ray tracing in this kind of application) are a common tool to study radiation propagation in random media when phase-dependent wave effects, such as interference and diffraction, can be neglected [220]. This method is particularly interesting to approach the problem of radiation propagation in luminescent solar concentrators, because of the possibility to incorporate multiple physics phenomena [209].

Monte Carlo algorithms are stochastic and are used to solve complex physical or mathematical problems [221]. When the number of variables is large and the solution is complex, exploring the solution space or events space randomly can give an accurate estimation of the solution. In a typical Monte Carlo algorithm, random draws following given distributions define a chain of local events that can characterize the global state. By repeating this process numerous times an approximation of the solution is obtained. The accuracy of this solution will depend on how well is the problem modelled and on the number of draws that are made [222, 223].

3.1 Introduction

Monte Carlo methods have been efficiently used to solve a wide variety of physical problems. Although Monte Carlo is trivially a straightforward tool to stimulate random processes, it can be used to solve problems that do not have immediate probabilistic interpretation. Be-

fore the development of the Monte Carlo method, simulations were used to test previously understood deterministic problems and statistical sampling was used to estimate uncertainties in the simulations. However, Monte Carlo simulations invert this approach, solving deterministic problems using a probabilistic analogy [224].

Nowadays, Monte Carlo methods are used to solve problems of two types entitled probabilistic or deterministic according to whether or not they are directly related with the behaviour and the outcome of random processes. In the case of a probabilistic problem the simplest Monte Carlo approach is to observe random numbers, chosen in such a way that they directly simulate the physical random process of the original problem, and allows the inference of the desired solution from the behaviour of these random numbers [223].

Monte Carlo methods have become the model of choice to simulate radiation propagation inside materials [225]. The Monte Carlo method describes local rules of photon propagation. In its simplest form, this type of model defines the step size between photon-material interaction sites, as well as the photon's absorption over the length of its path, based on probability distributions generated. The method is statistical in nature, however it relies on computational calculus of the propagation of a large number of photons. As a result, it requires a large amount of computation time. To avoid this issue, and turn it into something more practical for daily simulations we only chose a reduced number of photons to construct the diagrams of photons propagation behaviour [226]. The minimum number of photons required largely depends on the question being asked, the precision needed and the spatial resolution required. For example, to easily find the total diffuse reflectance from a material of specified optical properties, typically about 3×10^3 photons can yield a useful result. To map the spatial distribution of photons, $\phi(r, z)$, in a cylindrically symmetric problem, at least 10^4 photons are usually required to obtain an acceptable answer. To map spatial distributions in a more complex three dimensional problem, the number of required photons may exceed 10^5. The point to be remembered in this introductory remarks is that Monte Carlo simulations are rigorous, but necessarily statistical and therefore require significant computation time to achieve precision and resolution. Nevertheless, the flexibility of the method makes Monte Carlo a powerful modelling tool [226].

Another feature of the Monte Carlo method that can be used to simulate photon propagation is that it does not treat photons as a wave but as a particle and thus, phase and

polarization features are ignored, as previously said. The motivation for these simulations is to predict radiant energy transport in a specific media. The photons are scattered multiple times and that is why phase and polarization does not play an important role because they are quickly randomized. However Monte Carlo simulations may be capable of bookkeeping phase and polarization and treating wave phenomena statistically, they can be ignored [226]. The Monte Carlo simulations are based on macroscopic optical properties that are assumed to extend uniformly over small units of material volume.

Among the several areas of application, Monte Carlo simulations are suitable to describe phenomena in the field of photovoltaics, in particular in luminescent solar concentrators.

3.2 Historical background

This method was firstly used in the beginning of the 20^{th} century, however extensive applications came along with construction and use of modern digital computers from the late 1940s. Historically, the Monte Carlo method has first been successfully used to solve particle transport problems and it is still one of the areas where it is mostly used [227].

The real use of Monte Carlo methods as a research tool derives from work on the atomic bomb during Second World War. This work involved a direct simulation of probabilistic problems concerned with random neutron diffusion in fissile materials. But even at an early stage of these investigations, Von Neumann and Ulam refined this direct simulation with certain variance-reducing techniques, in particular Russian roulette and splitting methods [226]. However, the systematic development of these ideas had to await the work of Harris and Herman Kahn in 1948 [223]. Late in the Second World War, Von Neumann, Frankel and Metropolis began to carry out calculations on the first general-purpose electronic computer [228]. While his recovery from a surgery, Ulam had thought about playing hundreds of solitaire games to estimate statistically the probability of a successful outcome [229]. With the new computer in mind, he realized that the availability of computers made such statistical method very practical. Von Neumann immediately saw the significance of this insight and in March 1947 they proposed a statistical approach to the problem of the neutron diffusion into fissile materials.

The possibility of applying Monte Carlo methods to deterministic problems was noticed by Fermi, Von Neumann, and Ulam and popularized by them in the immediate post-war years.

About 1948 Fermi, Metropolis, and Ulam obtained Monte Carlo estimates for the eigenvalues of Schrödinger equation. The subsequent intensive study of Monte Carlo methods in 50s decade, particularly in USA, served paradoxically enough to discredit the subject. There was an understandable attempt to solve every problem insight by Monte Carlo, but not enough attention was paid to which of these problems it could handle efficiently and which it could only solve inefficiently; and proponents of conventional numerical methods were not above pointing to those problems where Monte Carlo methods were significantly inferior to numerical analysis [223].

In the 60s, Monte Carlo methods had come back into favour due to better recognition of those problems in which it is the best, and sometimes not the only, available technique. Such problems have grown in number, not only because of the improved variance-reducing techniques that made Monte Carlo efficient where it had previously been inefficient, but also because Monte Carlo methods represent a practical way so solve problems that involve mass of practical complications of the sort encountered more and more frequently as applied mathematics and operational research come to grips with realities [223].

Design studies of nuclear reactors and of telephone exchanges provide other examples of probabilistic problems. The fundamental particles of nuclear physics seem to obey probabilistic rather than deterministic laws. Therefore one can simulate the performance of a nuclear reactor by choosing random numbers that represent the random trajectories of the neutron inside it. In this way, it is possible to experiment with the reactor without increasing the cost, in money, time and safety of its actual physical construction. If the geometry of the reactor is complicated, which it actually is, one will need large-scale computing equipment to trace out the life-histories of each individual neutron according with the random numbers that governed them [223].

More complex applications include integral calculus, electron trajectory tracing and simulation for calibration of electron microscopy [230] or modelling of radiation transport in multi-layered tissues for biological application [225]. Prahl *et al.* described a method of modelling radiation transport in tissue. Their paper discussed internal reflections of a photon at boundaries, shown how the phase function may be used to generate new scattering angles, discussed variance reduction schemes to improve efficiency and shown results for validating the Monte Carlo implementation [220]. Monte Carlo Modelling of Light (MCML) models

multiple layers, refraction and reflection as well as absorption and scattering phenomena. However, it is limited in precision by a grid size, it is able to simulate radiation by packets issued from a single directional beam [225].

As above mentioned, Monte Carlo simulations are suitable to describe phenomena in the field of photovoltaics in particular in luminescent solar concentrators thus, some examples of those types of Monte Carlo method applications will be shown below.

Several research groups have already reported modelling radiation propagation behaviour inside LSCs in order to analyse the performance of this devices in detail. In 1983, Carrascosa *et al.* developed a Monte Carlo simulation where they tested the performance of luminescent solar collectors consisting of a PMMA plate with an attached film (or multiple-film stack) or dye-activated PMMA. In this work Rhodamine 6G and Fluorol 555 have been considered as dopant dyes. Direct and diffuse solar spectra were also simulated in order to compare extreme insolation conditions. The configuration used appears to be a convenient one as can be seen in Figure 3.1. These authors also determined efficiency factors as a function of the main geometrical and optical parameters of the LSC like the effective concentration factor G or effective electrical gain (ratio between the electrical power generated from a cell at the edge and that obtained when the cell directly faces the Sun at the upper face); the relative electrical collector efficiency η_{REL}, ratio between the total electrical power generated with the cells covering the edge of the collector and that obtained with the cells filling the upper face and directly facing the Sun; and the overall collector efficiency, η_{LSC}, ratio between the electrical power generated with the cells covering the edge and the total power of solar radiation impinging the upper surface of the collector. They concluded that a multiple-film based LSC offers better performances because of the extended spectral range for dye absorption [231].

In 2007, Kostro developed a Monte Carlo ray tracing software called PhotonSim for simulation of solar concentrators. The aim was to simulate the behaviour of radiation in materials with specific properties and offer to users a flexible tool for the design of concentrators with various photoluminescent characteristics, proportions and layouts. Materials of particular interest for these studies are organic dyes and quantum dots which have the capacity to absorb and re-emit radiation and thus can be used to concentrate both direct and diffuse radiation. Well knowing the characteristics of the luminescent material (emission and absorption spec-

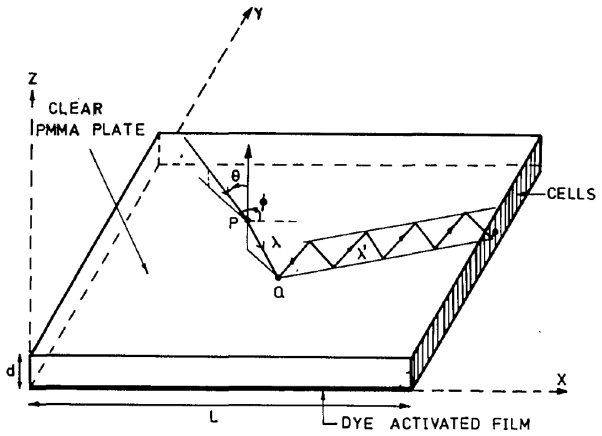

Figure 3.1: Schematic representation of a LSC, where can be seen the path of a useful light ray. P corresponds to the point of incidence of the solar ray, and Q is the point where it is absorbed and reemitted by the dye (λ exchanges to λ'). Some geometrical parameters are also indicated, d is the thickness and L is the length. θ and Φ are the angular coordinates (incidence and azimuth, respectively). Adapted from [231].

tra) one can easily modify the dimensions, layout and optical characteristics of a concentrator and estimate their impact on the performance. It also offers the possibility to try out different configurations: a volume concentrator could be compared to a layered concentrator where the external layers only have absorbing properties whereas the internal layer conducts radiation, for example [222].

In the same year, Sholin *et. al* using Monte Carlo simulations calculated the optical efficiency of LSCs where the photons collection could be made through a single-edge or through the full-perimeter. They simulated different quantum dots and organic dyes. The most efficient LSC were based on Rhodamine B with an optical conversion efficiency of 22.5 % for full-perimeter photons collection. They concluded that the overlap between the absorption and emission bands in commercially available quantum dots are a limiting factor in efficient LSCs. They also simulated both rectangular and square geometries suggesting that the dependence of the optical efficiency on the shape of the LSC is of minor importance. The development of infrared-emitting polymers for use in organic light-emitting diodes may soon provide several good LSC dyes allowing 30 % LSC optical efficiencies as needed for commercial applications [208].

Another example can be seen in the work of Şahin *et al.* where they tested semiconductor nanoparticles with a wide absorption band and small reabsorption probability as dopants in

luminescent solar concentrators. They used Monte Carlo simulations of photon transport to predict the performance of the LSCs based on type II CdSe-CdTe quantum dots, see Figure 3.2A, and CdSe-CdTe nanorods, see Figure 3.2B. Their computations suggests that semiconductor-based LSCs can be highly efficient resulting in an optical efficiency of 23.27 %. The optimum performance is reached with a fairly long LSC with a photovoltaic cell covering only one edge. In addition, when the LSC has CdSe-CdTe nanorods that are aligned perpendicularly to the top surface, the escape of photons from the top surface is significantly reduced. These results are encouraging for cost-effective LSC designs based on semiconductor nanoparticles [209].

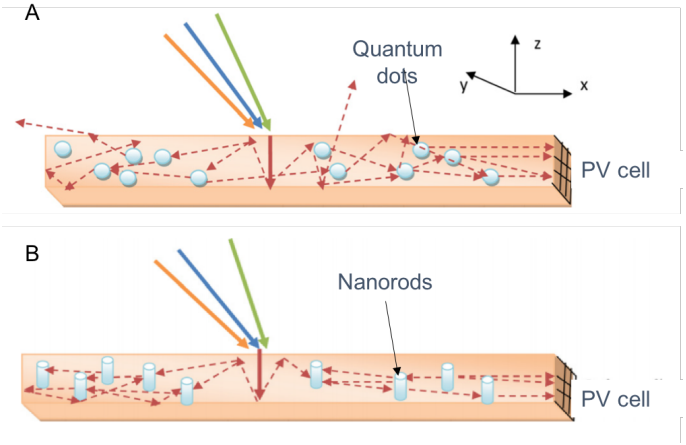

Figure 3.2: Illustration of radiation propagation in LSC with (A) quantum dots and (B) nanorods. Adapted from [209].

In 2014, Meinardi *et al.* using Monte Carlo simulations showed a 100-fold increase in efficiency using giant quantum dots compared with core-only nanocrystals. They demonstrate the feasibility of using high-optical-quality quantum dot-PMMA nanocomposites fabricated using a modified industrial method that preserves the radiation-emitting properties of giant quantum dots upon incorporation into the polymer. The results demonstrate the significant promise of Stokes-shift-engineered quantum dots for large-area luminescent solar concentrators and an optical efficiency of 10.2 % was obtained. Figure 3.3 shows two results obtained for different number of propagated photons [170].

More recently, the same authors, demonstrated the use of indirect band gap semiconductor nanostructures such as highly emissive silicon quantum dots. The simulations indicate that $\eta \geq 6\,\%$ is achievable on increasing the thickness of $12 \times 12\,cm^2$ devices to $2\,cm$, which enhances

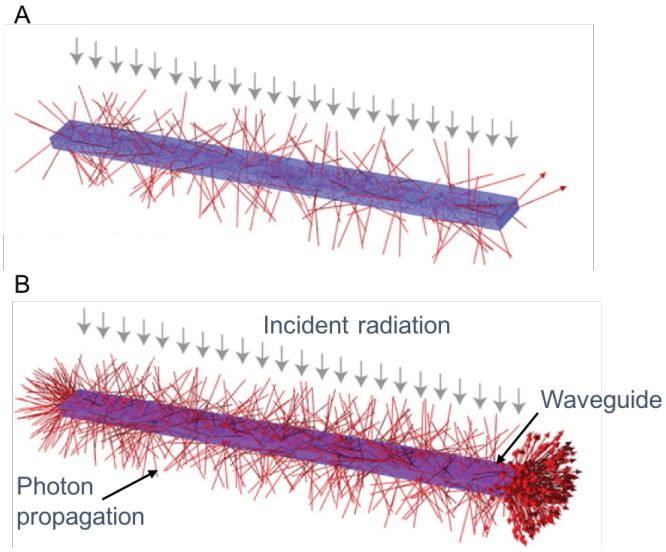

Figure 3.3: Illustration of radiation propagation in LSC with (A) quantum dots and (B) nanorods. Adapted from [209].

the solar harvesting capability of the experimental LSCs without significant reabsorption losses. Increasing the LSC area to $1\,m^2$ leads to the expected mild reduction of the optical efficiency due to the combined effect of weak reabsorption and scattering losses. However, the optical efficiency is preserved at larger than $3\,\%$ for 2-cm-thick slabs, and the device peak power output increases with the LSC dimensions, reaching over $30\,W$. They also study the ultimate device performances achievable using these LSCs simulating the situation in which the emission efficiency of the Si quantum dots reaches the fully optimized value ($100\,\%$). Their calculations indicate that $\eta = 15\,\%$ would be obtained by increasing the thickness of the experimental $12 \times 12\,cm^2$ LSC to $2\,cm$ and that efficiency as high as $\eta = 7\,\%$ would be achieved even for the $1 \times 1\,m^2$ device, which would therefore generate over $70\,W$ of peak optical power [232].

3.3 Monte Carlo ray-tracing algorithm

The scope and goal of this chapter is to study the working principle of Luminescent Solar Concentrators and understand its processes in order to develop a proper strategy to try to enhance its efficiency mostly through geometry optimization. With this goal in mind, a Ray-Tracing simulation model based on the Monte Carlo method was developed and implemented

in Matlab. I would like to enphasise that the algorithm described herein was implemented by M.Sc. Luis Minas at Instituto Superior Técnico, Universidade de Lisboa within the scope of his master thesis. I have since adapated the Monte-Carlo ray-tracing program to simulate the LSCs and LDS layers presented in this thesis. This method is based on splitting the radiation in a finite number of solar beams, so that a tracing of each ray that enters the LSC matrix can be done. By modelling the path described by each ray one can know whether the photons were trapped inside the substrate, absorbed by the luminescent species, how many reflections have they suffered, if they were lost in the matrix, or collected at the edges [222].

The Monte Carlo algorithm is stochastic and typically consists of random draws based on given distributions that characterize a sequence of local events that define a global one and lead to a final state. By repeating this process a considerable amount of times, an approximation of the solution is reached [233]. Hence, the more repetitions are made, the more accurate the solution will be. In order to ensure this, 10^6 photons are tested in each simulation.

As previously mentioned, Monte Carlo simulations are a common tool to study radiation propagation inside luminescent solar concentrators as phase-dependent wave effects can be negligible turning it into something more practical. Figure 3.4 shows the flowchart of the Monte Carlo algorithm that we intend to use. The inputs of the Monte Carlo ray-tracing simulation consist of the solar spectrum AM1.5G (280-1600 nm), the absorption and emission spectra, the absolute emission quantum yield and dispersion curve of each LSC. Furthermore, we consider a thin layer of air underneath the LSC.

With each run of the algorithm, a photon with a randomly selected wavelength is launched. The wavelength of the photon is generated accordingly with the AM 1.5G Solar Spectrum and then we begin to trace its position.

Being the initial position at the top of the matrix (air region), the user is allowed to assign either a 90° or a random angle incidence of the ray with respect to the surface of the LSC (to allow and predict the possibility of diffuse radiation hitting the LSC). If the photon does not miss the matrix or is reflected at the top, it enters the LSC region. Then a couple of tests are made to check if the luminescent species absorb and emit the radiation. Firstly, a comparison of a random generated number between 0 and 1 is compared with the absorption probability of the active centres for the previously predetermined wavelength of the photon.

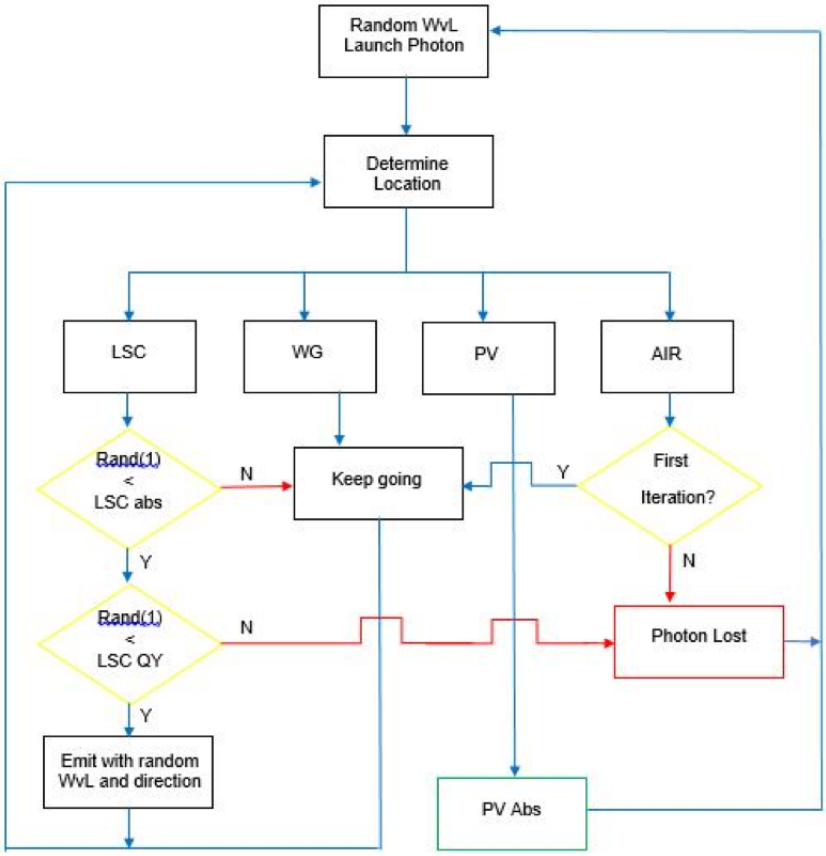

Figure 3.4: LSC Monte Carlo ray-tracing flow chart.

In order to get the absorption probability the A in $\eta_{abs} = 1 - 10^{-A}$ is replaced by:

$$A = \alpha_\lambda PhotonStep \tag{3.1}$$

being α_λ the attenuation coefficient per wavelength of the luminescent specie and *Photon Step* the desired minimum distance that the photon will travel in each iteration. If proves to be higher than the random number generated then an absorption event has taken place. If not the photon continues its path accordingly to its direction vector, until another check is made and it gets absorbed, reflected or refracted at one of the edges of the LSC. If an absorption event in the LSC is recorded, then another test is made, comparing once again a random number between 0 and 1 and the absolute emission quantum yield (η_{yield}) of the emitting centre for each photon wavelength. If the η_{yield} is higher than the number generated the active centre will fluoresce and emit a photon with a new wavelength (with respect to its emission spectrum) and a random direction. If the photon fail this test it is considered lost

to non-radiative losses and another photon is launched.

When the photon reaches an edge, either unabsorbed or after absorption and posterior re-emission, two possible outcomes are possible. It can be reflected and remain in the LSC region or it can be refracted and enter the waveguide, the PV cell or the air region. Considering that it hits the PV cell, a PV absorption is recorded, the corresponding position on the PV cell and the wavelength of the photon is saved to check if there is the possibility of photocurrent conversion and we move to the next photon.

Inside the waveguide region the photons suffers more reflections and refractions when it hits its edges and it may either return to the LSC region, hit the PV cell or even refract to an air surrounding region. There are two possibilities for the photon to be found in an air region. If it is its first iteration, it means that it is awaiting launch and it is allowed to move forward and try to penetrate the substrate. If not, then it has escaped from the matrix and is considered lost.

The possibility of adding more than one optically active layer on top of the waveguide was considered. This allow us to test the matrix behaviour with the feature of multilayer, being able to combine different absorption and emission spectra from several kinds of emitting centres to make a better use of the solar spectrum and try to diminish some performance cutback factors such as reabsorption events. The flow chart that can be seen in Figure 3.4 still applies either we have one, two or three optically active layers stacked up in the waveguide. The only difference is that when the photon leaves one LSC region, it can move to another layer, or as depicted before it can travel to the waveguide, PV cell or escape to an air region. All of the layers that may be included in the multilayer feature execute the same tests with the particularity that each one have distinct emitting centres encapsulated.

Using the algorithm above described it is possible to determine several quantities that allow the calculation of the theoretical η_{opt} values for each material and geometry simulated. For simulation purposes the η_{opt} is defined as the energy emitted (per unit of time) from the edge of the LSC divided by the solar energy falling on the LSC (per unit of time). Thus, the P_{in} and P_{out} can be written as follows:

$$P_{in} = \frac{hc}{\lambda} \#IncidentPhotons_{MC} \tag{3.2}$$

and

$$P_{out} = \frac{hc}{\lambda} \#Photons_{PV} \tag{3.3}$$

Assuming that all photons launched in the simulation hit the matrix in one second:

$$\#IncidentPhotons_{MC} = \frac{Photons_{MC}}{Area_{LSC}} [photons \cdot s^{-1} \cdot m^{-2}] \tag{3.4}$$

where the subscript MC stands for the Monte Carlo Simulations, we are able to determine the photon density used in our tests. Since to accurately reproduce the incident power of the Sun we would need a much larger number of photons, we apply a ratio with respect to the number we have used (one million in each sample):

$$CorrectionRatio = \frac{\#IncidentPhotons_{MC}}{\#IncidentPhotons_{LSC}} \tag{3.5}$$

In order to calculate the short circuit current generated by the PV cell, we can write the following expression:

$$\#ChargeCarriers_{PV} = Photons_{PV} \times EQE \tag{3.6}$$

where $Photons_{PV}$ represents the number of photons that have reached the PV cell from the LSC. The short circuit current generated after the ratio correction comes then:

$$I_{SC} = \frac{q \times \#ChargeCarriers_{PV}}{CorrectionRatio} [A]. \tag{3.7}$$

Chapter 4

Optically active layers processing

In this thesis, poly(methyl methacrylate) (PMMA) and organic-inorganic hybrids, named di/tri-ureasils, formed by polyether-based chains grafted to a siliceous backbone through urea cross linkages, were used as hosts for incorporation of the optically active centres. The PMMA was doped with ionogels based on Ln^{3+} like Tb^{3+}, Eu^{3+}, Yb^{3+} and Nd^{3+}. The Ln^{3+}-based ionogels were synthesized by Marita Cardoso MSc (PhD student at University of Aveiro) in close collaboration with the group of Professor Verónica de Zea Bermudez from University of Trás-os-Montes and Alto Douro. The ionogels incorporation in the PMMA and processing as films or monoliths were performed by myself and Marita Cardoso. The di-ureasil, d-U(600), and tri-ureasil, t-U(5000), organic-inorganic hybrids were doped with $Eu(tta)_3 \cdot 2H_2O$ (tta= 2-thenoyltrifluoroacetone) complex, Rhodamine 6G (Rh6G), Rhodamine 800 (Rh800), silicon 2,3-naphthalocyanine bis(trihexylsilyloxide) (SiNc or NIR775) organic dyes and chlorophyll molecules. The organic-inorganic hybrids and the $Eu(tta)_3 \cdot 2H_2O$ complex were synthesized by Lianshe Fu PhD (Principal researcher in physics department at University of Aveiro). The Eu^{3+}-based complex and organic dyes (Rh6G, Rh800 and SiNc) incorporation into the organic-inorganic hybrid materials were performed by myself. The chlorophyll molecules were extracted and purified by Edison Pecoraro PhD from the group of Professor Sidney Ribeiro from UNESP - Institute of Chemistry, São Paulo State University, Araraquara-São Paulo, Brazil. Also, R-phycoerythrin (R-PE), which is a phycobiliprotein, extracted from *Gracilaria sp.* algae was used as an aqueous solution. The R-PE was extracted and purified by Margarida Martins MSc (PhD student at University of Aveiro) and Sónia Ventura PhD (Principal researcher in chemistry department at University of Aveiro) from the group of Professor João

Coutinho from the chemistry department at University of Aveiro. The materials synthesis and extraction details are described below.

4.1 Lanthanide doped PMMA

4.1.1 Materials

The following chemicals were used as purchased: N-butylimidazole (BIm) (98 %, Aldrich), (3-chloropropyl)trimethoxysilane (TMSP) (97 %, Aldrich), Terbium(III) chloride hexahydrate ($TbCl_3$·
$6H_2O$) (99.9 %, Acros Organics), Europium(III) chloride hexahydrate ($EuCl_3 \cdot 6H_2O$) (99.99 %, Aldrich chem. co), Ytterbium (III) chloride hexahydrate ($YbCl_3 \cdot 6H_2O$) (99.9 %, Aldrich), Neodymium(III) chloride hexahydrate ($NdCl_3 \cdot 6H_2O$) (99.9 %, Aldrich), 2-thenoyltrifluoroacetone (TTA) (99 %, Aldrich), methyl methacrylate (99 %, Acros), benzoyl peroxide (97 %, Alfa Aesar), anhydrous acetic ester (98.8 %, Sigma-Aldrich), ethanol (EtOH) (99.8 %, Fisher Chemical) tetrahydrofuran (THF, Sigma-Aldrich) sodium hydroxide (NaOH, Merck), dichloromethane (DCM, Fisher Chemical). High purity distilled water was used in all experiments.

4.1.2 Synthesis of 1-butyl-3-[3-(trimethoxysilyl)propyl]imidazolium chloride ([B(TMSP)Im]Cl) ionic liquid

The novel ionic liquid 1-butyl-3-[3-(trimethoxysilyl)propyl]imidazolium chloride ([B(TMSP)Im]Cl) was synthesized by mixing one equivalent of N-butylimidazole (BIm) with one equivalent of (3-chloropropyl)trimethoxysilane (TMSP). The mixture was stirred at 70 $°C$ for 5 days under nitrogen atmosphere. Then, the pale-yellow viscous product was washed with anhydrous acetic ester (10 mL) three times. The resulting ionic liquid was dried under vacuum condition to remove the excess acetic ester and stored also under vacuum conditions.

4.1.3 Ln^{3+}-based complexes [NaLn(TTA)$_4$], with Ln = Tb, Eu, Yb and Nd.

The Ln^{3+}-based complexes [NaLn(TTA)$_4$], with Ln = Tb, Eu, Yb and Nd were synthesized following the procedure: 0.889 g (4 equivalent) of TTA was dissolved in EtOH and deprotonated with 0.16 g NaOH (4 equivalent) at 50-60$°C$ for 2 $hours$ followed by the drop-

wise addition of 1 equivalent of $LnCl_3{\cdot}6H_2O$, with Ln = Tb, Eu, Yb and Nd, respectively dissolved in ethanol. The mixtures were kept at 50-60 $°C$ for another 1 $hour$. Then, the ethanol was evaporated under reduced pressure on a rotary evaporator and dried for 3 days at 50$°C$. The Ln^{3+}-based complexes were then dissolved in THF to remove sodium chloride by precipitation and centrifugation (three times at 3000 rpm). The products were dried in an oven at 50$°C$, washed with ultrapure ice water and dried again in an oven at 50$°C$. The resulting powders were again dried under vacuum conditions and stored.

4.1.4 Synthesis of ionogel [B(TMSP]Im][Ln(TTA)$_4$], with Ln = Eu, Tb, Nd and Yb

The [B(TMSP]Im][Ln(TTA)$_4$] ionic liquids were produced by reacting 1 equivalent of [Na[Ln(TTA)$_4$] with 1 equivalent of [B(TMSP)Im]Cl in THF under nitrogen atmosphere. On the second stage of the synthesis, a volume of ethanol and water were added to the ionogel solution prepared in the previous step (molar proportion 1 [B(TMSP]Im][Ln(TTA)$_4$]:4 EtOH:1.5 H_2O) to initiate the sol-gel process, Figure 4.1. The mixture was stirred in a sealed flask for approximately 30 min, cast into a Teflon® mold, covered with Parafilm® and left in a fume cupboard for 24 $hours$. The mold was transferred to an oven at 50$°C$ and the ionogel sample was aged for a period of 4 weeks.

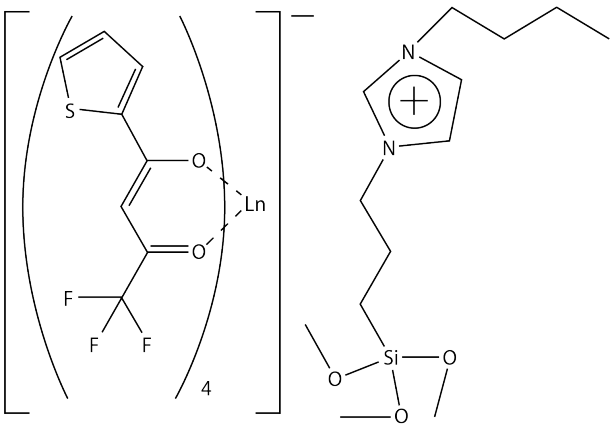

Figure 4.1: Schematic structure of the non-hydrolysed Ln^{3+}-based ionogels [B(TMSP)Im][Ln(TTA)$_4$] with Ln = Tb, Eu, Yb or Nd.

Elemental analysis (EA) on CHNS was performed with a TruSpec 630-200-200 CNHS Analyser at the Microanalysis Laboratory at the Department of Chemistry, University of

Aveiro with an accuracy of 1 % for each element.

Analysis calculated for $TbC_{42}H_{34}S_4N_2O_{11}SiF_{12}$: C, 39.23; H, 2.67; N, 2,18; S, 9.97. Found: C, 39.04; H, 3.02; N, 2.29; S, 9.38. Analysis calculated for $EuC_{42}H_{34}S_4N_2O_{11}SiF_{12}$: C, 39.44; H, 2.69; N, 2.19; S, 10.03. Found: C, 39.04; H, 2.85; N, 2.34; S, 8.04. Analysis calculated for $YbC_{42}H_{34}S_4N_2O_{11}SiF_{12}$: C, 38.80; H, 2.64; N, 2.16; S, 9.86. Found: C, 39.96; H, 3,05; N, 2.23; S, 8.31. Analysis calculated for $NdC_{42}H_{34}S_4N_2O_{11}SiF_{12}$: C, 39.68; H, 2.70; N, 2.20; S, 10.09. Found: C, 41.15; H, 3.44; N, 2.23; S, 8.20.

4.1.5 Synthesis of PMMA-based materials doped with the ionogels [B(TMSP]Im][Ln(TTA)$_4$], with Ln = Tb, Eu, Yb and Nd

The PMMA, Figure 4.2, matrix was produced mixing 10 g of methyl methacrylate (Acros organic, 99 %, stabilized) with 0.06 g of benzoyl peroxide (Alfa Aesar, 97 %) in a glass vial. The mixture was heated at 80-90°C for 30 min and then placed in an oven at 40°C until complete polymerization.

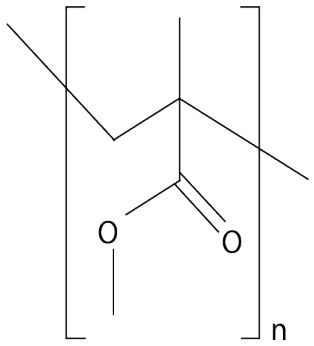

Figure 4.2: Schematic structure of the PMMA.

To produce the PMMA-based materials (BLn/PMMA/TMSPM-X, with X = miono-gel/mPMMA), a THF solution of [B(TMSP]Im][Ln(TTA)$_4$] was added to a PMMA solution in dichloromethane. A volume of ethanol and water was added to the solution prepared in the previous step (molar proportion 1 [B(TMSP]Im][Ln(TTA)$_4$]:4 EtOH:1.5 H_2O). The mixture was stirred in a sealed flask for approximately 30 min, cast into a glass mold, covered with Parafilm and left in a fume cupboard in a dark place until the solution dry and the film was formed. The PMMA-based materials samples doped with different concentrations of X =10 and 20 % (X = $m_{ionogel}/m_{PMMA}$) of Ln^{3+}-based ionogel were produced. The samples are designated as PMMA-Ln-X, where Ln=Tb, Eu, Nd and Yb and X= 10 and 20 %, as stated

in Table 4.1.

Table 4.1: Designation of the PMMA doped with Ln^{3+}-based ionogels.

Designation	Ln^{3+}	[Ionogel] (%)
PMMA-Tb-20	Tb^{3+}	20
PMMA-Eu-10	Eu^{3+}	10
PMMA-Eu-20		20
PMMA-Yb-20	Yb^{3+}	20
PMMA-Nd-20	Nd^{3+}	20

These compounds have been selected from many others Ln^{3+}-based complexes because of its high luminescence and their solubility in dichloromethane which is also a good solvent for PMMA. The PMMA is preferred because of its transparency, mechanically resistance, easy handling and chemical stability [234].

4.2 Sol-Gel process

The organic-inorganic hybrid materials were prepared by the sol-gel process and thus, this section summarises the main aspects of this method that are considered to be relevant for this thesis. The sol-gel method presents some features that are advantageous for the synthesis of organic-inorganic hybrids, such as the possibility of mixing organic and inorganic components at the nanometric scale, in mild synthesis conditions, including accessible and cheap precursors, the use of organic solvents, low processing temperatures and versatility of the colloidal state processing [235, 236].

The most widely used class of precursors are the alkoxides, namely, the metal alkoxides, $M(OR)_z$, where M is a metal, O is oxygen, R is an alkyl group and z is the number of alkoxy groups (OR) linked to the metal. The most studied example is silicon tetraethoxide (or tetraethoxysilane, or tetraethyl orthosilicate, TEOS) [236, 237]. The precursors are used to prepare the colloidal phase that is a suspension in which the dispersed phase is so small ($\sim$ 1-1000 nm) that gravitational forces are negligible and interactions are dominated by short-range forces, such as van der Waals attractions and surface charges. Metal alkoxides are popular because they react rapidly in the presence of water. The reaction is called

hydrolysis, since a hydroxyl group becomes attached to the metal atom [236]:

$$Si(OR)_4 + H_2O \rightarrow HO{-}Si(OR)_3 + ROH \tag{4.1}$$

where ROH is an alcohol. Depending on the amount of water and catalyst present, hydrolysis may be completed, in a way that all the OR groups are replaced by OH [236]:

$$Si(OR)_4 + 4H_2O \rightarrow Si(OH)_4 + 4ROH \tag{4.2}$$

or it may stop while the metal is only partially hydrolysed. Two partially hydrolysed molecules can link together in a condensation reaction:

$$(OR)_3Si{-}OH + HO{-}Si(OR)_3 \rightarrow (OR)_3Si{-}O{-}Si(OR)_3 + H_2O \tag{4.3}$$

or

$$(OR)_3Si{-}OR + HO{-}Si(OR)_3 \rightarrow (OR)_3Si{-}O{-}Si(OR)_3 + ROH \tag{4.4}$$

By definition, condensation liberates a small molecule, such as water or an alcohol. This type of reaction can continue to build larger silicon-containing structures by the process of polymerization [236]. A gel contains a continuous solid skeleton enclosing a continuous liquid phase. Ggelation can occur after a sol is cast into a mould, producing bulk materials in the desired shape (monolith) [236] or films through, for instance, spin- and dip-coating.

The sol-gel process involves multiple variables, such as time, temperature, nature of catalysts, reagents concentration, among others, that will condition the final features of the produced materials. The versatility in the processing of these materials is directly linked to the success of their development, together with the low cost and the availability of the precursors and of the processing equipment. Since the rheology of the hybrid colloidal suspension can be controlled and adjusted, there is a wide range of processing methodologies, such as: film deposition methods, fibre extrusion, fibre pulling, electrospinning, electro- chemical deposition, (soft) lithography based techniques, aerosol or spray, ink-jet printing, among others [235, 238], which allows the easy processing of films and coatings of plastic optical fibres (POFs) or hollow-core filling to fabricate the LSCs in this thesis.

4.3 Synthesis of non-doped organic-inorganic hybrids: Di- and Tri-Ureasils

The di-ureasil hybrid material is formed by polyether chains (with average molecular weight of $600\,g \cdot mol^{-1}$) covalently linked to a siliceous inorganic skeleton by urea bridges [239]. The non-hydrolysed precursor, d-UPTES(600), was prepared by the addition of isocyanate-propyl-triethoxysilane (ICPTES, Sigma-Aldrich, 95 %) to a solution of Jeffamine ED-600® (Sigma-Aldrich, 97 %) in dried tetrahydrofuran (THF, Sigma-Aldrich, 99.9 %) (the molar ratio Jeffamine ED-600® to ICPTES was 1 : 2). This solution was kept under stirring at room temperature for $24\,hours$ [239]. Then, the non-hydrolysed d-UPTES(600) was obtained as a transparent liquid after evaporation of THF at room temperature under vacuum, Figure 4.3.

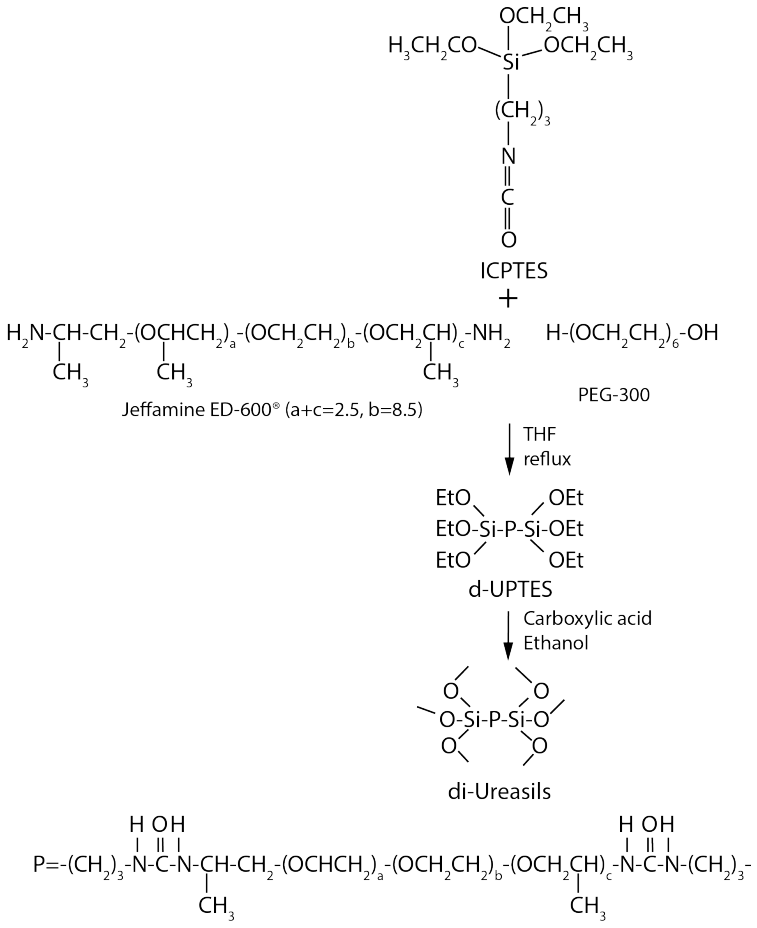

Figure 4.3: Schematic representation of the synthesis of the non-hydrolyzed precursor of d-U(600). Adapted from [240].

The t-UPTES(5000) was synthesised in an identical way to that of d-UPTES(600), except for the Jeffamine® used, which presents a branched chain structure with the amino groups located at the end of each branch, with a molecular mass of $5000\,g \cdot mol^{-1}$ (Huntsman) [241], Figure 4.4.

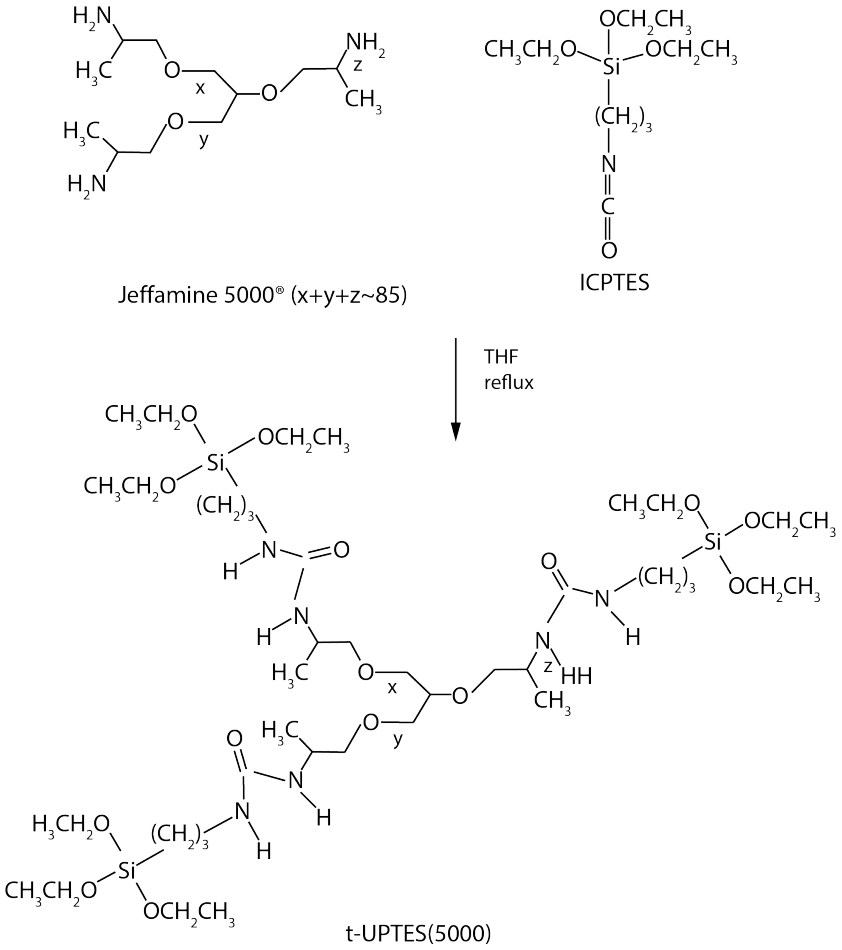

Figure 4.4: Schematic representation of the synthesis of the non-hydrolyzed precursor of t-U(5000). Adapted from [241].

4.4 Doped organic-inorganic materials

4.4.1 Eu^{3+} doped organic-inorganic materials

The synthesis of the $Eu(tta)_3 \cdot 2H_2O$ (Figure 4.5A) complex is fully described elsewhere [189, 242]. The chemicals europium chloride ($EuCl_3 \cdot 6H_2O$, Sigma-Aldrich, 99 %) and 2-thenoyltrifluoroacetone (Htta, Sigma-Aldrich) were used as received; $1\,mmol$ ($0.3662\,g$) of

$EuCl_3 \cdot 6H_2O$ was dissolved in 1.5 mL of ethanol (EtOH, Fisher Scientific, 99.9 %), under stirring. Then, 3 $mmol$ (0.6664 g) of Htta were added dropwise to the ethanolic solution of $EuCl_3 \cdot 6H_2O$. The pH of this solution was adjusted to 6-7 by adding an appropriate amount of an ethanolic sodium hydroxide (NaOH, Merck, 98 %) solution. The resulting mixture was stirred for 24 $hours$ at room temperature and then the solvent was slowly evaporated during 48 $hours$. The yellow solid obtained was washed with water and hexane (Sigma-Aldrich, $\geqslant$ 95 %) and recrystallized in EtOH and dried at 45°C during 48 $hours$.

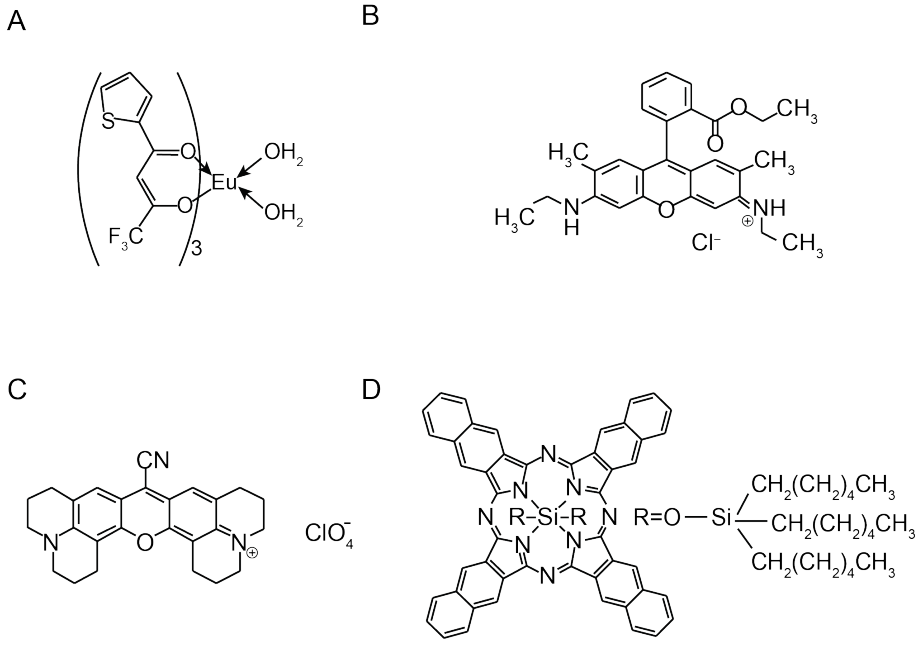

Figure 4.5: Scheme of the molecular structures of the (A) $Eu(tta)_3 \cdot 2H_2O$ complex, (B) Rhodamine 6G, (C) Rhodamine 800 and (D) SiNc organic dyes.

The rationale behind the selection of the $Eu(tta)_3 \cdot 2H_2O$ complex lies on its high $^5D_0$ emission quantum efficiency, of 0.74. [243], that must corresponds to one of the highest q values of Eu^{3+}-based complexes. Moreover, after incorporation on the hybrid host the water molecules coordinated to the Eu^{3+} ions will be replaced by the oxygen atoms from the carbonyl groups of the urea cross linkages contributing to suppress the Eu^{3+} emission quenching.

The Eu^{3+} complex described above was incorporated into the non-hydrolysed precursors. The t-UPTES(5000)-based hybrids were prepared using 60 mg of $Eu(tta)_3 \cdot 2H_2O$ complex dissolved in 2.250 mL of EtOH with 0.30 mL of phenyltrimethoxysilane (PTMS) and added to 3.0 g of t-UPTES(5000) in the presence of 7.0×10^{-2} mL of HCl (37 %) 1 M (in EtOH).

4.4.2 Dye doped organic-inorganic materials

The Rh6G (Sigma-Aldrich, dye content 99 %), Rh800 (Sigma-Aldrich) and SiNc Sigma-Aldrich, dye content 95 %) (Figure 4.5B, C and D, respectively) were incorporated into the non-hydrolysed precursors. The organic dyes were used as received. The Rh6G organic dye was selected due to its absorption and emission features, associated with a high q both in ethanolic solution (reported $q = 0.94$ in ethanol [244]) and when incorporated into a hybrid host ($q = 0.70 \pm 0.07$). The Rh800 and SiNc organic dyes were chosen mostly due to its NIR emitting spectral range.

The t-U(5000) based hybrids were prepared using $1.8\,mg$ of Rh6G dissolved in $2.250\,mL$ of EtOH with $0.30\,mL$ of PTMS and added to $3.0\,g$ of t-UPTES(5000) in the presence of $7.0 \times 10^{-2}\,mL$ of HCl $1\,M$ (in EtOH, from Sigma-Aldrich). For the Rh800-doped hybrid, $2.8\,mg$ of Rh800 were dissolved in $1.2\,mL$ of EtOH and added to the t-UPTES(5000) in the presence of $8.6 \times 10^{-2}\,mL$ of HCl $1\,M$. For the SiNc-doped hybrids, a volume of $1\,mL$ of a $2.3\,mM$ SiNc solution in THF was added to $1.5\,g$ of t-UPTES(5000) (molar ratio SiNc:t-UPTES(5000) = 1 : 114) followed by the addition of $220\,\mu L$ of EtOH and $25\,\mu L$ of water. The suspensions were kept at room temperature under magnetic stirring for 15 min. A volume of $20\,\mu L$ of a $0.2\,M$ HCl solution was then added to lower the pH from 9 to 2 to accelerate the sol-gel transition. The remaining part of the suspension was deposited on glass substrates (NORMAX, $7.6 \times 2.6 \times 0.1\,cm^3$) by a one-step spin-coating process (SPIN 150-NPP, APT) at $1000\,rpm$ for $60\,s$, at ambient conditions. The resulting films were heat-treated at $45°C$ for $24\,hours$ for residual solvents removal.

The hybrid materials, processed as monoliths and films, will be hereafter termed as termed in Table 4.2. It is noted that M and F stands for monoliths and films, respectively.

Table 4.2: Designation of the organic-inorganic hybrids doped with organic dyes.

Designation	Hybrid	Optically active centre
Eu-LSC	t-U(5000)	$Eu(tta)_3 \cdot 2H_2O$
Rh6G-LSC		Rhodamine 6G
Rh800-LSC		Rhodamine 800
F-M/t-U(5000)/SiNc		SiNc

4.4.3 Chlorophyll doped organic-inorganic materials

Chlorophyll was obtained from *Spirulina maxima* via solvent extraction and purified by column chromatography, Figure 7.2. An amount of $5\,g$ of *Spirulina maxima* powder (supplied by a local Brazilian pharmacy shop) were dispersed in $50\,mL$ of dichloromethane (Synth PA-ACS) in a $250\,mL$ Erlenmeyer flask at room temperature.

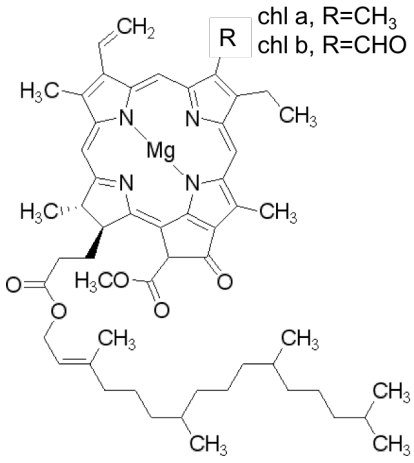

Figure 4.6: Scheme of the molecular structures of chl-a and chl-b.

The suspension was kept under magnetic stirring for 20 min and thereupon, filtered on standard filter paper (pleated fold). The liquid phase, containing chlorophyll-a (chl-a), chlorophyll-b (chl-b), β-carotene and xanthophylls, was transfer to an amber flask and stored in the refrigerator. The solid phase was re-suspended in $50\,mL$ of dichloromethane and underwent the same extraction process 3 additional times. The extract solution ($200\,mL$) was concentrated to a final volume of $5\,mL$ on a rotary evaporator under reduced pressure. Due to the presence of light in the environment where the extraction and purification processes are carried out, all the flasks containing the extract must be lightproof to avoid photo-degradation of chl-a. The extract purification was performed on a silica gel (200-400 mesh, $2\,cm$ in diameter and $15\,cm$ high) chromatographic column, packed with toluene. To prevent oxidation of the chlorophyll molecules, the column was wrapped with a black plastic film and the eluates were collected in amber flasks. The first elution was performed with the same column packing solvent ($150\,mL$ of toluene) to remove carotenes and xanthophyll, which are detected by the presence of yellow and orange colours. The elution of the dark blue/green solution, rich in chl-a, was performed with dichloromethane. Dark green chl-a crystals (ChE) were obtained

from the dichloromethane solution, by removing the solvent in a rotatory evaporator (over the course of the process, the solution was kept in a lightproof flask). The ChE were transferred to lightproof Petri dishes and stored within a vacuum desiccator at $15°C$ to avoid auto-oxidation processes.

The ChE were dissolved in ethanol (P.A. ACS reagent 96 %) under magnetic stirring for 15 min at room temperature. The d-UPTES(600) (or t-UPTES(5000)) precursor suspension was added to this solution and kept under magnetic stirring for 30 min at room temperature. Distinct concentrations of ChE were calculated since that ChE presents a 95 % purity (predominantly chl-a) and a molar mass of $893.51\,g \cdot mol^{-1}$ (Table 4.3). The volume of ethanol used to dissolve each mass was $2\,mL$ and the mass of the viscous suspension of each ureasil precursor was $3\,g$. The molecular density of ChE in the final materials, Table 4.3, was calculated based on the premise that all the solvent (added or produced over the sol-gel condensation) evaporated after the processing, and that the density of the resulting hybrids is $1.0\,g \cdot cm^{-3}$.

Table 4.3: List, designation and chlorophyll concentration ([chl]) of the organic-inorganic hybrids.

Designation	Hybrid host	[chl] $(molecules \cdot cm^{-3})$
dU6/tU5-chl-1	d-U(600)/t-U(5000)	3×10^{16}
dU6/tU5-chl-2		3×10^{17}
dU6/tU5-chl-3		3×10^{18}
dU6/tU5-chl-4		3×10^{19}
tU5-chl-5	t-U(5000)	6×10^{19}

In order to obtain monoliths and thin films based on organic-inorganic hybrids doped with chlorophyll, part of the as-prepared ChE-containing suspensions was submitted to sol-gel transition, by adding an ethanolic solution of HCl ($1.2\,M$) as a catalyst [$400\,\mu L$ for d-UPTES(600) and $200\,\mu L$ for t-UPTES(5000)]. Part of the volumes were cast onto polystyrene molds ($1.0 \times 1.0 \times 4.0\,cm^3$), covered with Parafilm®, and kept at 40° for 3 days, yielding greenish-transparent monoliths. The remaining volumes of the suspensions were deposited on glass substrates (NORMAX, $7.6 \times 2.6 \times 0.1\,cm^3$) by a one-step spin-coating process (SPIN 150-NPP, APT) at $1000\,rpm$ for $60\,s$, under ambient conditions. The resulting films were heat-treated at 45° for $24\,hours$ to remove the residual solvents.

4.5 R-PE based solutions

The red macroalgae *Gracilaria sp.* was grown in a land-based integrated aquaculture system at ALGAplus Lda, a company specialized in the production of marine macroalgae, located in Ílhavo, Portugal. The ammonium sulfate (99.5 %) used in phycobiliproteins precipitation was purchased at Merck. A commercial standard of R-phycoerythrin ($\geq 10.0\, mg \cdot mL^{-1}$) was purchased at Sigma- Aldrich.

The solid-liquid extraction procedure used here was adapted from the methodology already proposed by Martins *et al.* [245]. After the harvesting of the macroalgae, the samples were cleaned and washed with fresh and distilled water at least 3 times to eliminate small particles and residues. The marine biomass was then stored at $-20°C$. The red macroalgae samples were frozen in liquid nitrogen and ground to increase the contact surface, thus enhancing the extraction. Then, the biomass was homogenized in distilled water at a solid-liquid ratio of 0.5. The extraction was performed with water at $250\, rpm$ in an incubator (IKA KS 4000 ic control) protected from light exposure, during 20 min at room temperature. At the end of this step, a red/pinkish solution was obtained, filtered and centrifuged in a Thermo Scientific Heraeus Megafuge 16 R centrifuge at $5000\, rpm$ for 30 min at $4\,°C$. The resultant pellet was discarded while the phycobiliprotein-based red/pinkish supernatant was collected. The crude extract was pre-purified using ammonium sulphate at 30 %. The salt was dissolved and the solution was left at $4\,°C$ during 4 hours, being then centrifuged at $5000\, rpm$ for 30 min at $4\,°C$. After the precipitation of the target proteins, the pellet was resuspended in distilled water at several concentrations, Table 4.4.

Table 4.4: Designation and R-PE concentration ([R-PE], M) of the aqueous solutions.

Solution	[R-PE] ($\times 10^{-7}$)
RPE-1	0.4
RPE-2	1.7
RPE-3	2.1
RPE-4	2.5
RPE-5	3.3
RPE-6	4.2
RPE-7	5.8
RPE-8	7.5
RPE-9	17

The phycobiliprotein concentration of each extract was calculated using a UV-Vis microplate reader (Synergy HT micro-plate reader - BioTek) at 565 nm and a calibration curve previously established for the commercial standard R-phycoerytrin.

Chapter 5

Transparent luminescent down-shifting layers and planar luminescent solar concentrators

5.1 Introduction

In the first section of this chapter, we report Ln^{3+}-based ionogels as the luminescent material incorporated in PMMA. Ionogels are hybrid materials consisting of an ionic liquid confined inside the nano-sized pores of a silica matrix. The mechanical properties of the ionogels are very similar to those of regular sol-gel materials. Other interesting properties are high thermal stability, wide electrochemical window, high ionic conductivity and high quantum efficiency [246]. These materials were doped with Ln^{3+}-based complexes due to their attractive luminescent features as narrow emission bands, long emission lifetimes, wide emission range (tuneable from the UV to NIR). Although they offer poor mechanical properties and low thermal stability, the luminescent ionogels were incorporated into PMMA because it is a low-cost host, is environmentally friendly, and has high optical transparency. The ability to easily shape the ionogels provides an attractive versatility to prepare coatings, in particular, to be deposited on top of PV devices as LDS layers or in glass substrates as is the case of LSCs. Here, LDS layers and LSCs based on lanthanide-doped ionogels on PMMA with spectral absorption overlapping the AM1.5G spectrum and complementing that of PV cells,

emission in the visible-NIR spectral range and absolute emission quantum yield in the visible and in the NIR were fabricated. Ln^{3+}-based optical centres ensure large Stokes-shift enabling the production of transparent materials with negligible self-absorption allowing efficient solar radiation harvesting and conversion.

In the second section of this chapter, we quantify the performance of a NIR-emitting LSC using the silicon 2,3-naphthalocyanine bis-(trihexylsilyloxide) dye (SiNc or NIR775, Figure 4.5) entrapped in a tri-ureasil organic-inorganic hybrid host [136, 159, 189, 241, 247], t-U(5000), Figure 4.4. The SiNc dye molecule was first synthesized in 1984 and is characterized by a broad absorption range from the UV to the NIR [248], and an emission spectrum in the red/NIR spectral regions ($700 - 950\,nm$), which are desirable properties for PV conversion using c-Si PV cells [249–251]. Moreover, SiNc is thermally, chemically, and optically stable [252]. Previous studies showed that the use of SiNc as an additive in organic PV cells is advantageous in terms of enhancing the NIR emission, yielding an increase in the power conversion efficiency [251, 253]. To prevent the tendency of naphthalocyanines to aggregate due to their planar structure that enables $\pi - \pi$ stacking [254–258] and the consequent self-quenching of the emission (known as aggregation-caused quenching), SiNc must be encapsulated into a given medium that can trap and stabilize the dyes without aggregation, enhancing its photostability. Previously, SiNc was encapsulated into polymer dots and dendrimers [255] for cellular and in vivo imaging, where strong NIR emission is beneficial [259, 260]. Organic-inorganic hybrid hosts offer some advantages when compared to polymeric ones due to the presence of the inorganic skeleton that confers enhanced mechanical and thermal resistance and easy refractive index control. Moreover, organic-inorganic hybrids prevent the formation of non luminescent clusters or aggregates, with additional advantages of increasing the absolute emission quantum yield of some active centres and their photostability [89]. The incorporation of the dye into t-U(5000) and the ability of this novel SiNc-based tri-ureasil as a NIR-emitting layer for LSC applications demonstrated in this thesis pave the way for a new generation of NIR-emitting LSCs based on organic-inorganic hybrid materials.

5.2 Ln^{3+} based luminescent down-shifting layers and luminescent solar concentrators

This section aims to address the issue of the mismatch between the AM1.5G spectrum and the PV cells absorption curve, by using LDS layers and LSCs based on PMMA doped with Ln^{3+}- based ionogels with spectral absorption overlapping the AM1.5G spectrum and complementing that of PV cells and emission ranging from visible to NIR (c-Si PV cells maximum absorption). The use of LDS layers on PV cells may enhance their performance by acting in two aspects: (i) reducing the surface reflectance and (ii) increasing the EQE in the absorption range of the LDS layer. By coating a commercial c-Si PV cell with an Eu^{3+}-based layer, an absolute EQE increase of 25 % was achieved in the UV spectral region, which is among the top values reported so far. Concerning LSCs, Eu^{3+}- and Tb^{3+}-based optically active layers showed great potential for efficient and environmentally resistant LSCs, as η_{opt} values of 0.23 ± 0.01 % and 0.27 ± 0.01 %, were found, respectively. In what concerns NIR-emitting PMMA doped materials, the performance of the LDS layers and LSCs did not increase due to the low absolute emission quantum yield of these materials.

5.2.1 Optical characterization of the optically active layers

Figure 5.1A shows the room-temperature emission spectra of the PMMA-Ln-X samples, Table 4.1, excited at the wavelength that maximizes the emission intensity. The region marked with the asterisk is a superimposition between the Eu^{3+} $^5D_0 \rightarrow ^7F_{0-1}$ and the Tb^{3+} $^5D_4 \rightarrow ^7F_4$ transitions. The region marked with the cross is a superimposition between the Eu^{3+} $^5D_0 \rightarrow ^7F_2$ and the Tb^{3+} $^5D_4 \rightarrow ^7F_3$ transitions. The emission spectra of the PMMA-Tb-20, PMMA-Eu-10/20, PMMA-Yb-20 and PMMA-Nd-20 are dominated by the lines ascribed to the Tb^{3+} $^5D_4 \rightarrow ^7F_{6-3}$, Eu^{3+} $^5D_0 \rightarrow ^7F_{0-4}$, Yb^{3+} $^2F_{5/2} \rightarrow ^2F_{7/2}$ and to the Nd^{3+} $^4F_{3/2} \rightarrow ^4I_{11/2}$ transitions, respectively. Independently of the selected excitation wavelength (270-380 nm), no sign of the PMMA intrinsic emission could be observed, which readily suggests efficient PMMA-to-ligand or PMMA-to-Ln^{3+} energy transfer [261].

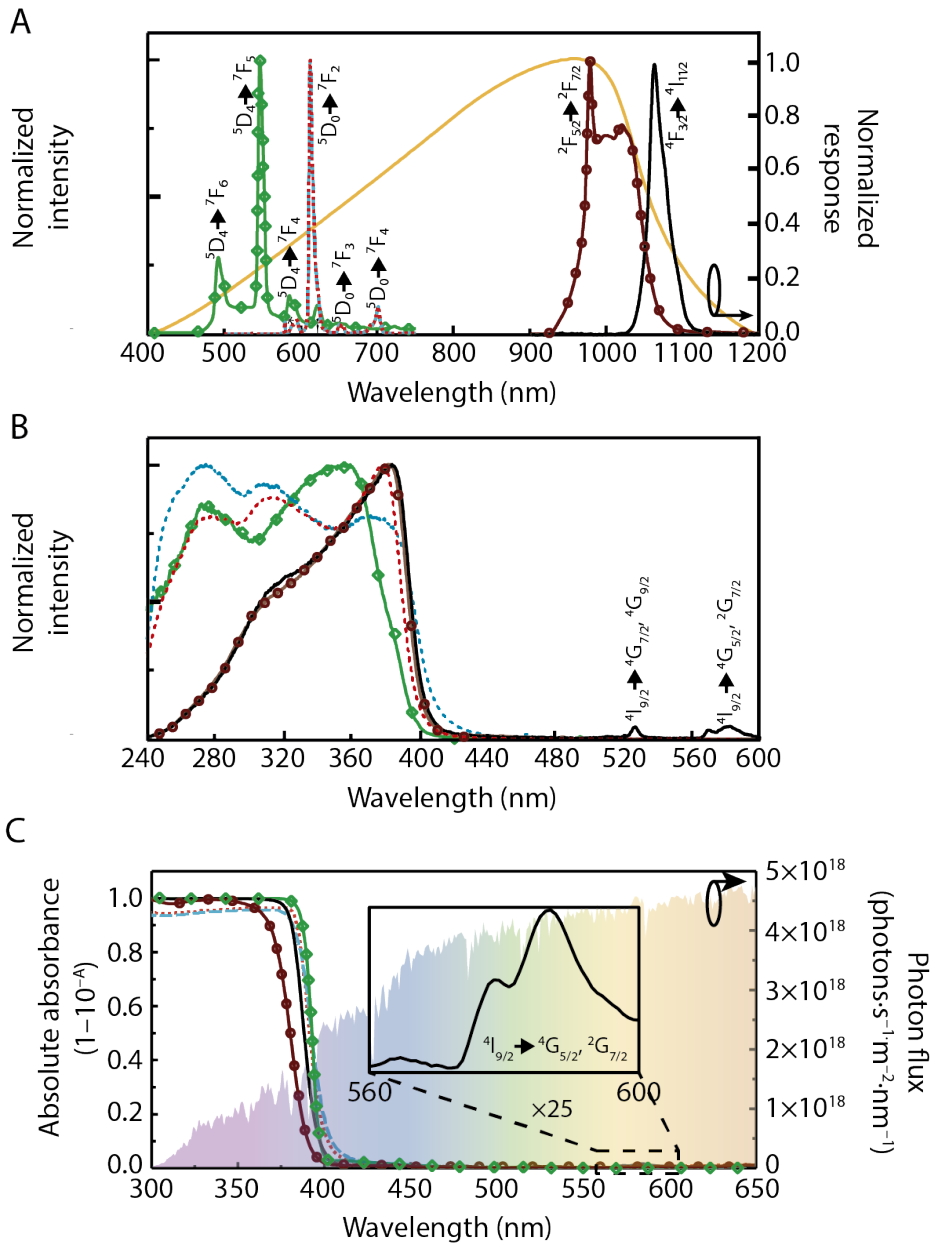

Figure 5.1: (A) Emission spectra excited at 360 nm for PMMA-Tb-20 (green squares) and 380 nm for PMMA-Eu-10 (red dots), PMMA-Eu-20 (light blue dashes), PMMA-Yb-20 (brown circles) and PMMA-Nd-20 (black line). The orange line is the normalized response curve of c-Si photovoltaic devices. (B) Excitation spectra for PMMA-Tb-20 monitored at 545 nm, PMMA-Eu-10 and PMMA-Eu-20 monitored at 612 nm, PMMA-Yb-20 monitored at 978 nm and for PMMA-Nd-20 monitored at 1062 nm. The transition around 530 nm $^4I_{9/2} \rightarrow ^4G_{7/2}$, $^4G_{9/2}$ and the transition around 580 nm $^4I_{9/2} \rightarrow ^4G_{5/2}$, $^2G_{7/2}$ are Nd^{3+} related transitions [262]. (C) Absorption spectra for PMMA-Tb-20, PMMA-Eu-10, PMMA-Eu-20, PMMA-Yb-20 and PMMA-Nd-20 (the colour code is the same as in (A)). and AM1.5G photon flux.

The excitation spectra were monitored around the maximum intensity peak positions, Figure 5.1B. In the case of the PMMA-Eu-10 and PMMA-Eu-20 the spectra show three main components peaking at 275, 320 and 380. The absence of relatively low intensity of the intra-$4f^6$ lines indicates that the Eu^{3+} excited states are mainly populated via ligand-sensitization rather than by direct excitation. The low wavelength components resemble those already observed for isolated $Eu(TTA)_3(H_2O)_2$ [263] and for organic-inorganic hybrids incorporating $Eu(TTA)_3(H_2O)_2$ and $Eu(TTA)_3$(phen) (phen=1,10-phenantroline), being ascribed to the π-π^* electronic transition of the organic ligands [264]. In the case of Tb^{3+}-, Yb^{3+}- and Nd^{3+}-based materials, the excited states are, as well, mainly populated via ligand-sensitization as almost no intensity of the $4f^n$-lines was measured. Apart from changes in the relative intensity, the UV-visible absorption spectrum reveals the same components detected in excitation spectra, Figure 5.1B and Figure 5.1C.

The shape of the absolute absorption spectra, Figure 5.1C, is identical for all samples with a minor low wavelength shift for the PMMA-Yb-20 sample and the appearance of the Nd^{3+} related $^4I_{9/2} \rightarrow {}^4G_{5/2}$, $^4G_{7/2}$ transition, in the PMMA-Nd-20.

The emission decay curves were monitored under UV excitation ($380\,nm$) revealing a single exponential behaviour, Figure 5.2. From the best data fit, the lifetime values were estimated, Table 5.1. We note that the lower value found for the higher concentrated Eu^{3+}-based sample (PMMA-Eu-20) compared with that of the PMMA-Eu-10 suggests that the concentration increase leads to an increase in the $^5D_0$ non-radiative transition probability.

Table 5.1: Emission lifetime (τ, $\times 10^{-3}\,s$) values of the PMMA-Ln-X excited at $380\,nm$ and monitored at distinct wavelengths (λ_e).

Sample	λ_e (nm)	τ
PMMA-Tb-20	544	0.061 ± 0.001
PMMA-Eu-10	612	0.641 ± 0.004
PMMA-Eu-20	612	0.494 ± 0.003
PMMA-Yb-20	978	0.017 ± 0.001
PMMA-Nd-20	1062	0.009 ± 0.001

The emission properties of the PMMA-Ln-X samples were further quantified through the measurement of the absolute emission quantum yield (q, Table 5.2), as function of the ex-

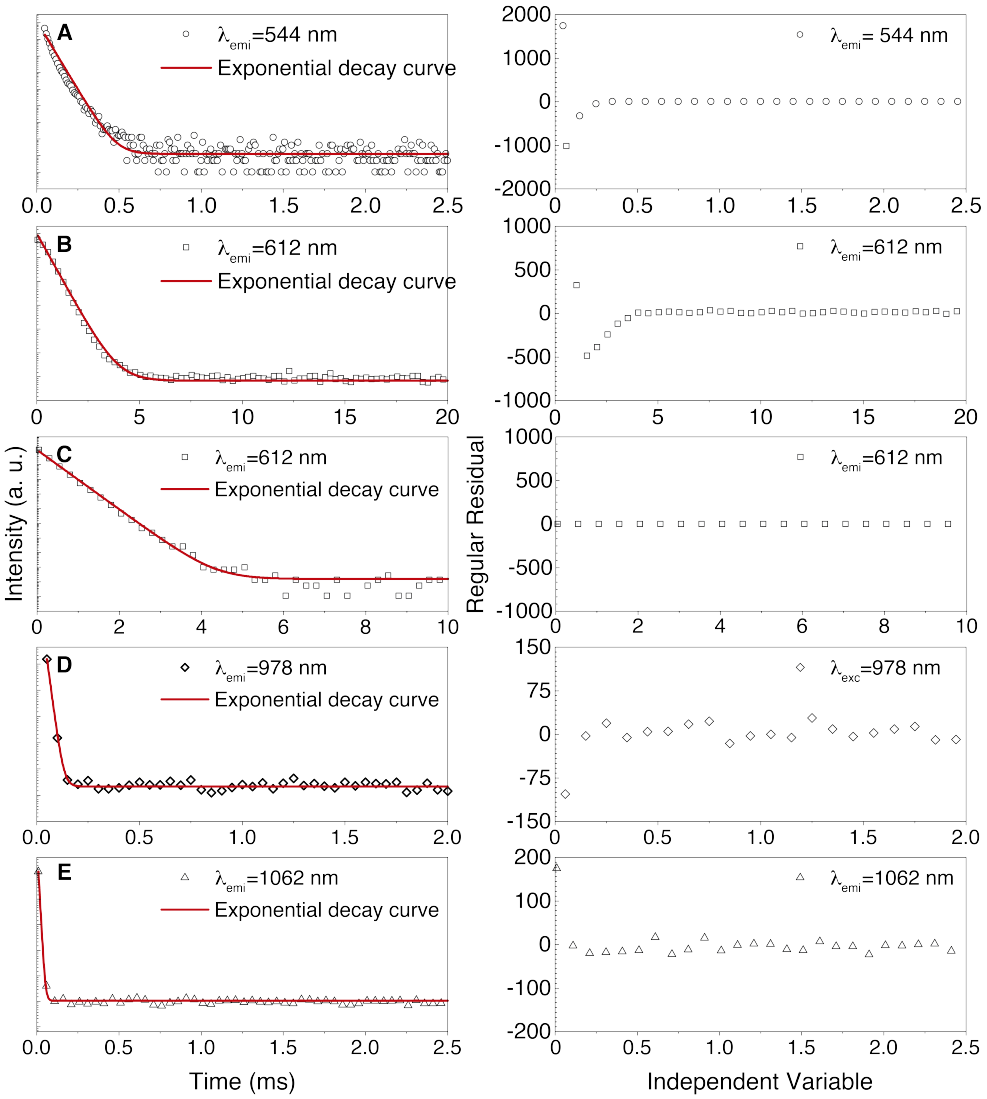

Figure 5.2: Room temperature emission decay curves for (A) PMMA-Eu-10, (B) PMMA-Eu-20, (C) PMMA-Tb-20, (D) PMMA-Yb-20 and (E) PMMA-Nd-20 excited at 380 nm and monitored at 612, 544, 1062 and 978 nm, respectively. The solid lines represent the best fit to the data ($r^2 > 0.99$) using a single exponential function. The respective residual plots are shown on the right-hand side.

citation wavelength (270-385 nm and 808 nm for the PMMA-Nd-20). The absolute emission quantum yield is higher for different excitation wavelengths in the UV spectral region depending on the material, Table 5.2, and for the PMMA-Nd-20 the highest absolute emission quantum yield value was measured exciting at 808 nm. However, these values are lower than those previously reported for PMMA doped with Tb^{3+}-, Eu^{3+}- and Nd^{3+} based complexes [61, 265].

Table 5.2: Integral overlap (O, $\times 10^{19}$ photons$\cdot s^{-1} \cdot m^{-2}$), absolute emission quantum yield (q), molar extinction coefficient (ε, $\times 10^4\, M^{-1} \cdot cm^{-1}$) and brightness ($B$, $M^{-1} \cdot cm^{-1}$) of the fabricated samples.

Sample	O	ε^*	q^*	B^*
PMMA-Tb-20	8.98	2.17	0.02	0.44×10^3
PMMA-Eu-10	9.87	2.05	0.49	10.10×10^3
PMMA-Eu-20	8.74	1.14	0.36	4.11×10^3
PMMA-Yb-20	7.63	2.65	< 0.001	1.98×10^1
PMMA-Nd-20	8.57	1.98	0.0008	2.65×10^1

*ε, q and B values refers to 357 nm for PMMA-Tb-20, 368 nm for PMMA-Eu-10, 315 nm for PMMA-Eu-20, 335 nm for PMMA-Yb-20 and 808 nm for PMMA-Nd-20.

Featuring PV related applications and in order to maximize the performance of LDS layers and LSCs, it is relevant to quantify the light harvesting ability [119]. In particular, the overlap integral between the materials absorbance and the sunlight available for PV conversion. The overlap integral is given by Eq. 2.12 [156]. A maximum value of 9.9×10^{19} photons$\cdot s^{-1} \cdot m^{-2}$ was calculated indicating a potential to absorb 2.2 % of the solar photon flux on the surface of the Earth (4.3×10^{21} photons$\cdot s^{-1} \cdot m^{-2}$) [5]. Using the Beer-Lambert law, the molar extinction coefficient (ε, $M^{-1} \cdot cm{-}1$) was calculated. Light emission efficiency and light harvesting ability can be related by the molar brightness (B), given by $B = q \times \varepsilon$ [266], allowing both properties to be compared across distinct samples. Taking into account the optical properties, namely the B value, PMMA-Eu-10 was chosen for testing on PV devices.

5.2.2 Luminescent down-shifting layers

Here, LDS layers of PMMA-Tb-20, PMMA-Eu-10, PMMA-Yb-20 and PMMA-Nd-20, with a thickness value of $1.6 \pm 0.1\, \mu m$, were deposited on top of commercial c-Si PV cells. One example of the PMMA-Eu-20 LDS layer deposited on top of c-Si PV cells is shown in Figure 5.3.

LDS layers will affect the reflectance and absorption ability of the PV devices. As evidenced in Figure 5.4, the Haze factor, Eq. 2.5, increases for all the LDS layers.

The Haze factor depends on both total and diffuse reflectance, Figure 5.4. Larger Haze values correspond to increased scattering and hence an increased optical path length, which

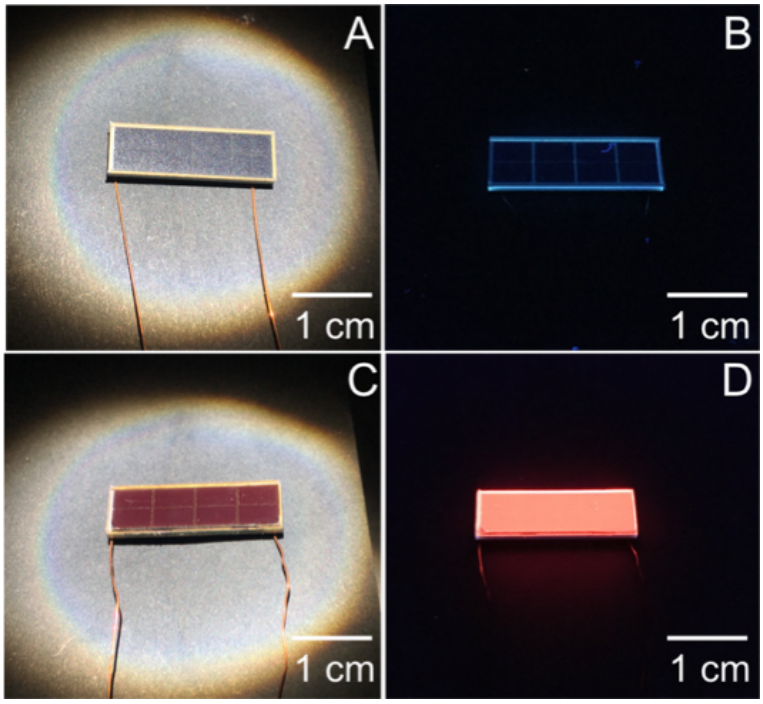

Figure 5.3: Photographs of the (A) bare c-Si PV cell under AM1.5G and (B) UV radiation at 365 nm and of the PMMA-Eu-10 LDS layer deposited on a c-Si PV cell under (C) AM1.5G and (D) UV radiation at 365 nm.

is of critical importance to improve radiation absorption [203, 204].

The active role of the mentioned LDS layers in enhancing PV device performance was inferred from the EQE calculated through Eq. 2.22, on the PV device with and without the presence of the LDS layers. For all the measurements, each bare PV cell was fully characterized before and after the deposition of the layer. This permits more consistency between the characterization protocols used for LDS layers because sometimes the increase caused by the LDS layers is in the same order of magnitude or lower than the differences between the response of each commercial PV cell. Although an increase of the Haze factor was verified for all the LDS layers, an enhancement of the PV cell performance was only measured for the PMMA-Eu-10 LDS layers, Figure 5.5 and 5.6. This result can be rationalized based on the low absolute emission quantum yield of the LDS layers materials. Since the PMMA-Eu-10 was the only LDS layer where a positive increase in the current and thus in the EQE was verified, only the results relative to such LDS layer will be discussed in this thesis, Figure 5.5.

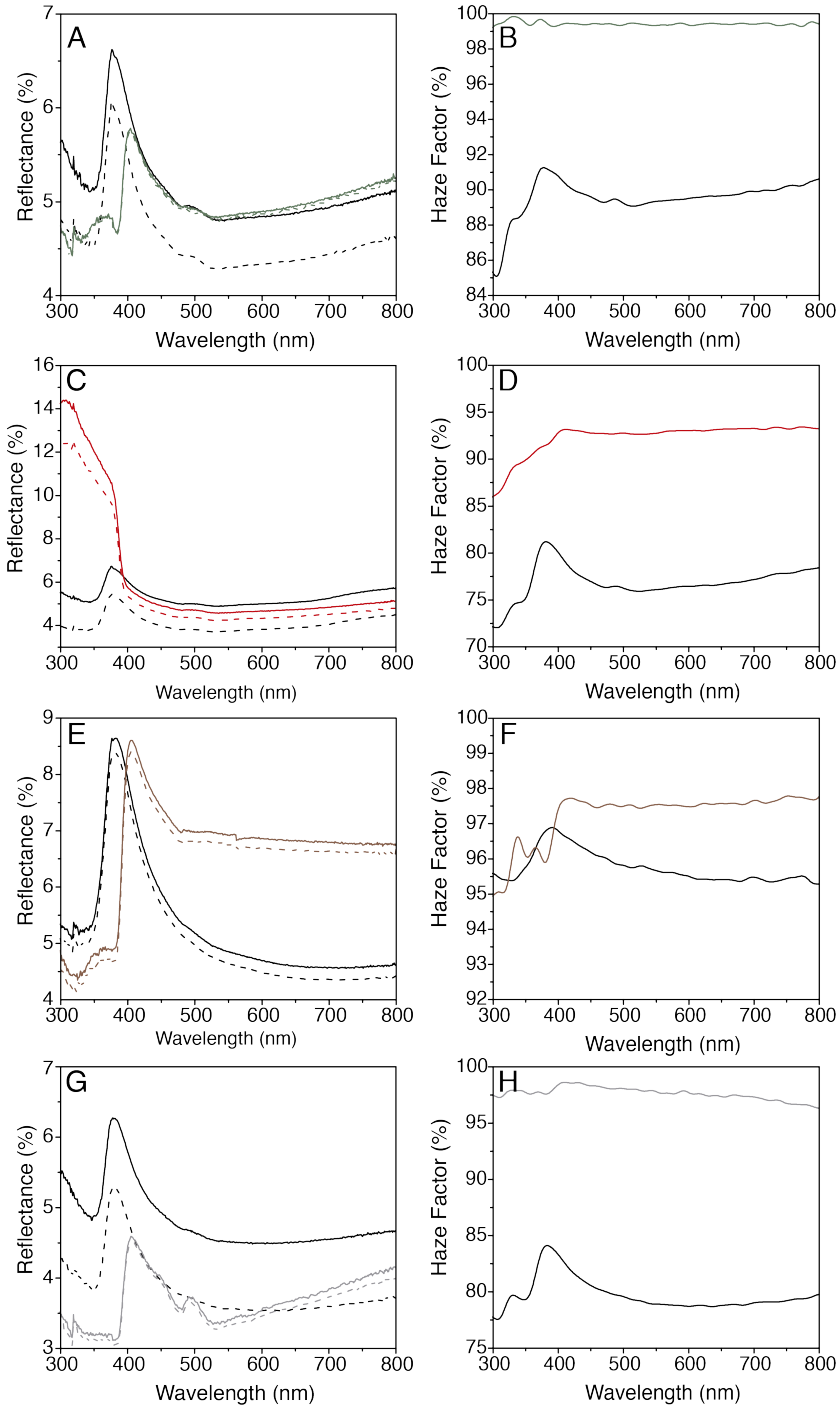

Figure 5.4: Total (solid lines) and diffuse (dashed lines) reflectance of the bare PV cells (black line) and of the PV cells with (A) PMMA-Tb-20, (C) PMMA-Eu-10, (E) PMMA-Yb-20 and (G) PMMA-Nd-20 LDS layers. Haze factor of (B) PMMA-Tb-20, (D) PMMA-Eu-10, (F) PMMA-Yb-20 and (H) PMMA-Nd-20 LDS layers.

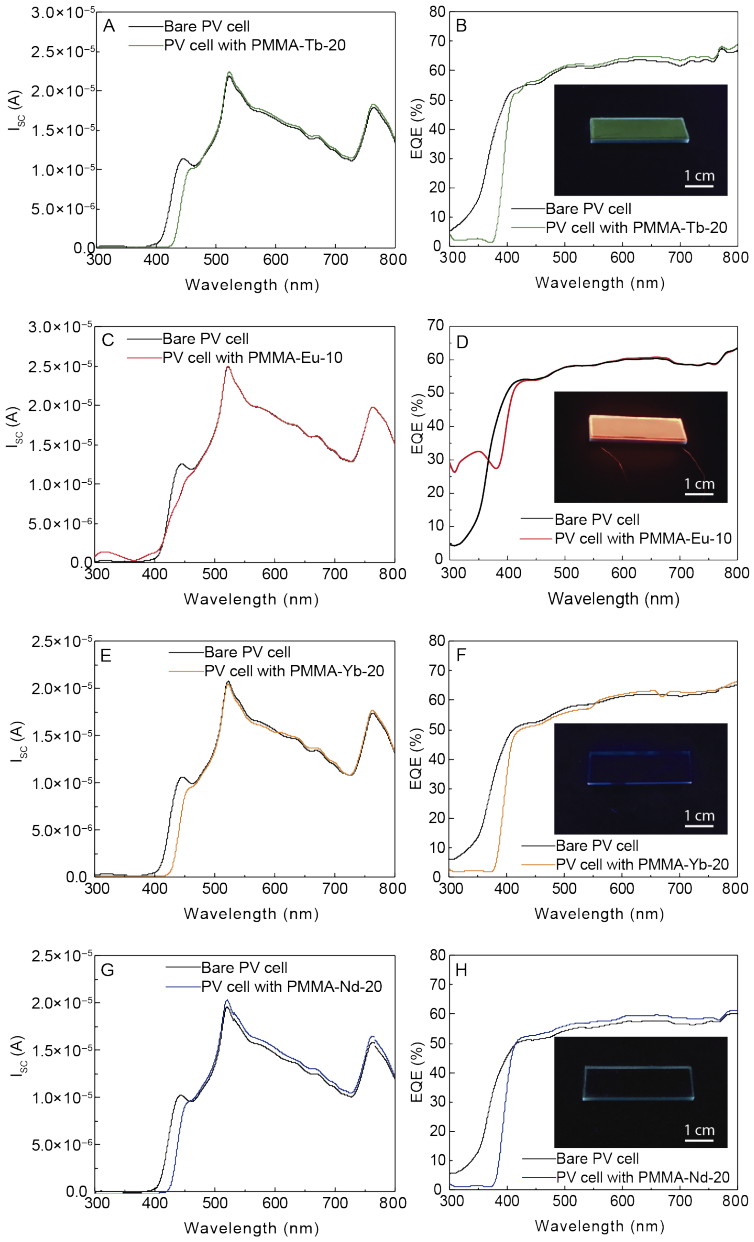

Figure 5.5: I_{SC} and EQE curves of the bare PV cell and of the PV cell with (A, B) PMMA-Tb-20, (C, D) PMMA-Eu-10, (E, F) PMMA-Yb-20 and (G, H) PMMA-Nd-20, respectively. LDS layers with thickness of $1.6 \pm 0.1\,\mu m$. The insets show the coated PV cells under UV radiation at $365\,nm$.

As shown in Figure 5.5 for the PMMA-Eu-10, an increase in the EQE is noticeable in the UV/blue region between 300 and $360\,nm$, which is the spectral range where Si PV cells

have lower performance and, also, corresponds to the absorption region of the LDS layer in use. Between 300 and 360 nm, an absolute increase of 25 %, equivalent to a gain of 6 can be observed (for 320 nm incident radiation). Moreover, although a small decrease in the EQE of the PV cell is noticed between 360 and 420 nm, the overall EQE performance of the device is enhanced by $\sim$ 3.7 % in the presence of the PMMA-Eu-10 LDS layer. Furthermore, from the I_{SC}-wavelength curves in the 300-360 nm spectral region, Figure 5.5, it is possible to calculate an average increase of 3.4 times of the I_{SC}. Such results will be rationalized based on Monte-Carlo ray-tracing simulations presented below.

The V-I curves of the PV cell with and without the LDS layers were also measured. A relative increase of 9.7 % in the I_{SC} generated by the cell with the layer when illuminated with AM1.5G is clearly seen for the PMMA-Eu-10 LDS layer, Figure 5.6B, and no enhancement of the short-circuit current was measured for the Tb^{3+}-, Yb^{3+}- and Nd^{3+}-based LDS layers.

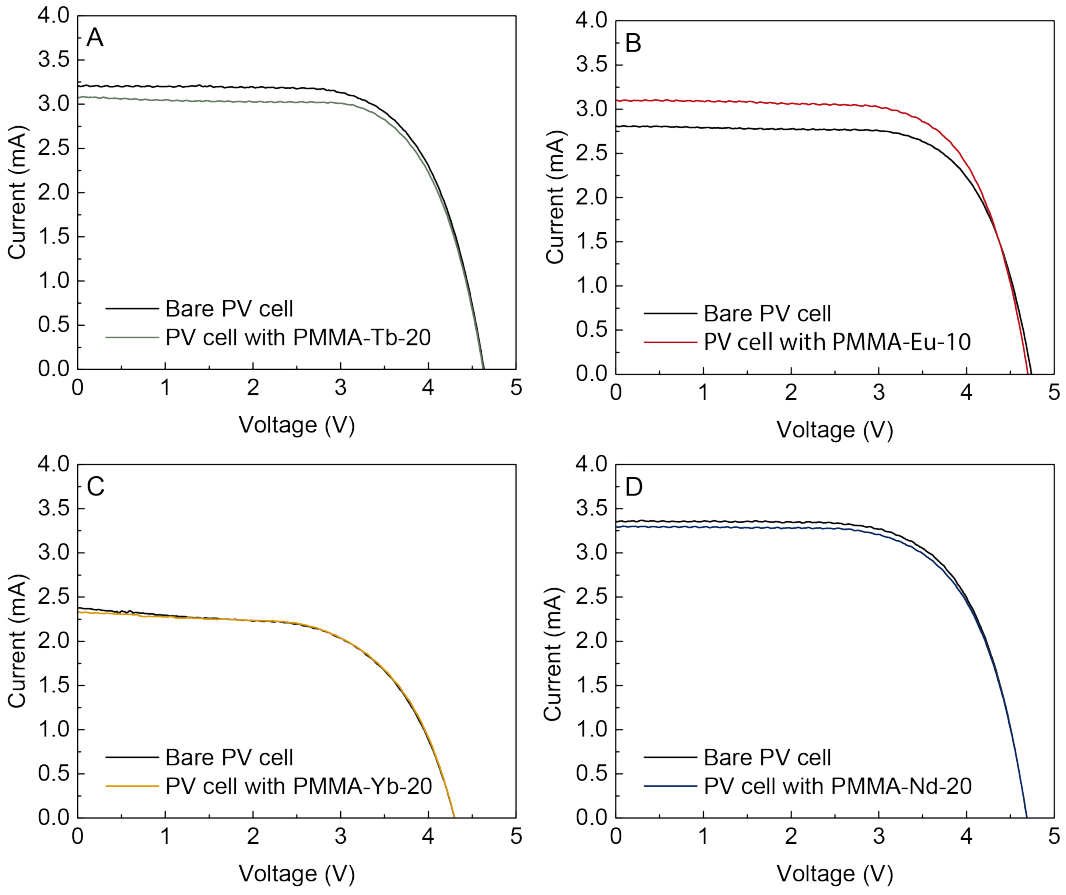

Figure 5.6: V-I curves of the bare PV cells and of the PV cells with the (A) PMMA-Tb-20, (B) PMMA-Eu-10, (C) PMMA-Yb-20 and (D) PMMA-Nd-20 LDS.

The absolute EQE increase results are among the highest values reported for PV cells coated with LDS layers in the UV spectral region, being of the same order of magnitude than that of the highest values reported for Ln^{3+}-based LDS layers [61, 80] mentioned in Table 5.3, except for the case of a LDS layer based on $Eu(TTA)_3 \cdot 2H_2O$ complex with 4,5-bis(pinene)-2,2-bipyridine ligand dispersed in polyvinyl acetate (PVA), which presented an absolute EQE increase of $\sim 50\,\%$ [267].

Table 5.3: Reported absolute EQE increase in the UV spectral region for Ln^{3+}-based LDS layers.

Optically active layer	PV devie	EQE increase	Ref.
PMMA-Eu-10	c-Si	25 %	This work
$[Eu(TTA)_3(tppo)_2]$/EVA		19 %	[61]
$[Eu(TTA)_3(phen)]$/EVA		17 %	
$[EuL_3]$/EVA		15 %	
$[TbL_3]$/EVA		15 %	
$[Eu(TTA)_3bpbpy]$/PVA		50 %	[267]
$[Eu(tfc)_3$:EABP] 1:1/EVA		5 %	[268]
$[Eu(tfc)_3/Eu(dbm)_3phen]$/PVA		5 %	[269]
Ba_2SiO_4:Eu^{2+}		3 %	[270]
SiO_2/Ba_2SiO_4:Eu^{2+}		3 %	[75]
$LaVO_4/Dy^{3+}$	DSSC	2 %	[271]
EuD_4TEA		25 %	[80]

EVA=ethylene-vinyl acetate; tppo=triphenylphosfine oxide; phen=1,10-phenanthroline;
L_3=triazole-pyridine-bistetrazolate; bpbpy=4,5-bis(pinene)-2,2'-bipyridine;
$Eu(tfc)_3$=tris[3-(trifluoromethylhydroxymethilene)-d-camphorate]europium(III);
EABP=4,40-bis(diethylamino)benzophenone; dbm=dibenzoylmethane;
EuD_4TEA=europium tetrakis dibenzoylmethide triethylammonium.

5.2.3 Luminescent solar concentrators

The Ln^{3+}-based ionogels incorporated in PMMA were also used to fabricate LSCs. In this case, a layer of each one of the materials was deposited on top of a glass substrate, Figure 5.7. From these photographs it is possible to see the emission of the PMMA-Tb-20

and PMMA-Eu-10/20 being guided to the edges of the glass substrates. The thickness of the active material of each LSC was measured by spectroscopic ellipsometry, Figure 5.8, and from this data it was possible to determine an average value of $10.8 \pm 0.5\,\mu m$, Table 5.4. Also, from the ellipsometric parameters the dispersion curves of the PMMA and the PMMA doped with the Ln^{3+}-based ionogels were determined, Figure 5.9.

Table 5.4: Thickness of the active layer of the LSCs deposited on glass determined by spectroscopic ellipsometry.

Sample	Thickness (μm)
PMMA-Tb-20	10.70 ± 0.05
PMMA-Eu-10	10.14 ± 0.02
PMMA-Yb-20	11.27 ± 0.04
PMMA-Nd-20	10.9 ± 0.1

In Figure 5.7 it is possible to see the emission concentrated at the edges of the LSCs and in Figure 5.10 the emission spectra measured at the edges of the LSCs.

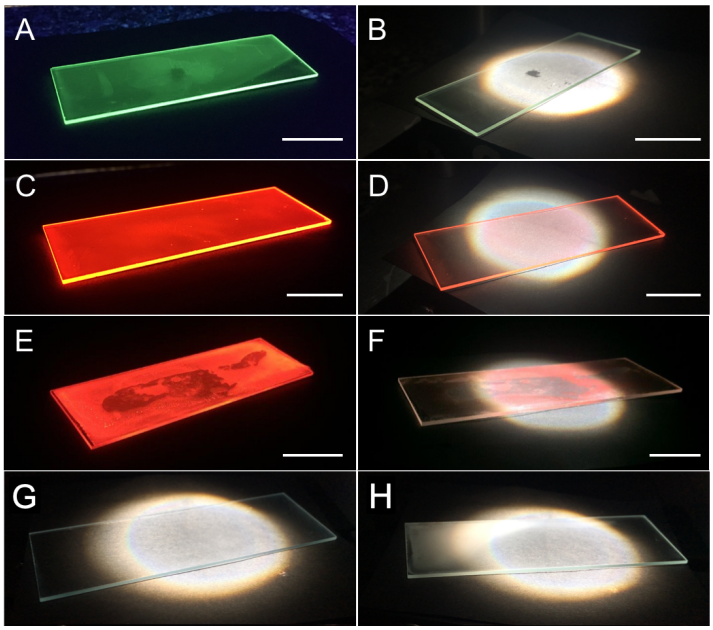

Figure 5.7: Photos of the produced LSCs based on (A) PMMA-Tb-20 under UV radiation at $365\,nm$, (B) PMMA-Tb-20 under AM1.5G, (C) PMMA-Eu-10 under UV radiation at $365\,nm$, (D) PMMA-Eu-10 under AM1.5G, (E) PMMA-Eu-20 under UV radiation at $365\,nm$, (F) PMMA-Eu-20 under AM1.5G, (G) PMMA-Yb-20 and (H) PMMA-Nd-20 under UV radiation at 365 nm (scale bar, $2\,cm$).

The LSC based on PMMA-Eu-20 was not uniform presenting whitish parts and the layer

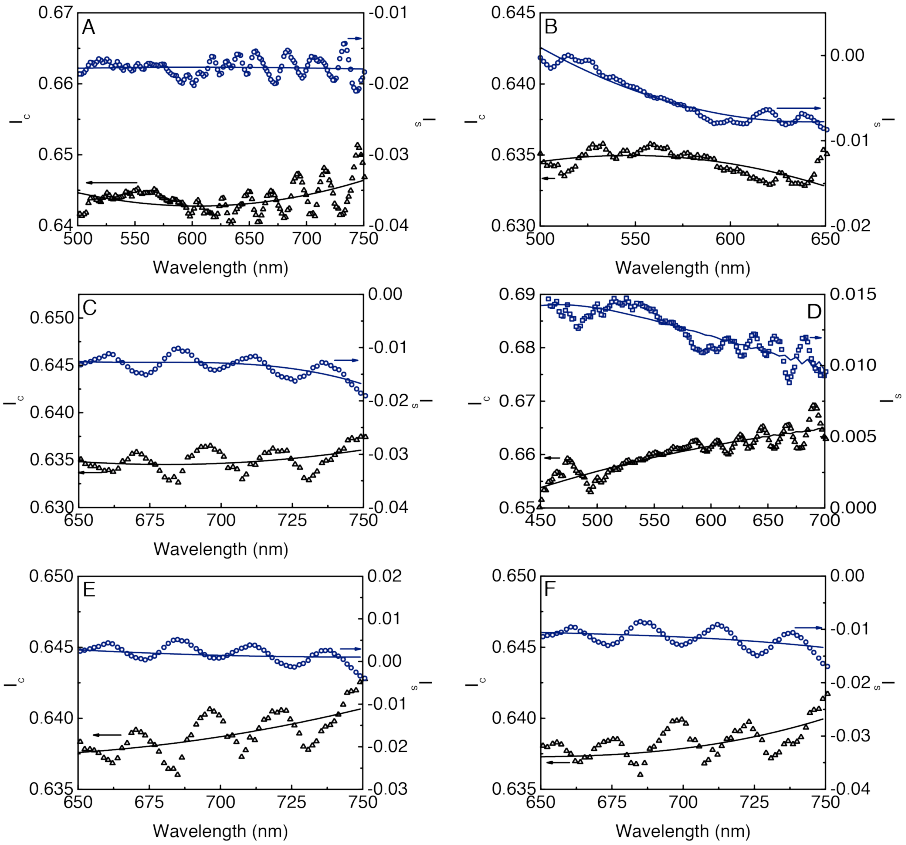

Figure 5.8: Ellipsometric parameters I_s (open circles) and I_c (open triangles) measured for (A) PMMA, (B) PMMA-Tb-20, (C) PMMA-Eu-10, (D) PMMA-Eu-20, (E) PMMA-Yb-20 and (F) PMMA-Nd-20. The solid lines represent the data best fit.

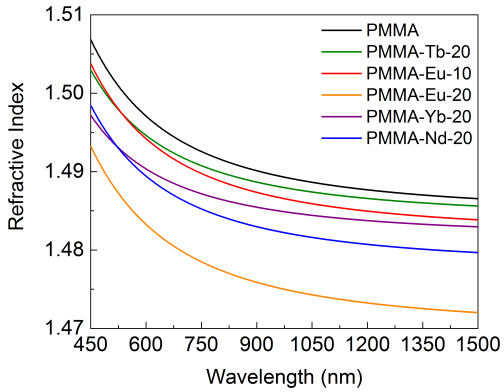

Figure 5.9: Dispersion curves for measured for PMMA, PMMA-Tb-20, PMMA-Eu-10, PMMA-Eu-20, PMMA-Yb-20 and PMMA-Nd-20.

started peeling off the glass. Also, the PMMA-Yb-20 and PMMA-Nd-20 did not show any light guidance and, thus, PMMA-Tb-20 and PMMA-Eu-10 LSCs are the ones studied below.

Those LSCs are presented in Figure 5.7, where it is clear the radiation emission and guidance to the edges under AM1.5G and UV radiation, Figure 5.10. It is observable that there are more Eu^{3+}-related emission reaching the edges of the LSCs when compared with the Tb^{3+}-one and more white light reaches the edges of the LSCs in the later case. The performance of the LSCs was quantified by the estimation of $\eta_{opt} \pm \Delta\eta_{opt}$ through Eq. 2.14, yielding values of $\eta_{opt} = 0.27 \pm 0.01\,\%$ and $0.23 \pm 0.01\,\%$ ($0.28 \pm 0.01\,\%$ and $0.32 \pm 0.01\,\%$ using Eq.2.19) for the LSCs based on PMMA-Tb-20 and PMMA-Eu-10, respectively. Also, the effective contribution of the LSCs on generating electric current was evaluated by calculating the PCE values, through Eq. 2.21, yielding values of $(7.8 \pm 0.01) \times 10^{-4}\,\%$ and $(9.6 \pm 0.01) \times 10^{-4}\,\%$, for PMMA-Tb-20 and PMMA-Eu-10 LSCs, respectively.

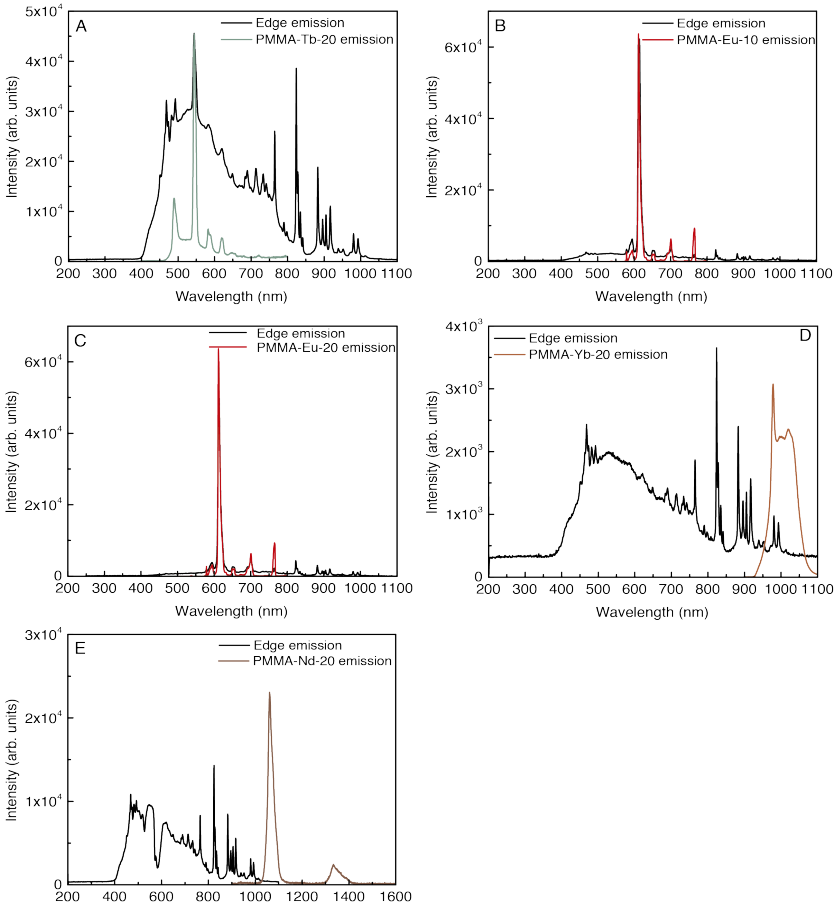

Figure 5.10: Emission of the LSCs collected at the edges of the LSCs based on (A) PMMA-Tb-20, (B) PMMA-Eu-10, (C) PMMA-Eu-20, (D) PMMA-Yb-20 and (E) PMMA-Nd-20.

Although the η_{opt} values here reported are lower than the best ones reported for planar UV-

downshifting Ln^{3+}-based LSCs [211, 272, 273], Table 5.5, these results praise the potential of these novel materials to be used as photovoltaic windows for urban integration of light harvesting devices.

Table 5.5: Reported η_{opt} (%) and PCE (%) values for Ln^{3+}-based planar LSCs.

Optically active layer	η_{opt} (%)	PCE (%)	Ref.
PMMA-Tb-20	0.27[a] 0.28[b]	7.8×10^{-4}	This work
PMMA-Eu-10	0.23[a] 0.32[b]	9.6×10^{-4}	
PMMA-Eu-20	0.25[a] 0.34[b]	10.6×10^{-4}	
$Eu(TTA)_3 \cdot 2H_2O$/F5	12.3[a]	-	[177]
$Eu(TTA)_3$phen/parylene	2.47[b]	0.19	[211]
$Eu(TTA)_3$phen/PVB	-	0.04	[273]
$Eu(TTA)_3$dpbt/PVB	-	0.05	
$Eu(TTA)_3(TTPO)_2$/PMMA	-	0.28	[272]

[a] η_{opt} values calculated using Eq. 2.14; [b] η_{opt} values calculated using Eq. 2.19;
phen=1,10-phenanthroline;
dpbt=2-(N,N-diethylanilin-4-yl)-4,6-bis(3,5-dimethylpyr-azol-1-yl)-1,3,5-triazine);
PVB=Polyvinyl-butyral; TTPO=triphenyl phosphine oxide.

5.2.4 Modelling

Simulations of the performance of the LDS layers and LSCs were carried out using a Monte Carlo ray-tracing approach, in which the photon propagation follows geometrical optical laws [232]. The thickness of the active layers (10^{-6} to $10^{-5}\,m$) is much larger than that of the light coherent length ($10^{-7}\,m$), thus, interference effects were neglected. The stochastic nature of the model is reflected in the fact that the propagated rays cannot split when reaching an interface but rather either transmitted or reflected, as predicted by Fresnel laws. We also

note that incident light polarization is not taken into account. By modelling the path of each propagated ray, it is possible to know whether the photons are trapped inside the luminescent layer, absorbed by the luminescent species, lost due to escape cone or absorption and if they were collected by the PV device.

The inputs of the Monte Carlo ray-tracing simulation consist of the solar spectrum AM1.5G (280-1600 nm, photons with angle of incidence between $-45°$ and $45°$), the absorption and emission spectra, the absolute emission quantum yield and dispersion curve of the PMMA-Ln-X samples, Figure 5.8 and 5.9.

This model does not include individual molecules or optically active centres but applies statistical averaging of the absorption. First the absorption probability is calculated ($p_{abs} = 1 - 10^{-\alpha d}$, where α is the attenuation coefficient in units cm^{-1} and d is the photon desired step size, step$=-log_{10}(\xi)/\alpha$, where ξ is a random number between 0 and 1 in each iteration, 1 μm for the Tb^{3+}- and Nd^{3+}-based samples and 2 μm for the Eu^{3+}- and Yb^{3+}-based ones) as function of the wavelength and compared with a random generated number between 0 and 1 for each launched photon. If p_{abs} proves to be higher than the random number the photon is absorbed otherwise, the photon continues to propagate accordingly to its direction vector. Once a photon is absorbed, the subsequent fate of the excitation (that is, emission or non-radiative relaxation) is again determined by the Monte Carlo sampling according to the absolute emission quantum yield. The direction of the emission is randomly distributed and the emission wavelength is sampled randomly from the normalized emission spectrum. The ultimate fate of each photon is either loss due to non-radiative recombination or escape the luminescent layer from one of the interfaces. When a photon hits the PV interface, it counts as a PV absorption and the wavelength of the photon and its position on the PV interface is recorded.

The performance of the LDS layers was simulated placing the PV cell under the layer. With that, we are able to estimate the current density generated by the PV cell (exposed area $1.0 \times 2.0\, cm^2$) with and without the LDS layer. The simulation of the performance of the PV cell with the PMMA-Eu-20 LDS layer were carried out considering incident radiation between 300-360 nm in 10 nm interval. The results of the simulation show us an increase in the generated current of the PV cell with layer when compared with the bare PV cell, Figure 5.11. From the simulation, we were able to estimate an average increase of ~ 4.3 of the I_{SC}.

These results corroborate the experimental data described above for the increase in the I_{SC} and for the EQE in the 300-360 nm spectral region.

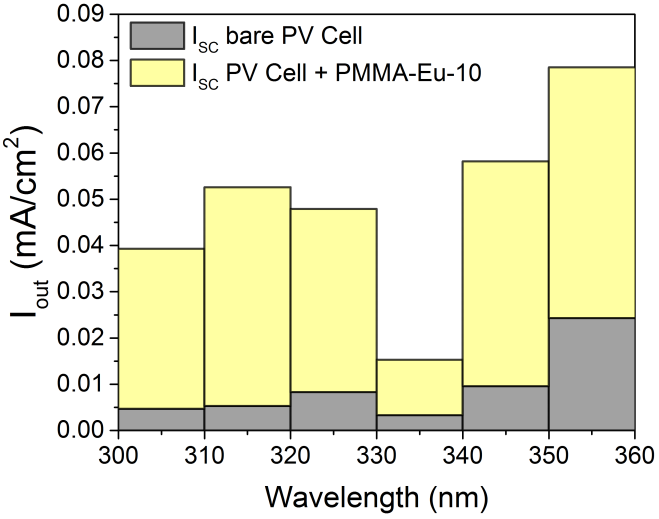

Figure 5.11: Monte Carlo ray-tracing short-circuit current as function of the wavelength comparing the performance of a bare PV cell and a PV cell with a PMMA-Eu-10 LDS layer.

The performance of the LSCs was simulated placing the PV cell on one of the edges of the LSC that is composed of a glass substrate with an active layer deposited on top of it. The η_{opt} for simulation purposes is defined by the energy emitted (per unit of time) from the edge of the LSC divided by the solar energy falling on the LSC (per unit of time), as stated in Eq. 2.14. The simulations were performed for the LSCs with dimensions of $7.50 \times 2.00 \times 10^{-3}\, cm^3$ and as function of the optically active layer properties. The η_{opt} values were predicted considering all the photons reaching the edge (η_{opt}, %) and considering only the fraction of converted photons (η'_{opt}, %), Table 5.6. The η_{opt} and η'_{opt} values corroborate the experimental values when taking into account for the direct radiation that reaches the PV device through the LSC. These values explain why it is possible to measure the η_{opt} values for the PMMA-Nd/Yb-20 samples having such low absolute emission quantum yield values. In this cases, the η_{opt} refers to direct radiation that is guided by the LSCs. The main difference in the η'_{opt} is mainly due to the difference in the absolute emission quantum yield between samples. Nevertheless, the simulated value (0.28 ± 0.01 % for PMMA-Eu-10) is very close to the experimental one, stating that this model fits well to our experimental conditions.

Table 5.6: Reported η_{opt} (%) and η'_{opt} (%) values for Ln^{3+}-based planar LSCs.

Sample	η_{opt}	η'_{opt}
PMMA-Tb-20	0.16	0.02
PMMA-Eu-10	0.28	0.15
PMMA-Eu-20	0.23	0.15
PMMA-Yb-20	0.13	6.36×10^{-5}
PMMA-Nd-20	0.14	4.07×10^{-4}

5.3 SiNC based LSCs

Herein, NIR-emitting LSCs are reported using silicon 2,3-naphthalocyanine bis(trihexylsilyloxide) (SiNc or NIR775) immobilized in an organic-inorganic tri-ureasil matrix, t-U(5000). The photophysical properties of the SiNc dye incorporated into the tri-ureasil host closely resembled those of SiNc in tetrahydrofuran solution (an absolute emission quantum yield of ~ 0.17 and a fluorescence lifetime of $\sim 3.6\,ns$). The LSC coupled to a Si-based PV device revealed an η_{opt} of $\sim 1.50 \pm 0.01\,\%$, which is among the largest values known in the literature for NIR-emitting LSCs. The LSCs were posteriorly coupled to a Si-based commercial PV cell, and the synergy between the t-U(5000) and SiNc molecules enabled an effective increase in the external quantum efficiency of PV cells, exceeding 20 % in the SiNc absorption region. This work was developed in close collaboration with Raquel Rondão PhD, former member of the Phantom-G group.

5.3.1 Structural and optical characterization of the optically active layer

X-ray diffraction (XRD), ^{29}Si magic-angle spinning (MAS), and ^{13}C cross polarization (CP) MAS NMR were used to characterize M/t-U(5000)/SiNc. The XRD pattern (Figure 5.12) of the SiNc doped hybrid is analogous to that of the isolated hybrids t-U(5000). For a better comparison with the non-doped M/t-U(5000), the previously published XRD pattern [241] was also depicted. The resemblance between both patterns is clear: (i) A peak appearing at lower angles ($\sim$ 2-3°), due to interparticle scattering interference [240, 241, 247, 274]; (ii)

a broad band centered at $\sim 20°$, which denotes the presence of amorphous siliceous domains; and iii) a shoulder at $\sim 11°$, attributed to intrasiloxane domains in-plane ordering [240, 241, 247, 274]. In fact, Oku *et al.* [250] reported the XRD pattern of a thin film made of a bulk heterojunction structure of PCBN:P3HT:SiNc (6,6-phenyl C61-butyric acid methyl ester: poly(3-hexylthiophene):SiNc), and associated peaks at $\sim 6°$ (more intense), 8°, 12° and 22° to SiNc.

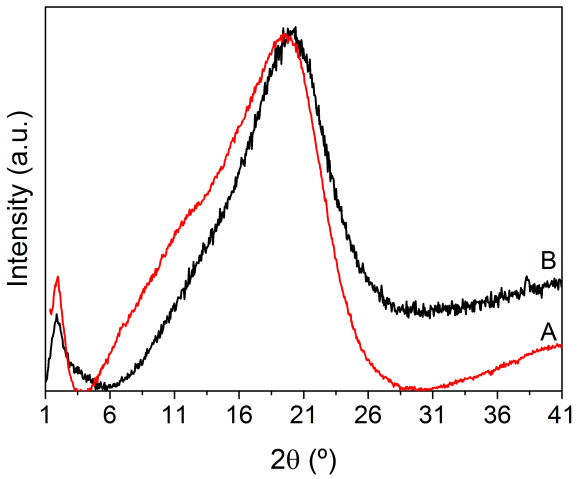

Figure 5.12: XRD patterns of (A) M/t-U(5000)/SiNc and (B) M/t-U(5000).

The ^{29}Si MAS NMR spectrum, Figure 5.13A, of M/t-U(5000)/SiNc displays three characteristic peaks at -57.6, -60.5 and $-65.4\,ppm$, assigned to $CH_2Si(OSi)(OR)_2$ (T^1), $CH_2Si(OSi)_2(OR)$ (T^2) and $CH_2Si(OSi)_3$ (T^3) silicon environments of the t-U(5000) host network, respectively [241, 247, 274]. According to the literature [275, 276], a peak around $-6\,ppm$ should appear related to a M-type site present in the R group of SiNc, i.e., to $Si(OSi)(CH_2(CH_2)_4CH_3)_3$ silicon environments, Figure 4.5D. However, due to the low amount of dye in M/t-U(5000)/SiNc, this signal could not be distinguished in the ^{29}Si NMR spectrum. The signals between ~ -90 and $-130\,ppm$ are assigned to $(\equiv SiO)_2Si(OH)_2$ (Q^2, geminal silanols), $(\equiv SiO)_3SiOH$ (Q^3, single silanol) and $(SiO)_4Si$ (Q^4, siloxane) local environments [277] indicating the pre-hydrolysis of the t-UPTES(5000) precursor.

The ^{13}C MAS NMR spectrum, Figure 5.13C, of M/t-U(5000)/SiNc is dominated by a pair of peaks located at 75.3 and $73.5\,ppm$, related to the methine and methylene groups of the poly(oxypropylene) chains, respectively [241, 247, 274, 278]. The intense peak at $17.8\,ppm$ is

due to the methyl groups of the oxypropylene repeat units [241, 247, 274].

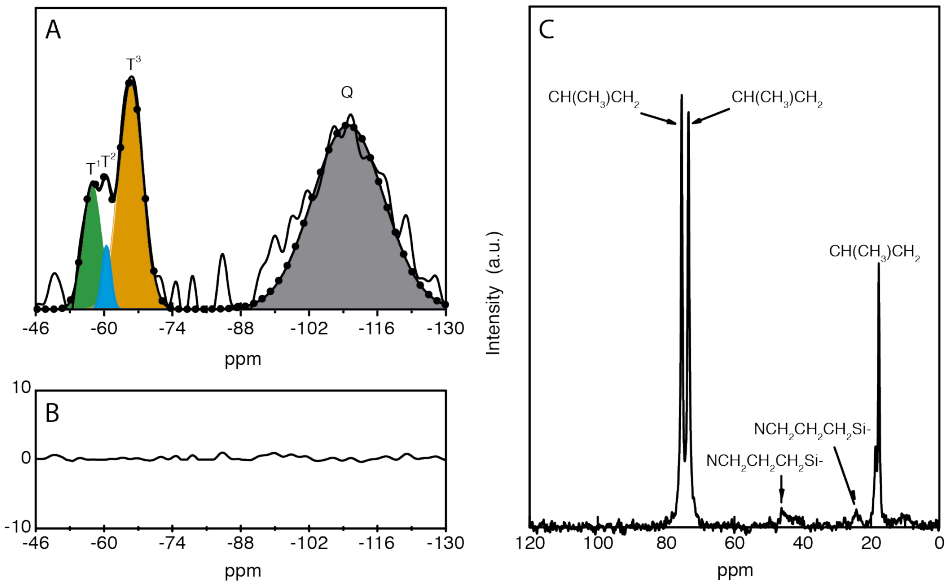

Figure 5.13: (A) ^{29}Si MAS NMR spectrum of M/t-U(5000)/SiNc. The deconvolution using a sum of Gaussian functions (shadowed areas) ascribed to T^1, T^2, T^3 and Q silicon environments, and the overall fit $R^2 > 0.99$ (circles) are also shown. (B) Residual plot of the overall fit. (C) ^{13}C CP/MAS NMR spectrum of M/t-U(5000)/SiNc.

These results reveal that the local structure of t-U(5000) [241, 247] remained essentially unaltered after the inclusion of the SiNc molecules. The thermogravimetric analysis (TGA, Figure 5.14) of the non-doped t-U(5000) host and of M/t-U(5000)/SiNc show that the thermal decomposition of the two hybrids occurred in a single step with an abrupt mass drop stage. The onset of degradation of the t-U(5000) host and of M/t-U(5000)/SiNc is located at $\sim 230°C$ and $\sim 185°C$, respectively. Beyond $\sim 400°C$ a stability plateau was attained and at $\sim 800°C$ a residue that represents 10 % of mass loss remained.

The interaction between the SiNc molecules and the t-U(5000) was further studied through the inspection of the IR spectrum of the doped-material in the amide I and amide II regions. The amide I mode, usually found between 1700 and 1600 cm^{-1}, is associated essentially with the C=O stretching vibration [278, 279]. The amide II region, typically ranging from 1600 to 1500 cm^{-1}, is associated with a complex mixture of the C-N and C-C stretching modes and the in-plane bending mode of the N-H group [241, 247, 274]. The ATR/FT-IR spectra of M/t-U(5000) and M/t-U(5000)/SiNc in the amide I and amide II regions are represented in Figure

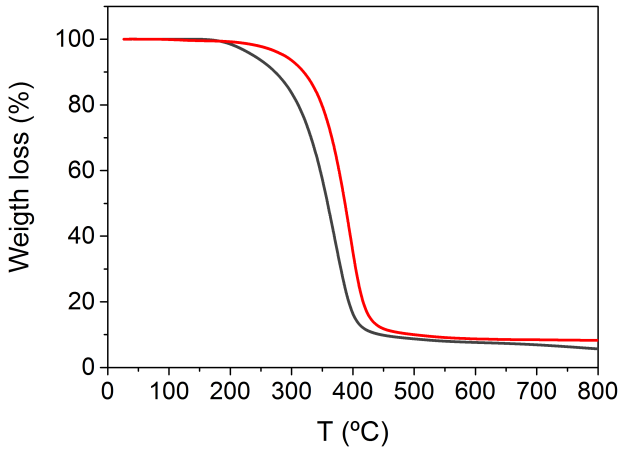

Figure 5.14: TGA curve of M/t-U(5000)/SiNc (black line) and of t-U(5000) (red line).

5.15A and Figure 5.15B, respectively. The amide I band of the ATR/FT-IR spectrum of M/t-U(5000) was resolved into five components at $\sim$ 1741, 1720, 1697, 1670 and 1645 cm^{-1}, Figure 5.15A. The amide II region exhibited a single component at about 1570 cm^{-1}.

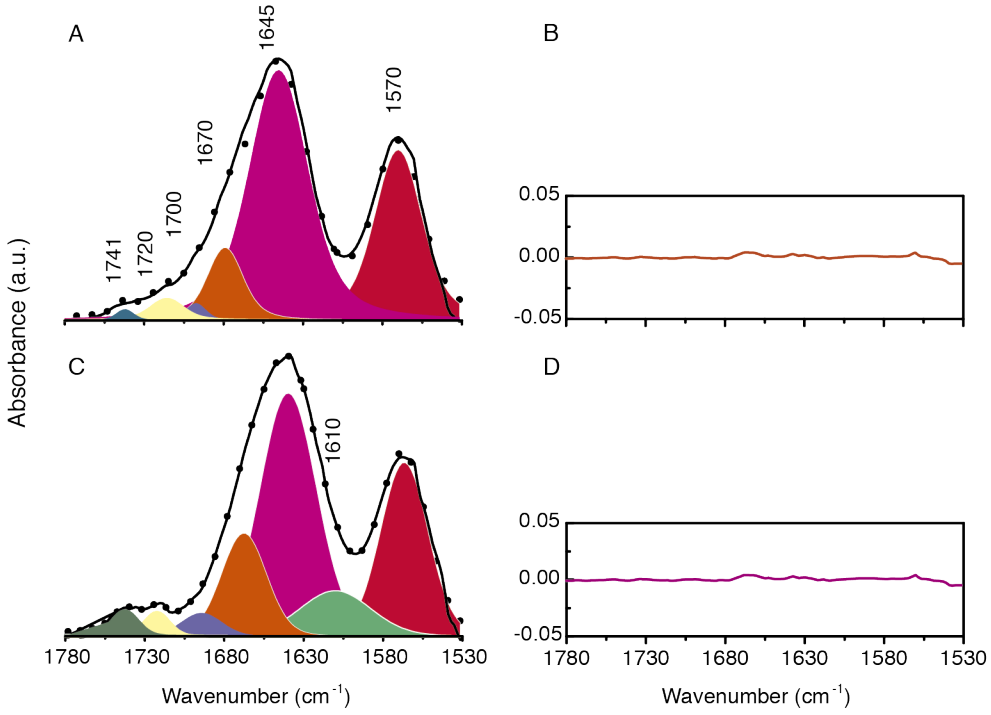

Figure 5.15: ATR/FT-IR spectra (solid line) and curve-fitting results $R^2 > 0.99$ (circles) of (A) M/t-U(5000) and (C) M/t-U(5000)/SiNc. (B) and (D) are the residual plots of the overall fit presented in (A) and (C), respectively.

In the case of the amide I region of M/t-U(5000)/SiNc, apart from the above components, an additional band was detected at 1610 cm^{-1}, Figure 5.15B. The band at 1645 cm^{-1} is assigned to C=O groups included in highly ordered hydrogen-bonded urea/urea aggregates [241, 247, 274, 278, 280]. The bands at 1720, 1700 and 1670 cm^{-1} are attributed with C=O groups belonging to disordered hydrogen-bonded poly(oxypropylene) (POP)/urea aggregates of increasing strength, whereas the band at 1741 cm^{-1} is ascribed to urea groups devoid of any hydrogen interaction [241, 247, 274, 278, 280]. The growth of the feature at 1610 cm^{-1}, originating from doping, points out that the incorporation of the chromophore molecule into t-U(5000) led to the formation of new hydrogen-bonded aggregates stronger than those initially present in the host hybrid framework. Considering the chemical structure of the SiNc molecule, Figure 4.5, with a rotor-like characteristic design composed of four helices including planar rigid aromatic rings (Figure 4.5), we suggest that the emergence of the new ordered hydrogen-bonded aggregates is presumably a consequence of the partial breakdown of the strongest aggregates of t-U(5000) caused by the bulkiness of SiNc.

The films refractive index dispersion curves were measured by spectroscopic ellipsometry, Figure 5.16. The η_t values depends on the refractive index (n) of the optically active layer at the emission wavelength. The trapping efficiency can be calculated from the dispersion curve data in Figure 5.16, using Eq. 2.2 at the emission wavelength (in this case, 758 nm). This parameter determines the fraction of photons confined within the substrate, accounting for the emission losses at the surface through a so-called escape cone with an aperture angle $\theta_c = 2 \times sin^{-1}(1/n_p)$. Attending to the dispersion curves of the chlorophyll-based hybrids, ($1.49 < n < 1.50$ at 675 nm), trapping efficiency values 74 % are predicted.

As a result of the $\pi - \pi^*$ transitions, phthalocyanines and naphthalocyanines exhibit two distinct absorption regions: one in 300-500 nm region, named B-band, and another one in the visible/NIR region (600-800 nm), termed as Q-band. Figure 5.17 shows the absorption spectra of SiNc in THF solution and of the F/t-U(5000)/SiNc and M/t-U(5000)/SiNc hybrids. In THF solution, SiNc presents a characteristic naphthalocyanine monomeric absorption, with the Q-band absorption at 772.0 nm assigned to the $S_0(0)$-$S_1(0)$ transition, and the B-band at $\sim$ 350 nm [248, 258]. Apart from changes in the absorbance values and of a minor bathochromic shift to 773.5 nm, the absorption spectra of M/t-U(5000)/SiNc and F/t-U(5000)/SiNc are similar to that of the SiNc molecules dissolved in THF, discarding the formation of SiNc

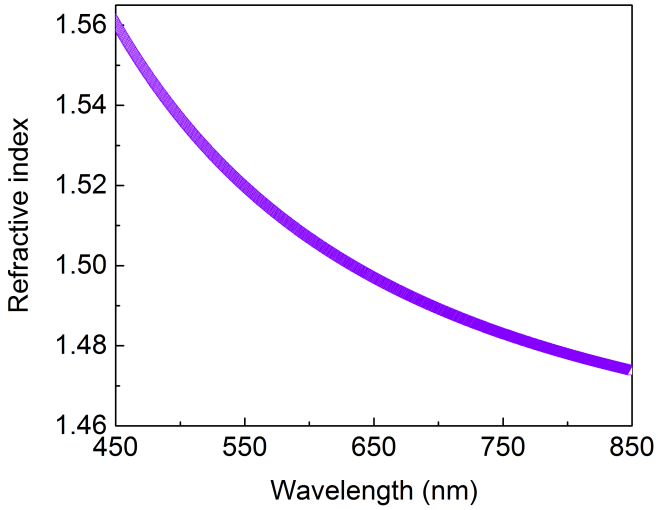

Figure 5.16: Refractive index dispersion curve of F/t-U(5000)/SiNc.

aggregates [255, 257, 258]. The molar extinction coefficient values (ε) were quantified for SiNc in THF solution and processed as thin film, resembling those previously reported ($4 \times 10^5\, M^{-1} \cdot cm^{-1}$) [248, 258].

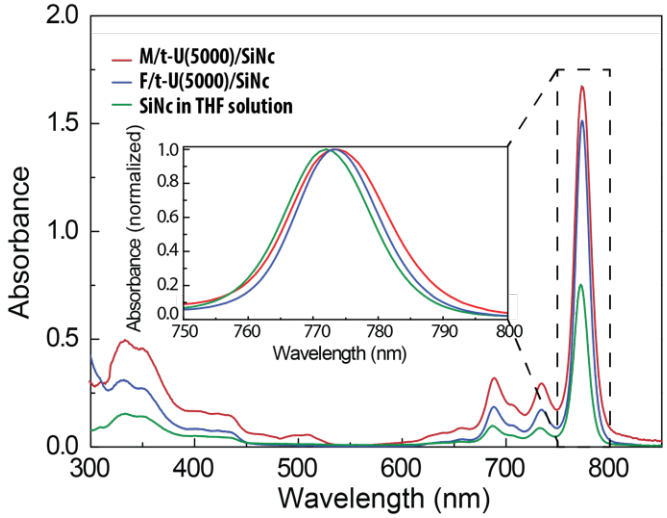

Figure 5.17: Absorption spectra of M/t-U(5000)/SiNc, F/t-U(5000)/SiNc and SiNc in THF solution. The inset shows a magnification of the absorption peak in the NIR spectral region.

Figure 5.18 depicts the emission spectra of SiNc in THF solution and of M/t-U(5000)/SiNc, which are, in both cases, dominated by the fluorescence of the dye in the red/NIR region from 700 to 900 nm, overlapping the optical response of c-Si-based PV

devices (also depicted in Figure 5.18). Almost all the SiNc emission spectra reported in the literature were recorded using detection conditions spectral limited to 800-850 nm, which disables the observation of the high-wavelength region emission ($> 800\,nm$) [259, 260]. Here, and also, for instance, in [255], the detection conditions provide the emission acquisition up to $1100\,nm$, unequivocally revealing that SiNc emission occurs in a larger region (700-950 nm) rather than the usual reported one (700-850 nm).

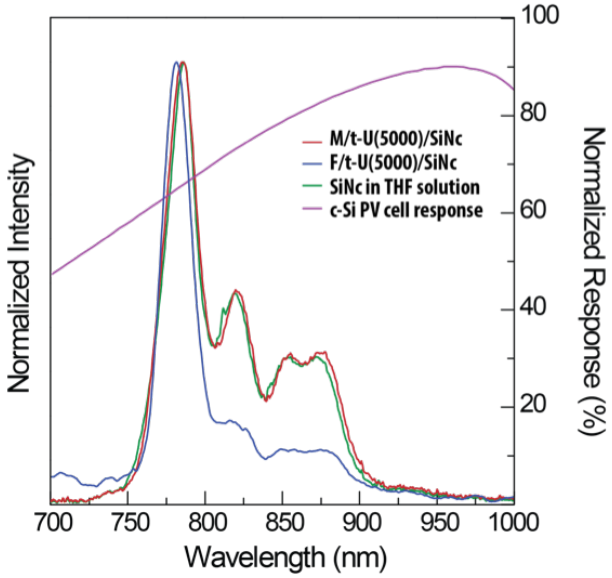

Figure 5.18: Emission spectra excited at 365 nm of M/t-U(5000)/SiNc, F/t-U(5000)/SiNc and SiNc in THF solution (left axis) and spectral relative response for the c-Si PV device provided by the manufacturer, IF D91, Industrial Fiber Optics, Inc. (right axis).

Despite a minor deviation of the emission spectrum of and F/t-U(5000)/SiNc, it overlaps with those of M/t-U(5000)/SiNc and of SiNc in THF solution (Figure 5.18) pointing out that the aggregation of the dye molecules inside the hybrid host was prevented, as already noticed by UV/Vis absorption spectroscopy (Figure 5.17). The presence of a very low-emission band in the blue region, inset on Figure 5.19A, arising from the dye fluorescence and from the t-U(5000) host [241, 247], is also observed. The negligible intensity of the t-U(5000)-related emission indicates the existence of energy transfer between the hybrid host and the dye. From the inset of Figure 5.19A one may conclude that the emission band at 410 nm exists for SiNc in solution and also for M/t-U(5000)/SiNc and F/t-U(5000)/SiNc. Figure 5.19B presents the emission of the non-doped M/t-U(5000) prepared under the same conditions as those used for M/t-U(5000)/SiNc. It is clear that the emission spectrum of SiNc suffered an increase of the

intensity at 410 nm when incorporated into t-U(5000) cumulative of both system emissions.

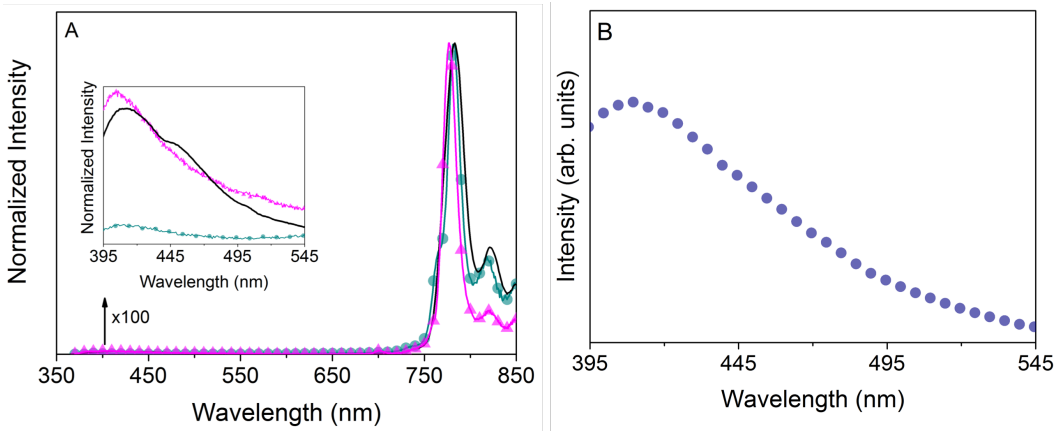

Figure 5.19: Emission spectra (excitation at 350 nm) of (A) SiNc in THF solution (green dots), M/t-U(5000)/SiNc (black line) and F/t-U(5000)/SiNc (pink triangles). The inset shows a magnification of the 395 to 545 nm spectral range. (B) Emission spectra (excitation at 350 nm) of non-doped M/t-U(5000).

The emission properties were quantified by the measurement of the absolute emission quantum yield, revealing larger values under UV excitation at 350 nm for M/t-U(5000)/SiNc and F/t-U(5000)/SiNc (see Table 5.7). We note that for F/t-U(5000)/SiNc the maximum q value (~ 0.17) is the same, within the experimental error, as that found for the diluted dye solution in THF. Therefore, we may conclude that the spectroscopic properties, as well as the photophysical parameters, were not significantly affected by the environment felt by the dye molecule in the t-U(5000) matrix.

Using the Beer-Lambert law, the molar extinction coefficient (ε, $M^{-1} \cdot cm{-}1$) was calculated from the linear dependence (slope) found for the absorbance vs. concentration, Figure 5.20.

The excitation spectra were monitored within the maximum emission band (Figure 5.21 resemble the absorption spectra in Figure 5.17, reinforcing that the SiNc incorporation into the hybrid matrix did not produce significant changes in the optical properties of the dye. In order to quantify the ability of F/t-U(5000)/SiNc to absorb the sunlight available for PV conversion, the overlap integral defined by Eq. 2.12 was calculated [159, 189] yielding $\sim 2.6 \times 10^{20}$ photons$\cdot s^{-1} \cdot m^{-2}$. The magnitude of the O value indicates that F/t-U(5000)/SiNc has the potential to absorb $\sim 6\,\%$ of the solar photon flux on Earth (4.3×10^{20} photons$\cdot s^{-1} \cdot m^{2}$) [5, 23, 127, 136].

Table 5.7: Photophysical parameters of SiNc in THF solution and processed as a monolith and as a thin film. The excitation wavelength used for the measurement of the absolute emission quantum yields is indicated in parenthesis.

Sample	ε $(M^{-1} \cdot cm^{-1})$	q	$\tau \times 10^{-9}$ (s)
SiNc in THF solution	$(5.4 \pm 0.1) \times 10^5$	0.17 ± 0.02 $(350\,nm)$ 0.10 ± 0.01 $(745\,nm)$	3.6 ± 0.1
M/t-U(5000)/SiNc	-	0.07 ± 0.01 $(350\,nm)$ 0.03 ± 0.01 $(745\,nm)$	3.6 ± 0.2
F/t-U(5000)/SiNc	$(3.4 \pm 0.2) \times 10^5$	0.16 ± 0.02 $(350\,nm)$ 0.08 ± 0.01 $(745\,nm)$	3.7 ± 0.1

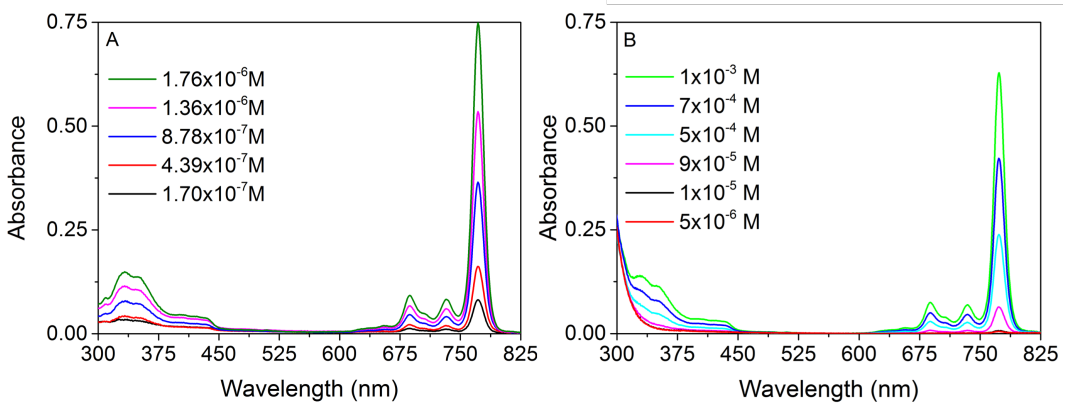

Figure 5.20: Absorption spectra used to calculate the molar extinction coefficient of (A) SiNc in THF solution and (B) F/t-U(5000)/SiNc deposited as thin film ($t = 2.0 \pm 0.2 \times 10^{-5}\,m$).

Time-resolved fluorescence measurements of SiNc in THF solution and embedded in the hybrid matrix (Figure 5.22) allowed the calculation of the excited state lifetime. The emission decay curves, monitored at $782\,nm$, revealed a single exponential decay, whose lifetime value found for the SiNc in THF solution is analogous to that found after the incorporation in the hybrid, Table 5.7. This evidence corroborates the fact that, when incorporated into tri-ureasil hybrid, the SiNc dye behaved like in solution medium, in contrast to reported in previous works [258, 281] where a shortening of the fluorescence lifetime occurred in solid films, indicating that non-radiative processes were activated. Moreover, the similarity between

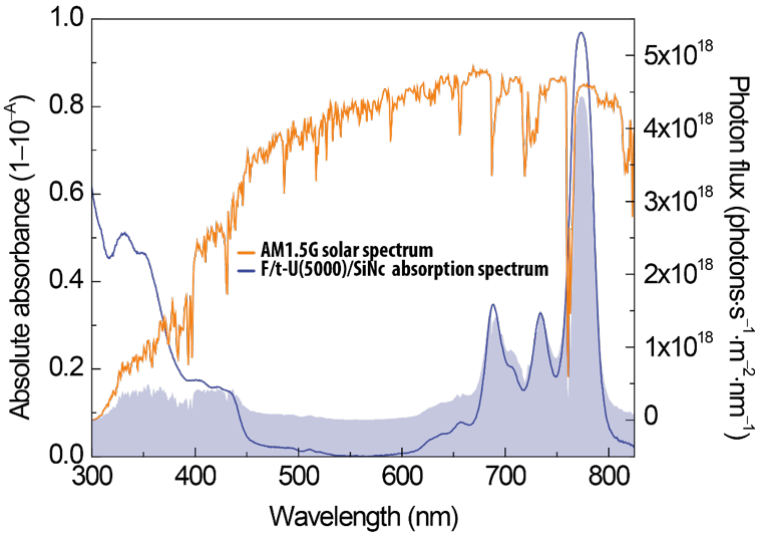

Figure 5.21: Absorption spectrum of F/t-U(5000)/SiNc) (left axis) and AM1.5G photon flux (right axis). The shadowed area represents the overlap integral O.

the lifetime values in Table 5.7 reinforces the conclusion taken from UV/vis absorption and emission spectra that the SiNc molecules preserved their monomeric structure.

Figure 5.23 shows F/t-U(5000)/SiNc and M/t-U(5000)/SiNc under UV illumination, illustrating the potential of the SiNc-doped tri-ureasils as NIR-emitting LSCs. It is evident that the radiation emitted at the surface is guided to the edges, where it can be collected by a PV cell.

The hybrids materials processed as films were selected to be tested as LSCs due to the larger absolute emission quantum yield compared with that found for the monoliths (Table 5.7). The F/t-U(5000)/SiNc was coupled to a Si-based photodiode and the LSC performance was quantified by measuring $\eta_{opt} \pm \Delta\eta_{opt}$. Considering the total incident number of photons, the calculated η_{opt} value was $1.50 \pm 0.01\,\%$. These results highlight the suitability of the t-U(5000)/SiNc-based LSC as a good alternative for QDs-based LSCs.

The performance of the LSCs was quantified coupling one of their edges to a c-Si PV cell and calculating the PV cell EQE (Eq. 2.22). As illustrated in Figure 5.24 for a representative LSC, the EQE of the PV cell coupled to the t-U(5000)/SiNc-based LSC is well correlated to the absorption spectra of the active layer (Figures 5.17 and 5.21). Despite the fact that the NIR region (between 700 and 800 nm) is the spectral range of maximum absorption of SiNc dye, the EQE enhancement is more evident in the UV spectral region (300-380 nm) compared with that found in the NIR. The distinct contributions of the LSCs for the PV

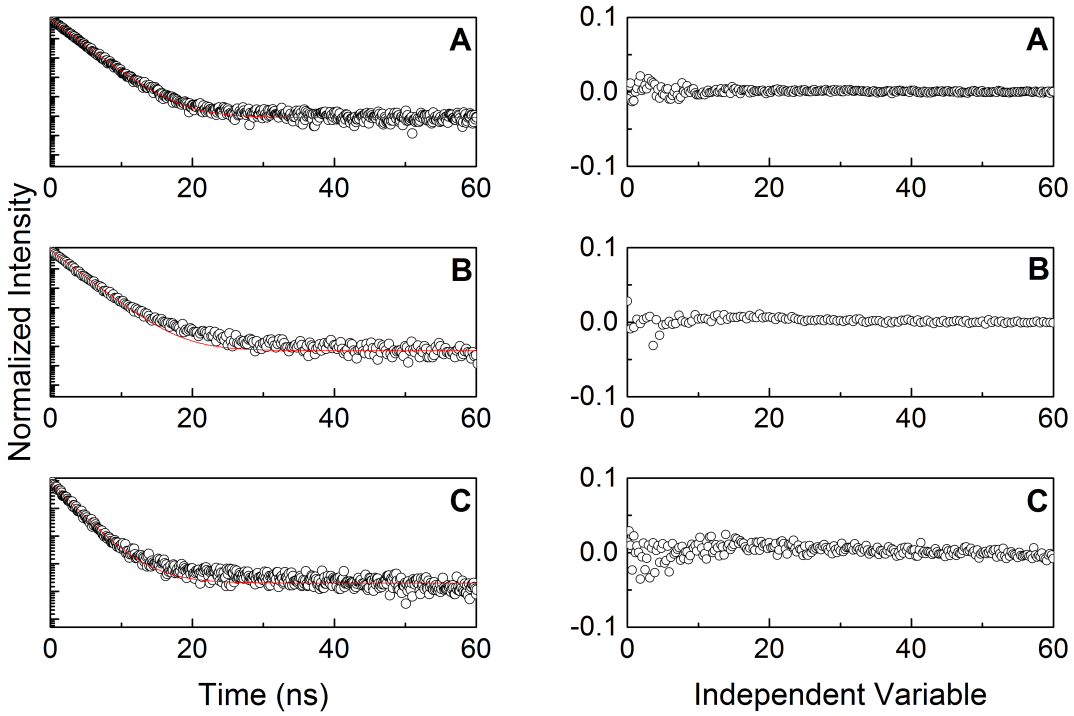

Figure 5.22: Emission decay curves of (A) SiNc in THF solution, (B) M/t-U(5000)/SiNc and (C) F/t-U(5000)/SiNc. The solid lines represent the data best fits ($r^2 > 0.99$) obtained using a single exponential function. The respective residual plots are shown on the right side. All the decay curves were recorded exciting at 329 nm and monitoring the emission at 782 nm.

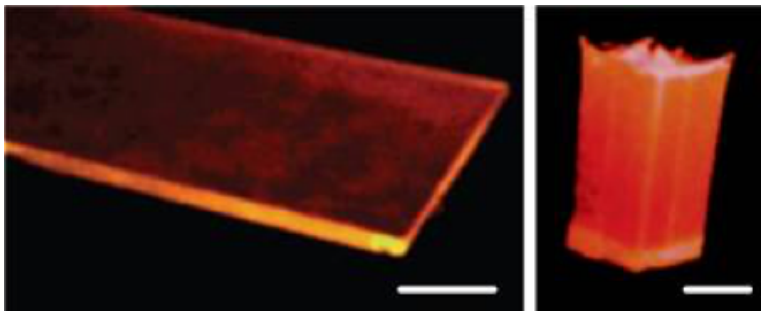

Figure 5.23: Photographs of (left) F/t-U(5000)/SiNc and (right) M/t-U(5000)/SiNc under UV illumination (scale bar, 1 cm). The photographs were taken using a webcam to which the infrared filter was manually removed, and using a negative film as a filter in the visible spectral region and the photographs were enhanced by a false colour rendering method (*pseudocolour*).

cell EQE may be rationalized as follows. The small EQE increase in the NIR spectral region (750-800 nm) results from the lower q values (Table 5.7) and the low emission Stokes-shift

(strong self-absorption) of the SiNc. Nevertheless, we note the larger increase of the EQE in the UV benefiting from the fact that in the UV spectral range the Si PV cells have lower performance and the active layer displays larger q values (Table 5.7), together with a larger Stokes-shift (negligible self-absorption). The adding contribution of the LSC in the UV region projects c-Si PV cells with nearly flat EQE curve over a large wavelength range from the UV to the NIR.

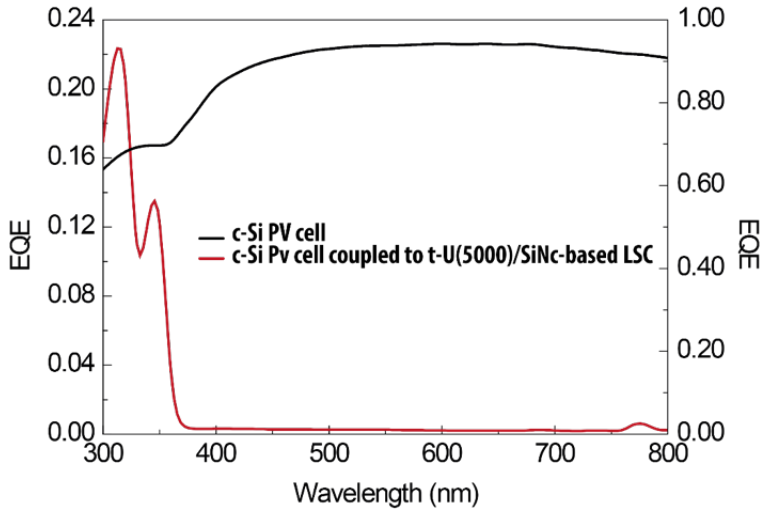

Figure 5.24: Experimentally measured EQE curves for c-Si PV cell in the standard configuration coupled to the t-U(5000)/SiNc-based LSC (left axis) and in the absence of any LSC (right axis).

5.4 Conclusions

LDS layers and LSCs made of PMMA doped with Ln^{3+} based ionic liquids were studied. The absorption spectra overlaps mainly the UV component of the solar irradiance on Earth (300-400 nm) and the emission spectra covers the visible-NIR spectral regions. The performance of the LDS layer coupled to a c-Si PV cell was also studied with an absolute increase in PV cell EQE of 25 % between 300-360 nm. LSCs based on Eu^{3+} and Tb^{3+} were also produced showing promising results. In what concerns PMMA doped with Yb^{3+} and Nd^{3+}-based ionogels, the performance of the LDS layers and LSCs did not increase due to low absolute emission quantum yield. Moreover, the use of PMMA doped with Ln^{3+} based ionogels as optically active centres in LDS layers and LSCs, demonstrates the potential of

ionogels in LDS layers and LSCs as a relevant step towards highly efficient and resistant to ambient conditions devices.

The use of NIR dyes as active centers in LSCs can be a promising step towards the engineering of new devices. A naphthalocyanine derivative (SiNc) was studied, due to its wide coverage of the solar spectrum (absorption at 300-450 nm and 600-850 nm) and emission centred around 785 nm, where the fraction of radiation absorbed by Si-PV cells is high. The incorporation of this dye into a tri-ureasil organic-inorganic hybrid matrix enabled the easy coating of a PV cell without affecting the SiNc photophysical properties. Thin dye doped hybrid films (F/t-U(5000)/SiNc) with absolute emission quantum yield of 0.17 and lifetime of 3.7 ns were produced and their performance in LSCs was evaluated achieving an $\eta_{opt} \sim 1.50 \pm 0.01\,\%$ and EQE values exceeding 20 % in the UV region. The SiNc-based tri-ureasil is, therefore, an intriguing example of a NIR layer for LSC devices.

Chapter 6

Transparent and flexible luminescent solar concentrators

In this chapter, we present a new geometry for LSCs based on triangular hollow-core POFs filled with organic-inorganic hybrid materials doped with Rh6G, Rh800 or an Europium β-diketonate complex. Large area LSCs are built from POFs bundle structures, whose assembling is favoured by the fibre triangular cross-section that also contributes to maximize the coverage of a PV cell surface compared with that of cylindrical POFs. Each bundle fibre behaves as an individual LSC absorbing UV/blue components of the solar spectrum and emitting visible and NIR radiation. The LSCs are characterized by optical conversion efficiency values up to $\eta_{opt} \sim 5.28 \pm 0.01\,\%$, among the largest values reported up to now for single-layer LSCs. Moreover, the coupling between the LSCs to commercial Si PV cells yield maximum power conversion efficiency values of $PCE \sim 0.74 \pm 0.01\,\%$. The individual waveguiding features of each fibre in the bundle contributes to reduce the re-absorption, as lower performance values ($\eta_{opt} \sim 1.54 \pm 0.01\,\%$; $PCE = 0.09 \pm 0.01\,\%$) were estimated for a planar LSC with analogous surface collection area and radiation harvesting absorbance.

6.1 Introduction

Besides the emission spectral range of the LSCs, performance is also set by geometry. In fact, theoretical studies pointed out that the optical concentration of cylindrical LSCs is up to 1.9 times greater than that of planar ones [186, 282]. We highlight here the main advantages of fibre-based LSCs arising from the intrinsic properties of the fibre themselves. Indeed, light-weight, flexibility, and the easy coupling to other optical fibres for radiation wave-guiding permit remote light harvesting with new fields of applications, such as mobile applications [283] and indoor daylighting [284]. Moreover, the cylindrical approach requires a smaller area of solar cells to produce the same amount of electricity as an equivalent square LSC [23, 282]. Visible-to-NIR-emitting LSCs made of triangular shape hollow-core POFs in which the circular core is filled with a modified tri-ureasil organic-inorganic hybrid host doped with $Eu(TTA)_3{\cdot}2H_2O$, Rh6G, or Rh800, Figure 6.1 were fabricated. Hollow-core fibres compared to coated ones add the advantages of mechanical and environmental protection to the optically active layer, which is an extra feature for real outdoors applications. The use of organic-inorganic hybrids to incorporate emitting centres lies on the well-known advantages of such materials that combine the thermal stability of the inorganic part with the flexibility of the organic one [180]. Moreover, the role of di-ureasils in the LSC design optimization was already recognized [169, 171, 206, 285–287]. Bundle structures of POFs-based LSCs were fabricated to increase the exposed area and the coverage of the PV cell surface. Although, a total coverage of the PV cell area could be attained using fibres with square or rectangular cross-section to form the bundle [283], higher optical efficiencies (2-5 %) and larger photon concentrations (30-33 %) are expected for cylindrical LSCs relative to that of square ones [186]. These bundles display η_{opt} values up to $\sim 5.28 \pm 0.01$ % and a maximum $PCE \sim 0.74 \pm 0.01$ %, when coupled to a Si PV cell. These values are larger than those measured for a planar LSC with analogous surface collection area and light harvesting absorbance, demonstrating the relevance of the fibre-based geometry in the performance.

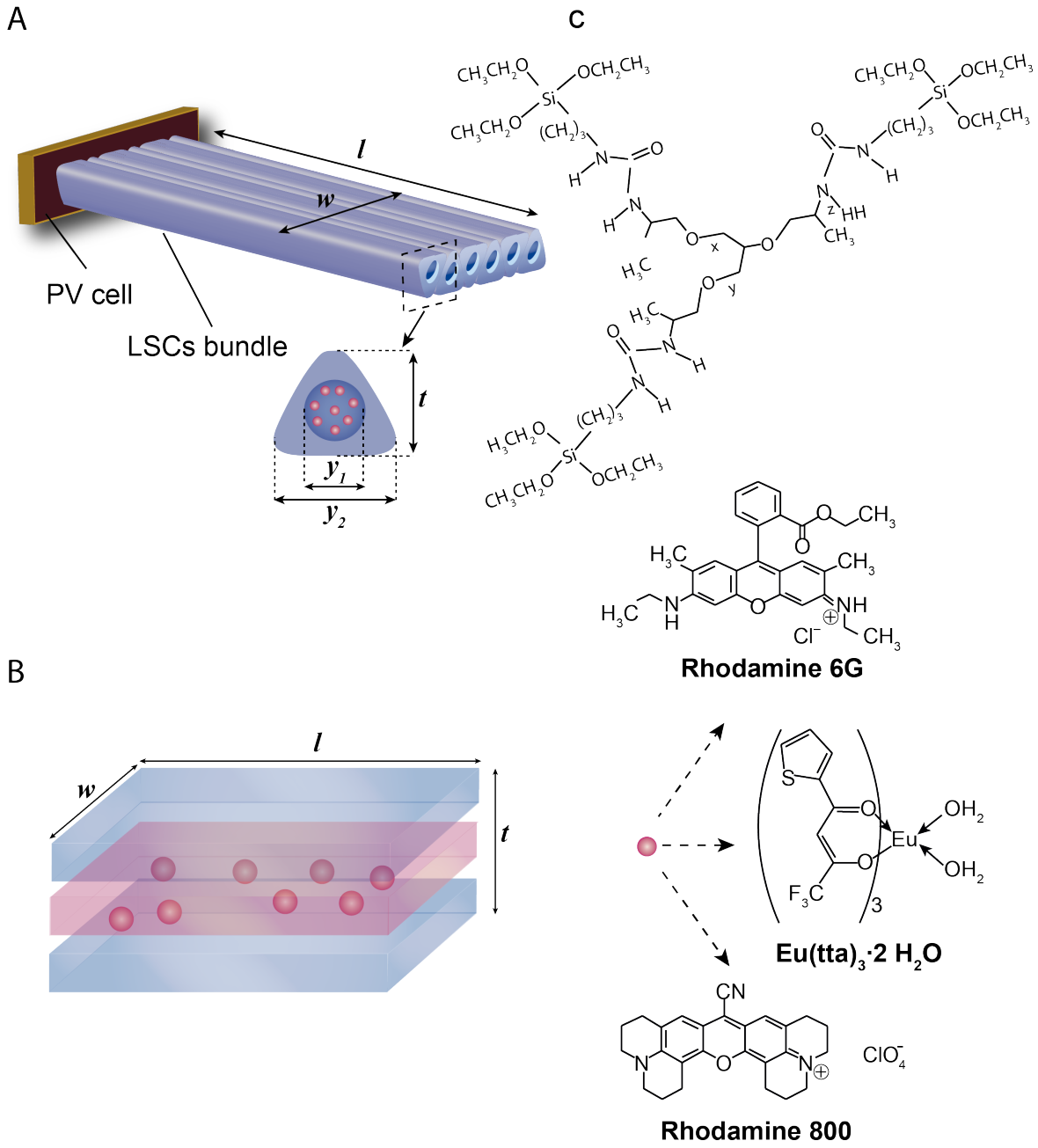

Figure 6.1: Schematic representations of the fabricated (A) cylindrical LSCs made of hollow-core POFs assembled in a bundle structure, with magnification of the edge of one fibre, where $y_1 = 1.1 \times 10^{-3}\,m$, $y_2 = 1.5 \times 10^{-3}\,m$, and $t = 1.3 \times 10^{-3}\,m$ and of the (B) planar LSC composed of two PMMA and one hybrid layers. The bundle and planar LSCs dimensions are $l = 10 \times 10^{-2}\,m$, $w = 2 \times 10^{-2}\,m$ and the thickness= t is indicated in the figure. The optical active layer is the Ln^{3+}, Rh6G- or Rh800-doped t-U(5000) organic-inorganic hybrid embedded into the (A) fibre hollow core or (B) in the middle of the two PMMA slabs. The chemical structure of the (C) tri-ureasil organic-inorganic non-hydrolysed precursor is also presented.

6.2 Optical characterization of the LSCs optically active layer

Figure 6.2 shows the POF-based LSCs under UV and solar simulator AM1.5G radiation illumination evidencing that the emission is guided to the edges of the device through total internal reflection. The emission spectra of the guided radiation at the fibre extremities is ascribed to the ${}^5D_0 \rightarrow {}^7F_{0-4}$ transitions, for the Eu^{3+}-based LSC, and to the dyes fluorescence, for Rh6G- and Rh800-LSCs, as illustrated in Figure 6.2. In all the cases, the emission overlaps the spectral response curve of c-Si based PV devices (Figure 6.3 and Figure 6.4a), as required for efficient LSC devices.

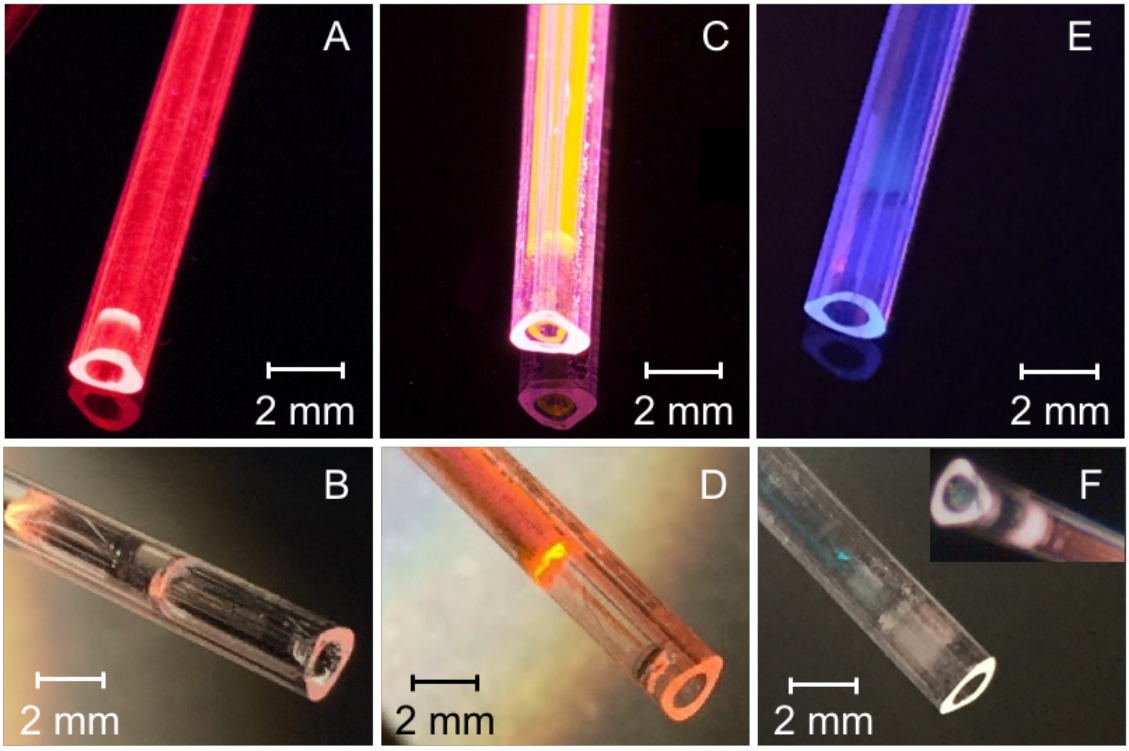

Figure 6.2: Fabricated (A,B) Eu-, (C,D) Rh6G- and (E,F) Rh800-LSCs under UV radiation at 365 nm (top) and solar simulator AM1.5G (bottom). The inset on (F) is a photograph of the Rh800-LSC taken with an infrared camera.

The emission properties of the optically active layers were further quantified, being characterized by maximum absolute emission quantum yield values of 0.89 ± 0.09 and 0.21 ± 0.02 (excitation at $320\,nm$) for Eu- and Rh800-LSCs, respectively, and 0.95 ± 0.10 (excitation at $560\,nm$) for the Rh6G-LSC. We note that the incorporation of the $Eu(TTA)_3 \cdot 2H_2O$ complex in the hybrid induced an increase in the values due to coordination ability of the organic

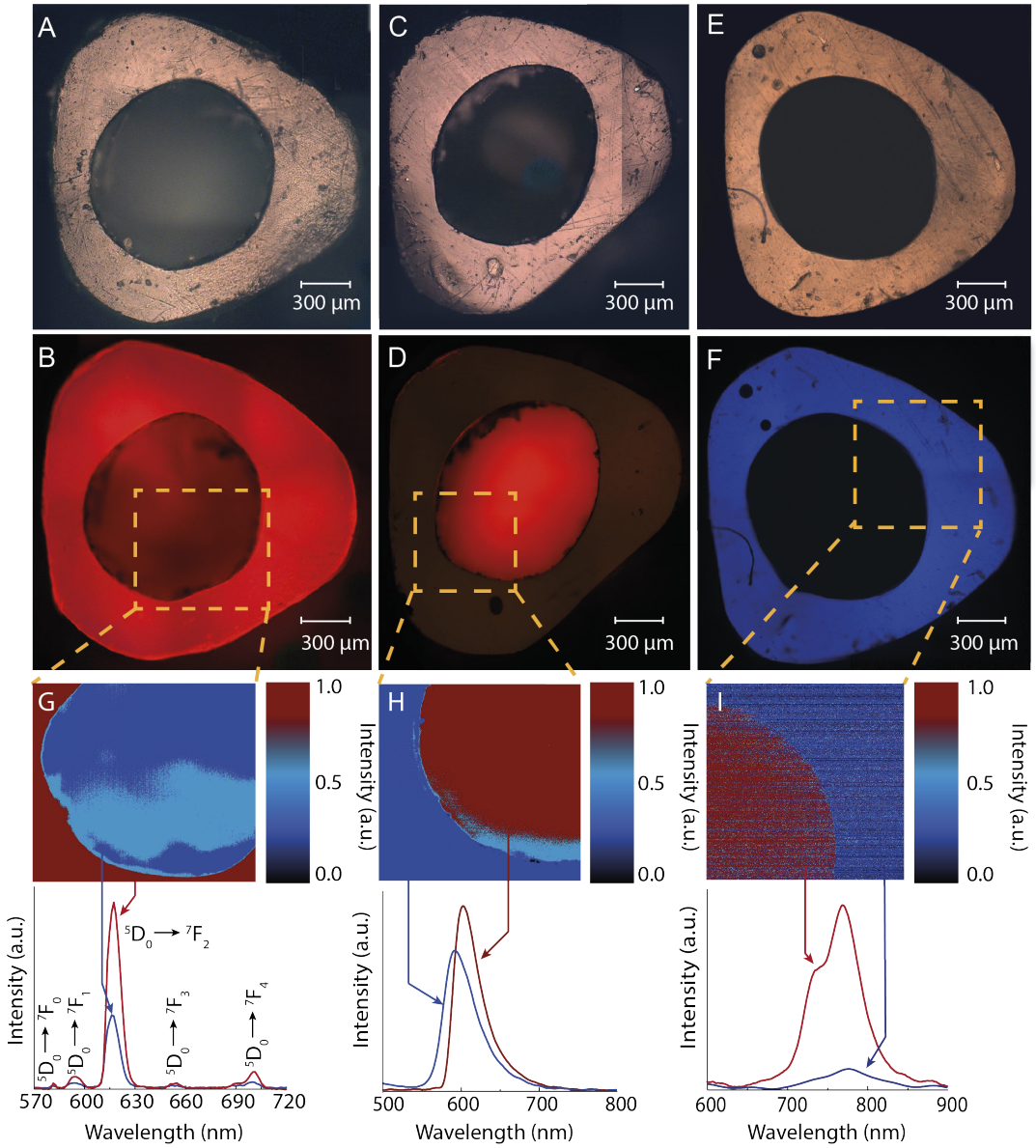

Figure 6.3: Cross-section optical microscopy images of the (A,B) Eu-, (C,D) Rh6G- and (E,F) Rh800-LSCs under white light illumination (A,C,E) and UV irradiation at 365 *nm* (B,D,F). Hyperspectral images of selected areas of (G) Eu-, (H) Rh6G- and (I) Rh800-LSCs and the corresponding emission spectra measured in the core and cladding regions.

counterpart of the host structure which is strong enough to displace water molecules of the complex from the rare earth neighbourhood after the incorporation process [156]. For the Rh800- and Rh6G-LSCs, the absolute emission quantum yield value is identical to the isolated dyes [190, 192] and there is no indication of formation of J-type aggregates [288, 289],

pointing out that the hybrid host is appropriated for an efficient incorporation of organic dye molecules.

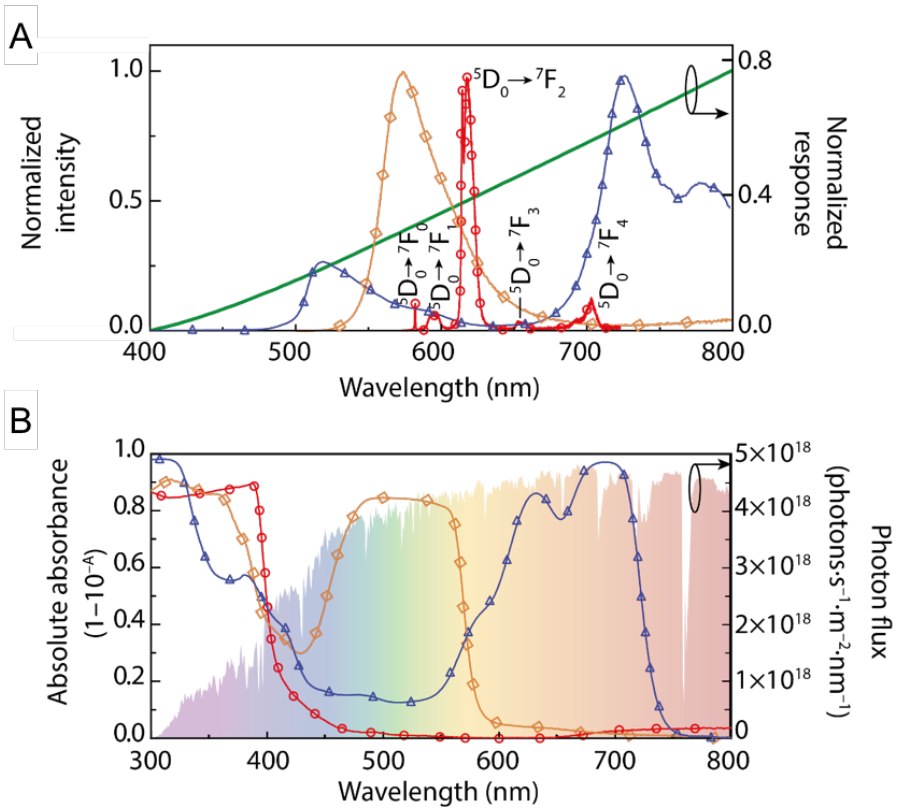

Figure 6.4: (A) Emission spectra excited at 370, 480 and 620 nm for Eu- (red circles), Rh6G- (orange diamonds) and Rh800-LSCs (blue triangles), respectively. The green line is the normalized response curve of c-Si photovoltaic devices. (B) Absorption spectra for Eu-, Rh6G- and Rh800-LSCs and AM1.5G photon flux (the colour code is the same than in (A)).

In order to quantify the ability of the LSCs to absorb the sunlight available for PV conversion, we calculate the overlap integral between the optically active layer excitation spectrum and the solar irradiation on Earth by [287], Eq. 2.12. The larger values for the overlap integral (Figure 6.4B) were found for the Rh800-based hybrid, revealing 7.1×10^{20} photons$\cdot s^{-1} \cdot m^{-2}$ compared with 1.0×10^{20} and 5.1×10^{20} photons$\cdot s^{-1} \cdot m^{-2}$ found for the Eu- and Rh6G-based ones. The estimated O values indicates that the Eu-, Rh6G- and Rh800-LSCs have the potential to absorb, respectively, $\sim 2\,\%$, $\sim 12\,\%$ and $\sim 17\,\%$ of the solar photon flux on the Earth, estimated as 4.3×10^{21} photons$\cdot s^{-1} \cdot m^{-2}$ [127, 163, 285].

The excitation spectra of the dye-doped hybrid layers were monitored within the emission peak position, Figure 6.5, namely around $590\,nm$ and $715\,nm$, for Rh6G- and Rh800-LSC,

respectively, and within the ${}^5D_0 \rightarrow {}^7F_2$ transition for the Eu^{3+}-LSC. These spectra resemble the absorption ones in Figure 6.4B. The excitation spectrum of the Eu^{3+}-LSC is formed of a broad band (full width at half maximum of 130 nm) in the UV spectral region with two main components at 280 nm and at 330-370 nm mainly ascribed to the hybrid host and to the TTA triplet states [189, 243]. The high-relative intensity of the TTA-related band readily indicates that the ligand-excited states are the main intra-${}^4f_6$ population path. The excitation spectra of the Rh6G- and Rh800-LSC overlaps the hybrid host excitation region (240-450 nm) and present broad bands (450-550 nm for Rh6G-LSC and 550-720 nm for Rh800-LSC) ascribed to direct excitation of the dye related states [257, 290]. In the case of the Rh800-LSC, the excitation spectrum peaks at 690 nm. The absence of the emission bands typically of the undoped host [241] in the emission spectra of the LSCs and of the TTA excited states in the Eu^{3+} case [189] points an effective hybrid-to-optically active centre energy transfer [291].

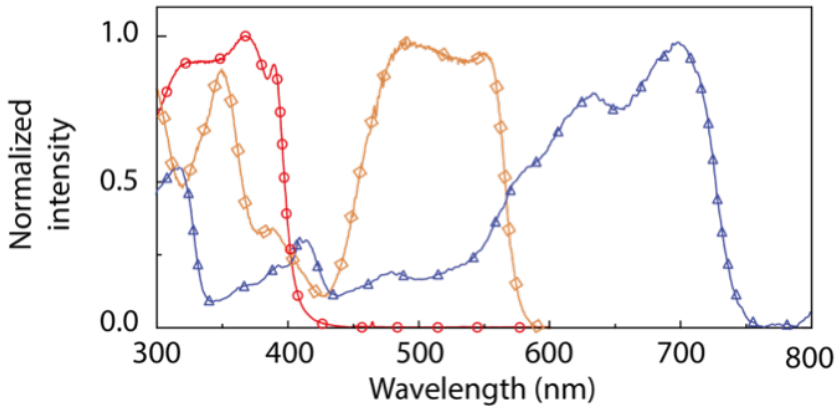

Figure 6.5: Excitation spectra monitored at 615, 590 and 715 nm for Eu-LSCs (red circles), Rh6G-LSCs (orange diamonds) and Rh800-LSC (blue triangles), respectively.

As evidenced in Figure 6.3, radiation trapping depends on the optically active layer. Whereas for the Eu-LSCs the emission intensity guided in the PMMA cladding is larger (~ 3 times) than that in the hybrid layer, for the Rh6G- and Rh800-LSC the radiation propagation is more intense in the hybrid layer at the fibre core than in the cladding (Figure 6.3). We note that the increased PMMA attenuation[159, 287] in the Rh800 emission range also accounts for the significant relative increase of the intensity at the core (by a factor of ~ 6) for the Rh800-LSC.

These later results may be further rationalized using a simple analytic expression Eq. 2.3 that, for a uniform distribution of emitting centres and isotropic emission over a solid angle,

depends on the difference between the refractive index values (at the emission wavelength range) of the optically active layer at the core (n_{core}) and at the PMMA (n_{clad}) [292].

Refractive index dispersion curves of the doped hybrids were measured by spectroscopic ellipsometry and the elipsometric parameters are shown Figure 6.6. Whereas for the refractive index of the PMMA ($n_{clad} \sim 1.49$) is very close to that of the Rh6G ($n_{core} = 1.50$) and Rh800 ($n_{core} = 1.49$) optically active layers, n_t tends to a minimum value, which readily indicates that the radiation emitted at the core is also guided within the PMMA cladding. In the case of the Eu-LSCs, the larger refractive index of the cladding ($n_{clad} \sim 1.49$) compared with that of the core ($n_{core} = 1.46$) yields to a dominant radiation guidance in the PMMA, Figure 6.7.

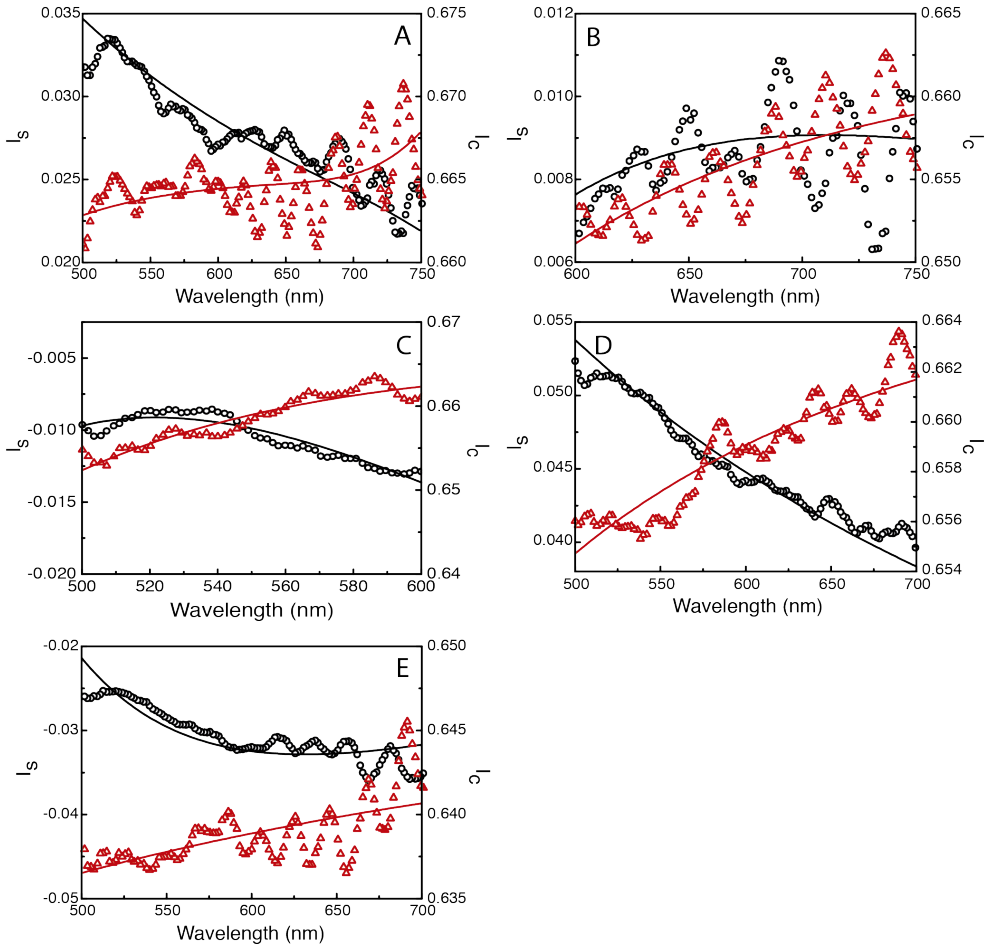

Figure 6.6: Ellipsometric parameters I_s (circles) and I_c (triangles) measured for the active layer of (A) Eu-LSC, ($r^2 > 0.498$), (B) Rh6G-LSC ($r^2 > 0.404$) and (C) Rh800-LSC ($r^2 > 0.948$), (D) POF ($r^2 > 0.928$), and (E) undoped t-U(5000) ($r^2 > 0.633$). The lines represent the best data fit.

Another parameter that contributes to n_t is the distance r from the fibre centre at which the emission occurs which, for a POF with external diameter R, is given by Eq. 2.4 [202], with a maximum value near the surface, that decreases as r approaches the centre of the POF (Figure 6.7). We note that for the geometry here proposed, $R \sim 1.5\,mm$ the emission guidance occurs in the core, $0 \geq r \geq 1.1 \times 10^{-3}\,m$ and, therefore, average n_t values of 0.39 were estimated for the Eu-, Rh6G- and Rh800-based LSCs, respectively.

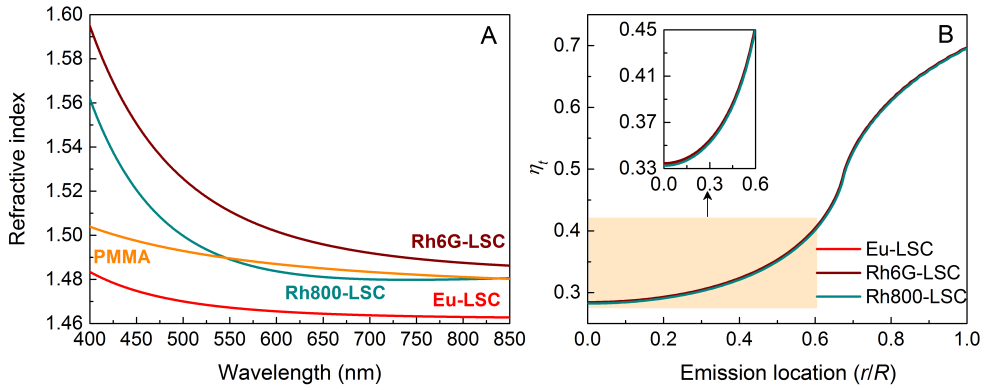

Figure 6.7: (A) Refractive index dispersion curves of the LSC optically active layers and PMMA and (B) trapping efficiency (n_t) as function of the ratio r/R (Eq. 2.4).

To demonstrate the real applicability of the triangular-shaped LSCs the experimental η_{opt} values were also determined under natural daylight illumination ($\sim 944\,W \cdot m^{-2}$). We should note that the dependence of optical path on the geometry is weighted through the geometrical gain G ($G = A_s/A_e$), by considering in the calculus of A_s (surface area) the effective length L_c of each LSC (equivalent length for a fibre without attenuation) and A_e as the area of the two edges, as it is expected the same radiation concentration at each LSC end, and thus $G \approx 11$. The calculated L_c values are similar to those reported for long-length hollow-core LSCs, despite the much shorter length of the POFs used here [158].

The spectra acquired at the edges of the fibre is illustrated in the Figure 6.8 where the AM1.5G spectrum is shown, as well as the emission at the edges for the illustrative case of Rh6G-based LSC. This later spectrum, Figure 6.8B, reveals the contribution of the Rh6G emission and also, as expected, the solar radiation in the region not absorbed by the material. The ratio between both spectra is presented in Figure 6.8C, where it is clear the contribution of the Rh6G related emission.

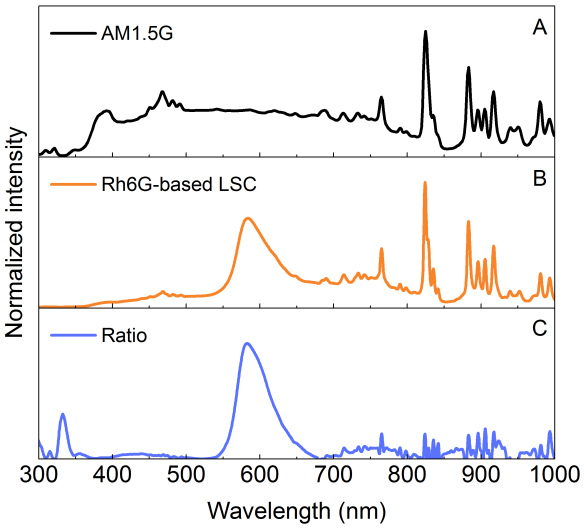

Figure 6.8: (A) Solar simulator AM1.5G spectrum, (B) spectrum measured at the edges of the Rh6G-based LSC and (C) the ratio between them showing the contribution of the optically active layer emission.

The diameter of the hybrid layer is $\sim (1.11 \pm 0.03) \times 10^{-3}\, m$, the same order as the POF thickness and thus, the probability of absorption of the emitted photons with higher order modes (photons emitted with an angle closer to θ_c, Eq. 2.1) is increased, due to the fact that the optical path is greater for these photons than for the lower mode ones. Furthermore, there is an additional attenuation of the optical signal of the evanescent electromagnetic field propagated through the PMMA. In summary, the radiation is also guided within the hybrid layer, besides the PMMA cladding.

Since the radiation guidance preferentially occurs in the hybrid layer, additional losses are predicted as the absorption coefficient of the hybrid material is larger than that of POF (Figure 6.9 and 6.10). Thus, radiation will travel a shorter length compared to the total length of the LSCs fabricated. Similarly to that recently reported [158], the discussion of the radiation propagation must also take into account the absorption spectra of the hybrid and PMMA layers (Figure 6.4). Such length was experimentally quantified by a piano test [191], in which the LSCs were covered by pieces of black paper cut into 1 *cm*-wide piano-key-like strips. The P_{out} was quantified under natural daylight conditions as function of the distance L of the illuminated area to the detector (Figure 6.9). Due to the short length of the LSCs, the data were analysed in logarithmic scale and fitted to a linear function, in which the slope would be

considered as the LSC attenuation coefficient (α). Therefore, α is $\sim 17.6\,m^{-1}$, $\sim 8.8\,m^{-1}$ and $\sim 18.0\,m^{-1}$ for Rh6G-LSC, Eu-LSC and Rh800-LSC, respectively. For Rh6G- and Rh800-based LSCs, the effective length L_c (equivalent length for a fibre without attenuation) is $\sim 4.0 \times 10^{-2}\,m$; for Eu-LSC, $L_c \sim 5.0 \times 10^{-2}\,m$.The fibre maximum L_c was estimated to be $\sim 6.0 \times 10^{-2}\,m$ for Rh6G- and Rh800-based LSCs and $\sim 11 \times 10^{-2}\,m$ for Eu-LSC by replacing the values into Eq. 2.23.

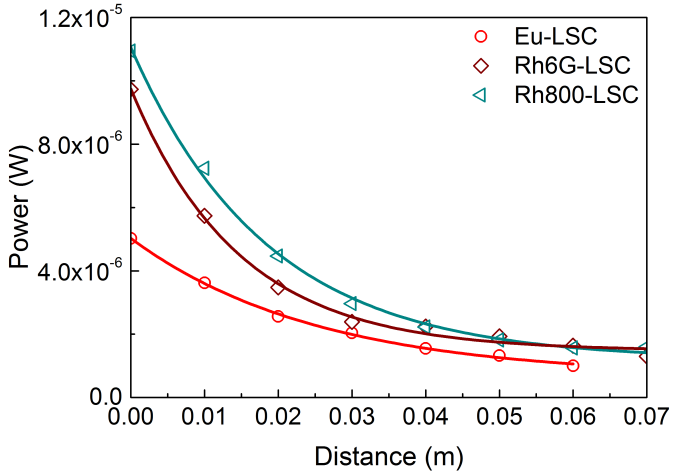

Figure 6.9: Output power as function of the distance measured in the piano test [172]. The solid lines correspond to the data best fit ($r^2 > 0.90$). The data is in logarithmic scale.

Considering the total incident spectral range, $\eta_{opt} \pm \Delta\eta_{opt}$ values of $0.65 \pm 0.01\,\%$, $2.07 \pm 0.01\,\%$ and $0.49 \pm 0.01\,\%$ were measured for Eu-, Rh6G-and Rh800-LSCs, respectively. We notice that these values although smaller than those of ZnS-coated CISeS QDs incorporated in poly(lauryl methacrylate) ($\eta_{opt} = 3.27\,\%$) [172], and tri-ureasil-Rh6G-based LSCs based on cylindrical POFs ($\eta_{opt} = 8.0\,\%$) [158], are analogous to the figure of merit recently reported for single-layer LSCs (without external devices such as reflectors) to enhance η_t, namely LSCs based on Stokes-shift-engineered QDs embedded in PMMA ($\eta_{opt} \sim 1\,\%$) [170].

Aiming at compare the relevance of the fibre geometry for the LSCs performance, the η_{opt} and PCE were also quantified for analogous LSCs based on fibres with circular geometry, Table 6.1. We noticed an increase in both parameters for the triangular shaped, when compared with the performance of the circular LSCs, independently of the optically active layer (Table 6.1) experimentally confirming the relevance of triangular geometry.

Table 6.1: Comparison of the fibre-based LSC performance (η_{opt} and PCE) for devices with analogous length (l) and diameter (y) and distinct geometries.

Active centre	Fibre geometry	$L\ (m)$	$y\ (m)$	η_{opt} (%)	PCE (%)
Eu^{3+}	hollow-triangular	3.5×10^{-2}	10^{-3}	1.14	0.058
Rh6G				1.52	0.074
Eu^{3+}	hollow-cylindrical			0.02	0.001
Rh6G				0.33	0.018
Eu^{3+}	bulk-coated			0.06	0.001
Rh6G				0.18	0.004

6.3 Large area LSCs: bundle structures and planar devices

Beside the contribution of the triangular geometry for the LSCs performance, illustrated in Table 6.1, the triangular design of the POFs allows an easier coupling between them, when compared to cylindrical ones, giving the possibility of fabricating large area LSCs based on bundle structures (Figure 6.10). One of the advantages of the proposed fibres assembled in parallel is that each LSC behaves as an individual device, avoiding re-absorption of the emitted radiation by adjacent optical centres, as detailed below. Also, as each fibre can incorporate distinct emitting materials, broad absorption and emission bands are achieved, to ensure the use of as much of the solar radiation spectrum as possible.

Another advantage of the triangular geometry is related to its packing ability. For instance, considering a square PV cell with dimensions $2.0 \times 0.2\,cm^2$, and a bundle of cylindrical LSCs with $d = 0.2\,cm$, the maximum number of LSCs that could be coupled to PV cell would be 10; otherwise, if we consider a bundle of triangular LSCs, each side of the triangle with $0.2\,cm$, the maximum number of LSCs that could be coupled to the PV cell should be 20. Using these example dimensions, the overall covered area of the PV cell would be $0.31\,cm^2$ and $0.34\,cm^2$ for the cylindrical and triangular LSCs bundle, respectively. The portion of the PV cell not covered would correspond to $\sim 22\,\%$ and $\sim 15\,\%$ of its total area. Thus, by using the triangular geometry instead of the cylindrical one, the coverage of the PV surface could be improved in $\sim 7\,\%$.

Since it is expected to have a higher amount of photons reaching the PV device comparing with the standalone LSCs, to evaluate the electrical performance of the bundles, PCE values

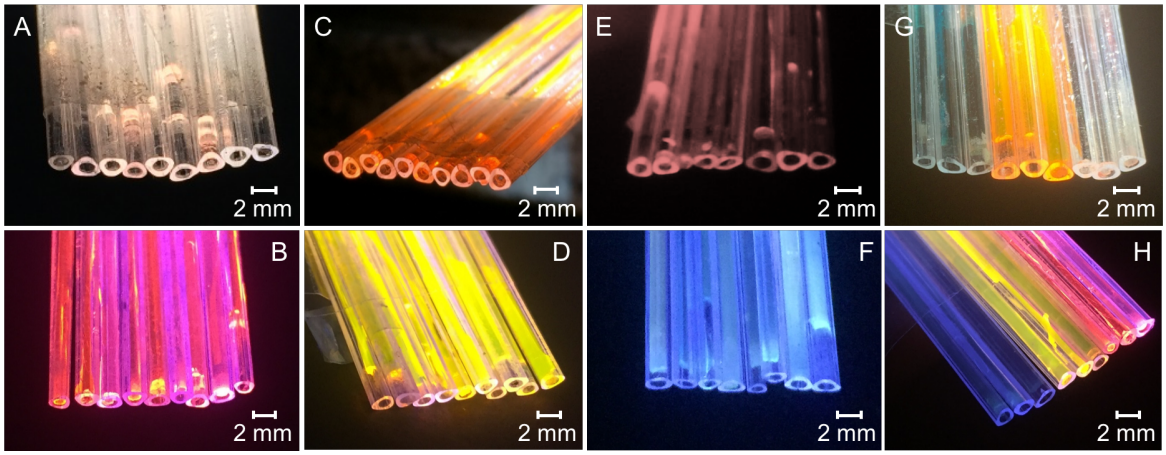

Figure 6.10: Photographs of bundles of (A,B) Eu-LSCs, (C,D) Rh6G-LSCs, (E,F) Rh800-LSCs and (G,H) Eu-, Rh6G- and Rh800-LSCs simultaneously under AM1.5G radiation (top) and UV radiation at 365 nm (bottom). The photograph on (E) was taken with an infrared camera.

of a coupled Si-based PV cell were calculated through Eq. 2.21, under natural daylight illumination ($\sim 724\,W \cdot m^{-2}$), resulting in $0.08 \pm 0.01\,\%$, $0.21 \pm 0.01\,\%$ and $0.74 \pm 0.01\,\%$ considering the two edges of the bundles of Eu-, Rh6G- and Rh800-LSCs, respectively. These values are very promising when compared with PCE values of 0.2 % and 0.54 % reported for a cylindrical LSC based on an Eu^{3+}-doped organic-inorganic hybrid [159] and for a planar LSC based on an organic-inorganic hybrid material doped with Lumogen Red, respectively [292].

The EQE curve of the Si-based PV cell coupled to the large area LSCs was measured (Figure 6.11). The same measurements were performed for the c-Si photodiode coupled to each standalone LSC, yielding similar results (Figure 6.12). As can be noticed in Figure 6.11A-C and in Figure 6.12, for all the fabricated large area and standalone LSCs, the EQE curves correlate well with the excitation spectra of the active layers (details of these spectra are presented in Figure 6.5).

To experimentally demonstrate the relevance of the geometry for the performance, a three layers planar LSC (Figure 6.1B) formed by a couple of PMMA slabs with the same surface area of the bundle was fabricated. The space between the PMMA slabs was filled with the doped organic-inorganic hybrid materials with thickness values tuned to have the same absorbance of the corresponding bundle (Figure 6.13). To that, planar LSCs formed of two PMMA slabs filled with Rh6G-based tri-ureasil hybrid were fabricated. The hybrid layer was deposited

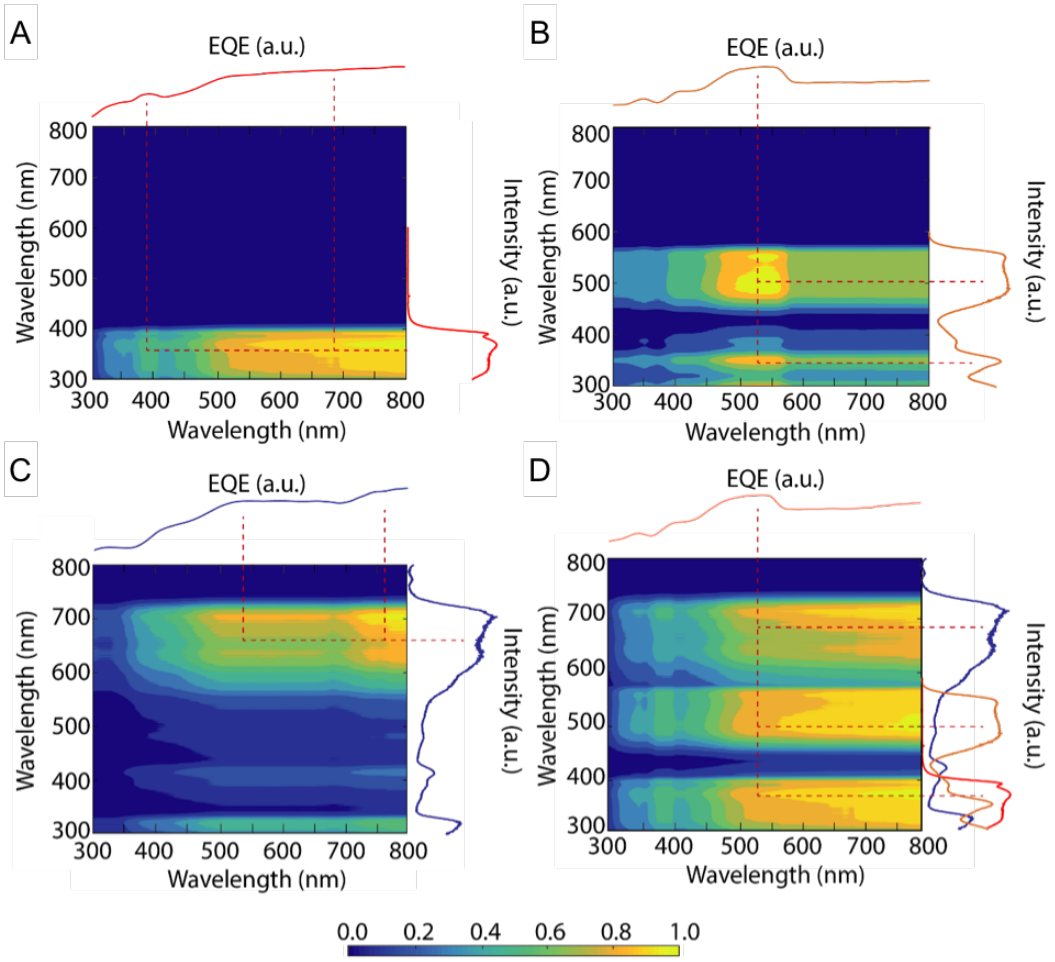

Figure 6.11: Cross correlation between the c-Si PV cell EQE when coupled to the bundles and the excitation spectra of the active layers: bundles of (A) Eu-, (B) Rh6G-, (C) Rh800-LSCs and of (D) Eu-, Rh6G- and Rh800-LSCs simultaneously.

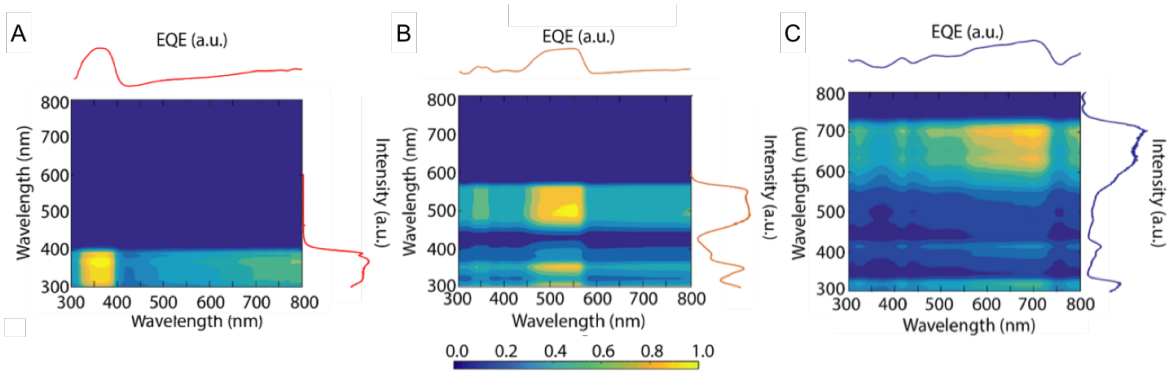

Figure 6.12: Cross correlation between the photodiode EQE when coupled to the LSCs and the excitation spectra of the active layers: (A) Eu-, (B) Rh6G- and (C) Rh800-LSCs.

with distinct thickness values (t) to tune the LSC absorbance to values analogous to those of the corresponding bundle, as illustrated in Figure 6.13. The absorbance spectra of the fibre-based and planar LSC are identical, revealing a variation only in the relative intensity of the components in the UV (280-390 nm), probably related with the processing methodology that induces a distinct kinetic of the sol-gel process affecting the gelation times, namely hours for the films deposited by drop cast and few seconds for the fibres filled under vacuum, which modulates the degree of organization of the materials [176, 188, 293]. Neverthless, we note that in the visible spectral range with larger overlap with Sun spectral irradiance the spectra are identical being dominated by the Rh6G lowest triplet state. Based on the experimental data in Figure 6.13, we characterized the performnace of the LSC with a Rh6G-based layer with $t = 5.9 \times 10^{-4}\, m$ and compare it with that of the fibres bundle.

To discuss the effect of the re-absorption mechanism in the proposed bundle geometry compared with that found in planar LSCs, we selected the Rh6G-based layer to fabricate the planar LSC because it combines larger self-absorption probability (small Stokes-shift compared with that of Eu^{3+}-based LSCs) and higher optical performance.

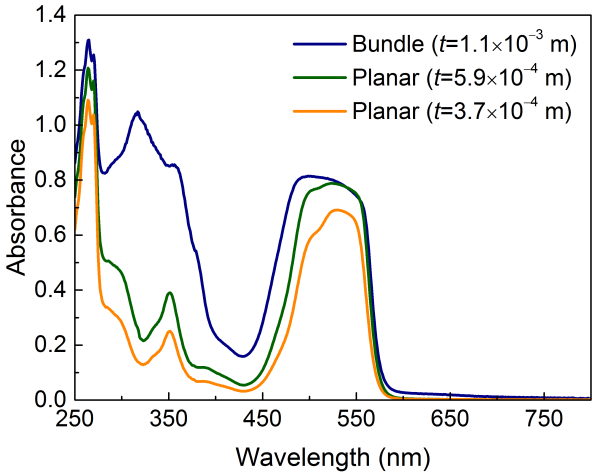

Figure 6.13: Absorbance spectra of the Rh6G-based layer in the bundle-based LSC and in the planar one. The spectra demonstrate that the thickness (t values in the graph) of the optically active layer in each LSC was tuned to ensure a similar radiation harvesting ability.

Figure 6.14 shows photographs of the planar LSCs under AM1.5G illumination, whose performance was quantified through Eq. 2.14. We note that lower η_{opt} values were measured for the Rh6G-based planar LSC ($1.54 \pm 0.01\,\%$), relatively to that found for the bundle

structure (5.28±0.01 %). The lower η_{opt} of the planar LSC yielded a poor PCE (0.09±0.01 %), compared with the above mentioned for the bundle structure (0.21 ± 0.01 %), unequivocally supporting the relevance of the novel LSC structure based on triangular-shaped POFs.

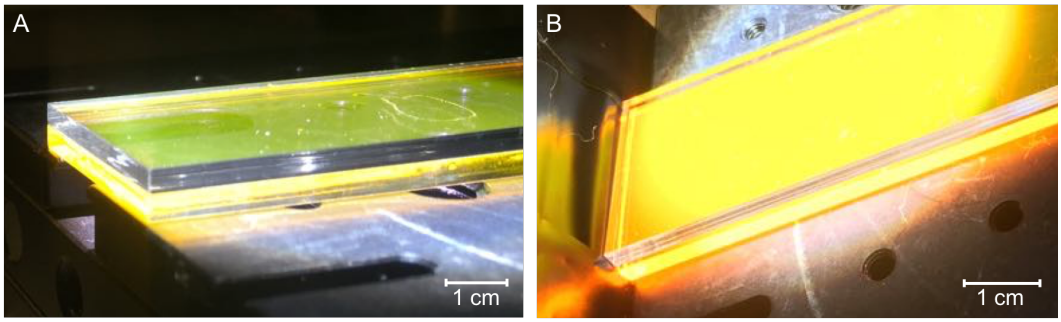

Figure 6.14: Photographs of Rh6G-based planar LSCs under AM1.5G radiation from (A) side and (B) top views.

Further advantages of the bundle structure for large-area LSCs is the possibility to incorporate distinct optically active centres in each fibre, which would not be possible in a conventional planar LSC. This bundle enables the UV and visible solar radiation absorption in a single device with visible-to-NIR tunable emission, resonant with the spectral region of c-Si devices greatest performance. To prove this concept, a bundle simultaneously incorporating Eu-, Rh6G- and Rh800-LSCs was fabricated and tested (Figure 6.10G,H). The contributions of the three active layers is discerned in the spectral regions of the EQE curve, overlapping their excitation spectra (Figure 6.11d), yielding $PCE = 0.33 \pm 0.01$ %, accounting for the average contribution of each fibre in the bundle.

6.4 Modelling

The optical model relies on two PMMA layers and on one organic-inorganic Rh6G-based hybrid layer in between (Figure 6.1b). The thickness of the PMMA and hybrid layers ($\sim 2 \times 10^{-3}\, m$) are much larger than that of the light coherent length ($\sim 10^{-7}\, m$), thus, interference effects were neglected.

The geometrical inputs of the Monte Carlo ray-tracing simulation consist of a planar LSC with three layers with analogous surface area ($20 \times 10^{-4}\, m^2$) and thickness values of $2 \times 10^{-3}\, m$ and $5.9 \times 10^{-4}\, m$ for the PMMA and Rh6G-based layers, respectively. The input concerning the spectral data consist of the solar spectrum AM1.5G (280-1600 nm, photons with angle

of incidence between $-45°$ and $45°$), the absorption (Figure 6.13) and emission (Figure 6.4) spectra, the absolute emission quantum yield and the dispersion curves for the PMMA and Rh6G-based layer (Figure 6.7). Furthermore, we consider a thin layer of air underneath the LSC.

The description of the simulation is described in Chapter 5. In this case, the photon desired step size is $2 \times 10^{-4}\, m$.

The output of the simulation considering the photons reaching one of the LSC edges yielded to $\eta_{opt} = 0.74 \pm 0.01\,\%$, which is very close to that found experimentally ($\eta_{opt} = 0.33 \pm 0.01\,\%$) for a single PV cell placed at one of the LSC edges, pointing out that the simulation describes the main optical LSC waveguiding features.

6.5 Conclusions

A new triangular geometry for hollow-core LSCs was presented, whose core was filled with an organic-inorganic hybrid doped with $Eu(TTA)_3 \cdot 2H_2O$, Rh6G or Rh800. The Rh800 dye allowed the fabrication of NIR emitting LSCs, which are scarce in the literature. The standalone fibre LSCs presented a maximum η_{opt} of $\sim 2.07 \pm 0.01\,\%$ for the Rh6G-based ones. The fibres were assembled in bundles and coupled to c-Si PV cells and EQE measurements were performed. The EQE curve of the PV cell resembled the excitation spectra of the optically active layer in use. The building of large area LSCs based on easily-assembled triangular POFs minimizes the self-absorption and transport spectral losses originated from adjacent fibres, as each fibre behaves as an individual LSC. Furthermore, this methodology permits to tune the radiation harvesting and emission spectral ranges to absorb the solar irradiation and to match the efficiency of the target PV cell, respectively, pointing out the suitability of these LSCs in real applications.

Chapter 7

Sustainable luminescent solar concentrators

This chapter will be focus on the development of LSCs based on natural dyes or pigments that have light harvesting ability, high absolute emission quantum yield and the emission in the NIR is perfectly tuned with the c-Si PV cell higher efficiency spectral region. Also, pointing out the potential of this approach for the development of natural-based LSCs meeting the requirements of reliable, sustainable and competitive energy systems.

In the first section of this chapter, we report novel chlorophyll-based LSCs with emission properties in the red-NIR spectral region. The chlorophyll molecules were extracted from Spirulina maxima which is an abundant cyanobacteria and an attractive natural source. To enable the easy and controlled processing of planar LSCs, the chlorophyll molecules were incorporated into amine-functionalized organic-inorganic hybrids (di- and tri-ureasils) with the added advantages of avoiding the formation of non-luminescent dye-clusters or dye-aggregates, enhancing the absolute emission quantum yield and photostability. In the second section of this chapter, the R-phycoerythrin (R-PE) protein, which is one of the most abundant phycobiliproteins in red macroalgae, was used as optically active centre for LSC applications. In this case, the R-PE was extracted from marine biomass, namely fresh *Gracilaria sp.* red algae by an extraction and purification method which does not affect its conformational structure or chromophore structural integrity. We should note that the use of *Gracilaria sp.* algae takes advantage of local resources, since it is an abundant algae in Ria de Aveiro, Portugal.

7.1 Introduction

Aiming at following a sustainable route for designing LSCs, photosynthesis may be an inspiring natural mechanism if PV solar energy conversion is compared to an artificial photosynthesis process which is stopped short [124]. The optical and electrical functions of LSCs and their attached PV cells mimic the radiation collection and charge generation processes, respectively [124]. In photosynthesis, one key molecule is chlorophyll as it is responsible for sunlight harvesting [294] with emission properties in the red/NIR spectral region. The attractive properties of natural-based dye molecules for LSCs have been poorly explored.

Novel chlorophyll-based LSCs are processed and optically characterised, Figure 7.1A, in the first part of this chapter. The chlorophyll molecules were extracted from *Spirulina maxima* which is an abundant cyanobacteria and an attractive natural source. To enable the easy and controlled processing of planar LSCs, the chlorophyll molecules were incorporated into amine-functionalized organic-inorganic hybrids (di- and tri-ureasils) with the added advantages of avoiding the formation of non-luminescent dye-clusters or dye-aggregates [156], enhancing the absolute emission quantum yield and photostability [89]. The chlorophyll-based LSCs were coupled to a Si-based PV device, revealing η_{opt} and PCE values around 3.70±0.01 % and 0.10 ± 0.01 %, respectively, demonstrating the huge potential of nature-inspired LSCs for sustainable PV energy conversion. A quantitative evaluation of the chlorophyll-based LSCs performance was corroborated by Monte Carlo ray-tracing simulations, indicating that the optical efficiency can still be maintained for larger devices.

The potential replacement of synthetic organic dyes by luminescent organic molecules extracted from renewable and natural materials could make LSCs cheaper and sustainable, keeping other inherent features such as synthetic versatility, high absorption coefficients and absolute emission quantum yields [125, 295]. As a matter of fact, previous studies proved the advantages and the possibility of using natural and renewable materials for energy harvesting [296] and, specifically, for LSCs [297]. The most common natural dyes used in LSCs are based on phycobilisomes. These are photosynthetic complexes, mainly composed of phycobiliproteins, with light-harvesting ability over a broad range of the visible spectrum and which concentrate the captured energy at the photosynthetic reaction centre [124, 126, 298]. Nevertheless, studies reporting natural dye molecules for LSCs are scarce. A recent example reports the use of BODIPY emitter covalently linked to oligofluorene and dispersed in lauryl

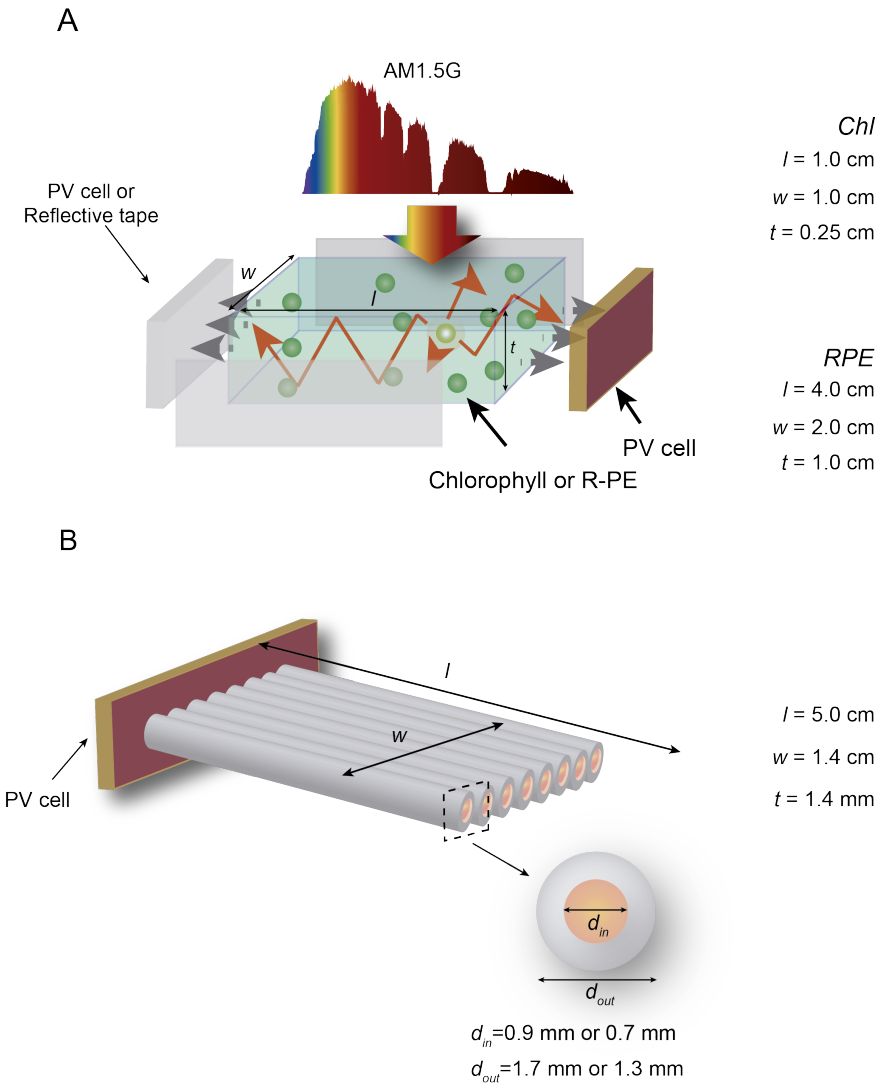

Figure 7.1: Representative scheme of the (A) planar Chl- and RPE-based LSCs attached to the c-Si PV cells and (B) bundle RPE-based LSC where different cylindrical POFs are stacked side by side.The arrows inside the LSC indicate total internal reflection of the emitted radiation. The dashed arrows represent the PV cells coupling or reflective tape region.

methacrylate and ethylene glycol dimethacrylate, which when coupled to Si PV cells yielded an EQE maximum value of 2.44 % [125]. Another p-LSC example is based on phycobilisomes dispersed in acrylamide films [124, 126], which presented $\eta_{opt} = 12.5\,\%$ [124]. In this study, the use of phycobilisomes in liquid medium confined in a glass cuvette was also tested, but considered disadvantageous due to the refractive index mismatch between the solution and the cuvette [126].

Several LSCs based on optically active centres dispersed in a liquid medium have been

proposed in literature [124, 126, 186, 208, 284, 299–304] but studies reporting LSCs performance quantification (η_{opt}, EQE or PCE) figures of merit are not abundant [206, 305, 306]. The maximum η_{opt} values were found for PbS QDs dispersed in toluene (η_{opt} = 12.6 %, considering collection along the four edges) [206] and for K_I organic dye dispersed in a liquid polymer (η_{opt} = 20.2 % for direct radiation) [303]. Very recently, an interesting work reporting temperature-responsive LSCs using a liquid crystal as host for a coumarine-derivative/perylene bisimide pair with η_{opt} = 2.4 % in the cold state and η_{opt} = 3.2 % when warmed was published, stating the potential for LSCs with liquid optically active layers [305]. Despite the advantages of bio-based dyes in liquid medium, only one report mentions the use of phycobilisomes in liquid medium for LSCs however, without mentioning any performance quantification [126].

Among the natural dyes, phycobilisomes are very promising since donor and acceptor molecules are already aggregated in an ideal configuration [126] and phycobiliproteins can be efficiently extracted, without compromising their conformational structure or chromophore structural integrity through a method already reported by some of us [245]. Moreover, R-phycoerythrin (R-PE), which is one of the most abundant phycobiliproteins in red macroalgae, has been pointed out as an important macromolecule in the field of medical diagnosis and biomedical research [307] due to its high absorption coefficient and absolute emission quantum yield [245]. Recently, laser effect was observed from R-PE from 602 to 620 nm with pulsed optical excitation in a Fabry-Pérot resonator [308].

In the second part of this chapter, we merge two complementary aspects towards enhanced performance sustainable LSCs devices: i) the use of R-PE, extracted from fresh *Gracilaria sp.* red algae and dispersed in an aqueous solution, ii) the exploit of the geometrical factor fabricating c-LSCs based on bundles of cylindrical hollow-core POFs, Figure 7.1B, and p-LSCs composed of a glass container, Figure 7.1A. The use of *Gracilaria sp.* algae takes advantage of local resources and markets. The fact of being dispersed in water makes this approach sustainable and without waste nor significant negative impact towards the environment. Different concentrations (0.4×10^{-7} to $17 \times 10^{-7}\,M$) of R-PE in aqueous solutions with high molar brightness (B) values (2.2×10^5 to $6.2 \times 10^5\,M^{-1} \cdot cm^{-1}$) were used to fabricate c-LSCs, Figure 7.1B, and p-LSCs, Figure 7.1A. Electrical measurements were performed in coupled c-Si PV devices, yielding maximum η_{opt} values of 5.55 ± 0.01 % (p-LSC) and 2.71 ± 0.01 %

(c-LSCs bundle), and PCE of $0.27 \pm 0.01\,\%$ (p-LSC) and $(23.03 \pm 0.01) \times 10^{-3}\,\%$ (c-LSCs bundle).

7.2 Chlorophyll based luminescent solar concentrators

Chlorophyll molecules extracted from Spirulina maxima, an abundant cyanobacteria and an attractive natural source, are immobilized in organic-inorganic di- and tri-ureasil matrice enabling the production of sustainable LSCs. At low chlorophyll concentrations ($< 3 \times 10^{17}$ molecules$\cdot cm^{-3}$), the photophysical properties of the chlorophyll molecules after incorporation into the hybrids closely resemble those in ethanolic solution (with an absolute emission quantum yield of ~ 0.16 and a fluorescence lifetime of $\sim 8\,ns$). The LSCs were coupled to a Si-based commercial PV device revealing η_{opt} and PCE values of $3.70 \pm 0.01\,\%$ and $0.10 \pm 0.01\,\%$, respectively, illustrating the potential of this approach for the development of natural-based LSCs meeting the requirements of reliable, sustainable and competitive energy systems.

7.2.1 Structural and optical characterization of the LSCs optically active layer

The local-structure of the chlorophyll-based organic-inorganic hybrids was studied by X-ray diffraction (XRD) and ^{29}Si magic-angle spinning (MAS) NMR spectroscopy. The XRD patterns (Figure 7.2) of the chlorophyll-related hybrids are analogous to that of the isolated d-U(600) [278, 309] and t-U(5000) [241, 247] hosts. The patterns show a broad band centred at 21.20° and 20°, respectively, associated with the presence of amorphous siliceous domains [240, 278, 310, 311]. The second order of these bands appears as an even broader weak hump around 39-44° [261]. Additionally, between 12 and 14° a shoulder is clearly discerned in all patterns. This feature has been ascribed to other intra-siloxane domains in-plane ordering with a characteristic distance of ca. $7.0\,\AA$. For the d-U(600) based hybrids a characteristics distance of $d = 4.2 \pm 0.2\,\AA$ and for the t-U(5000) based hybrids a distance of $d = 4.4 \pm 0.2\,\AA$ were estimated using the Bragg law [240, 241]. The fact that there are no significant changes in the patterns after incorporating the chlorophyll, suggests that the local structure of the hybrid host remains essentially unaltered.

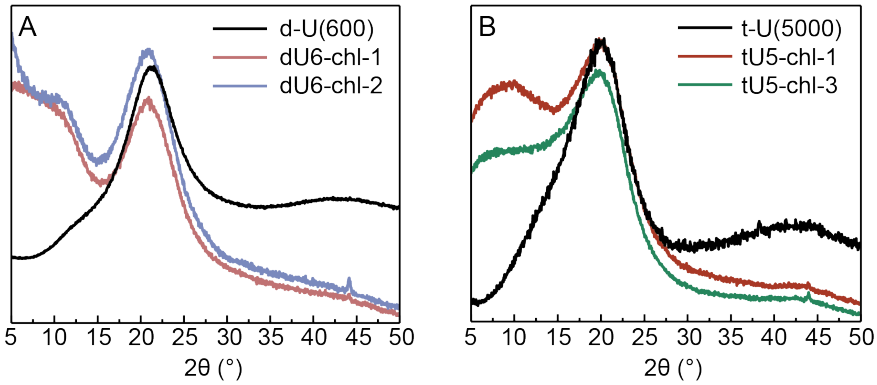

Figure 7.2: XRD patterns of (A) d-U(600)- and (B) t-U(5000)-based hybrids.

Furthermore,the ^{29}Si MAS NMR spectra of tU5-chl-1 and dU6-chl-2 (Figure 7.3) are very similar being dominated by characteristic peaks at −60.5 and −65.4 ppm, assigned to the $CH_2Si(OSi)_2(OR)$ (T^2) and $CH_2Si(OSi)_3$ (T^3) silicon environments [241, 247, 309]. For the d-U(600)-based hybrids another low-intensity peak at −57.6 from the $CH_2Si(OSi)(OR)_2$ (T^1) local sites is also discerned. The signals between ca. −90 and −130 ppm are assigned to $(\equiv SiO)_2Si(OH)_2$ (Q^2, geminal silanols), $(\equiv SiO)_3SiOH$ (Q^3, single silanol) and $(\equiv SiO)_4Si$ (Q^4, siloxane) local environments indicating the pre-hydrolysis of the t-UPTES(5000) and d-UPTES(600) precursor, respectively [277].

The fact that there are no significant changes in the XRD patterns and NMR spectra after incorporating the chlorophyll, suggest that the local structure of the organic-inorganic hosts, d-U(600) and t-U(5000), remained essentially unaltered after the inclusion of the chlorophyll molecules (Figure 7.2 and Figure 7.3) and revealing that ureasils are efficient hosts for dye molecules [156].

The interaction between the d-U(600) and t-U(5000) hosts and the chlorophyll molecules was further studied by ATR/FT-IR spectroscopy (Figure 7.4 and Figure 7.5). The intrinsic molecular electron density distribution in chlorophyll molecules is characterized by i) polar bonds to magnesium located at the chlorin ring; ii) few polar functional groups and iii) a hydrocarbon tail, thus, the interaction with the hybrids amide non-polar groups by means of London forces is expectable. In this sense, the analysis of ATR-FTIR focus on the amide I (1700-1600 cm^{-1}) and amide II (1600-1500 cm^{-1}) regions [239], Figure 7.4A. The hydrogen bonding in amide I and II regions arises from interactions between urea groups of different chains, and between bonded urea groups and the PEO chains [239]. The amide I region

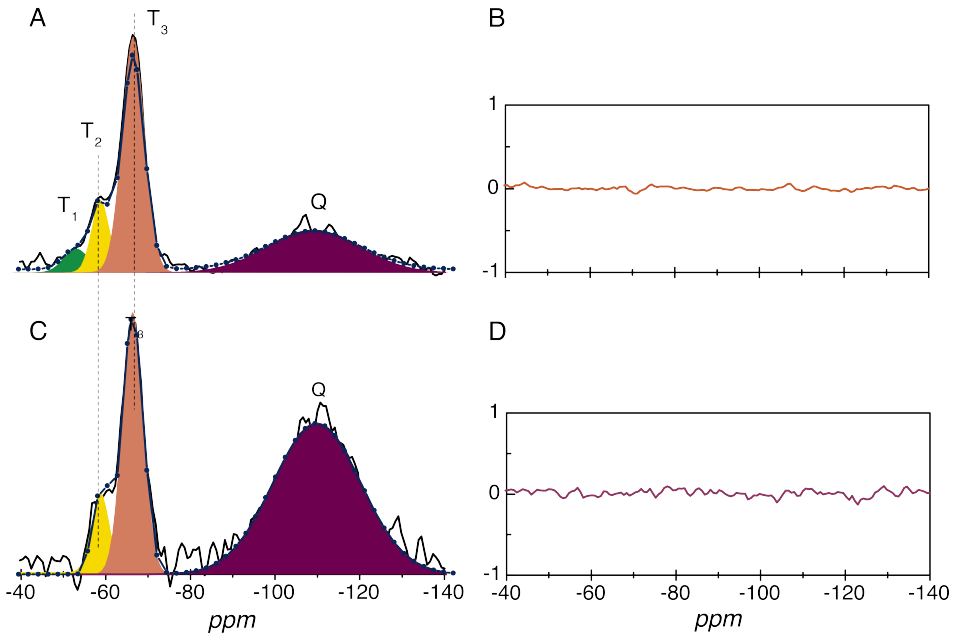

Figure 7.3: ^{29}Si MAS NMR spectra of (A) dU6-chl-2 and (C) tU5-chl-1. The spectral fitting using a sum of Gaussian functions (shadowed areas) are ascribed to T^1, T^2, T^3 and Q silicon environments, and the overall fit (circles) is also shown. (B,D) are the residual plot of the overall fits.

provides information about the degree of hydrogen bonding interactions, mainly associated with $\upsilon_{C=O}$ ($1637\,cm^{-1}$), Figure 7.4B and C, which are involved in more ordered hydrogen-bonded urea-urea associations [239]. The absence of the peak at $1750\,cm^{-1}$ in the chl-doped hybrids indicates there are no free urea groups (not associated by means of hydrogen bonds). After the incorporation of the chlorophyll, the position of the energetic peak of amide I remains constant ($1637\,cm^{-1}$), Figure 7.4B and C, indicating that the ureaurea aggregates are unaffected as the chlorophyll concentration increases [242]. However, a narrowing of the peak full-width-at-half-maximum (fwhm) is observed as the concentration of chlorophyll increases, Figure 7.4D. The larger variation of the fwhm in the t-U(5000)-based hybrids suggests a stronger interaction between the chlorophyll molecules with the t-U(5000) compared with that occurring with the d-U(600).

Focusing on amide II, the energy and fwhm of the dominant peak at $1560\,cm^{-1}$ remains unchanged, as the chlorophyll concentration increases in both hybrids (a negligible red-shift below $1.6\,cm^{-1}$ was detected for the d-U(600)-based materials). Thus, it can be concluded that chlorophyll (or pheophytin) molecules interact with oxygen atoms from the carbonyl

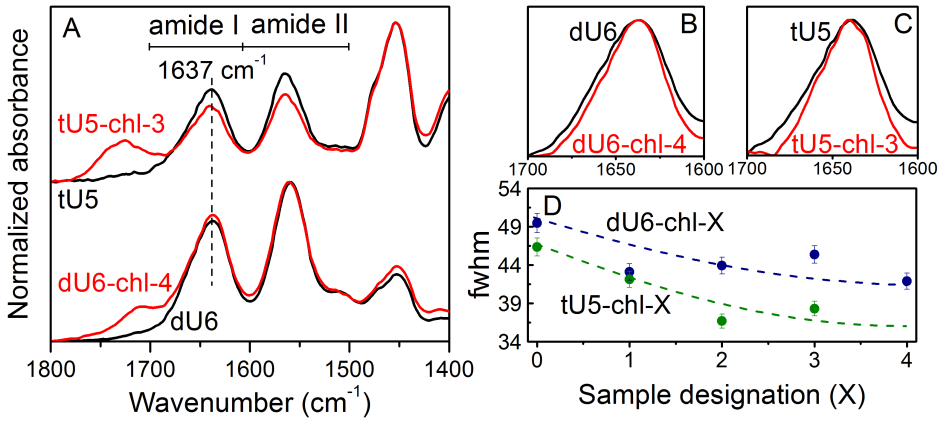

Figure 7.4: (A) ATR-FTIR spectra for d-U(600) and t-U(5000) hosts (black lines) and for selected chl-doped hybrids (red lines). (B) and (C) are amplifications of the amide I region. (D) Amide I fwhm peak as function of the chl concentration; the dashed lines are visual guides.

groups, which also leads to a reorganization of hydrogen bonds in the amide I environment [242], in which the observed narrowing, Figure 7.4D, can be associated to a more organized environment induced by the chlorophyll incorporation.

The predominant interaction of the chlorophyll molecules with the oxygen atoms of the urea groups rather than with those from the PEO chains is also inferred from the ATR/FT-IR spectra acquired at lower frequencies (Figure 7.5). In this energetic region, the transitions are associated mainly to the PEO chains, namely at 1350 cm^{-1} (ω_{CH2}), 1250-1195 cm^{-1} (τ_{CH2}), to the siliceous nanodomains at 1083 $cm{-}1$ (υ_{CO},υ_{SiOSi} for SiO_2 clusters) and polar groups attached to the chlorin ring of chlorophyll and pheophytin at 1031 cm^{-1} (υ_{CO} and υ_{COCH3}) and 918 cm^{-1} (υ_{CC} and ρ_{CH2}). Apart from a minor blue-shift ($\sim 7\,cm^{-1}$) of the maximum frequency of the peak at 1083 cm^{-1} and a decrease in the relative intensity between this peak and that at 918 cm^{-1} for d-U(600), no significant changes are observed after the chlorophyll incorporation.

Figure 7.5A,B shows the ATR/FT-IR spectra for selected chlorophyll-based hybrids and those of the undoped d-U(600) [239] and t-U(5000) [241] are also presented to render easier the analysis. Range (A,B) includes υ_{NH} hydrogen-bonded amide II×2 (3350 cm^{-1}), $\upsilon_a CH_3$ (2965 cm^{-1}), $\upsilon_a CH_2$ (2920 cm^{-1}) and $\upsilon_s CH_3$ (2870 cm^{-1}); range (C,D) includes transitions associated to ketone, propionate and carbomethoxy $\upsilon_{C=O}$ (1712 cm^{-1}) from chlorophyll and pheophytin, $\upsilon_{C=O}$ amide I (1637 cm^{-1}), δNH amide II (1560 cm^{-1}), δCH2, δCH3 (1453 cm^{-1})

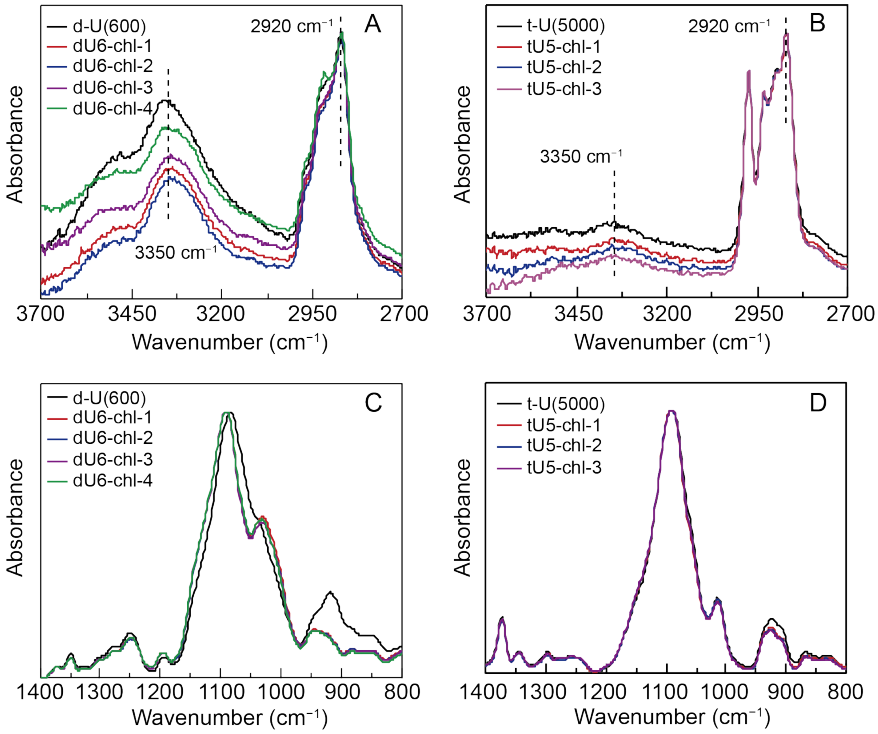

Figure 7.5: ATR/FT-IR spectra for (A,C) d-U(600) and (B,D) t-U(5000) hybrids doped and undoped with chlorophyll extract, over different ranges.

and δCH from phytol (1470-1460 cm^{-1} - C_{20} hydrocarbon tail from chlorophyll and pheophytin) [312]. Figure 7.3 (C,D) includes transitions associated mainly to PEO chain, such as 1350 cm^{-1} (ω_{CH2}), 1250-1195 cm^{-1} (τ_{CH2}); siliceous nanodomains, 1083 cm^{-1} (υ_{CO}, υ_{SiOSi} for SiO_2 clusters) and polar groups attached to the chlorin ring of chlorophyll and pheophytin, 1031 cm^{-1} (υ_{CO} and υ_{COCH3}) and 918 cm^{-1} (υ_{CC} and ρ_{CH2}). The analysis of the range (A,B) shows that the t-U(5000) host presents very low hydrogen bonding interactions for amide II groups, once the relative intensity of the peak at 3350 cm^{-1} to the group of peaks centred at $\sim$ 2920 cm^{-1} (corresponding to vibrations of CH_2 and CH_3 PEO groups) is much lower than for the d-U(600) host. Person *et al.* [313] have demonstrated that the reduction in intensity of this mode (and sometimes also in frequency), may be correlated with a decrease in hydrogen-bonding strength. This would imply that the hydrogen bonds in t-U(5000) are weaker than in d-U(600). It seems such feature is correlated to the length of the PEO chain [239].

The light-harvesting ability of all the chlorophyll-based hybrids was studied by absorp-

tion spectroscopy, Figure 7.7A. To enable an accurate interpretation, the same analysis was performed for the isolated chlorophyll molecules by diluting a Spirulina maxima extract in ethanol, as illustrated in Figure 7.6.

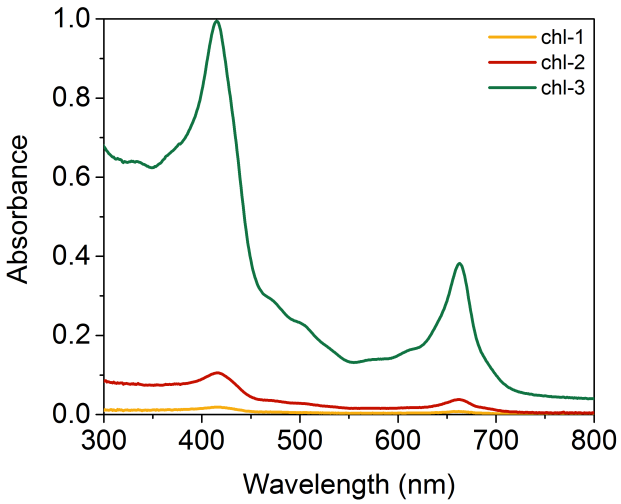

Figure 7.6: Absorption spectra of ethanolic solutions of chlorophyll with concentration values of 3×10^{16} (chl-1), 3×10^{17} (chl-2) and 3×10^{18} molecules$\cdot cm^{-3}$ (chl-3).

The *Spirulina maxima*-related spectrum reveals two main components at 415 nm and 665 nm ascribed to the monomer form of chl-a, and two shoulders around 465 nm and 648 nm attributed to the contribution of chlorophyll b (chl-b) monomers, Figure 7.7A. The larger relative intensity of chl-a, compared with that of chl-b points out a larger concentration of the chl-a species. The two main absorption bands of chl-a are ascribed to $\pi - \pi^*$ transitions, where the high-energy component in the blue region (415 nm) is termed a Soret band, and the low-energy one in the red spectral range (648 nm) is ascribed to the $S_0(0) - S_1(0)$ transition [314, 315].

After the incorporation of the *Spirulina maxima* extract into the hybrid hosts, the spectra reveal minor changes, when compared with those of the solutions, as illustrated in Figure 7.7A for selected hybrid materials. Such minor changes can be correlated to the acid environment, to which the precursor suspensions were submitted over the course of acid catalysed sol-gel transition. A slight blue shift is observed for the maximum wavelengths of the UV-Vis peaks in the spectra of the chlorophyll extract, assigned to the conversion of chl-a to pheophytin-a, when the porphyrinic Mg^{2+} is replaced by two H^+ at low pHs [316]. The spectra are clearly

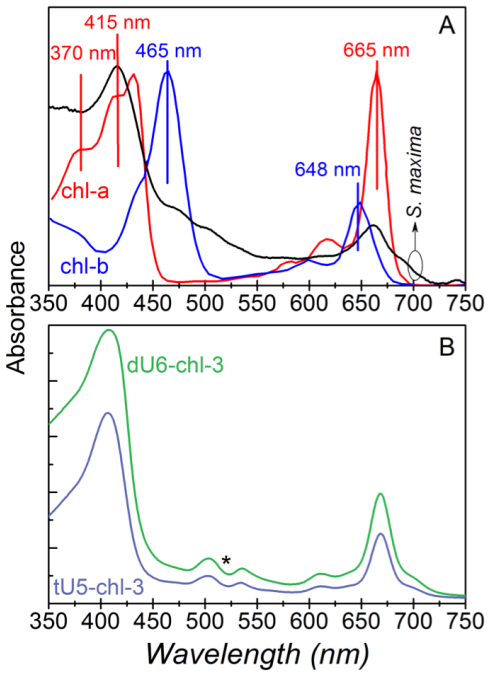

Figure 7.7: Absorption spectra of (A) chl-a, chl-b [315], and chlorophyll extract in an ethanolic solution [$10^5\,M$] and of (B) tU5-chl-3 and dU6-chl-3.

dominated by the chl-a contribution, reinforcing that the chlorophyll extracts are mainly from chl-a. Whilst for the Soret band a blue shift of $\sim 474\,cm^{-1}$ ($\sim 8\,nm$) is detected; the $S_0(0) - S_1(0)$ transition broadens and deviates towards the red $159\,cm^{-1}$ ($7\,nm$) for both hybrid hosts, with respect to the absorption spectrum of the chlorophyll extract solution. This red-shift of the $S_0(0) - S_1(0)$ transition points out the formation of dimers [314, 317] and the emission broadening observed after the incorporation of the chlorophyll in the hybrids is probably related to changes in local structure of the chlorophyll molecules due to the rigidity of the host [241], as demonstrated by ATR/FT-IR, Figure 7.4. The absorbance around $615\,nm$ can be ascribed to the presence of dimers in solid state. We note the presence of excited states within 450-550 nm (marked with an asterisk in Figure 7.7B), most likely due to the presence of carotenoids as contaminants [318].

When excited within the region of the absorption spectra, the emission of the chlorophyll-based hybrids is visible to the naked eye in the red spectral range, Figure 7.8.

To discern the contribution of chl-a and chl-b, the fluorescence spectra of the ethanolic solution with *Spirulina maxima* extract incorporated into the hybrids were compared with those arising from ethanolic diluted solutions containing only chl-a and chl-b molecules, Figure

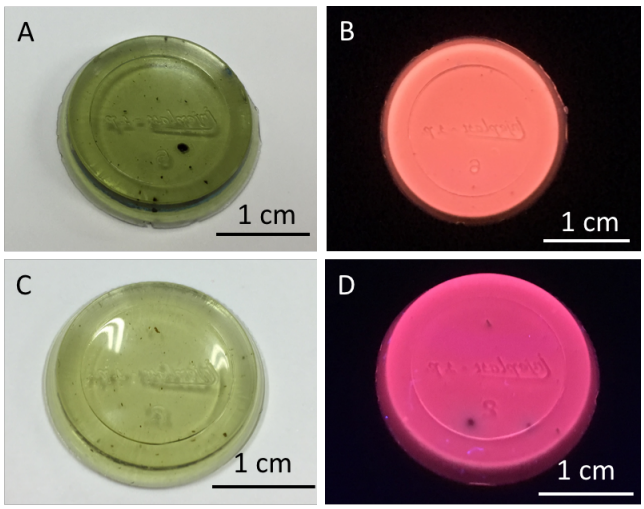

Figure 7.8: Photographs of (A,B) dU6-chl-3 and (C,D) tU5-chl-3 under (left) white light and (right) UV illumination at 365 nm.

7.9A and B.

In good agreement with that suggested by absorption spectroscopy measurements, the emission spectra of the *Spirulina maxima* extract resemble those of chl-a, whose emission peak lies at around 675 nm. We note that the typical emission of chl-b around 650 nm is not discerned. The broadening of the chl-a emission spectrum for the case of *Spirulina maxima* suggest that chl-a experiences distinct microenvironments in the extract [319]. After the extract incorporation into the hybrids, the emission spectra depend on the chlorophyll concentration, Figure 7.9B. For the less concentrated samples, the room-temperature emission spectra are dominated by the overlap between the blue-green emission attributed to electron-hole recombination occurring in the urea groups and within oxygen defects in the siliceous skeleton of the hosts [278, 280] and the chl-a fluorescence peak in the red spectral region [314], as illustrated in Figure 7.9B.

Increasing the chlorophyll concentration, the relative intensity of the hybrid host emission decreases, Figure 7.9B, suggesting the presence of efficient hybrid-to-chlorophyll energy transfer since more molecules are located near the hybrids emitting centres, as suggested by ATR/FT-IR data, Figure 7.4. This means that there is a higher number of amide-based emitting centres transferring energy to the chlorophyll molecules, thus contributing to a continuous decrease of the hybrids radiative transitions. The emission spectra for the lowest concentrated sample, Figure 7.10, make it obvious that the t-U(5000)-based samples show

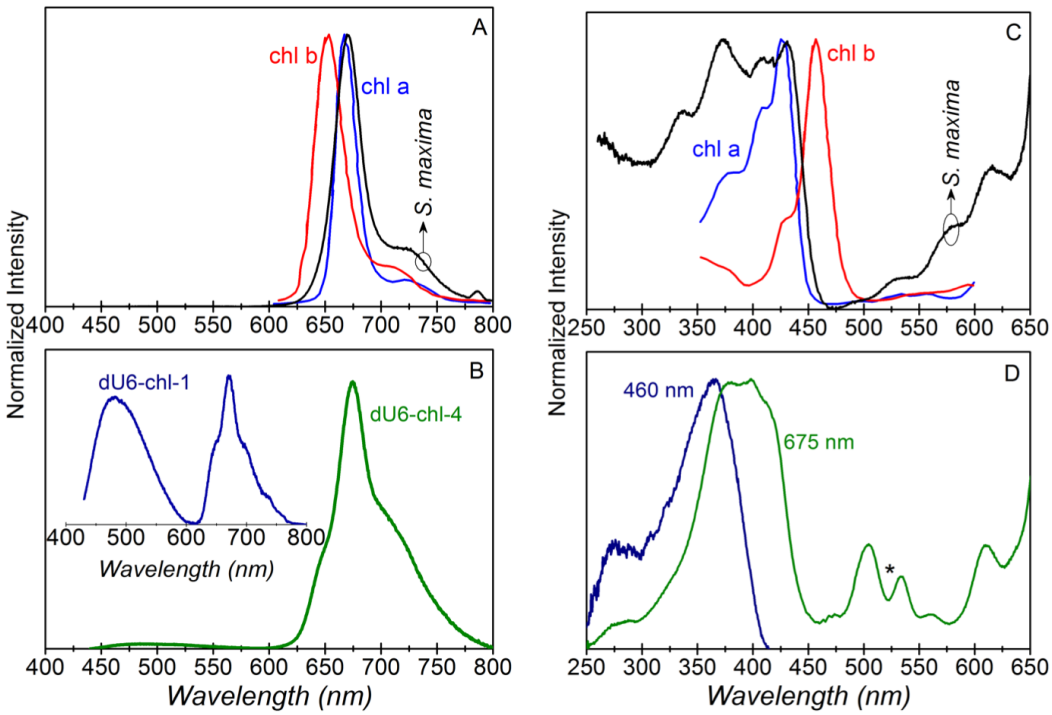

Figure 7.9: Emission spectra of (A) chl-a and chl-b in diluted $[10^{-5}\,M]$ ethanolic solution from [320, 321] and chlorophyll extract and (B) dU6-chl-4 and dU6-chl-1 excited at $360\,nm$. Excitation spectra of (C) chl-a and chl-b in diluted $[10^{-5}\,M]$ ethanolic solution from [322] and chlorophyll extract and (D) dU6-chl-4 monitored at $460\,nm$ and $675\,nm$.

a more efficient energy-transfer process between the host and the chlorophyll molecules that the d-U(600)-based ones, in good agreement with the ATR/FT-IR analysis, Figure 7.4, that suggests a larger chlorophyll interaction over amide groups in t-U(5000)-based hybrids compared with the d-U(600) ones. The presence of two distinct chl-a related components ($675\,nm$ and $720\,nm$) in all the emission spectra points out the formation of aggregates in the solid state, Figure 7.9B, and Figure 7.10) [317]. Also, by increasing chlorophyll concentration it is possible to observe a red-shift in the emission peak, relatively to the absorption spectrum, suggesting the presence of J-dimers [323], Figure 7.10.

Focusing our attention on the chlorophyll related emission, it is noticeable the presence of a main component at $675\,nm$ and a shoulder at $720\,nm$ is noticeable, and ascribed to the chl-a monomeric and dimeric contributions, respectively [314, 324]. Another component is present at $645\,nm$ (most evident for the d-U(600)-based samples), see Figure 7.10, is also ascribed to microenvironments of chl-a emission [320]. Lowering the temperature to $11\,K$, whereas

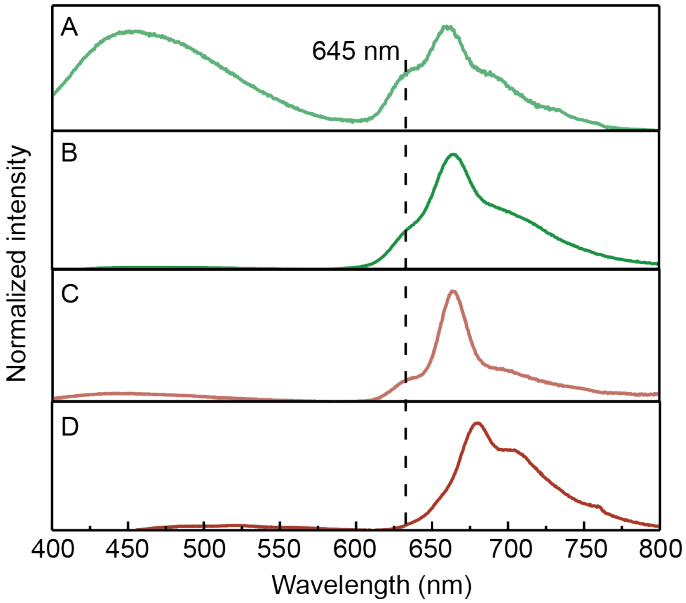

Figure 7.10: Room temperature emission spectra of (A) dU6-chl-1, (B) dU6-chl-4, (C) tU5-chl-1 and (D) tU5-chl-4 excited in the blue region (410-435 nm).

for the d-U(600)-based samples, the spectra are dominated by the host contribution, for the t-U(5000), apart from an increase in the relative intensity of the hybrids intrinsic emission, the spectra are analogous to those acquired at 300 K, Figure 7.11.

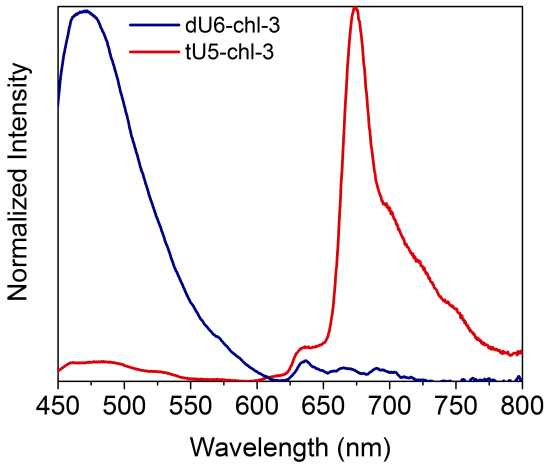

Figure 7.11: Emission spectra (11 K) of dU6-chl-3 and tU-chl-3.

Comparing the absorption and the emission spectra of the chlorophyll solutions the Stokes-shift is 314 cm^{-1} (14 nm), Figure 7.12. Upon the incorporation of the chlorophyll in the d-U(600) and t-U(5000), there is a decrease in the Stokes-shift to values below 66 cm^{-1} (3 nm)

and 133 cm^{-1} (6 nm) for the t-U(5000) and d-U(600) based samples, respectively, Figure 7.12, tentatively attributed to an increase in the rigidity of the chromophore environment that excludes non-fluorescent relaxation to a ground state [325, 326]. Although the Stokes-shift for the hybrids-based samples is significantly lower than that measured for the chlorophyll solutions, Figure 7.12, the Stokes-shift increases with increasing concentration for both hybrids, indicating that greater intermolecular interactions are occurring between the hybrid and the chlorophyll chromophore molecules.

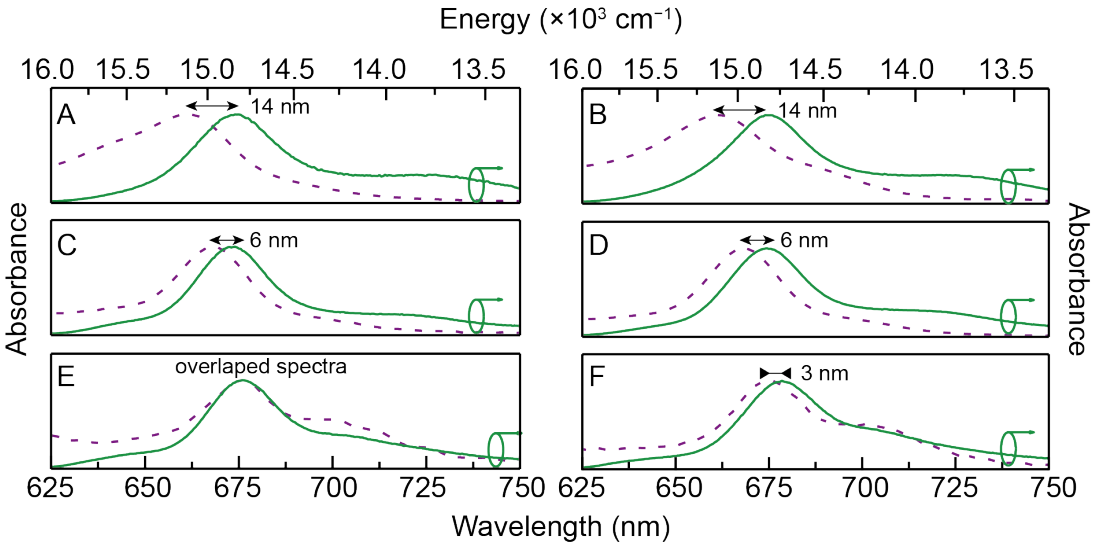

Figure 7.12: Room temperature absorption (purple dashed line) and emission spectra of (A) chl-2, (B) chl-3, (C) dU6-chl-2, (D) dU6-chl-3, (E) tU5-chl-2 and of (F) tU5-chl-3 excited at 415 nm.

Figure 7.9C,D show the excitation spectra of an ethanolic diluted solution of chl-a and chl-b and the excitation spectrum of an ethanolic solution with Spirulina maxima extract. All the spectra resemble the absorption spectra, Figure 7.7, revealing essentially the main bands ascribed to chl-a excited states. Figure 7.9D illustrate the typical excitation spectrum monitored within the chlorophyll maximum emission peak (675 nm) and within the hybrid emission band (460 nm). The former reveals the characteristic bands of chl-a, as already noticed in the absorption spectrum, Figure 7.7B, despite a minor blue-shift when compared with the excitation spectrum of the solution of chlorophyll extract, Figure 7.9C and Figure 7.13.

Moreover, we note that the contribution of the hybrid host excited states to chlorophyll-related emission cannot be neglected as the excitation spectrum monitored within the host

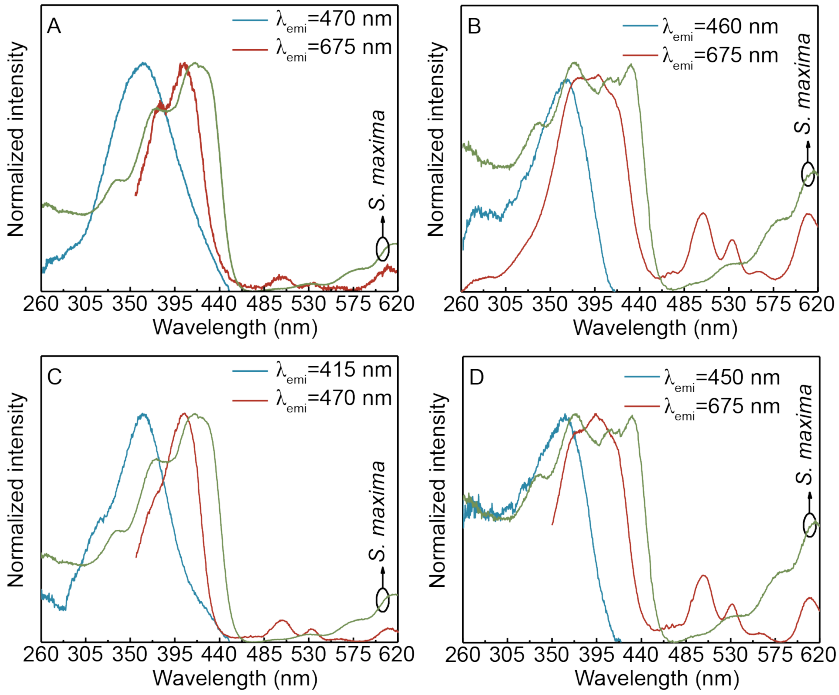

Figure 7.13: Room temperature excitation spectra monitored at different wavelengths for (A) tU5-chl-1, (B) dU6-chl-4, (C) tU5-chl-1 and (D) dU6-chl-4. The spectra for the ethanolic solutions (A,C) chl-1 [$10^{-5}\,M$] and (B,D) chl-4 [$10^{-2}\,M$] are also shown.

emission broad band overlaps with that monitored within the chl-a band, in particular in the UV spectral region (250-400 nm). When the excitation spectrum is monitored within the hybrid emission band (460 nm) the hybrid-related excited states appear as expected for both d-U(600) and t-U(5000), Figure 7.13, showing excitation maxima peaking between 350 nm and 370 nm, depending on the monitoring wavelength [241, 278]. The presence of the hybrid states in this spectral region are in good agreement with the hypothesis of hybrid-to-chlorophyll energy transfer. The excitation spectra of both chlorophyll-based hybrids remain practically unchanged when the concentration varies, apart from minor changes in the relative intensities, Figure 7.13.

Further evidence of hybrid-to-chlorophyll energy transfer was found by time-resolved fluorescence measurements of chlorophyll solution incorporated in both hybrids, namely, through the calculation of the fluorescence lifetime for selected samples. The emission decay curves were selectively monitored for the hybrid host (445 nm) and the chl-a excited states at 675 nm. In all cases, the experimental curves are well described by single exponential functions, Figure 7.14.

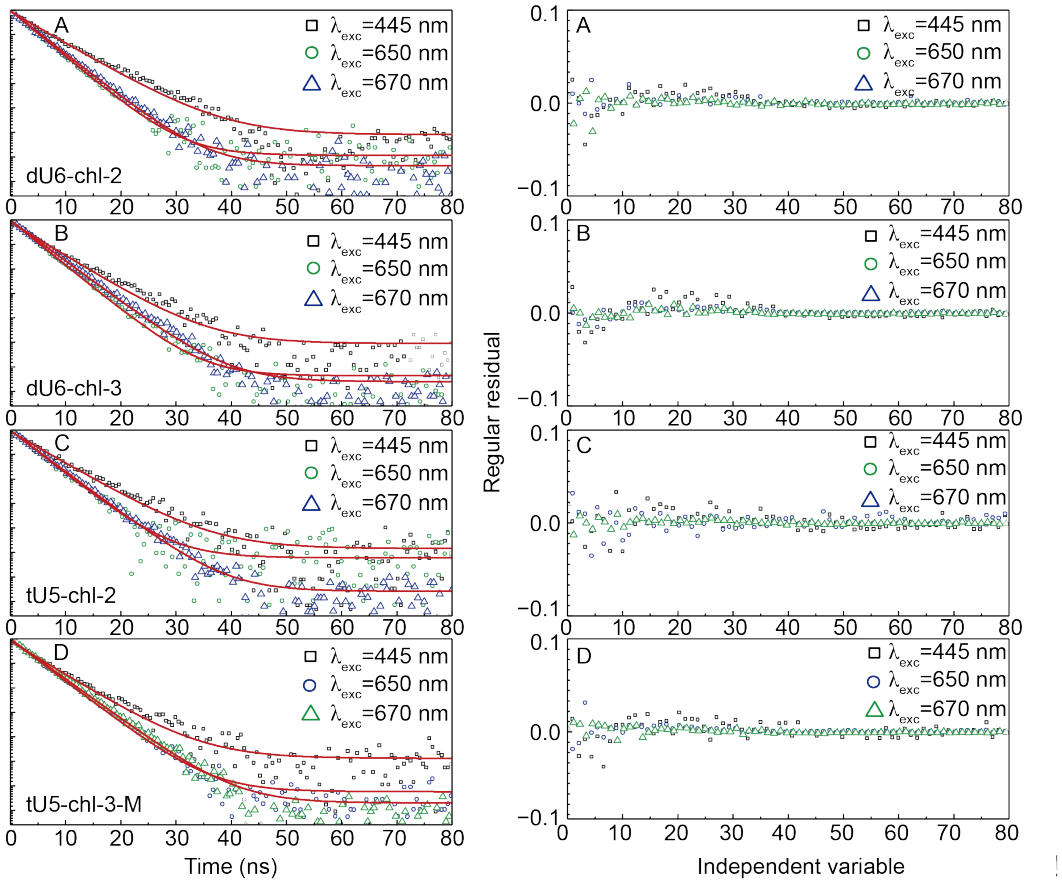

Figure 7.14: Room temperature emission decay curves of (A) dU6-chl-1, (B) dU6-chl-3, (C) tU5-chl-1 and (D) tU5-chl-3 excited at 390 nm and monitored at 455 nm, 640 nm and 675 nm. The solid lines represent the best fit to the data ($r^2 > 0.99$) using a single exponential function. The respective residual plots are shown on the right-hand side.

The lifetime values monitored within the hybrids emission band, Table 7.1, are lower than those previously reported for the isolated hybrids d-U(600) ($\sim$ 2-15 $\times$ 10^{-9} s) [327] and t-U(5000) (30.2 $\pm$ 0.2 $\times$ 10^{-9} s) [241]. Moreover, the lifetime values obtained monitoring the chlorophyll emission band are similar, Table 7.1, to those previously reported for chl-a in ethanolic solutions (6.1 $\pm$ 0.2 $\times$ 10^{-9} s) [319]. The decrease in the lifetime of the hybrid host excited states is in good agreement with the hybrid-to-chlorophyll energy transfer [261]. Moreover, we also note that the hybrids lifetime values slightly decrease (5-6 %) as the concentration increases from dU6/tU5-chl-2 to dU6/tU5-chl-3, Table 7.1, suggesting an increase in the non-radiative transition probability at higher chlorophyll concentrations.

The emission properties were further quantified through the measurement of the absolute emission quantum yield (q, Table 7.2), as function of the excitation wavelength (360-530 nm)

Table 7.1: Emission lifetime values ($\tau \pm 0.1$, $10 \times^{-9} s$) of the chlorophyll-based hybrid materials excited at $390\,nm$ and monitored at distinct wavelengths (λ_e, nm)

λ_e (nm)	dU6-chl-2	dU6-chl-3	tU5-chl-2	tU5-chl-3
445	7.6	7.2	7.6	7.2
650	5.3	5.4	5.6	5.8

and of the chlorophyll concentration. For all samples, the absolute emission quantum yield is higher when the excitation wavelength is resonant with the chl-a Soret band (370 and 410 nm). However, at higher chl-a concentrations (dU6/tU5-chl-4), the absolute emission quantum yield values are very similar, within the experimental error, and maximal (0.16 ± 0.02) for the tU5-chl-2. This value is analogous to that measured for the chlorophyll diluted solution, pointing out that the incorporation in t-U(5000) and d-U(600) did not contribute to an emission quenching and that the optical properties of the extract are well preserved in the solid state (at the concentration values in analysis). We note that, despite analogous absolute emission quantum yield values, as the concentration increases from samples dU6/tU5-chl-1 to dU6/tU5-chl-3, the relative intensity of the chlorophyll-emission with respect to that of the hybrid host is larger, Figure 7.9B. Therefore, featuring PV-related applications, samples with a larger contribution of chlorophyll emission (dU6/tU5-chl-2 or dU6/tU5-chl-3) are preferred as low energy photons (chlorophyll emission compared with those from the hybrid) coincide with larger Si-based PV devices efficiency.

When the concentration is increased, the absolute emission quantum yield values of the dU6-chl-4 and tU5-chl-4 samples decrease to 0.03 ± 0.01 and 0.05 ± 0.01, respectively. Nevertheless, these absolute emission quantum yield values are larger than those found in the solution with the same concentration (0.02 ± 0.01), indicating that at higher chlorophyll solution concentrations the hybrid hosts may prevent partial dye agglomeration. The strong quenching of the absolute emission quantum yield for the more concentrated samples means these are not viable for use in LSCs.

Focusing our attention on the less concentrated samples and aiming at selecting the chlorophyll-based hybrids with larger potential to maximize the performance of LSCs, Figure 7.15A, it is relevant to quantify the light harvesting ability [119], by the overlap integral given by Eq. 2.12 [156]. The spectral overlap is illustrated in Figure 7.15B (shadowed area). The

Table 7.2: Integral overlap (O, $\times 10^{20}$ photons$\cdot s^{-1} \cdot m^{-2}$), absolute emission quantum yield (q), molar extinction coefficient (ε, $\times 10^5\, M^{-1} \cdot cm^{-1}$) and brightness ($B$, $\times 10^4\, M^{-1} \cdot cm^{-1}$) of the chlorophyll-based organic-inorganic hybrids. The subscript indexes in q, ε and B indicate the wavelength (nm).

	O	q_{370}*	q_{410}*	ε_{370}	ε_{410}	B_{370}	B_{410}
dU6-chl-1	-	0.11	0.12			-	
dU6-chl-2	3.0	0.12	0.08	2.7	2.2	3.3	1.8
dU6-chl-3	7.3	0.07	0.07	1.1	1.5	0.8	1.1
dU6-chl-4	-	0.03	0.03			-	
tU5-chl-1		0.09	0.014				
tU5-chl-2	2.0	0.10	0.16	1.5	1.9	1.5	3.0
tU5-chl-3	5.3	0.09	0.15	0.8	1.4	0.7	2.1
tU5-chl-4	-	0.04	0.05			-	

*The absolute emission quantum yield error is 10 %.

maximum value was calculated for dU6-chl-3, as listed in Table 7.2, indicating a potential to absorb 17 % of the solar photon flux on the surface of the Earth (4.3×10^{21} photons$\cdot s^{-1} \cdot m^{-2}$) [5]. The observed increment of O as the concentration increases results from the larger absorbance measured at higher concentrations.

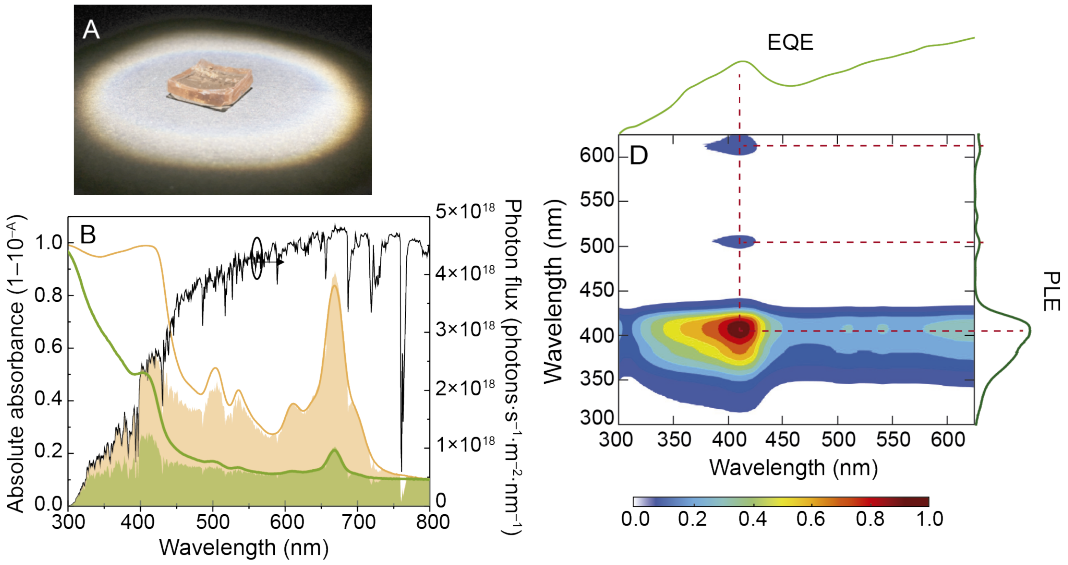

Figure 7.15: (A) Photograph of dU6-chl-3 LSC ($1 \times 1\, cm^2$) under AM1.5G illumination. (B) Absorption spectra (left axis) for dU6-chl-2 (green line) and dU6-chl-3 (orange line) and AM1.5G photon flux (right axis); the shadowed area represents the overlap integral O; (C) 2D-cross correlation between the EQE (%) and the excitation spectrum (PLE, a.u.) intensity for dU6-chl-2.

Further quantification of the light harvesting ability can be performed using the Beer-Lambert law, to calculate the molar extinction coefficient (ε, $M^{-1} \cdot cm^{-1}$), where the chl-a concentration was estimated following a methodology described elsewhere [328]. The values were quantified for the *Spirulina maxima* extract in ethanolic solution and after the incorporation in the hybrids, Table 7.2. The values found for the ethanolic solutions resemble those previously reported ($7.0 \times 10^4\, M^{-1} \cdot cm^{-1}$, at $665\, nm$), Table 7.3. After the chl-a incorporation in the hybrid, despite a small decrease in the molar extinction coefficients at $665\, nm$, Table 7.3, there is an increase in the UV spectral region ascribed to the contribution of the hybrid host excited states in the UV.

Table 7.3: Molar extinction coefficient (ε) at $665\, nm$ for chlorophyll ethanolic solutions and chlorophyll-doped hybrids.

Designation	ε ($\times 10^4\, M^{-1} \cdot cm^{-1}$)
chl-2	6.9
chl-3	6.9
dU6-chl-2	3.7
dU6-chl-3	5.7
tU5-chl-2	3.5
tU5-chl-3	4.7

Refractive index dispersion curves and thickness (10-13 $\times 10^{-6}\, m$) of the films were measured by spectroscopic ellipsometry, Figure 7.16. The reported values for the thickness and refractive index are the average of three measurements performed for each sample with a maximum standard deviation of 1 %, see Table 7.4. These films were only used to ensure the refractive index of the materials as will be shown later.

Another relevant parameter for LSC performance is the trapping efficiency (η_t) that accounts for emission losses at the surface [136]. The η_t values depends on the refractive index (n) of the optically active layer at the emission wavelength. The trapping efficiency can be calculated from the dispersion curve data in Figure 7.17, using Eq. 2.2, considering n_p at the emission wavelength (in this case, $670\, nm$). This parameter determines the fraction of photons confined within the substrate, accounting for the emission losses at the surface through a so-called escape cone with an aperture angle $\theta_c = 2 \times sin^{-1}(1/n_p)$. Attending to

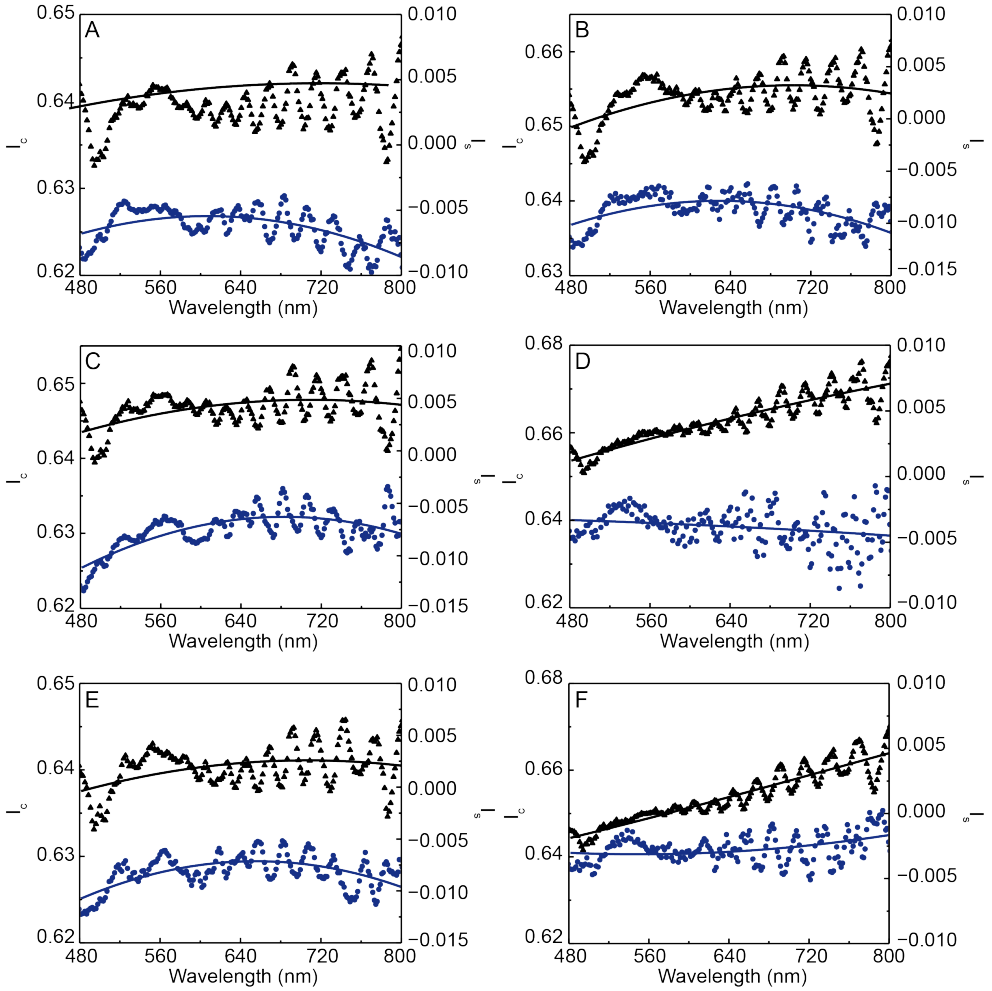

Figure 7.16: Ellipsometric parameters I_c (black triangles) and I_s (blue circles) measured for the active layer of (A) d-U(600), (B) t-U5000, (C) dU6-chl-2, (D) tU5-chl-2, (E) dU6-chl-3, (F) tU5-chl-3; the lines represent the best data fit ($r^2 > 0.9$).

Table 7.4: Thickness values of the films prepared by spin-coating on a glass substrate.

Designation	Thickness ($\times 10^{-6}\, m$)
d-U(600)	10.650 ± 0.107
dU6-chl-2	11.200 ± 0.112
dU6-chl-3	10.900 ± 0.109
t-U(5000)	12.200 ± 0.122
tU5-chl-2	13.500 ± 0.135
tU5-chl-3	12.900 ± 0.129

the dispersion curves of the chlorophyll-based hybrids, ($1.49 < n < 1.50$ at $675\,nm$), trapping efficiency values 75 % are predicted, Figure7.17.

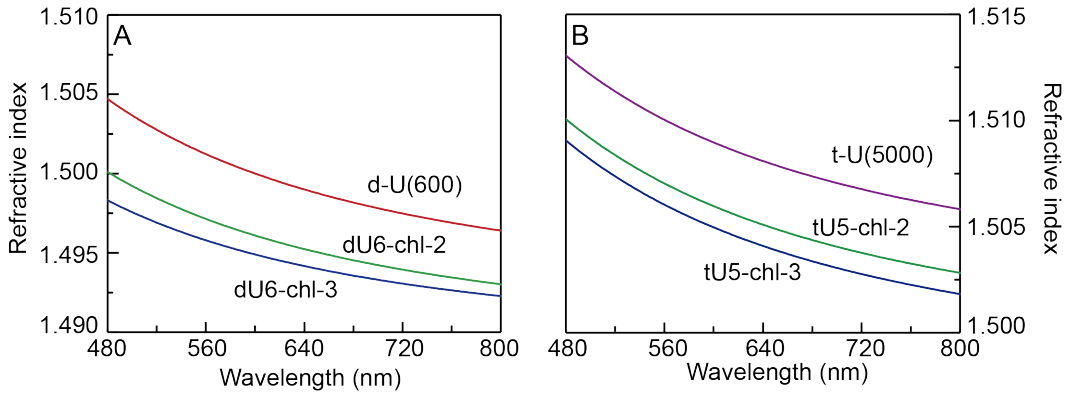

Figure 7.17: Dispersion curve of the refractive index for the (A) d-U(600) and (B) t-U(5000) based samples.

The B values were calculated for the hybrids with larger q values, Table 7.2, and are analogous to those reported for other organic-dye molecules, with radiation emission in the 530-650 nm range [329, 330]. We note a decrease of B as the concentration of chl-a increases for both ureasil hosts, mainly due to the concentration quenching.

Based on the results, dU6-chl-2, was selected to be tested as planar LSCs ($1.0\times1.0\times0.3\,cm^3$ and geometrical gain, $G = 3.3$) because it combines larger B values with higher integral overlap at lower chlorophyll concentration doping, Table 7.2. The LSC performance was quantified by $\eta_{opt} \pm \Delta\eta_{opt}$ through Eq. 2.14 and Eq. 2.19, yielding $\eta_{opt} = 3.70 \pm 0.01$ % and $\eta_{opt} = 5.55 \pm 0.01$ %, respectively, in the total incident spectral range.

In an attempt to compare these values with those in the literature, care must be taken, in what concerns the LSC geometry, emitting range and the use of external devices to enhance LSC performance, as all these aspects directly contribute to η_{opt}. We note that considering single planar red/NIR emitting LSCs without back-reflectors, the value from Eq. 2.14 can only be directly compared with that reported for the t-U(5000)/SiNc LSCs ($\eta_{opt} = 1.50 \pm 0.01$ %) [156], as a similar definition was used to estimate η_{opt}, Table 7.5. In what concerns the η_{opt} derived from Eq. 2.19, it has been used to quantify the performance of visible (blue, green or red)-emitting devices based on organic synthetic dyes, Table 7.5. Independently of the followed η_{opt} definition, the results here highlight the potential of the chlorophyll-based hybrids as a sustainable alternative for LSCs.

Table 7.5: Emission peak wavelength ($\lambda_e m$, nm) and η_{opt} (%) of red/NIR emitting LSCs based on dyes and QDs embed in distinct hosts. η_{opt} values calculated from [a] Eq. 2.14, [b] Eq. 2.19, [c] Integrating sphere and [d] no definition is mentioned. PMMA=poly(methyl methacrylate); DCJTB=4-(dicyanomethylene)-2-tert-butyl-6-(1,1,7,7-tetramethyljulolidin-4-yl-vinyl)-4H-pyran; LR305= Lumogen F-Red 305; PLMA=poly(lauryl methacrylate).

Materials	$\lambda_e m$	η_{opt}	Reference
dU6/chl-2	675	3.70^a 5.55^b	this work
tU5/SiNc	780	1.5^a	[156]
PMMA/Coumarin 6	502	6.7^b	[331]
Epoxy/Coumarin 6		7.4^b	
PMMA/DCJTB	555	3.84^b	[210]
PMMA/LR305	610	2.77^b	[232]
		4.8^b	[332]
dU6/LR305		9.2^c	[155]
PLMA/CISeS-ZnS QDs	840	3.27^d	[172]
PLMA/Si QDs	815	2.85^d	[232]

Measurements performed in an LSC aged during 7 months under ambient conditions show no variation in its performance. Moreover, the photo stability of the LSC was also assessed by measuring the I_{SC}^L under continuous AM1.5G illumination ($1000\,W \cdot m^{-2}$). The temporal relative variation of the short-circuit current reveals that the LSC is stable with a minor relative variation ($\Delta I_{SC}^L / I_{SC}^L \sim 1\%$) after $40\,h$, Figure 7.18. An analogous result demonstrating the ability of the organic-inorganic hybrid hosts to efficiently incorporate and stabilize organic dyes and lanthanide-based organic complexes for LSC applications was already reported [159].

The active role of the chlorophyll-based LSC in enhancing PV device performance was inferred from the calculation of the EQE, Eq. 2.22, on the PV device in the presence of the LSC. As can be noticed in Figure 7.15C, the EQE dependence on the wavelength correlates well with the excitation spectrum of the active layer. For the LSC based on dU6-chl-2, the EQE variation is more noticeable in the UV/blue region between 300 and $440\,nm$ (EQE= $0.2022 \pm (2 \times 10^{-4})\,\%$), benefiting from the fact that in the UV/blue spectral range, the Si PV device has lower performance. Also, in that region the chlorophyll-based hybrids display

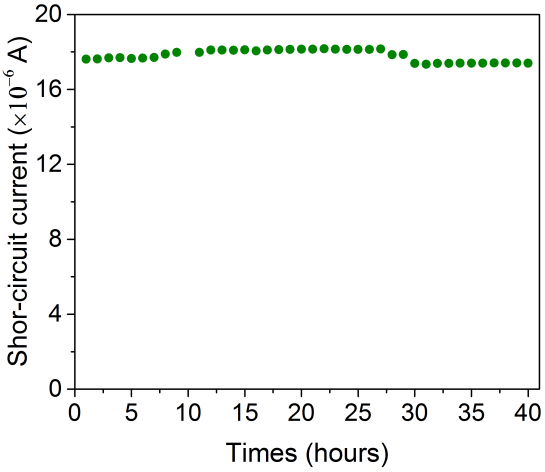

Figure 7.18: Temporal relative variation of the short-circuit current of dU6-chl-2.

larger sunlight harvesting and conversion efficiency, Table 7.2.

The effective contribution of the LSCs on the PV device was further quantified by coupling the LSC to a Si-based PV device and calculating the PCE Eq. 2.21, yielding PCE= 0.10 ± 0.01 % and confirming that the use of chlorophyll-based LSCs as external devices for Si-based PV devices is advantageous. The highest value for PCE involving single planar LSCs coupled to Si-based PV devices (c-Si) without back-reflectors was reported for PbSe QDs (4.74 %) [332]. In what concerns single dye-based LSCs, lower values were found, Table 7.6. An increase in dye-based LSCs performance was only reported in the case of LSCs based on more than one emitting centre, like the co-doping with two dyes, as listed in Table 7.6. The value found for chlorophyll-based LSCs although smaller than the previous examples, is higher than that reported for planar Ln^{3+}-based LSCs.

This highlights the potential of the proposed approach in the use of natural-based dyes for the production of new and sustainable materials with tailored optical properties applied as efficient layers to energy conversion, enhancing the efficiency of commercial PV cells. We note that PCE is dependent on the optical properties of the semiconductor used to fabricate the PV cell. The PCE values reported for dye-doped LSCs coupled to GaAs- and CIGS-based PV cells are also listed in Table 7.6.

As mentioned, the PV cell coupling to the LSCs edges is a very interesting strategy for PV urban integration, as LSCs could be embedded in facades, roofs, windows and walls and

Table 7.6: PCE (%) values of single-layer planar LSCs coupled to different PV devices. Ac-Tc=antracene-tetracene; PDMS=polydimethylsiloxane; C440=Coumarin 440; DSF=disodium fluorescein; Alq_3=tris-(8-hydroxyquinolinato) aluminium; PVB =polyvinyl butyral; CRS040=fluorescence yellow dye.

Materials	PV Cell	PCE (%)	Reference
dU6/chl-2	c-Si	0.10	this work
dU6/LR305		0.31	[155]
PMMA/LR305		0.51	[175]
Perylene/LR305		0.57	[181]
PMMA/Perylene		1.59	[333]
PLMA/PbSe QDs		4.74	[332]
PMMA/Ac-Tc cocrystals		2.5	[334]
PMMA/LR305-perylene perinone		3.4	[335]
PDMS/C440-DSF		4.62	[336]
Epoxy/Alq_3-DCJTB		5.3	[337]
t-U(5000)/Eu^{3+} complex		0.007	[136]
PVB/Eu^{3+}		0.0499	[272]
PMMA/CRS040-LR305	GaAs	7.1	[112]
PMMA/LR305	CIGS	8.14	[178]

coupled to efficient and small PV cells, allowing everyday buildings to be transformed into harvesting machines. We note that PCE= 0.10 % indicated that the chl-based LSC will be able to provide for the PV cell an output electrical power, $P_{out}^{el} = 10^{-4}\,W$, Eq. 2.21. To increase this value, the scaling-up of the chl-based LSCs is required to permit its use as large-area devices applicable as PV windows able to supply enough energy, as the one delivered from a USB port and to charge low-voltage devices (e.g. such as mobile phones, sensors, wi-fi routers, Table 7.7.

Simulations of the performance of larger dimensions LSCs were carried out using a Monte Carlo ray-tracing approach, to demonstrate the feasibility of scaling-up the proposed chl-based LSC. As detailed in the next section, an average electrical power of $4\,W$ can be provided by a $50\,cm$-wide waveguide ($A_s = 2.5 \times 10^{-2}\,m^{-2}$) unequivocally demonstrating the potential of the chl-based LSCs for PV integration.

Table 7.7: Typical values for the electrical power interval available at a USB port and required to charge small electronic devices. The number and size of dU6-chl-based LSCs needed are also indicated. * Estimated minimum surface area for a chl-based LSC (thickness of 1 cm) based on Monte-Carlo ray-tracing simulations.

		Power (W)	LSC A_s (m^2)*
PC USB		2.5	1.5×10^{-2}
Devices	Mobile phone	5	3.0×10^{-2}
	Tablets	12	10^{-1}
	LED lamps	2.3-18	1.2×10^{-2}
	Movement sensors	0.32-0.45	2×10^{-3}
	Wi-fi routers	0.85-11	5×10^{-3}

7.2.2 Modelling

The thickness of the simulated chl-based layer ($\sim 10^{-3}\,m$) is much larger than that of the light coherent length ($\sim 10^{-7}\,m$), thus, interference effects were neglected.

The inputs of the Monte Carlo ray-tracing simulation consist of the solar spectrum AM1.5G (280-1600 nm, photons with angle of incidence between $-45°$ and $45°$), the absorption and emission spectra, the absolute emission quantum yield and dispersion curve of each LSC. Furthermore, we consider a thin layer of air underneath the LSC.

The description of the simulation is described in Chapter 5. In this case, the photon desired step size is $2 \times 10^{-2}\,cm$.

The output of the simulation yield to $\eta_{opt} = 3.47 \pm 0.01\,\%$ for the dU6-chl-2 LSC with $1.00 \times 1.00 \times 0.25\,cm^3$. This value is very close to that found experimentally ($3.70 \pm 0.01\,\%$) and to the value estimated through the η_{opt} definition based on the LSC main losses, Eq. 2.9, ($2.4\,\%$).

The good-agreement between the ray-tracing prediction and the experimental results, points out that the simulation describes the main optical features and allow us to use the experimental device parameters to estimate the optical performances potentially achievable using waveguides of increasingly larger area or slab thickness [112, 232].

The η_{opt} was also estimated for lager area LSCs to discuss the feasibility of scaling-up the chl-based devices. A constant thickness of $10^{-3}\,m$ (typical value for a glass window)

was considered in all the simulations and A_s was varied ($10^{-4} < A_s < 10^{-2}\,m^2$). For these dimensions, η_{opt} is approximately constant ($4.61 \pm 0.01\,\%$, Figure 7.19A, which indicates that optical conversion efficiency can still be maintained at a relatively high level for larger devices. The PCE can be related to η_{opt} through the efficiency of the PV solar cells (PCE= $\eta_{PV}\eta_{opt}$). Therefore, based on the experimental PCE value of $0.1\,\%$, we may estimate the A_s value expect to produce the desired P^{el}_{out}, though

$$P^{el}_{out} = \eta_{PV}\eta_{opt}A_s I_{AM1.5G} \tag{7.1}$$

where η_{PV} is the Si-PV cell efficiency ($4\,\%$ accordingly to the manufacturer) and $I_{AM1.5G} = 1000\,W \cdot m^{-2}$. For a set $P^{el}_{out} = 4\,W$ we estimate that an LSC with $A_s = 2.5 \times 10^{-2}\,m^2$ is required.

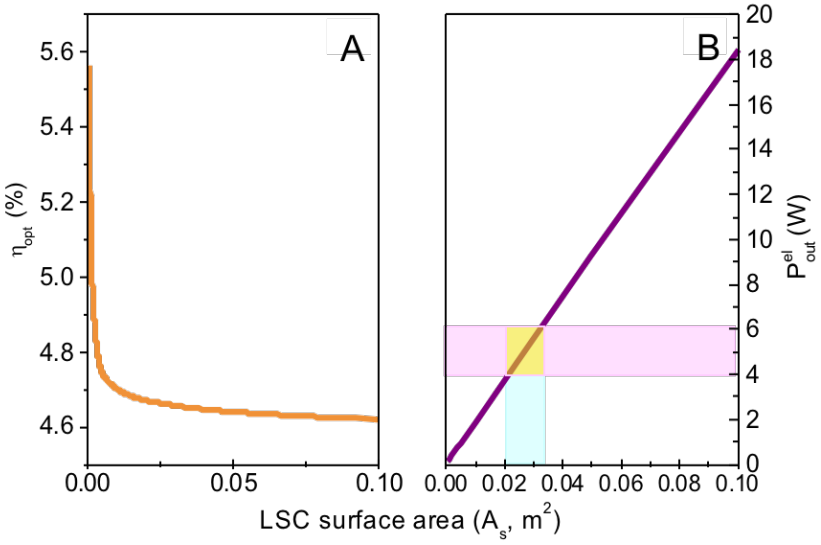

Figure 7.19: (A) Monte Carlo ray-tracing optical conversion efficiency as function of the LSC surface area and (B) predicted output electrical power (the shadow area highlight the power vs surface required for low-voltage devices).

7.3 R-PE based luminescent solar concentrators

Here, we present LSCs composed of a glass container and based on bundles of cylindrical hollow-core POFs. The glass container and the fibres hollow-core were filled with aqueous solutions at different concentrations of R-PE, which is a phycobiliprotein, extracted from *Gracilaria sp.* algae. The R-PE solutions absorb in the UV/visible spectral range (300-

550 nm) and convert this radiation into red-emission (550-700 nm) with a maximum absolute emission quantum yield of ~ 0.39. In this section, LSCs with distinct geometries are reported, in which the R-PE emission yields η_{opt} values up to $\sim 6.88 \pm 0.01\,\%$ and $\sim 4.74 \pm 0.01\,\%$ for a planar device and for a bundle of cylindrical LSCs, respectively, which are the largest values known for liquid-based LCSs using sustainable emitting centres. Moreover, the coupling of the LSCs to commercial Si-based PV devices yielded PCE values of $\sim 0.27 \pm 0.01\,\%$ (planar) and $\sim (23.03 \pm 0.01) \times 10^{-3}\,\%$, (bundle). These values illustrate the potential of this approach for the development of natural-based LSCs meeting the requirements of reliable, sustainable and competitive energy systems.

7.3.1 Optical characterization of the R-PE solutions as LSCs optically active layer

The c-LSCs were based on hollow-core POFs with distinct diameter values, Figure 7.1B, resulting in different geometrical gain factors (G). The POFs fabricated using a semi-industrial fibre optic manufacturing facility [158] and cut with length $l \sim 5 \times 10^{-2}\,m$. The hollow-core was filled with the RPE solutions with a syringe. The edge coupled to the PV device was sealed with a polymeric resin NOA68®, while the opposite one was kept open. The individual POFs were assembled into bundles, Figure 7.1B. The p-LSCs were fabricated using a optical glass cuvette (CM Scientific) with dimensions tailored to fit the PV cell surface, as illustrated in Figure 7.1A.

Figure 7.20 shows the emission spectra of the R-PE based solutions which are formed by a broad band typical of R-PE fluorescence [245], whose relative intensity depends on the dye concentration. For the less concentrated solutions (RPE-1 to RPE-5), the room-temperature emission spectra is dominated by the R-PE characteristic emission with one component centred around 577 nm and the other around 632 nm. The presence of two distinct dye-related components in the emission spectrum points out the formation of dye aggregates [338]. In fact, by increasing the concentration, the relative intensity of the low-energy component (655 nm) increases and the main peak (577 nm) red-shifts around 6 nm, suggesting the presence of J-dimers [323].

The excitation spectra, Figure 7.21A, are dominated by the RPE-excited states in the visible spectral range, revealing also the presence of components in the UV/blue (320-440 nm)

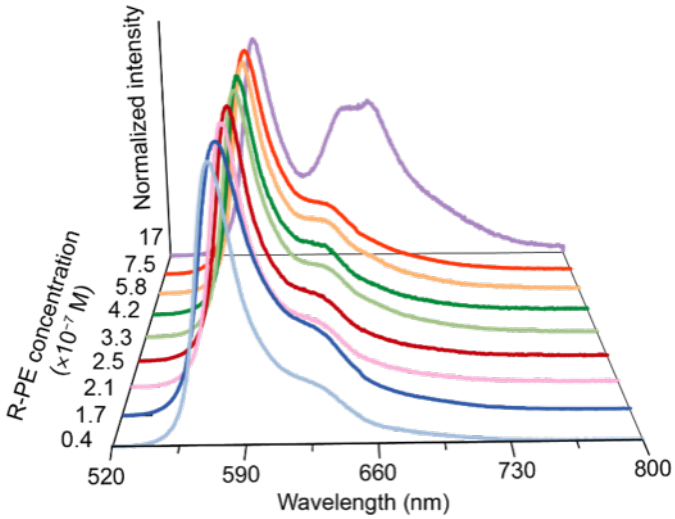

Figure 7.20: Emission spectra of the R-PE solutions excited at 498 nm.

attributed to the chromophores' singlet states. The band at 278 nm arises from amino acid residues of the apoprotein [339].

The emission properties of the aforementioned samples were also quantified through the measurement of the absolute emission quantum yield (q, Table 7.8), as function of the excitation wavelength (310-540 nm). Although a maximum absolute emission quantum yield is observed under excitation in the visible range (498 nm), as the concentration is increased, this value decreases from 0.37 ± 0.04 (RPE-1) to 0.16 ± 0.02 (RPE-9). These values are lower than those previously reported on literature of 0.82-0.85 [340, 341], found for R-PE in phosphate buffers and for less concentrated samples ($\sim 10^{-15}\, M$) [340].

Table 7.8: Integral overlap (O, photons$\cdot s^{-1} \cdot m^{-2}$), molar extinction coefficient (ε, $M^{-1} \cdot cm^{-1}$), absolute emission quantum yield (q) and brightness (B, $M^{-1} \cdot cm^{-1}$) as function of the R-PE concentration ([R-PE], M). The ε, q and B values refer to 498 nm.

Solution	[R-PE] ($\times 10^{-7}$)	O ($\times 10^{20}$)	ε ($\times 10^{6}$)	q	B ($\times 10^{5}$)
RPE-1	0.4	0.9	1.7	0.37 ± 0.04	6.2
RPE-2	1.7	2.1	1.0	0.39 ± 0.04	4.0
RPE-3	2.1	3.0	1.3	0.34 ± 0.03	4.2
RPE-4	2.5	3.8	1.4	0.32 ± 0.03	4.5
RPE-5	3.3	4.8	1.4	0.30 ± 0.03	4.0
RPE-6	4.2	5.5	1.4	0.28 ± 0.03	3.7
RPE-7	5.8	6.9	1.5	0.25 ± 0.03	3.8
RPE-8	7.5	8.0	1.6	0.24 ± 0.02	3.2
RPE-9	17	10.4	1.5	0.16 ± 0.02	2.2

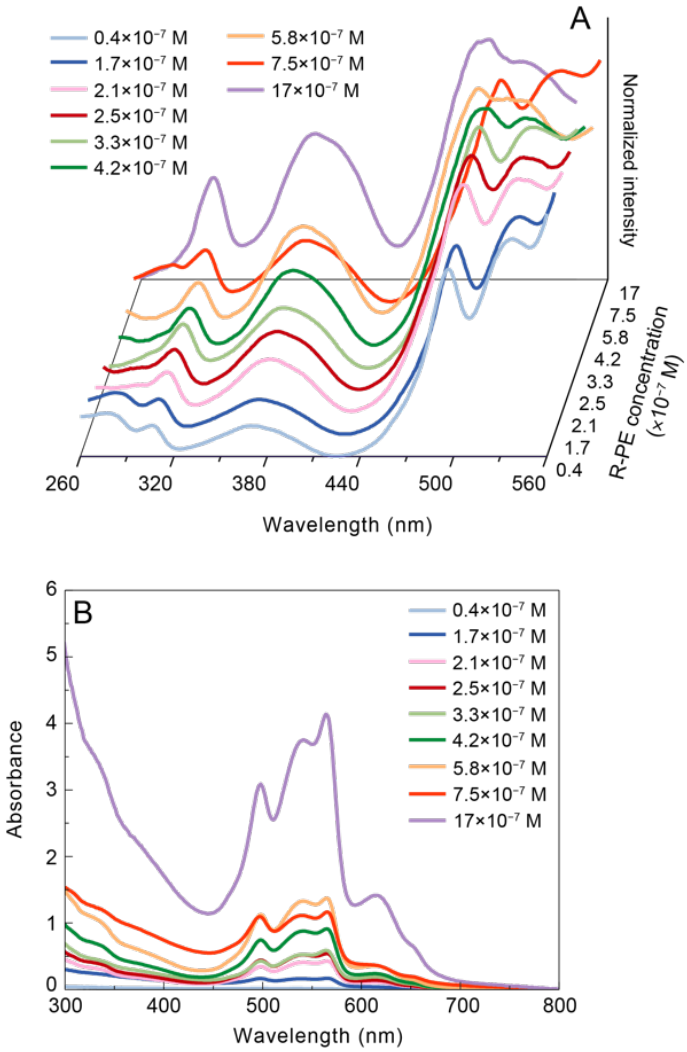

Figure 7.21: (A) Excitation monitored at 580 nm and (B) absorption spectra of the R-PE solutions.

The light-harvesting ability of all the R-PE aqueous solutions relative to the AM1.5G spectrum presented in Figure 7.22A was studied by absorption spectroscopy. Figure 7.22B shows the absorption spectra of three selected R-PE aqueous samples (absorption spectra of all samples in Figure 7.21), which resemble the excitation spectra above mentioned, apart from the presence of a component around 590-690 nm, probably ascribed to the presence of other phycobiliproteins, such as phycocyanin and allophycocyanin [124]. There are no significant spectral changes in the absorption spectra as the concentration is varied, although the absolute absorbance value increases with concentration, Figure 7.21B and 7.22B. The

absorbance dependence on the concentration was rationalized by the calculation of the molar extinction coefficient values (ε), revealing that with exception of the low-concentrated solution (RPE-1, $0.4 \times 10^{-7}\,M$), analogous values within 1.3-1.9 $\times 10^{6}\,M^{-1}cm^{-1}$ were found, in good agreement with previous studies in the literature [340, 341].

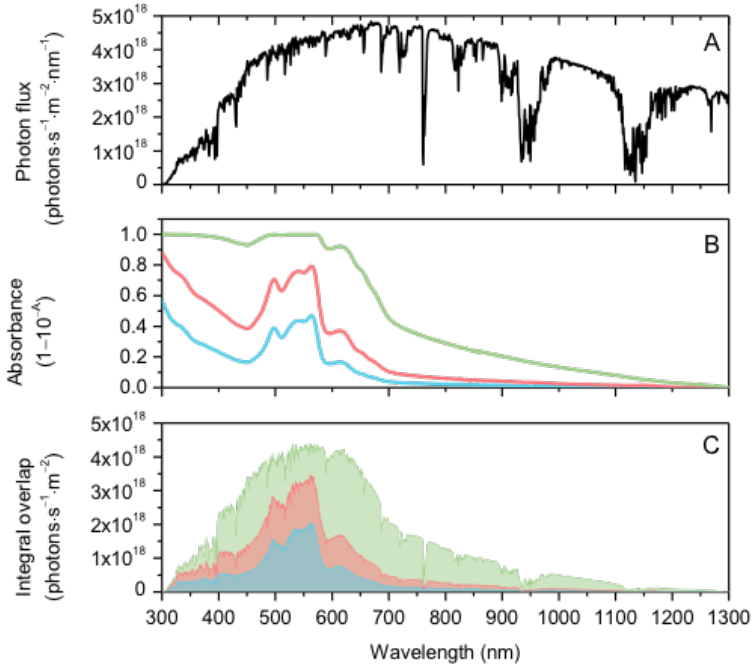

Figure 7.22: (A) Solar photon flux on Earth at AM1.5G, (B) absolute absorbance of RPE-2 (blue line), RPE-5 (red line) and RPE-9 (green line) and (C) integral overlap between the solar photon flux and the absolute absorbance.

Moreover, in order to quantify the ability of the LSCs to absorb the sunlight available for PV conversion, the overlap integral between the R-PE solutions absorption spectra and the solar irradiation on Earth through Eq. 2.12 was calculated. The O values increase with increasing concentration, Figure 7.22C and Table 7.8. The maximum calculated O value indicates that the RPE-9 ($17 \times 10^{-7}\,M$) aqueous solution have the potential to absorb $\sim 27\,\%$ of the solar photon flux on the Earth (4.30×10^{21} photons$\cdot s^{-1} \cdot m^{-2}$) [156].

Light emission efficiency and light harvesting ability can be related by the molar brightness B [266], allowing both properties to be compared across distinct samples. The B values were calculated as function of the R-PE concentration, Table 7.8, and are one order of magnitude larger than those reported for other organic-dye molecules, with radiation emission in the 530-650 nm range [329, 330]. We note that the larger B values are found in the concentration

region between RPE-3 and RPE-7 solutions. At higher concentrations, namely for RPE-8 and RPE-9, B decreases due to the concentration quenching, as suggested from the emission spectra analysis. At lower concentrations RPE-1 and RPE-2 the q values are higher, resulting in larger B values although the absorption coefficient is decreased.

Taking advantage of the ability of the R-PE solution to harvest the AM1.5G radiation and convert it into visible emission, the solutions were incorporated into hollow core POFs, Figure 7.1B, allowing the fabrication of c-LSCs based on natural dyes in a liquid medium. The fabrication of these short-length c-LSCs aims at establishing the potential to design large area c-LSCs made from the assembling of POFs filled with the R-PE aqueous solution in bundle structures. As Figure 7.23A illustrates, when illuminated by AM1.5G solar radiation, the orange-red emission of the R-PE based solutions is guided to the edges of the device through total internal reflection.

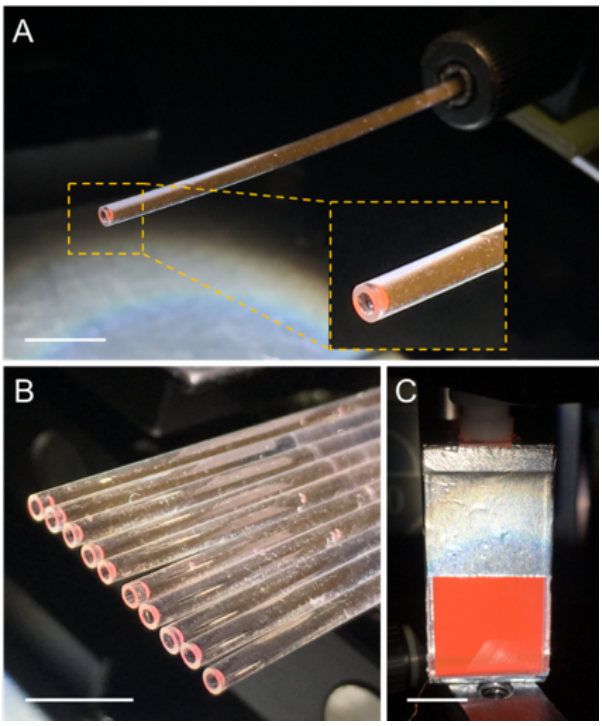

Figure 7.23: Photographs of the (A) c-LSC based on RPE-9 solution coupled to the PV device, (B) bundle structure of c-LSCs based on RPE-6 solution and of (C) p-LSC (with reflective tape) based on RPE-5 solution coupled to PV device and under AM1.5G illumination (scale bars: $1 \times 10^{-2}\, m$).

Also, as evidenced in Figure 7.24, the emission intensity guided in the PMMA cladding is larger (~ 2 times) than that in the hollow-core.

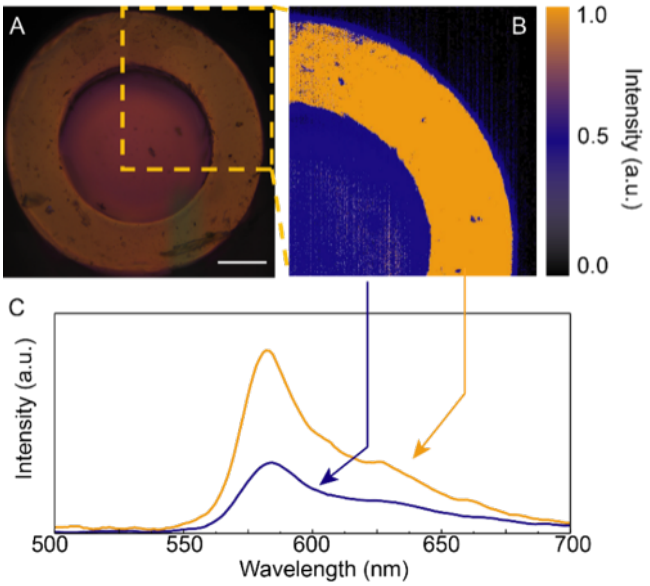

Figure 7.24: (A) Cross-section optical microscopy images of the c-LSC under white light illumination (scale bar: $3 \times 10^{-4}\, m$), (B) hyperspectral image of a selected area and (C) corresponding emission spectra measured in the core and PMMA regions.

Another parameter that contributes to n_t is the distance r from the fibre centre at which the emission occurs which, for a POF with external diameter R, is given by Eq. 2.4 [202], with a maximum value near the surface, that decreases as r approaches the centre of the POF (Figure 6.7). We note that for the geometry here proposed, for both cases of G$\sim$ 7 and G$\sim$ 9, average values of 0.37 were calculated (Figure 7.25).

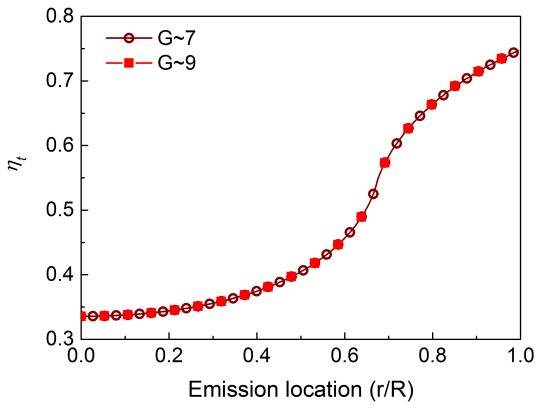

Figure 7.25: Trapping efficiency (η_t) as function of the ratio r/R (Eq. 2.4).

The refractive index of the R-PE solutions was measured using a refractometer at $22°C$ yielding a value of $n \sim 1.3335$ at $589\, nm$. The refractive index of the glass cuvette used in

the p-LSC was measured by spectroscopic ellipsometry. The ellipsometric parameters and the dispersion curve of are shown in Figure 7.26

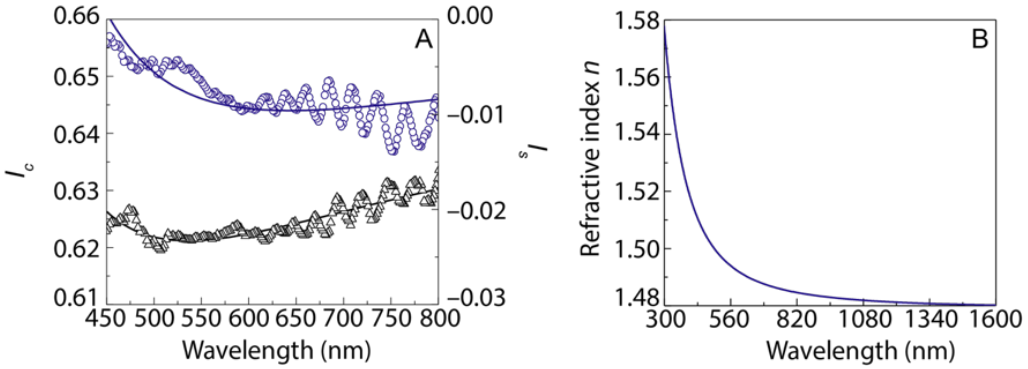

Figure 7.26: (A) Ellipsometric parameters I_s (open circles) and I_c (open triangles) measured for the glass cuvette. The solid lines represent the data best fit; (B) dispersion curve of the cuvette glass of the p-LSC.

The relative performance of the c-LSCs based on a single POF was quantified by the estimation of η_{opt} through Eq. 2.14 for all the c-LSCs based on a single POF (Table 7.9), whose maximum values ($\eta_{opt} = 0.16 \pm 0.02\,\%$) were found for the c-LSCs ($G \sim 7$) with the concentration of the solutions within RPE-4 and RPE-7.

Table 7.9: Optical conversion efficiency (η_{opt}, %) values of R-PE based c-LSCs made of a single POF.

Solution	G$\sim$ 7	$G \sim 9$
RPE-1	0.137 ± 0.004	0.073 ± 0.003
RPE-2	0.153 ± 0.005	0.093 ± 0.003
RPE-3	0.105 ± 0.003	0.091 ± 0.003
RPE-4	0.193 ± 0.006	0.089 ± 0.003
RPE-5	0.162 ± 0.005	0.065 ± 0.002
RPE-6	0.164 ± 0.005	0.077 ± 0.003
RPE-7	0.151 ± 0.005	0.058 ± 0.002
RPE-8	0.101 ± 0.003	0.085 ± 0.003
RPE-9	0.134 ± 0.004	0.102 ± 0.004

The performance of the c-LSCs was also evaluated by measuring I_{SC}^{L} as function of the incident wavelength and calculating the EQE of the PV devices coupled to the c-LSCs. For

all the c-LSCs, the maximum EQE values for the PV device are well correlated with the peaks found in the absorption spectra of the active layer (Figure 7.27 and Figure 7.28), with the larger EQE variation between 500 and 600 nm. The maximum value of EQE= $0.1647 \pm 0.0002\,\%$ was found for the c-LSC with G$\sim$ 7 filled with RPE-6 aqueous solution. The effective contribution of this c-LSCs on a PV device was also quantified by estimating the PCE value as $3.2 \pm 0.1 \times 10^{-3}\,\%$.

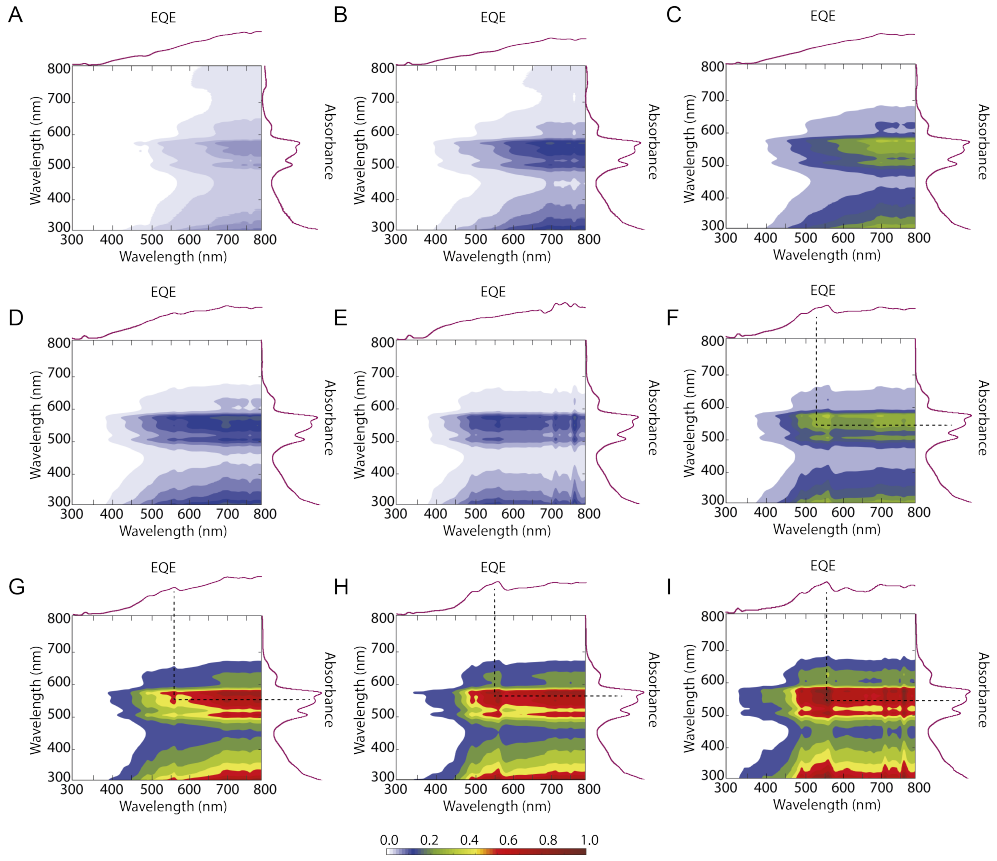

Figure 7.27: Cross correlation between the photodiode EQE and the absorption spectrum of the coupled LSC based of the illustrative examples of (A) RPE-1, (B) RPE-2, (C) RPE-3, (D) RPE-4, (E) RPE-5, (F) RPE-6, (G) RPE-7, (H) RPE-8 and (I) RPE-9 for LSCs with $G \sim 7$.

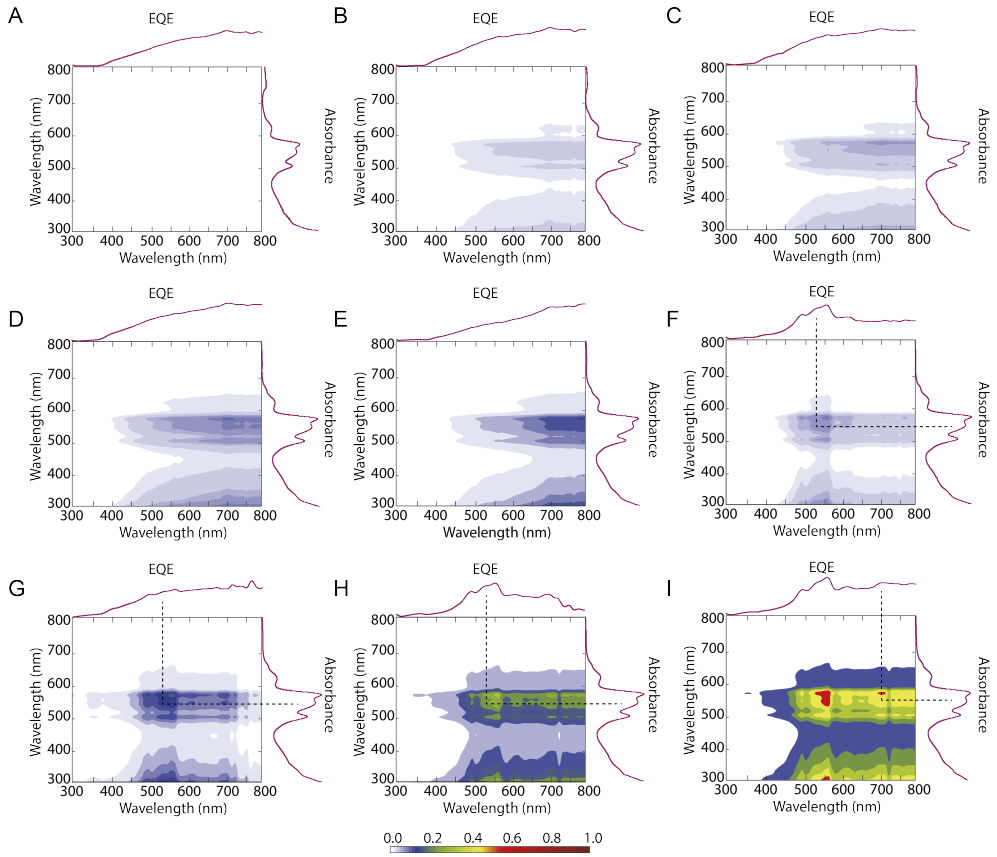

Figure 7.28: Cross correlation between the photodiode EQE and the absorption spectrum of the coupled LSC based of the illustrative examples of (A) RPE-1, (B) RPE-2, (C) RPE-3, (D) RPE-4, (E) RPE-5, (F) RPE-6, (G) RPE-7, (H) RPE-8 and (I) RPE-9 for LSCs with $G \sim 9$.

7.3.2 Bundle of c-LSC and p-LSC

The previous results point out that POFs filled with R-PE solutions can be used to fabricate c-LSCs and that the use of optically active centres dispersed in a liquid medium in LSCs presents some advantages when compared to the case of a solid matrix LSC. For instance, the concentration of the solutions can be easily varied [299, 300, 302, 304], liquids are easily moulded to the container geometry, the performance of the solar cells at the edges of the LSC is fixed and constant, removing the variability when comparing different fluorophores and concentrations [304], and liquid solutions can be easily replaced when compared with materials that undergo a phase exchange to solid [208].

To demonstrate the potential of the proposed approach, it is necessary to enlarge A_s and, consequently, PCE values which will permit to envisage the application in PV cell to

supply low-power consumption devices. Therefore, to enhance the PV cell performance in the presence of a LSC, A_s was increased following two approaches: i) c-LSCs based on ten POFs assembled into a bundle structure, Figure 7.23B, and ii) p-LSC based on a glass container, Figure 7.23C. The solutions with concentration values within 3.3-4.2 $\times$ 10^{-7} M (RPE-5 to RPE-6) combine larger absolute emission quantum yield, brightness and integral overlap, and, therefore, they were used to fabricate a bundle of c-LSC and a p-LSC. When coupled to a Si-based PV device maximum $\eta_{opt} \pm \Delta\eta_{opt}$ values of $2.71 \pm 0.07\,\%$ and $5.55 \pm 0.15\,\%$ ($4.74 \pm 0.01\,\%$ and $6.88 \pm 0.01\,\%$ when using 2.19) respectively, were found. These values are larger than those reported for c-LSCs formed of a single POF. Also, the PCE values found for the p-LSC and c-LSCs bundle were $0.27 \pm 0.01\,\%$ and $(2.30 \pm 0.02) \times 10^{-3}\,\%$, respectively. EQE measurements were performed showing good correlation with the absorption spectra, yielding maximum values of $2.7134 \pm 0.0002\,\%$, for the p-LSC (Figure 7.29). It is worth noting that, considering LSCs based on natural organic dyes, the η_{opt} value of the p-LSC here reported is higher than the recently reported p-LSC based on chlorophyll with $\eta_{opt} = 3.70 \pm 0.01\,\%$ [128].

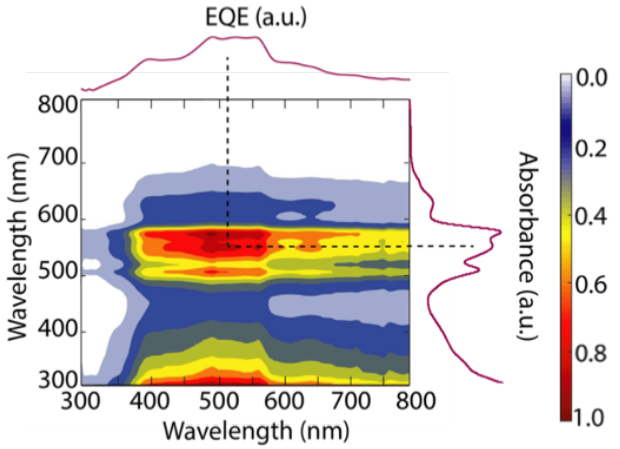

Figure 7.29: Cross correlation between the PV cell EQE and the absorption spectrum of the coupled p-LSC based on RPE-5.

As far as we know, only p-LSCs in which the optically active centres are dispersed in liquid medium were reported. All the studies refer to the use of synthetic dyes or QDs in organic solvents, rather than natural dyes in water. The η_{opt} values calculated in the present work ($\eta_{opt} = 5.55 \pm 0.01\,\%$) are among the highest values in the literature (Table 7.10). Higher values were only reported for LSC based on synthetic dyes (Rhodamine B [208], Red F [208, 306], K_I, Sulphorhodamine 101, BASF-402 and BASF-241 dyes) [303], and PbS QDs [206].

Table 7.10: Reported η_{opt} (%) and PCE (%) values for cylindrical (c-LSCs) and planar (p-LSC) LSCs based on active centres dispersed in distinct liquid media. The concentration ([ ], M) of the active enters on the liquid media, the LSC surface area A_s ($l \times w$, cm^2) and geometrical gain (G) are also presented.

	Medium	Active centre	[ ]	A_s (G)	η_{opt}	PCE	Ref.
c-LSCs	Water	R-PE	4.2×10^{-7}	3.5×1.4 (6)	2.7	0.02 (Si)	This work
	Water	R-PE	3.3×10^{-7}	2.0×2.0 (2)	5.55	0.27 (Si)	
p-LSCs	PPC/EG	RhB	-	2.5×7.6 (16)	15.3	-	[208]
		LDS698			3.6		
		LDS821	$\sim 10^{-4}$		2.9		
	Cl- benzene	MDMO-PPV	$\sim 10^{-3}$		5.9		
		MEH-DOO -PPV	-		5.0		
		Red F	8×10^{-6}		19.8		
	Toluene	CdSe/ZnS	3×10^{-6}		1.6		
	TX-100	K_l	-	5×10 (3)	20.2	-	[303]
		S-101			18.2		
		BASF-402			19.7		
		BASF-241			13.9		
	Toluene	CdSe/ZnS	3×10^{-6}	4.5×1.2 (11)	0.5	1.2 (Si)	[206]
		PbS	1.93×10^{-4}		12.6	3.2 (Si)	
	LC E7	Coumarin/ Perylene	8×10^{-3}	5×5 (∗)	3.2	-	[305]
	Toluene	Lumogen F Red 300	4×10^{-3}	2×2 (∗)	12.0	-	[306]
	Toluene	Lumogen Red 305	1.23×10^{-7}	10×3.5 (10)	-	2.3 (Si)	[342]

l=length; w=width; RhB=Rhodamine B, Liquid crystal Nematic=LC E7, TX-100=polymer Triton X-100, PPC=Propylene carbonate, EG=ethylene glycol, Cl-bez= Chlorobenzene; S-101= Sulphorhodamine 101; ∗: the information provided in the report is not enough to perform accurate G calculations for comparison with other reported LSCs.

Concerning PCE, care should be taken for comparison purposes, as it is dependent on the optical properties of the semiconductor used to fabricate the PV cell. For LSCs characterized with similar Si-PV cells, the values here reported are lower than those reported for other LSCs with optically active centres dispersed in liquid medium (Table 7.10). In this case, a direct comparison between the PCE values calculated in the presence of the p-LSC and of the bundle-based LSCs cannot be made due to induced differences in the PV cell responsivity, Figure 7.30.

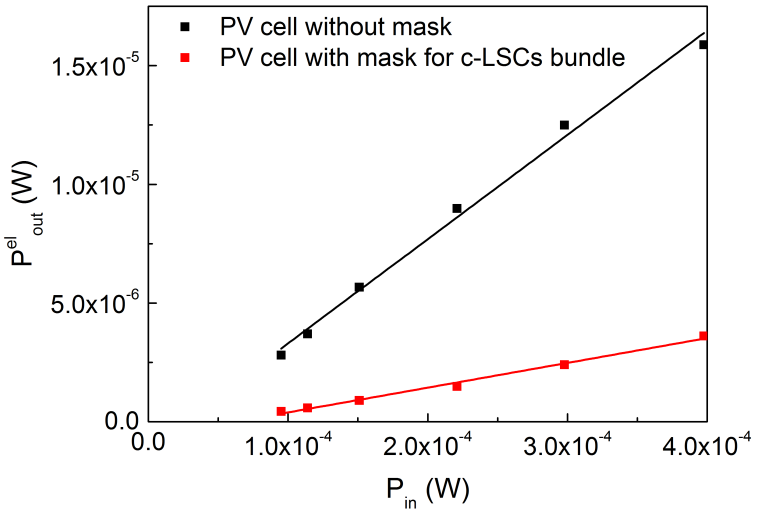

Figure 7.30: Electrical power output P_{out}^{el} as function of the incident optical power P_{in} for the PV cell as used for the p-LSC and for the bundle structure of the c-LSCs (with mask matching A_e), for 580 nm incident radiation. The solid lines represent the best data fit ($r^2 > 0.99$).

Nevertheless, we note that these values are higher than that reported for a p-LSC based on optically active layers deposited as thin films, namely tri-ureasil and polyvinyl butyral doped with an Eu^{3+}-based beta-diketonate complexes (0.007 % [136] and 0.0499 % [273], respectively), being, however, smaller that the values found for LSCs based on Lumogen® F Red 305-doped parylene (0.57 %) [181]. The highest values for PCE (5.23 ± 0.01 %) involving p-LSCs coupled to Si-based PV cells was reported using a more complex device structure with multi-stack optical layers and back-reflector using polydimethylsiloxane doped with Coumarin 440 and disodium fluorescein, correspondent to 4.62 ± 0.02 % for single module [336]. For QD-based LSCs using Si PV cells, the PCE record is 4.74 % for PbSe in P(LMA-co-EGDMA) [332].

Table 7.11: Reported η_{opt} (%) and PCE (%) values for cylindrical LSCs in which the optically active layer is incorporated as coating or filling of a POF or the layers are moulded in the shape of a c-LSC.

Optically active centre	η_{opt}	PCE	Ref.
Coumarin 6/Eu(TTFA)$_3$Phen	0.23		[343]
QDs (detailed composition and structure are proprietary)	0.03		[207]
PbS	6.5		[180]
$Eu(TTA)_3 \cdot 2H_2O$	1.2	0.140	[159]
Rhodamine 6G	8.0		[158]
$Eu(TTA)_3 \cdot 2H_2O$	1.1	0.058	[157]
	0.02	0.001	
	0.06	0.001	
Rhodamine 6G	1.52	0.074	
	0.33	0.018	
	0.18	0.004	

In what concerns the c-LSCs, our comparison can only be made for LSCs in which the optically active layer is incorporated as coating of a POFs or the layers are moulded in the shape of a c-LSC. Similarly to that found for the p-LSCs, any example refers to natural-based dyes. Even though, the η_{opt} values here reported are higher than those known for such c-LSCs, Table 7.11.

7.3.3 Modelling

The thickness of the active layer ($\sim 10^{-2}\, m$) is much larger than that of the light coherent length ($\sim 10^{-7}\, m$), thus, interference effects were neglected.

The input of the Monte Carlo ray-tracing simulation consists in photons following the solar spectrum probability density function AM1.5G (280-1600 nm, photons with angle of incidence between $-45°$ and $45°$), the absorption and emission spectra, the absolute emission quantum yield and refractive index of the R-PE aqueous solutions ($n \sim 1.3335$) and the dispersion curve of the cuvette glass. Furthermore, we consider a thin layer of air underneath the LSC.

The description of the simulation is described in Chapter 5. In this case, the photon

desired step size is $2 \times 10^{-2}\, cm$.

The simulations (10^6 photons) were performed for a p-LSC with dimensions of $2.00 \times 2.00 \times 1.00\, cm^3$ and as function of the concentration of the RPE solution. The optical conversion efficiency was predicted considering all the photons reaching the edge (η_{opt}, %) and considering only the fraction of converted photons (η'_{opt}, %), Table 7.12. In what concerns η_{opt}, the values are nearly independent of the concentration except for the more concentrated solutions (RPE-8 and RPE-9) for which a decrease is noticed. This decrease may be rationalised based on the absolute emission quantum yield decrease, induced by the formation of dye-aggregates at higher concentrations. If only the fraction of converted photons is taken into consideration, η'_{opt} is nearly constant only in the concentration range of RPE-3 to RPE-7 solutions. Whereas the lower η_{opt} and η'_{opt} values found for low concentrated solutions (RPE-1 and RPE-2) arise from lower ε (despite the higher q), those of the higher concentrated ones (RPE-8 and RPE-9) are mainly caused by the decrease in q (despite the higher ε).

Table 7.12: Simulated optical conversion efficiency values considering all the photons reaching the edge (η_{opt}, %) and only the fraction of converted photons (η'_{opt}, %) for p-LSCs using R-PE solutions with different concentrations.

Solution	η_{opt}	η'_{opt}
RPE-1	5.787	0.000
RPE-2	6.013	0.236
RPE-3	6.423	0.906
RPE-4	6.350	0.980
RPE-5	6.284	1.171
RPE-6	6.168	1.234
RPE-7	5.870	1.250
RPE-8	5.321	0.978
RPE-9	3.448	0.418

Taking also into consideration the integral overlap (O, Table 7.8) and the simulation results in Table 7.12 and , the RPE-5 solution displays the better optical performance at lower dye concentration and that was the rationale behind the selection of this solution for the fabrcation of the p-LSC. We note that only the η_{opt} values are directly comparable with the experimental ones, as it is not possible to experimentally neglect the contribution of non-converted AM1.5 guided photons (even if no direct radiation is incident on the PV cell). In this case, we highlight that the simulated η_{opt} value for RPE-5 (6.28 ± 0.01 %) are in good agreement with

that experimentally determined ($5.55 \pm 0.01\,\%$), pointing out that the simulation describes the main optical features [112, 232]. The larger simulated values indicates that the device may be further optimised, in particular the PV cell coupling.

7.4 Conclusions

In this chapter, natural-based LSCs made of chlorophyll molecules dispersed in organic-inorganic ureasil hybrids were studied. The chlorophyll-based active layer displays a large overlap with the solar irradiance on Earth, (absorption at 300-450 nm and 600-850 nm) and emission spectra centred around 675 nm. At low chlorophyll concentration values (10^{17} molecules$\cdot cm^{-3}$), the optical properties (fluorescence lifetime, absolute emission quantum yield and brightness) are preserved after the incorporation into the hybrids hosts. The optimised hybrid sample ($\eta_{opt} = 3.70 \pm 0.01\,\%$) was tested as LSC coupled to commercial Si-based PV devices, revealing an effective contribution to its performance, namely, an increase in the PCE ($0.10 \pm 0.01\,\%$).

Also, natural-based LSCs made of R-PE aqueous solutions were studied. These optically active centres display large overlap with the solar irradiance on Earth (absorption at 300-700 nm) and emission spectra centred around 580 nm. LSCs composed of R-PE aqueous solutions with distinct concentrations were tested (4.2×10^{-8} to $1.7 \times 10^{-6}\,M$), as well as the effect of the geometrical gain ($G \sim 7$ and ~ 9) on the performance. The best performance found for c-LSCs was for the case of the hollow-core fibre with $G \sim 7$ filled with the aqueous solutions with R-PE concentration of $4.2 \times 10^{-7}\,M$. Also, the fibre LSCs were assembled in a bundle structure, which yielded η_{opt} and PCE values of $2.71 \pm 0.07\,\%$ and $(2.30 \pm 0.02) \times 10^{-3}\,\%$, respectively. Nevertheless, the top performance device of this work was a p-LSC based on a glass cuvette, with η_{opt} and PCE values of $5.55 \pm 0.01\,\%$ and $0.27 \pm 0.01\,\%$, respectively.

The use of natural red/NIR emitting dyes, such as chlorophyll and R-PE molecules as optically active centres in LSCs, demonstrate the potential of nature-inspired LSCs as a relevant step towards cheap and sustainable PV energy conversion.

Chapter 8

General conclusions and perspectives

In this chapter, I will briefly summarize the main results presented and discussed throughout the different chapters of this thesis.

The main objectives of this thesis were achieved. Here, we produced and characterized transparent organic-inorganic hybrids with controlled thickness and refractive index using PMMA with incorporated Ln^{3+}-based ionogels, and organic-inorganic hybrids with incorporated Eu^{3+} ions and organic dyes, such as Rhodamine 6G, Rhodamine 800, SiNc and chlorophyll molecules, and R-PE based aqueous solutions, which were in turn used to produce LDS layers and LSCs. Although LDS layers were produced and characterized, most of the work done was based on LSCs with cylindrical and planar geometries. Experimental results were validated through Monte-Carlo ray-tracing simulations, which were used to estimate the performance of LDS layers and LSCs.

The main conclusion of this thesis is that the incorporation of natural-based molecules provides a sustainable approach to LSCs, as the results presented for planar and cylindrical LSCs incorporating such molecules are comparable to those reported for non-natural based LSCs, and are therefore a definite step towards reliable, sustainable and competitive energy systems.

Several physical and chemical challenges were addressed over the course of this thesis in order to produce LDS layers and LSCs. The physical challenges are related with: the dimension of the LSCs, planar LSCs can be scaled up as predicted by Monte Carlo Ray-tracing;

geometry, planar and cylindrical geometries were studied, and it was shown that the individual waveguiding features of each fibre in the bundle contribute to reduce reabsorption, as lower performance values were estimated for a planar LSC with analogous surface collection area and light-harvesting absorbance, and the number of optically active centres can be increased while ensuring large G values by varying the diameter of the core. In what concerns chemical challenges, the absolute emission quantum yield of NIR-emitting centres, as well as the contrast between the refractive indices of the waveguide and the optically active materials must still be increased, and the concentration of optically active materials should be optimised in order to obtain the highest brightness possible without forming non-luminescent aggregates.

Optically active centres that emit in the NIR range are well-suited for optimising LDS layers and LSC devices, as the coupled Si PV cells have maximum absorption in this spectral range. Here, LDS layers and LSCs with PMMA doped with Tb^{3+}-, Eu^{3+}-, Yb^{3+}- and Nd^{3+}-based ionogels were produced and studied. These optically active centres absorb mainly in the UV spectral region (300-400 nm) and their emission is centred in the visible-NIR spectral region. The performance of the LDS layers based on Eu^{3+} coupled to c-Si PV cells was studied, and an absolute increase in PV cell EQE of 25 % was observed between 300-360 nm. These results are very promising and among the highest values reported for absolute EQE increase in the UV spectral region for PV cells coated with LDS layers. Furthermore, LSCs based on Eu^{3+} and Tb^{3+} were produced showing promising results. In what concerns PMMA doped with Yb^{3+} and Nd^{3+}-based ionogels, the performance of the LDS layers and LSCs did not increase due to the low absolute emission quantum yield of the materials. Moreover, the use of PMMA doped with Ln^{3+} based ionogels demonstrated the potential of these materials in the production of LDS layers and LSCs for use in devices that are highly efficient and resistant to ambient conditions.

We also used SiNc, a NIR-emmitting dye, due to its wide coverage of the solar spectrum (absorption at 300-450 nm and 600-850 nm) and emission centred around 785 nm, where the fraction of radiation absorbed by Si-PV cells is high. The incorporation of this dye into a tri-ureasil organic-inorganic hybrid matrix enabled it to be easily coupled to PV cells without affecting the photophysical properties of SiNc. Thin dye-doped hybrid films (F/t-U(5000)/SiNc) with an absolute emission quantum yield of 0.17 and a lifetime of 3.7 ns

were produced and their performance as LSCs was evaluated, achieving an $\eta_{opt} \sim 1.5\,\%$ and EQE values exceeding 20 % in the UV region. The SiNc-based tri-ureasil is, therefore, an intriguing example of a NIR layer for LSC devices. Moreover, the mechanical features of the emitting layer provided by the hybrid host open up new opportunities for flexible NIR waveguiding photovoltaics, with additional advantages compared to planar rigid LSCs, such as, for instance, wearable solar-harvesting fabrics for mobile energy.

As mentioned above, challenges for LSCs are related with increasing the geometrical gain and, consequently, the concentration factor that quantifies the overall performance of a LSC. For this reason, both planar and cylindrical LSCs were fabricated. LSCs based on a novel cylindrical and flexible geometry were produced by filling PMMA plastic optical fibres with the optically active hybrids. This all-polymer fibre-LSC benefits from large area and is lightweight, towards low-cost solar-energy harvesting. This innovative approach presents advantages relatively to coated plastic optical fibres such as environmental protection for the layer, opening the gate to explore a large number of architectures involving hollow-core fibres. Also, one of the goals of this thesis was to modify the outer geometry of the LSCs to allow easier coupling between them, and form a LSC matrix (bundle), that maximizes the coverage area of a square PV cell. These variations in the LSC configuration resulted in distinct geometric gain factors and thus, one of the objectives was to study the impact of this factor in the performance of LSCs. In this context, a new triangular geometry for hollow-core LSCs was presented, filled with an organic-inorganic hybrid doped with $Eu(TTA)_3 \cdot 2H_2O$, Rh6G or Rh800. The Rh800 dye allowed the fabrication of NIR emitting LSCs, which are scarce in the literature. The standalone fibre LSCs presented a maximum η_{opt} of $\sim 2.1\,\%$, observed for the Rh6G-based ones. The fibres were assembled in bundles, and coupled to c-Si PV cells and EQE measurements were performed. The EQE curve of the PV cell resembled the excitation spectra of the optically active layer in use. The construction of large area LSCs based on easily-assembled triangular POFs minimizes self-absorption and transport spectral losses at the interface between adjacent fibres, as each fibre behaves as an individual LSC. Furthermore, this methodology enables the light harvesting and emission spectral ranges to be tuned to absorb the solar irradiation and to match the efficiency of the target PV cell, respectively, pointing out the suitability of these LSCs in real applications.

Challenges for the luminescent layer also include the use of abundant and sustainable

natural organic molecules. In the search for a sustainable approach to LSC design and processing, photosynthesis may be an inspiring natural mechanism if PV solar energy conversion is compared to an artificial photosynthesis stopped short. In photosynthesis, chlorophyll is responsible for sunlight harvesting, and its emission properties in the red-NIR spectral region are resonant with the absorption of the most used Si PV cells. In this thesis, natural-based LSCs made of chlorophyll molecules dispersed in organic-inorganic ureasil hybrids were studied. The chlorophyll-based active layer displays a large overlap with the solar irradiance on Earth, (absorption at 300-450 nm and 600-850 nm) and an emission spectrum centred around 675 nm. At low chlorophyll concentrations (10^{17} molecules$\cdot cm^{-3}$) the optical properties (fluorescence lifetime, absolute emission quantum yield and brightness) are preserved after the incorporation into the hybrid hosts. The optimised hybrid sample ($\eta_{opt} = 3.70 \pm 0.01\,\%$) was tested as a LSC coupled to commercial Si-based PV devices, revealing an increased PCE ($0.10 \pm 0.01\,\%$) and thus effectively improving the performance of the cell.

In addition, R- phycoerythrin (R-PE), which is a phycobiliprotein, extracted from *Gracilaria sp.* algae was also used in different LSCs geometries, which were subsequently studied. These optically active centres display large overlap with the solar irradiance on Earth (absorption at 300-700 nm) and emission spectra centred around 580 nm. LSCs composed of R-PE aqueous solutions with distinct concentrations were tested (4.2×10^{-8} to $1.7 \times 10^{-6}\,M$), as well as the effect of the geometrical gain ($G \sim 7$ and ~ 9) on performance. The best performance found for c-LSCs was for hollow-core fibre devices filled with the aqueous solutions with R-PE concentration of $4.2 \times 10^{-7}\,M$, and with $G \sim 7$. The above fiber LSCs were also assembled into bundles, which yielded η_{opt} and PCE values of 2.7 % and 22.2×10^{-3} %, respectively. Nevertheless, the best performing device was a p-LSC based on a glass cuvette, with η_{opt} and PCE values of 5.55 % and 0.27 %, respectively.

The use of natural emitting dyes, such as chlorophyll and R-PE molecules as optically active centres in LSC, demonstrates the potential of nature-inspired LSCs as a relevant step towards cheap and sustainable PV energy conversion.

In conclusion, to charge every-day devices such as mobile phones, tablets and LED lamps, LCSs must and can be scaled-up. In fact, LSCs have already been implemented in full-scale solar noise barriers. It is thus evident that LSCs are a promising technology with efficiencies able to compete for a place in the renewable energy market.

The aforementioned results were validated through the implementation of a Monte Carlo ray-tracing simulator to predict the performance of LDS layers and LSCs as a function of the geometry and materials (absorption and emitting spectral range and absolute emission quantum yield).

Finally, a short note about the potential supply disruption of Ln^{3+}, or rare earth elements. These elements are crucial in the transition to a green economy, due to their essential role in a large variety of technologies (permanent magnets, lamp phosphors, catalysts, rechargeable batteries and photonics) and are, therefore, in high demand [344, 345]. The low concentration in which they are present in the Earth's crust makes economic exploitation difficult and the consequent potential risk of a supply disruption is a present concern [346, 347]. Although risk analysis lies completely outside the scope of this thesis, the relatively small amount of these elements that are used (the optically active layers contain typically an amount of Ln^{3+} ions less than 10-20 %, in weight) makes that potential shortage not so problematic, relatively to what can be anticipated in other research areas.

Future work for LDS layers should include the evaluation of the performance of the LDS layers in function of the thickness of the layers in order to see how reflectance varies in such conditions.

Research should continue to focus on the production of hollow-core LSCs, because they provide additional protection to the active layer, with enlarged L_c in order to increase the exposed area and, consequently, the concentration factor. Additionally, light propagation was also observed in the active layer, and not exclusively in the PMMA. Thus, future work should be done towards increasing the refractive index contrast between the active layer and the waveguide, for instance, by using different types of polymer for the POF waveguide with increased refractive index. Also, the performance of the LDS layers and LSCs should be evaluated under direct and diffuse radiation in order to quantify the behaviour under such conditions. This would be a step forward in making LSCs market competitive and stimulating the much needed change in world energy consumption.

In what concerns liquid LSCs, the use of chlorophyll molecules in solution should also be tested encapsulated in PMMA hollow-core fibres. Although one of the focal points of this thesis was the construction of a proof-of-concept liquid LSCs based on R-PE solutions extracted from the red macroalgea, the stability of the dye is still a pertinent issue and

strategies to address this issue (for instance, fluid motion to avoid over exposure of the same molecules, preventing protein oxidation with sugar [348] or using singlet oxygen scavengers such as dithiothreitol and n-propyl gallate that show protective effects against R-PE photodegradation [349]) need to be addressed in future work. As carotenoids have been shown to protect chlorophyll from photo-destruction [350, 351], it may also be of interest to study non-purified samples incorporating chlorophyll and carotenoids should be of interest as well as non-purified R-PE solutions. The incorporation of the R-PE solution in hosts like organic-inorganic hybrids or PMMA should be optimized in order to obtain the emission properties of the R-PE molecules with the mechanical properties and protection to photo-degradation of the host.

Chapter 9

Appendix A - Experimental techniques

9.1 X-ray diffraction (XRD)

XRD patterns were recorded using a Philips XPert MPD powder X-ray diffractometer. The samples were exposed to CuK_α radiation (1.54 Å) in a 2θ range between 1.00 and 70.00° with a step of 0.05 and time-acquisition of $40\,s$ per step.

9.2 ^{29}Si magic-angle spinning (MAS) nuclear magnetic resonance (NMR) and ^{13}C cross-polarization (CP) MAS NMR spectra

The ^{29}Si MAS NMR spectra were recorded with a Bruker III Avance 400 and Bruker III Avance 500 ($9.4\,T$) spectrometer at 79.49 and $100.62\,MHz$, respectively. ^{29}Si MAS NMR spectra were recorded with $2\,\mu s$ (ca. 30°) rf pulses, a recycle delay of $60\,s$ and at a $5.0\,kHz$ spinning rate. ^{13}C CP/MAS NMR spectra were recorded with $4\,\mu s$ $1H$ 90° pulses, $2\,ms$ contact time, a recycle delay of $4\,s$ and at a spinning rate of $8\,kHz$.

9.3 Thermogravimetric analysis (TGA)

The TGA experiments were acquired from room temperature up to $800°C$ using an Instruments Shimadzu TGA-50 thermobalance at a heating rate of $10°C \cdot min^{-1}$. The purging gas employed was dried nitrogen supplied at constant flow rate ($40\,mL \cdot min^{-1}$).

9.4 Attenuated Total Reflectance (ATR)/Fourier Transform Infrared (FT- IR) Spectroscopy

ATR/FT-IR spectra were registered on a Thermo Scientific Nicolet iS50 FT-IR spectrometer, resorting to an ATR accessory with a diamond crystal.

9.5 UV/Visible Absorption

UV/visible absorption spectra were measured using a Lambda 950 dual-beam spectrometer (Perkin-Elmer).

9.6 Photoluminescence Spectroscopy

The photoluminescence spectra were recorded at room temperature with a modular double grating excitation spectrofluorimeter with a TRIAX 320 emission monochromator (Fluorolog-3, Horiba Scientific) coupled to a R928 Hamamatsu photomultiplier. Emission decay curves were recorded at room temperature on a Fluorolog TCSPC spectrofluorometer (Horiba Scientific) coupled to a TBX- 04 photomultiplier tube module ($950\,V$), a $200 \times 10^{-9}\,s$ time-to-amplitude converter with a delay of $70 \times 10^{-9}\,s$. The exciting source was a Horiba/JobinYvon pulsed diode (NanoLED-390, peak at $388\,nm$, $1.2 \times 10^{-9}\,s$ pulse duration, $1\,MHz$ repetition rate, and $150 \times 10^{-9}\,s$ synchronization delay).

9.7 Absolute Emission Quantum Yield

The absolute emission quantum yield values were measured at room temperature using a C9920-02 Hamamatsu system. The method is accurate within 10 %.

9.8 Spectroscopic ellipsometry

The dispersion curves were experimentally determined through spectroscopic ellipsometry using an AutoSE ellipsometer (HORIBA Scientific). The measurements were made with a total of 250 points out of the absorbance wavelength range of each material, an incidence angle of 69.8°, a signal to noise ratio of 25 and a measurement spot area of $250 \times 250\,\mu m^2$. The refractive index values of the films were calculated assuming a two-layer structure model. The data were minimised using the Simplex algorithm. For the hybrids, the dispersion curves were determined using Cauchy absorbent model, given by:

$$n(\lambda) = A + \frac{B}{\lambda^2} + \frac{C}{\lambda^4} \tag{9.1}$$

where A, B and C are constants.

9.9 LSCs optical power

The optical power at the cylindrical LSCs output was estimated using a commercial photodiode (IF D91, Industrial Fiber Optics, Inc.), with a wall plug efficiency to the AM1.5G solar spectrum distribution of 4 % coupled to the LSCs, according to the coupling scheme in Figure 2.7a. The optical power at the bundle and planar LSCs was estimated using a commercial c-Si PV cell (KXOB22-01X8F-ND) with an open circuit voltage of $4.7\,V$ under AM1.5G illumination.

9.10 External quantum efficiency (EQE) measurements

The EQE was estimated using a monocrystalline silicon PV cell (KXOB22-12X1L, IXYS), according to the coupling scheme in Figure 2.7b. I_{SC} measurements according to excitation wavelength were performed (to estimate EQE values) using a $150\,W$ xenon lamp as the light source coupled to a monochromator (Triax 180, Horiba Scientific), controlled by a LabVIEW routine. The I_{SC} values of the PV cell were measured using a semiconductor device analyser (B1500A, Keysight Technologies). The power of the incident beam (P_{in}) was measured with an integrating sphere (ISP 150L, Instrument Systems) connected to a detector (MAS40-121, Instrument Systems).

9.11 Optical microscopy

Optical microscopy images were obtained by an Olympus BX51 brightfield microscope (10 objective), in the reflection mode, equipped with a hyperspectral imaging system (CytoViva Inc., Auburn, AL). The system integrates an optical imaging CCD camera (QImaging Retiga 4000R), a visible-NIR hyperspectral camera (Cytoviva), a motorized stage and a halogen light source (Fiber-lite, DC-950). The light scattered from the sample in the 400 to 1000 nm spectral region was captured by the hyperspectral camera at each line for each pixel in the sample combining motion of the microscope stage. The hyperspectral scanning is vertical and each image results from 696 lines with each pixel field-of-view on the hyperspectral images corresponding to $1.3 \times 1.3\,\mu m^2$ on the sample plane. All the hyperspectral data were acquired and analysed using ENVI 4.8 software.

Chapter 10

Appendix B - List of Publications

- **A. R. Frias**, M. A. Cardoso, A. R. N. Bastos, S. F. H. Correia, P. S. André, L. D. Carlos, V. de Zea Bermudez and R. A. S. Ferreira,Transparent luminescent solar concentrators using Ln^{3+}-based ionosilicas towards photovoltaic windows, *Energies* 2019, 12(3), 451.

- **A. R. Frias**, S. F. H. Correia, M. Martins, S. P. M. Ventura, E. Pecoraro, S. J. L. Ribeiro, P. S. André, R. A. S. Ferreira, J. A. P. Coutinho, and L. D. Carlos. "Sustainable Liquid Luminescent Solar Concentrators", *Advanced Sustainable Systems*, 2019, 1800134.

- **A. R. Frias**, E. Pecoraro, S. F. H. Correia, L. M. G. Minas, A. R. Bastos, S. Garca-Revilla, R. Balda, S. J. L. Ribeiro, P. S. Andr, L. D. Carlos and R. A. S. Ferreira, Sustainable luminescent solar concentrators based on organicinorganic hybrids modified with chlorophyll, *Journal of Materials Chemistry A*, 2018, 6, 8712-8723.

- S. F. H. Correia, **A. R. Frias**, L. Fu, R. Rondo, E. Pecoraro, S. J. L. Ribeiro, P. S. Andr, R. A. S. Ferreira, L. D. Carlos, LargeArea Tunable VisibletoNearInfrared Luminescent Solar Concentrators, *Advanced Sustainable Systems*, 2018, 1800002.

- R. Rondão, **A. R. Frias**, S. F. H. Correia, L. Fu, V. de Zea Bermudez, P. S. Andr, R. A. S. Ferreira, and L. D. Carlos, High-Performance Near-Infrared Luminescent Solar Concentrators, *ACS Applied Materials & Interfaces*, 9 (14), 2017, 12540-12546.

- S. F. H. Correia, **A. R. Frias**, L. D. Carlos, Paulo S. André, Rute A. S. Ferreira, "Red-to-green emitting organic-inorganic coatings for photovoltaics", *in preparation.*

- S. F. H. Correia, **A. R. Frias**, P.S. André, R. A. S. Ferreira, and L. D. Carlos, "Concentradores solares luminescentes: o que são e para que servem", *in preparation*.
- **A. R. Frias**, S. F. H. Correia, P. S. André, R. A. S. Ferreira, L. D. Carlos, Materials and design for efficient spectral converters, in *Nanocomposites for Photonics and Electronics Applications*, Elsevier to be published in 2019. Book chapter.

Bibliography

[1] International Energy Outlook 2018. *EIA U.S. Energy Information Administration, last visited on 04/10/2018*. 2018. URL: https://www.eia.gov/outlooks/ieo/.

[2] S. Krauter. *Solar electric power generation*. Springer, 2006.

[3] O. Y. Edelenbosch et al. "Luminescent solar concentrators with fiber geometry". In: *Opt. Express* 21.S3 (2013), A503–A514.

[4] X. Huang et al. "Enhancing solar cell efficiency: the search for luminescent materials as spectral converters". In: *Chem. Soc. Rev.* 42 (Jan. 2013), pp. 173–201.

[5] J.-C. G. Bünzli and A.-S. Chauvin. "Lanthanides in Solar Energy Conversion". In: *Handbook on the Physics and Chemistry of Rare-Earths*. Ed. by Jean-Claude G. Bünzli and Vitalij K. Pecharsky. Vol. 44. Amsterdam: Elsevier B. V., 2014, pp. 169–281.

[6] M. A. Green et al. "Solar cell efficiency tables (version 47)". In: *Prog. Photovolt: Res. Appl.* 24.1 (), pp. 3–11. eprint: https://onlinelibrary.wiley.com/doi/pdf/10.1002/pip.2728.

[7] L. El Chaar, L. A. Lamont, and N. El Zein. "Review of photovoltaic technologies". In: *Renew. Sust. Energ. Rev.* 15 (June 2011), pp. 2165–2175.

[8] R. Harikisun and H. Desilvestro. "Long-term stability of dye solar cells". In: *Solar Energy* 85.6 (2011), pp. 1179–1188.

[9] J. Seo, J. H. Noh, and S. Seok. "Rational strategies for efficient perovskite solar cells". In: *Acc. Chem. Res.* 49.3 (2016), pp. 562–572.

[10] G. Hodes. "Perovskite-based solar cells". In: *Science* 342.6156 (2013), pp. 317–318.

[11] K. A. Bush et al. "23.6%-efficient monolithic perovskite/silicon tandem solar cells with improved stability". In: *Nat. Energy* 2.4 (2017), p. 17009.

[12] A. B. Djurišić et al. "Perovskite solar cells-An overview of critical issues". In: *Prog. Quant. Electron.* 53 (2017), pp. 1–37.

[13] M. A. Loi and J. C. Hummelen. "Hybrid solar cells: perovskites under the sun". In: *Nat. Mater.* 12.12 (2013), pp. 1087–1089.

[14] B. S. Richards. "Enhancing the performance of silicon solar cells via the application of passive luminescence conversion layers". In: *Sol. Energy Mater. Sol. Cells* 90 (Sept. 2006), pp. 2329–2337.

[15] W. Shockley and H. J. Queisser. "Detailed Balance Limit of Efficiency of P-N Junction Solar Cells". In: *J. Appl. Phys.* 32 (1961), pp. 510–519.

[16] B. McKenna and R. C. Evans. "Towards Efficient Spectral Converters through Materials Design for Luminescent Solar Devices". In: *Adv. Mater.* 29 (July 2017), p. 1606491.

[17] W. G. J. H. M. van Sark, A. Meijerink, R. E. I. Schropp, et al. "Solar spectrum conversion for photovoltaics using nanoparticles". In: *CIER-E-2012-8* (2012), pp. 1–28.

[18] C. Strümpel et al. "Modifying the solar spectrum to enhance silicon solar cell efficiency - An overview of available materials". In: *Sol. Energy Mater. Sol. Cells* 91.4 (2007), pp. 238–249.

[19] B. S. Richards. "Luminescent layers for enhanced silicon solar cell performance: Down-conversion". In: *Sol. Energ. Mat. Sol. C.* 90.9 (2006), pp. 1189–1207.

[20] A. Shalav, B. S. Richards, and M. A. Green. "Luminescent layers for enhanced silicon solar cell performance: Up-conversion". In: *Sol. Energ. Mat. Sol. C.* 91.9 (2007), pp. 829–842.

[21] T. Trupke et al. "Efficiency enhancement of solar cells by luminescent up-conversion of sunlight". In: *Sol. Energ. Mat. Sol. C.* 90.18 (2006), pp. 3327–3338.

[22] G. Conibeer. "Third-generation photovoltaics". In: *Mater. Today* 10.11 (2007), pp. 42–50.

[23] M. G. Debije and P. P. C. Verbunt. "Thirty Years of Luminescent Solar Concentrator Research: Solar Energy for the Built Environment". In: *Adv. Energy Mater.* 2 (Jan. 2012), pp. 12–35.

[24] D. Agostino, P. Zangheri, and L. Castellazzi. "Towards nearly zero energy buildings in Europe: A focus on retrofit in non-residential buildings". In: *Energies* 10.1 (2017), p. 117.

[25] P. Torcellini et al. "Zero energy buildings: A critical look at the definition". In: *NREL and Department of Energy, US* (2006).

[26] Avancis CNBM. *Rooftop systems with state-of-the-art CIS solar modules, last visited on 20/09/2018*. 2018. URL: https://www.avancis.de/en/rooftop-systems/.

[27] Avancis CNBM. *Solar facades for architects, engineers and planners, last visited on 20/09/2018*. 2018. URL: https://www.avancis.de/en/solar-facades/.

[28] F. M. Vossen, M. P. J. Aarts, and M. G. Debije. "Visual performance of red luminescent solar concentrating windows in an office environment". In: *Energ. Buildings* 113 (2016), pp. 123–132.

[29] The Kuggen. *Building in Gothenburg, Sweden, last visited on 01/10/2018*. 2018. URL: https://twistedsifter.com/2015/10/kuggen-building-gothenburg-sweden/.

[30] Carabanchel 24. *Building in Madrid, Spain, last visited on 01/10/2018*. 2018. URL: https://trendland.com/contemporary-building-blocks-color-blocked-architecture/.

[31] MUSAC (Museo de Arte Contemporaneo de Castilla y Leon). *Building in Leon, Spain, last visited on 01/10/2018*. 2018. URL: https://duranvirginia.wordpress.com/2014/02/20/12-amazingly-colorful-buildings/.

[32] The Gherkin. *Building in London, United Kingdom, last visited on 01/10/2018*. 2018. URL: https://londontopia.net/site-news/featured/30-st-mary-axe-10-interesting-facts-figures-gherkin/.

[33] El Captivador. *Building in Alicante, Spain, last visited on 01/10/2018*. 2018. URL: http://www.knstrct.com/architecture-blog/2014/6/25/environmental-education-centre-el-captivador-designed-by-crystalzoo.

[34] The Palais des congres de Montreal. *Building in Montreal, Quebec, Canada, last visited on 01/10/2018*. 2018. URL: https://congresmtl.com/en/convention-center/society/organization-chart/.

[35] Marina Bay Sands. *Building in Singapore, last visited on 01/10/2018*. 2018. URL: https://gurumustsee.ru/otel-marina-bay-sands-nastoyashhaya-skazka-v-singapure/.

[36] Y. Li et al. "Review on the Role of Polymers in Luminescent Solar Concentrators". In: *J. Polym. Sci. A* (2018).

[37] M. G. Debije and V. A. Rajkumar. "Direct versus indirect illumination of a prototype luminescent solar concentrator". In: *Solar Energy* 122 (2015), pp. 334–340.

[38] M. Kanellis et al. "The solar noise barrier project: 1. Effect of incident light orientation on the performance of a large-scale luminescent solar concentrator noise barrier". In: *Renew. Energy* 103 (2017), pp. 647–652.

[39] I. G. Lim et al. "Wearable wireless power transmission apparatus and wireless power transmission method using the same". (US). 2014.

[40] Tommy Hilfiger. *Solar Clothing, last visited on 02/10/2018*. 2018. URL: http://www.pvilion.com/solar-clothing/.

[41] Gratzel Solar Backpack 2. *Solar bag, last visited on 02/10/2018*. 2018. URL: https://shop.epfl.ch/en/product/solar-bag-graetzel.

[42] Solaires Solar-Powered Backpacks Charge Gadgets on the Go. *Solar bag, last visited on 02/10/2018*. 2018. URL: https://inhabitat.com/ecouterre/project-solaires-solar-powered-backpacks-charge-gadgets-on-the-go/.

[43] Lux Solar Panel Necklace Lights Up Any Outfit. *Solar bag, last visited on 02/10/2018*. 2018. URL: https://inhabitat.com/ecouterre/couture-solar-panel-necklace-lights-up-any-outfit/.

[44] Soofa. *Smart bench, last visited on 02/10/2018*. 2018. URL: https://www.news5cleveland.com/news/local-news/oh-cuyahoga/no-need-to-be-off-the-grid-when-youre-at-one-shaker-heights-park-thanks-to-soofa-smart-bench.

[45] eTree. *Tree-like street furniture, last visited on 02/10/2018*. 2018. URL: https://www.jcdecaux.com/blog/street-furniture-goes-sustainable-and-self-sufficient-jcdecaux.

[46] Wearable solar panels. *Solar-Powered Soldiers to Revolutionize Australian Combat, last visited on 02/10/2018*. 2018. URL: https://www.jcdecaux.com/blog/street-furniture-goes-sustainable-and-self-sufficient-jcdecaux.

[47] M. G. Debije et al. "The solar noise barrier project: 2. The effect of street art on performance of a large scale luminescent solar concentrator prototype". In: *Renew. Energy* 113 (2017), pp. 1288–1292.

[48] M. G. Debije et al. "The solar noise barrier project: 3. The effects of seasonal spectral variation, cloud cover and heat distribution on the performance of full-scale luminescent solar concentrator panels". In: *Renew. Energy* 116 (2018), pp. 335–343.

[49] SONOB. *Installation on Dutch Highways , last visited on 02/10/2018*. 2018. URL: https://www.savingwithsolar.com.au/tag/solar-panel-sound-barriers/.

[50] E. Klampaftis et al. "Enhancing the performance of solar cells via luminescent down-shifting of the incident spectrum: A review". In: *Sol. Energy Mater. Sol. Cells* 93 (Aug. 2009), pp. 1182–1194.

[51] G. J. J. Draaisma et al. "Ligand exchange as a tool to improve quantum dot miscibility in polymer composite layers used as luminescent down-shifting layers for photovoltaic applications". In: *J. Mater. Chem. C* 4 (2016), pp. 5747–5754.

[52] S. D. Hodgson et al. "The impact of quantum dot concentration on the optical properties of QD/PMMA luminescent down-shifting films applied to CdTe photovoltaic devices". In: *Nano Energy* 4 (2014), pp. 1–6.

[53] D. K. G. de Boer et al. "Progress in phosphors and filters for luminescent solar concentrators". In: *Opt. Express* 20.S3 (May 2012), A395–A405.

[54] A. Solodovnyk et al. "Optimization of Solution-Processed Luminescent Down-Shifting Layers for Photovoltaics by Customizing Organic Dye Based Thick Films". In: *Energy Technol.* 4.3 (2016), pp. 385–392.

[55] D. Alonso-Álvarez et al. "Luminescent down-shifting experiment and modelling with multiple photovoltaic technologies". In: *Prog. Photovolt. Res. Appl.* 23.4 (2015), pp. 479–497.

[56] T. S. Parel, L. Danos, and T. Markvart. "Application of concentrating luminescent down-shifting structures to CdS/CdTe solar cells with poor short wavelength response". In: *Sol. Energy Mater. Sol. Cells* 140 (2015), pp. 306–311.

[57] Y. H. Ghymn et al. "A luminescent down-shifting and moth-eyed anti-reflective film for highly efficient photovoltaic devices". In: *Nanoscale* 7.44 (2015), pp. 18642–18650.

[58] M. Hong et al. "Air-exposing microwave-assisted synthesis of CuInS 2/ZnS quantum dots for silicon solar cells with enhanced photovoltaic performance". In: *RSC Adv.* 5.124 (2015), pp. 102682–102688.

[59] Y. Li et al. "Rational design of tetraphenylethylene-based luminescent down-shifting molecules: photophysical studies and photovoltaic applications in a CdTe solar cell from small to large units". In: *Phys. Chem. Chem. Phys.* 16.47 (2014), pp. 26193–26202.

[60] W.-B. Hung and T.-M. Chen. "Efficiency enhancement of silicon solar cells through a downshifting and antireflective oxysulfide phosphor layer". In: *Sol. Energy Mater. Sol. Cells* 133 (2015), pp. 39–47.

[61] T. Fix et al. "Enhancement of silicon solar cells by downshifting with Eu and Tb coordination complexes". In: *Prog. in Photovoltaics* 24 (Sept. 2016), pp. 1251–1260.

[62] K. Kawano et al. "Application of rare-earth complexes for photovoltaic precursors". In: *Sol. Energy Mater. Sol. Cells* 48 (Nov. 1997), pp. 35–41.

[63] E. Cattaruzza et al. "Ion exchange doping of solar cell coverglass for sunlight down-shifting". In: *Sol. Energy Mater. Sol. Cells* 130 (2014), pp. 272–280.

[64] F. Bella et al. "Performance and stability improvements for dye-sensitized solar cells in the presence of luminescent coatings". In: *J. Power Sources* 283 (2015), pp. 195–203.

[65] S. Marchionna et al. "Photovoltaic quantum efficiency enhancement by light harvesting of organo-lanthanide complexes". In: *J. Lumin.* 118 (June 2006), pp. 325–329.

[66] T. Maruyama, A. Enomoto, and K. Shirasawa. "Solar cell module colored with fluorescent plate". In: *Sol. Energy Mater. Sol. Cells* 64.3 (2000), pp. 269–278.

[67] B. S. Richards and K. R. McIntosh. "Overcoming the poor short wavelength spectral response of CdS/CdTe photovoltaic modules via luminescence down-shifting: ray-tracing simulations". In: *Prog. Photovolt. Res. Appl.* 15.1 (2007), pp. 27–34.

[68] K. Machida et al. "Preparation and application of lanthanide complex incorporated ormosil composite phosphor films". In: *J. Lumin.* 87-9 (May 2000), pp. 1257–1259.

[69] D. Pintossi et al. "Luminescent Downshifting by Photo-Induced Sol-Gel Hybrid Coatings: Accessing Multifunctionality on Flexible Organic Photovoltaics via Ambient Temperature Material Processing". In: *Adv. Electron. Mater.* 2.11 (2016), p. 1600288.

[70] T.-T. Xuan et al. "Microwave synthesis of high luminescent aqueous CdSe/CdS/ZnS quantum dots for crystalline silicon solar cells with enhanced photovoltaic performance". In: *RSC Adv.* 5.10 (2015), pp. 7673–7678.

[71] V. Svrcek et al. "A silicon nanocrystal/polymer nanocomposite as a down-conversion layer in organic and hybrid solar cells". In: *Nanoscale* 7.27 (2015), pp. 11566–11574.

[72] I. Levchuk et al. "Industrially scalable and cost-effective Mn 2+ doped Zn x Cd 1-x S/ZnS nanocrystals with 70% photoluminescence quantum yield, as efficient down-shifting materials in photovoltaics". In: *Energy Environ. Sci.* 9.3 (2016), pp. 1083–1094.

[73] H.-V. Han et al. "A highly efficient hybrid GaAs solar cell based on colloidal-quantum-dot-sensitization". In: *Sci. Rep.* 4 (2014), p. 5734.

[74] G. C. Glaeser and U. Rau. "Improvement of photon collection in Cu (In, Ga) Se2 solar cells and modules by fluorescent frequency conversion". In: *Thin Solid Films* 515.15 (2007), pp. 5964–5967.

[75] J. Y. Chen et al. "Efficiency improvement of Si solar cells using metal-enhanced nanophosphor fluorescence". In: *Sol. Energy Mater. Sol. Cells* 120 (Jan. 2014), pp. 168–174.

[76] J. Xu et al. "Light Trapping and Down-Shifting Effect of Periodically Nanopatterned Si-Quantum-Dot-Based Structures for Enhanced Photovoltaic Properties". In: *Part. Part. Syst. Char.* 31.4 (2014), pp. 459–464.

[77] M. Brossard et al. "Novel Non-radiative Exciton Harvesting Scheme Yields a 15% Efficiency Improvement in High-Efficiency III–V Solar Cells". In: *Adv. Opt. Mater.* 3.2 (2015), pp. 263–269.

[78] P. Song, C. Zhang, and P. Zhu. "Eu3+-Mn2+-doped bi-functional glasses with solar photon downshifting: Application to CdS/CdTe solar cells". In: *J. Alloy. Comp.* 661 (2016), pp. 14–19.

[79] H. Ahmed, J. Doran, and S. J. McCormack. "Increased short-circuit current density and external quantum efficiency of silicon and dye sensitised solar cells through plasmonic luminescent down-shifting layers". In: *Solar Energy* 126 (2016), pp. 146–155.

[80] G. Griffini et al. "Multifunctional Luminescent Down-Shifting Fluoropolymer Coatings: A Straightforward Strategy to Improve the UV-Light Harvesting Ability and Long-Term Outdoor Stability of Organic Dye-Sensitized Solar Cells". In: *Adv. Energy Mater.* 5 (Feb. 2015).

[81] Z. Hosseini et al. "Enhanced light harvesting with a reflective luminescent down-shifting layer for dye-sensitized solar cells". In: *ACS Appl. Mater. Interfaces* 5.12 (2013), pp. 5397–5402.

[82] G.-F. Ma et al. "Performance enhancement of polymer solar cells with luminescent down-shifting sensitizer". In: *Appl. Phys. Lett.* 103.4 (2013), 126_1.

[83] J. L. Huang et al. "An easy approach of preparing strongly luminescent carbon dots and their polymer based composites for enhancing solar cell efficiency". In: *Carbon* 70 (2014), pp. 190–198.

[84] N. Chander et al. "Reduced ultraviolet light induced degradation and enhanced light harvesting using YVO4: Eu3+ down-shifting nano-phosphor layer in organometal halide perovskite solar cells". In: *Appl. Phys. Lett.* 105.3 (2014), p. 033904.

[85] X. Hou et al. "High-performance perovskite solar cells by incorporating a ZnGa2O4: Eu3+ nanophosphor in the mesoporous TiO2 layer". In: *Sol. Energy Mater. Sol. Cells* 149 (2016), pp. 121–127.

[86] F. Bella et al. "Improving efficiency and stability of perovskite solar cells with photocurable fluoropolymers". In: *Science* 354.6309 (2016), pp. 203–206.

[87] C. P. Thomas, A. B. Wedding, and S. O. Martin. "Theoretical enhancement of solar cell efficiency by the application of an ideal down-shifting thin film". In: *Sol. Energy Mater. Sol. Cells* 98 (2012), pp. 455–464.

[88] T. Jin et al. "Photovoltaic cell characteristics of hybrid silicon devices with lanthanide complex phosphor-coating film". In: *Journal of the Electrochemical Society* 144 (Nov. 1997), pp. 4054–4058.

[89] L. D. Carlos et al. "Lanthanide-Containing Light-Emitting Organic-Inorganic Hybrids: A Bet on the Future". In: *Adv. Mater.* 21 (Feb. 2009), pp. 509–534.

[90] P. Chung, H. Chung, and P. H. Holloway. "Phosphor coatings to enhance Si photovoltaic cell performance". In: *J. Vac. Sci. Technol. A* 25.1 (2007), pp. 61–66.

[91] K. R. McIntosh et al. "Increase in external quantum efficiency of encapsulated silicon solar cells from a luminescent down-shifting layer". In: *Prog. Photovoltaics Res. App.* 17.3 (2009), pp. 191–197.

[92] M. Stupca et al. "Enhancement of polycrystalline silicon solar cells using ultrathin films of silicon nanoparticle". In: *Appl. Phys. Lett.* 91.6 (2007), p. 063107.

[93] C. Wang et al. "Long Afterglow SrAl2O4: Eu2+, Dy3+ Phosphors as Luminescent Down-Shifting Layer for Crystalline Silicon Solar Cells". In: *Int. J. Appl. Ceram. Tec.* 12.4 (2015), pp. 722–727.

[94] F. Steudel et al. "Luminescent borate glass for efficiency enhancement of CdTe solar cells". In: *J. Lumin.* 164 (2015), pp. 76–80.

[95] Y.-K. Liao et al. "Highly Efficient Flexible Hybrid Nanocrystal-Cu (In, Ga) Se2 (CIGS) Solar Cells". In: *Adv. Energy Mater.* 5.2 (2015), p. 1401280.

[96] K. Bouras et al. "Structural, optical and electrical properties of Nd-doped SnO2 thin films fabricated by reactive magnetron sputtering for solar cell devices". In: *Sol. Energy Mater. Sol. Cells* 145 (2016), pp. 134–141.

[97] M. Jørgensen et al. "Stability of polymer solar cells". In: *Adv. Mater.* 24.5 (2012), pp. 580–612.

[98] J. Kettle et al. "Printable luminescent down shifter for enhancing efficiency and stability of organic photovoltaics". In: *Sol. Energy Mater. Sol. Cells* 144 (2016), pp. 481–487.

[99] O. Moudam et al. "Application of UV-absorbing silver (I) luminescent down shifter for PTB7 organic solar cells for enhanced efficiency and stability". In: *RSC Adv.* 5.16 (2015), pp. 12397–12402.

[100] M. Prosa et al. "Integration of a silk fibroin based film as a luminescent down-shifting layer in ITO-free organic solar cells". In: *RSC Adv.* 4.84 (2014), pp. 44815–44822.

[101] T. A. Berhe et al. "Organometal halide perovskite solar cells: degradation and stability". In: *Energy Environ. Sci.* 9.2 (2016), pp. 323–356.

[102] A. Zastrow et al. "On the conversion of solar radiation with fluorescent planar concentrators (FPCs)". In: *Photovoltaic Sol. Energy Conference*. Springer. 1981, pp. 413–417.

[103] F. Vollmer and W. Rettig. "Fluorescence loss mechanism due to large-amplitude motions in derivatives of 2, 2-bipyridyl exhibiting excited-state intramolecular proton transfer and perspectives of luminescence solar concentrators". In: *J. Photochem. Photobiol. A* 95.2 (1996), pp. 143–155.

[104] W. G. J. H. M. van Sark et al. "Luminescent Solar Concentrators - A review of recent results". In: *Opt. Express* 16 (Dec. 2008), pp. 21773–21792.

[105] J. S. Batchelder, A. H. Zewail, and T. Cole. "Luminescent Solar Concentrators .2. Experimental and Theoretical-Analysis of Their Possible Efficiencies". In: *Appl. Opt.* 20 (1981), pp. 3733–3754.

[106] A. M. Hermann. "Luminescent solar concentrators - a review". In: *Solar Energy* 29.4 (1982), pp. 323–329.

[107] B. A. Swartz, T. Cole, and A. H. Zewail. "Photon trapping and energy transfer in multiple-dye plastic matrices: an efficient solar-energy concentrator". In: *Opt. Lett.* 1.2 (1977), pp. 73–75.

[108] J. M. Drake et al. "Organic dyes in PMMA in a planar luminescent solar collector: a performance evaluation". In: *Appl. Opt.* 21.16 (1982), pp. 2945–2952.

[109] I. Baumberg et al. "Effect of polymer matrix on photo-stability of photo-luminescent dyes in multi-layer polymeric structures". In: *Polym. Degrad. Stabil.* 73.3 (2001), pp. 403–410.

[110] A. F. Mansour et al. "Laser dyes doped with poly(ST-Co-MMA) as fluorescent solar collectors and their field performance". In: *Polym. Test.* 24.4 (2005), pp. 519–525.

[111] R. Kinderman et al. "IV performance and stability study of dyes for luminescent plate concentrators". In: *J. Sol. Energy Eng.* 129.3 (2007), pp. 277–282.

[112] L. H. Slooff et al. "A luminescent solar concentrator with 7.1% power conversion efficiency". In: *Phys. Status Solidi Rapid Res. Lett.* 2 (Dec. 2008), pp. 257–259.

[113] J. Yoon et al. "Flexible concentrator photovoltaics based on microscale silicon solar cells embedded in luminescent waveguides". In: *Nat. Commun.* 2 (2011), p. 343.

[114] L. R. Wilson and B. S. Richards. "Measurement method for photoluminescent quantum yields of fluorescent organic dyes in polymethyl methacrylate for luminescent solar concentrators". In: *Appl. Opt.* 48.2 (2009), pp. 212–220.

[115] M. G. Debije et al. "Measured surface loss from luminescent solar concentrator waveguides". In: *Appl. Opt.* 47.36 (2008), pp. 6763–6768.

[116] M. G. Debije et al. "Promising fluorescent dye for solar energy conversion based on a perylene perinone". In: *Appl. Opt.* 50.2 (2011), pp. 163–169.

[117] R. Reisfeld et al. "Luminescent solar concentrators based on thin films of polymethylmethacrylate on a polymethylmethacrylate support". In: *Sol. Energy Mater.* 17.6 (1988), pp. 439–455.

[118] G. Seybold and G. Wagenblast. "New perylene and violanthrone dyestuffs for fluorescent collectors". In: *Dyes Pigm.* 11.4 (1989), pp. 303–317.

[119] R. Reisfeld, D. Shamrakov, and C. Jorgensen. "Photostable Solar Concentrators Based on Fluorescent Glass-Films". In: *Sol. Energy Mater. Sol. Cells* 33 (Aug. 1994), pp. 417–427.

[120] A. F. Mansour. "Optical efficiency and optical properties of luminescent solar concentrators". In: *Polym. Test.* 17.5 (1998), pp. 333–343.

[121] A. F. Mansour et al. "Optical study of perylene dye doped poly (methyl methacrylate) as fluorescent solar collector". In: *Polym. Int.* 51.5 (2002), pp. 393–397.

[122] F. Castiglione et al. "Spectroscopic characterization of red perylimide/surfactant nanocomposites". In: *J. Mater. Sci.* 46.19 (2011), pp. 6402–6407.

[123] S. M. Reda. "Stability and photodegradation of phthalocyanines and hematoporphyrin doped PMMA as solar concentrators". In: *Solar Energy* 81.6 (2007), pp. 755–760.

[124] C. L. Mulder et al. "Luminescent Solar Concentrators Employing Phycobilisomes". In: *Adv. Mater.* 21 (Aug. 2009), pp. 3181–3185.

[125] N. J. L. K. Davis et al. "Star-shaped fluorene-BODIPY oligomers: versatile donor-acceptor systems for luminescent solar concentrators". In: *J. Mater. Chem. C* 5 (2017), pp. 1952–1962.

[126] R. Bose et al. "Resonance Energy Transfer in Luminescent Solar Concentrators". In: *35th IEEE Photovoltaic Specialists Conference* (2010), pp. 467–470.

[127] M. J. Currie et al. "High-efficiency organic solar concentrators for photovoltaics". In: *Science* 321 (July 2008), pp. 226–228.

[128] A. R. Frias et al. "Sustainable luminescent solar concentrators based on organic-inorganic hybrids modified with chlorophyll". In: *J. Mater. Chem. A* 6 (2018), pp. 8712–8723.

[129] J. A. Levitt and W. H. Weber. "Materials for luminescent greenhouse solar collectors". In: *Appl. Opt.* 16.10 (1977), pp. 2684–2689.

[130] W. H. Weber and J. Lambe. "Luminescent Greenhouse Collector for Solar-Radiation". In: *Appl. Opt.* 15 (1976), pp. 2299–2300.

[131] M. A. El-Shahawy and A. F. Mansour. "Optical properties of some luminescent solar concentrators". In: *J. Mater. Sci. Mater. Electron.* 7.3 (1996), pp. 171–174.

[132] Y. Ren, M. Szablewski, and G. H. Cross. "Waveguide photodegradation of nonlinear optical organic chromophores in polymeric films". In: *Appl. Opt.* 39.15 (2000), pp. 2499–2506.

[133] N. A. Bakr, A. F. Mansour, and M. Hammam. "Optical and thermal spectroscopic studies of luminescent dye doped poly (methyl methacrylate) as solar concentrator". In: *J. Appl. Polym. Sci.* 74.14 (1999), pp. 3316–3323.

[134] J. B. Birks. "Photophysics of Aromatic Molecules". In: *Berichte der Bunsengesellschaft für physikalische Chemie* 74.12 (1970), pp. 1294–1295.

[135] G. D. Scholes et al. "Lessons from nature about solar light harvesting". In: *Nat. Chem.* 3.10 (2011), p. 763.

[136] S. F. H. Correia et al. "Luminescent solar concentrators: challenges for lanthanide-based organic-inorganic hybrid materials". In: *J. Mater. Chem. A* 2 (2014), pp. 5580–5596.

[137] R. C. Evans, P. Douglas, and C. J. Winscom. "Coordination complexes exhibiting room-temperature phosphorescence: evaluation of their suitability as triplet emitters in organic light emitting diodes". In: *Coord. Chem. Rev.* 250.15-16 (2006), pp. 2093–2126.

[138] B. Mahler et al. "Towards non-blinking colloidal quantum dots". In: *Nat. Mater.* 7.8 (2008), p. 659.

[139] K. Yu et al. "Low-Temperature Noninjection Approach to Homogeneously-Alloyed PbSe x S1- x Colloidal Nanocrystals for Photovoltaic Applications". In: *ACS Appl. Mater. Interfaces* 3.5 (2011), pp. 1511–1520.

[140] W. Zhang and X. Zhong. "Facile synthesis of ZnS- CuInS2-alloyed nanocrystals for a color-tunable fluorchrome and photocatalyst". In: *Inorg. Chem.* 50.9 (2011), pp. 4065–4072.

[141] F. Purcell-Milton and Y. K. Gun'ko. "Quantum dots for Luminescent Solar Concentrators". In: *J. Mater. Chem.* 22 (33 2012), pp. 16687–16697.

[142] K. M. Tsoi et al. "Are quantum dots toxic? Exploring the discrepancy between cell culture and animal studies". In: *Acc. Chem. Res* 46.3 (2012), pp. 662–671.

[143] S. Y. Lim, W. Shen, and Z. Gao. "Carbon quantum dots and their applications". In: *Chem. Soc. Rev.* 44.1 (2015), pp. 362–381.

[144] C. M. Gonzalez and J. G. C. Veinot. "Silicon nanocrystals for the development of sensing platforms". In: *J. Mater. Chem. C* 4.22 (2016), pp. 4836–4846.

[145] P. P. C. Verbunt et al. "Controlling light emission in luminescent solar concentrators through use of dye molecules aligned in a planar manner by liquid crystals". In: *Adv. Funct. Mater.* 19.17 (2009), pp. 2714–2719.

[146] M. G. Debije. "Solar energy collectors with tunable transmission". In: *Adv. Funct. Mater.* 20.9 (2010), pp. 1498–1502.

[147] M. G. Debije et al. "Combining Positive and Negative Dichroic Fluorophores for Advanced Light Management in Luminescent Solar Concentrators". In: *Adv. Opt. Mater.* 2.7 (2014), pp. 687–693. eprint: `https://onlinelibrary.wiley.com/doi/pdf/10.1002/adom.201400132`.

[148] B. J. Bruijnaers, A. P. H. J. Schenning, and M. G. Debije. "Capture and concentration of light to a spot in plastic lightguides by circular luminophore arrangements". In: *Adv. Opt. Mater.* 3.2 (2015), pp. 257–262.

[149] C. L. Mulder et al. "Dye alignment in luminescent solar concentrators: I. Vertical alignment for improved waveguide coupling". In: *Opt. Express* 18.101 (2010), A79–A90.

[150] B. C. Rowan, L. R. Wilson, and B. S. Richards. "Advanced material concepts for luminescent solar concentrators". In: *IEEE J. Sel. Top. Quantum Electron.* 14.5 (2008), pp. 1312–1322.

[151] B. G. Ranby and J. F. Rabek. *Photodegradation, photo-oxidation, and photostabilization of polymers*. New York, Wiley, 1975.

[152] J. W. E. Wiegman and E. van der Kolk. "Building integrated thin film luminescent solar concentrators: Detailed efficiency characterization and light transport modelling". In: *Sol. Energy Mater. Sol. Cells* 103 (2012), pp. 41–47.

[153] F. Rey-García et al. "Sol–gel coatings: An alternative route for producing planar optical waveguides". In: *Thin Solid Films* 519.22 (2011), pp. 7982–7986.

[154] S. Parola et al. "Optical Properties of Hybrid Organic-Inorganic Materials and their Applications". In: *Adv. Funct. Mater.* 26.36 (2016), pp. 6506–6544.

[155] A. Kaniyoor et al. “Design and Response of High-Efficiency, Planar, Doped Luminescent Solar Concentrators Using Organic-Inorganic Di-Ureasil Waveguides”. In: *Adv. Opt. Mater.* 4 (Mar. 2016), pp. 444–456.

[156] R. Rondão et al. “High-performance near-infrared luminescent solar concentrators”. In: *ACS Appl. Mater. Interfaces* 9 (2017), pp. 12540–12546.

[157] S. F. H. Correia et al. “Large-Area Tunable Visible-to-Near-Infrared Luminescent Solar Concentrators”. In: *Advanced Sustainable Systems* (2018), p. 1800002.

[158] S. F. H. Correia et al. “Scale up the collection area of luminescent solar concentrators towards metre-length flexible waveguiding photovoltaics”. In: *Prog. in Photovoltaics* 24 (Sept. 2016), pp. 1178–1193.

[159] S. F. H. Correia et al. “High-efficiency luminescent solar concentrators for flexible waveguiding photovoltaics”. In: *Sol. Energy Mater. Sol. Cells* 138 (July 2015), pp. 51–57.

[160] M. M. Nolasco et al. “Engineering highly efficient Eu (III)-based tri-ureasil hybrids toward luminescent solar concentrators”. In: *J. Mater. Chem. A* 1.25 (2013), pp. 7339–7350.

[161] A. Goetzberger and W. Greubel. “Solar-Energy Conversion with Fluorescent Collectors”. In: *Appl. Phys.* 14 (1977), pp. 123–139.

[162] J. S. Batchelder, A. H. Zewai, and T. Cole. “Luminescent solar concentrators. 1: Theory of operation and techniques for performance evaluation”. In: *Appl. Opt.* 18.18 (1979), pp. 3090–3110.

[163] R. Reisfeld and S. Neuman. “Planar solar energy convertor and concentrator based on uranyl-doped glass”. In: *Nature* 274 (1978), pp. 144–145.

[164] R. Reisfeld and Y. Kalisky. “Improved planar solar converter based on uranyl neodymium and holmium glasses”. In: *Nature* (1980).

[165] R. Reisfeld and C. K. Jørgensen. “Luminescent solar concentrators for energy conversion”. In: *Sol. Energ. Mater.* Springer, 1982, pp. 1–36.

[166] R. Reisfeld. "Potential uses of chromium (III)-doped transparent glass ceramics in tunable lasers and luminescent solar concentrators". In: *Mat. Sci. Eng.* 71 (1985), pp. 375–382.

[167] R. Reisfeld. "New developments in luminescence for solar energy utilization". In: *Opt. Mater.* 32 (July 2010), pp. 850–856.

[168] W. G. J. H. M. van Sark. "Luminescent solar concentrators - A low cost photovoltaics alternative". In: *Renew. Energy* 49 (Jan. 2013), pp. 207–210.

[169] Y. Zhao and R. R. Lunt. "Transparent Luminescent Solar Concentrators for Large-Area Solar Windows Enabled by Massive Stokes-Shift Nanocluster Phosphors". In: *Adv. Energy Mater.* 3 (Sept. 2013), pp. 1143–1148.

[170] F. Meinardi et al. "Large-area luminescent solar concentrators based on 'Stokes-shift-engineered' nanocrystals in a mass-polymerized PMMA matrix". In: *Nat. Photonics* 8 (May 2014), pp. 392–399.

[171] Y. Zhou et al. "Near infrared, highly efficient luminescent solar concentrators". In: *Adv. Energy Mater.* 6 (2016), p. 1501913.

[172] F. Meinardi et al. "Highly efficient large-area colourless luminescent solar concentrators using heavy-metal-free colloidal quantum dots". In: *Nat. Nanotechnol.* 10 (Oct. 2015), pp. 878–885.

[173] J. L. Banal et al. "Concentrating aggregation-induced fluorescence in planar waveguides: a proof-of-principle". In: *Sci. Rep.* 4 (2014), p. 4635.

[174] J. L. Banal et al. "A Transparent Planar Concentrator Using Aggregates of gem-Pyrene Ethenes". In: *Adv. Energy Mater.* 5 (Oct. 2015).

[175] G. Griffini, M. Levi, and S. Turri. "Novel crosslinked host matrices based on fluorinated polymers for long-term durability in thin-film luminescent solar concentrators". In: *Sol. Energy Mater. Sol. Cells* 118 (Nov. 2013), pp. 36–42.

[176] J. Graffion et al. "Luminescent coatings from bipyridine-based bridged silsesquioxanes containing Eu3+ and Tb3+ salts". In: *J. Mater. Chem.* 22 (2012), pp. 13279–13285.

[177] V. T. Freitas et al. "Eu3+-Based Bridged Silsesquioxanes for Transparent Luminescent Solar Concentrators". In: *ACS Appl. Mater. Interfaces* 7 (Apr. 2015), pp. 8770–8778.

[178] A. Jimenez-Solano et al. “Design and realization of transparent solar modules based on luminescent solar concentrators integrating nanostructured photonic crystals”. In: *Prog. in Photovoltaics* 23 (Dec. 2015), pp. 1785–1792.

[179] M. Peng et al. “Integration of fiber dye-sensitized solar cells with luminescent solar concentrators for high power output”. In: *J. Mater. Chem. A* 2 (2014), pp. 926–932.

[180] R. H. Inman et al. “Cylindrical luminescent solar concentrators with near-infrared quantum dots”. In: *Opt. Express* 19 (Nov. 2011), pp. 24308–24313.

[181] G. Maggioni et al. “Dye-doped parylene-based thin film materials: Application to luminescent solar concentrators”. In: *Sol. Energy Mater. Sol. Cells* 108 (Jan. 2013), pp. 27–37.

[182] A. F. Mansour et al. “Laser dyes doped with poly(ST-Co-MMA) as fluorescent solar collectors and their field performance”. In: *Polym. Test.* 24.4 (2005), pp. 519–525.

[183] J. C. Goldschmidt et al. “Increasing the efficiency of fluorescent concentrator systems”. In: *Sol. Energ. Mat. Sol. C.* 93.2 (2009), pp. 176–182.

[184] M. Otmar, K. W. Krämer, and E. van der Kolk. “Efficient luminescent solar concentrators based on self-absorption free, Tm 2+ doped halides”. In: *Sol. Energ. Mat. Sol. C.* 140 (2015), pp. 115–120.

[185] N. D. Bronstein et al. “Quantum Dot Luminescent Concentrator Cavity Exhibiting 30-fold Concentration”. In: *ACS Photonics* (2015).

[186] L. R. Bradshaw et al. “Nanocrystals for luminescent solar concentrators”. In: *Nano Letters* 15 (Feb. 2015), pp. 1315–23.

[187] M. Debije. “Renewable energy: Better luminescent solar panels in prospect”. In: *Nature* 519.7543 (2015), pp. 298–299.

[188] J. Graffion et al. “Modulating the Photoluminescence of Bridged Silsesquioxanes Incorporating Eu^{3+}-Complexedn,n’-Diureido-2,2’-bipyridine Isomers: Application for Luminescent Solar Concentrators”. In: *Chem. Mater.* 23 (2011), pp. 4773–4782.

[189] M. M. Nolasco et al. “Engineering highly efficient Eu(III)-based tri-ureasil hybrids toward luminescent solar concentrators”. In: *J. Mater. Chem. A* 1 (2013), pp. 7339–7350.

[190] K. R. McIntosh, N. Yamada, and B. S. Richards. "Theoretical comparison of cylindrical and square-planar luminescent solar concentrators". In: *Appl. Phys. B* 88 (2007), pp. 285–290.

[191] W. Wu et al. "Hybrid solar concentrator with zero self-absorption loss". In: *Solar Energy* 84 (2010), pp. 2140–2145.

[192] G. Colantuono, A. Buckley, and R. Erdélyi. "Ray-optics modelling of rectangular and cylindrical 2-Layer solar concentrators". In: *J. Light. Technol.* 31 (2013), pp. 1033–1044.

[193] B. Vishwanathan et al. "A comparison of performance of flat and bent photovoltaic luminescent solar concentrators". In: *Solar Energy* 112 (2015), pp. 120–127.

[194] J.-Y. Chen et al. "Electrospun nanofibers with dual plasmonic-enhanced luminescent solar concentrator effects for high-performance organic photovoltaic cells". In: *J. Mater. Chem. A* 3.29 (2015), pp. 15039–15048.

[195] J. C. Goldschmidt et al. "Theoretical and experimental analysis of photonic structures for fluorescent concentrators with increased efficiencies". In: *Phys. Status Solidi A* 205.12 (2008), pp. 2811–2821.

[196] A. Bozzola et al. "A Multi-optical Collector of Sunlight Employing Luminescent Materials and Photonic Nanostructures". In: *Adv. Opt. Mater.* 4.1 (2016), pp. 147–155.

[197] H. J. Hovel, R. T. Hodgson, and J. M. Woodall. "The effect of fluorescent wavelength shifting on solar cell spectral response". In: *Sol. Energy Mater.* 2.1 (1979), pp. 19–29.

[198] R. Rothemund et al. "External quantum efficiency analysis of Si solar cells with II-VI nanocrystal luminescent down-shifting layers". In: *Energy Procedia* 10 (2011), pp. 83–87.

[199] W. A. Shurcliff and R. C. Jones. "The Trapping of Fluorescent Light Produced within Objects of High Geometrical Symmetry". In: *J. Opt. Soc. Am.* 39.11 (Nov. 1949), pp. 912–916.

[200] T. Dienel et al. "Spectral-based analysis of thin film luminescent solar concentrators". In: *Solar Energy* 84.8 (2010), pp. 1366–1369.

[201] J. D. Weiss. "Trapping efficiency of fluorescent optical fibers". In: *Opt. Eng.* 54 (Feb. 2015), p. 027101.

[202] T. X. Wang et al. "A theoretical model of a cylindrical luminescent solar concentrator with a dye-doping coating". In: *J. Opt.* 15 (May 2013), p. 055709.

[203] C. Preston et al. "Optical haze of transparent and conductive silver nanowire films". In: *Nano Res.* 6.7 (2013), pp. 461–468.

[204] D. B. Mahadik, R. V. Lakshmi, and H. C. Barshilia. "High performance single layer nano-porous antireflection coatings on glass by sol–gel process for solar energy applications". In: *Sol. Energy Mater. Sol. Cells* 140 (2015), pp. 61–68.

[205] M. D. Hughes et al. "Performance comparison of wedge-shaped and planar luminescent solar concentrators". In: *Renew. Energy* 52 (2013), pp. 266–272.

[206] G. V. Shcherbatyuk et al. "Viability of using near infrared PbS quantum dots as active materials in luminescent solar concentrators". In: *Appl. Phys. Lett.* 96 (May 2010), p. 191901.

[207] C. Wang, H. Abdul-Rahman, and S. P. Rao. "Daylighting can be fluorescent: Development of a fiber solar concentrator and test for its indoor illumination". In: *Energ. Buildings* 42 (May 2010), pp. 717–727.

[208] V. Sholin, J. D. Olson, and S. A. Carter. "Semiconducting polymers and quantum dots in luminescent solar concentrators for solar energy harvesting". In: *J. Appl. Phys.* 101 (June 2007), pp. 1231141–1231149.

[209] D. Şahin, B. Ilan, and D. F. Kelley. "Monte-Carlo simulations of light propagation in luminescent solar concentrators based on semiconductor nanoparticles". In: *J. Appl. Phys.* 110.3 (2011), p. 033108.

[210] W. Zhou, M. C. Wang, and X. J. Zhao. "The properties of PMMA/DCJTB thin-film luminescent solar concentrator with various thicknesses". In: *Solar Energy* 120 (Oct. 2015), pp. 419–427.

[211] M. Tonezzer et al. "Luminescent solar concentrators employing new $Eu(TTA)_3$phen-containing parylene films". In: *Prog. Photovolt. Res. Appl.* 23 (Aug. 2015), pp. 1037–1044.

[212] S. J. Gallagher, B. Norton, and P. C. Eames. "Quantum dot solar concentrators: Electrical conversion efficiencies and comparative concentrating factors of fabricated devices". In: *Solar Energy* 81 (2007), pp. 813–821.

[213] C. Liu and B. Li. "Multiple dyes containing luminescent solar concentrators with enhanced absorption and efficiency". In: *J. Opt.* 17 (Feb. 2015), p. 025901.

[214] I. Coropceanu and M. G. Bawendi. "Core/shell quantum dot based luminescent solar concentrators with reduced reabsorption and enhanced efficiency". In: *Nano Letters* 14 (July 2014), pp. 4097–4101.

[215] J. Bomm et al. "Fabrication and full characterization of state-of-the-art quantum dot luminescent solar concentrators". In: *Sol. Energy Mater. Sol. Cells* 95 (2011), pp. 2087–2094.

[216] X. Sheng et al. "Doubling the Power Output of Bifacial Thin-Film GaAs Solar Cells by Embedding Them in Luminescent Waveguides". In: *Adv. Energy Mater.* 3 (Aug. 2013), pp. 991–996.

[217] J. L. Banal, K. P. Ghiggino, and W. W. H. Wong. "Efficient light harvesting of a luminescent solar concentrator using excitation energy transfer from an aggregation-induced emitter". In: *Phys. Chem. Chem. Phys.* 16 (2014), pp. 25358–25363.

[218] M. Pravettoni et al. "External quantum efficiency measurements of luminescent solar concentrators: a study of the impact of backside reflector size and shape". In: 2009, pp. 332–335.

[219] J.-M. Liu. *Principles of Photonics*. Cambridge University Press, 2016.

[220] S. A. Prahl. "A Monte Carlo model of light propagation in tissue". In: *Dosimetry of laser radiation in medicine and biology*. Vol. 10305. International Society for Optics and Photonics. 1989, p. 1030509.

[221] D. P. Kroese, T. Taimre, and Z. I. Botev. *Handbook of monte carlo methods*. Vol. 706. John Wiley & Sons, 2013.

[222] A. Kostro, B. Huriet, and A. Schüler. "PhotonSim: developing and testing a Monte-Carlo ray-tracing software for the simulation of planar luminescent solar concen-

trators". In: *Proceedings of the CISBAT 2007 International Conference, Lausanne, Switzerland*. 2007, pp. 4–5.

[223] J. M. Hammersly and D. C. Handscomb. "Monte Carlo Methods (Methuen and Company, London)". In: (1964).

[224] N. Metropolis and S. Ulam. "The monte carlo method". In: *J. Am. Stat. Assoc.* 44.247 (1949), pp. 335–341.

[225] L. Wang, S. L. Jacques, and L. Zheng. "MCML-Monte Carlo modeling of light transport in multi-layered tissues". In: *Comput. Methods Programs Biomed.* 47.2 (1995), pp. 131–146.

[226] A. S. Householder, G. E. Forsythe, and H. H. Germond. *Monte Carlo Method*. National Bureau of Standards, 1951.

[227] L. L. Carter and E. D. Cashwell. *Particle-transport simulation with the Monte Carlo method*. Tech. rep. Los Alamos Scientific Lab., N. Mex.(USA), 1975.

[228] N. Metropolis. "MONTE CARLO METHOD". In: *From Cardinals to Chaos: Reflection on the Life and Legacy of Stanislaw Ulam* (1989), p. 125.

[229] R. Eckhardt. "Stan ulam, john von neumann, and the monte carlo method". In: *Los Alamos Sci.* 15.131-136 (1987), p. 30.

[230] P. Hovington, D. Drouin, and R. Gauvin. "CASINO: A new Monte Carlo code in C language for electron beam interaction-Part I: Description of the program". In: *Scanning* 19.1 (1997), pp. 1–14.

[231] M. Carrascosa, S. Unamuno, and F. Agullo-Lopez. "Monte Carlo simulation of the performance of PMMA luminescent solar collectors". In: *Appl. Opt.* 22.20 (1983), pp. 3236–3241.

[232] F. Meinardi et al. "Highly efficient luminescent solar concentrators based on earth-abundant indirect-bandgap silicon quantum dots". In: *Nat. Photonics* 11 (Mar. 2017), pp. 177–185.

[233] S. W. Leow et al. "Monte Carlo ray-tracing simulations of luminescent solar concentrators for building integrated photovoltaics". In: *High and Low Concentrator Systems for Solar Electric Applications VIII*. Vol. 8821. International Society for Optics and Photonics. 2013, p. 882103.

[234] T. Monzon-Hierro et al. "A new cost-effective polymeric film containing an Eu(III) complex acting as UV protector and down-converter for Si-based solar cells and modules". In: *Sol. Energy Mater. Sol. Cells* 136 (May 2015), pp. 187–192.

[235] C. Sanchez et al. "Applications of hybrid organic-inorganic nanocomposites". In: *J. Mater. Chem.* 15 (35-36 2005), pp. 3559–3592.

[236] C. J. Brinker and G. W. Scherer. *Sol-gel science: the physics and chemistry of sol-gel processing*. Academic press, 2013.

[237] U. Schubert, N. Huesing, and A. Lorenz. "Hybrid Inorganic-Organic Materials by Sol-Gel Processing of Organofunctional Metal Alkoxides". In: *Chem. Mater.* 7.11 (1995), pp. 2010–2027. eprint: `https://doi.org/10.1021/cm00059a007`.

[238] C. Sanchez et al. "Applications of advanced hybrid organic–inorganic nanomaterials: from laboratory to market". In: *Chem. Soc. Rev.* 40.2 (2011), pp. 696–753.

[239] V. de Zea Bermudez, L. D. Carlos, and L. Alcacer. "Sol-gel derived urea cross-linked organically modified silicates. 1. Room temperature mid-infrared spectra". In: *Chem. Mater.* 11 (Mar. 1999), pp. 569–580.

[240] L. S. Fu et al. "Photoluminescence and quantum yields of urea and urethane cross-linked nanohybrids derived from carboxylic acid solvolysis". In: *Chem. Mater.* 16 (Apr. 2004), pp. 1507–1516.

[241] V. T. Freitas et al. "Luminescent urea cross-linked tripodal siloxane-based hybrids". In: *J. Sol-Gel Sci. Technol.* 65 (Jan. 2013), pp. 83–92.

[242] M. Fernandes et al. "Incorporation of the Eu(tta)(3)(H2O)(2) complex into a co-condensed d-U(600)/d-U(900) matrix". In: *J. Lumin.* 128 (Feb. 2008), pp. 205–212.

[243] C. Molina et al. "Enhanced emission from Eu(III) β-diketone complex combined with ether-type oxygen atoms of di-ureasil organic–inorganic hybrids". In: *J. Lumin.* 104 (2003), pp. 93–101.

[244] M. Fischer and J. Georges. "Fluorescence quantum yield of rhodamine 6G in ethanol as a function of concentration using thermal lens spectrometry". In: *Chem. Phys. Lett.* 260 (Sept. 1996), pp. 115–118.

[245] M. Martins et al. "Recovery of phycobiliproteins from the red macroalga Gracilaria sp using ionic liquid aqueous solutions". In: *Green Chem.* 18 (Aug. 2016), pp. 4287–4296.

[246] K. Lunstroot et al. "Lanthanide-doped luminescent ionogels". In: *Dalton Trans.* 2 (2009), pp. 298–306.

[247] V. T. Freitas et al. "Boosting the Emission Quantum Yield of Urea Cross-Linked Tripodal Poly(oxypropylene)/Siloxane Hybrids Through the Variation of Catalyst Concentration". In: *Eur. J. Inorg. Chem.* (Nov. 2012), pp. 5390–5395.

[248] B. L. Wheeler et al. "A silicon phthalocyanine and a silicon naphthalocyanine: synthesis, electrochemistry, and electrogenerated chemiluminescence". In: *J. Am. Chem. Soc.* 106.24 (1984), pp. 7404–7410.

[249] H. Eichhorn. "Mesomorphic phthalocyanines, tetraazaporphyrins, porphyrins and triphenylenes as charge-transporting materials". In: *J. Porphyr. Phthalocyanines* 4.1 (2000), pp. 88–102.

[250] Ta. Oku et al. "Fabrication and characterization of silicon naphthalocyanine, gallium phthalocyanine and fullerene-based organic solar cells with inverted structures". In: *J. Phys. Conf. Ser.* Vol. 433. 1. IOP Publishing. 2013, p. 012025.

[251] H. Xu et al. "Near-IR dye sensitization of polymer blend solar cells". In: *Polymer* 55.12 (2014), pp. 2856–2860.

[252] J. Andzelm et al. "Optical properties of phthalocyanine and naphthalocyanine compounds". In: *J. Chem. Theory Comput.* 3.3 (2007), pp. 870–877.

[253] B. H. Lessard et al. "Bis (tri-n-hexylsilyl oxide) silicon phthalocyanine: a unique additive in ternary bulk heterojunction organic photovoltaic devices". In: *ACS Appl. Mater. Interfaces* 6.17 (2014), pp. 15040–15051.

[254] L. B. Josefsen, R. W. Boyle, et al. "Photodynamic therapy and the development of metal-based photosensitisers". In: *Metal-based drugs* 2008 (2008).

[255] O. Taratula et al. "Dendrimer-encapsulated naphthalocyanine as a single agent-based theranostic nanoplatform for near-infrared fluorescence imaging and combinatorial anticancer phototherapy". In: *Nanoscale* 7.9 (2015), pp. 3888–3902.

[256] S. Tai and N. Hayashi. "Strong aggregation properties of novel naphthalocyanines". In: *J. Chem. Soc., Perkin Trans. 2* 8 (1991), pp. 1275–1279.

[257] M. Katayose et al. "Novel Silicon Naphthalocyanines - Synthesis and molecular arrangement in thin-films". In: *J. Chem. Soc., Perkin Trans. 2* (Mar. 1992), pp. 403–409.

[258] Z. Y. Li et al. "Effect of aggregation on nonlinear optical properties of a naphthalocyanine". In: *J. Photochem. Photobiol. A* 188 (May 2007), pp. 311–316.

[259] Y. Jin et al. "Near-infrared fluorescent dye-doped semiconducting polymer dots". In: *ACS Nano* 5.2 (2011), pp. 1468–1475.

[260] J. Geng et al. "Near-infrared fluorescence amplified organic nanoparticles with aggregation-induced emission characteristics for in vivo imaging". In: *Nanoscale* 6.2 (2014), pp. 939–945.

[261] P. P. Lima et al. "Energy transfer mechanisms in organic-inorganic hybrids incorporating europium(III): A quantitative assessment by light emission spectroscopy". In: *J. Phys. Chem. C* 111 (Nov. 2007), pp. 17627–17634.

[262] A. Seminara and A. Musumeci. "Absorption and emission spectra of neodymium (III) and europium (III) complexes". In: *Inorganica Chim. Acta* 95.6 (1984), pp. 291–307.

[263] J. A. Kai et al. "Intermolecular energy transfer and photostability of luminescence-tuneable multicolour PMMA films doped with lanthanide-beta-diketonate complexes". In: *J. Mater. Chem.* 21 (2011), pp. 3796–3802.

[264] M. Fernandes et al. "Highly photostable luminescent poly(epsilon-caprolactone)siloxane biohybrids doped with europium complexes". In: *Chem. Mater.* 19 (Aug. 2007), pp. 3892–3901.

[265] Z. Ahmed and K. Iftikhar. "Sensitization of visible and NIR emitting lanthanide (III) ions in noncentrosymmetric complexes of hexafluoroacetylacetone and unsubstituted monodentate pyrazole". In: *J. Phys. Chem. A* 117.44 (2013), pp. 11183–11201.

[266] P. Reineck et al. “Brightness and Photostability of Emerging Red and Near-IR Fluorescent Nanomaterials for Bioimaging”. In: *Adv. Opt. Mater.* 4 (Oct. 2016), pp. 1549–1557.

[267] J. Liu et al. “Improving spectral response of monocrystalline silicon photovoltaic modules using high efficient luminescent down-shifting Eu3+ complexes”. In: *Prog. in Photovoltaics* 21 (June 2013), pp. 668–675.

[268] A. Le Donne et al. “Rare earth organic complexes as down-shifters to improve Si-based solar cell efficiency”. In: *Opt. Mater.* 33 (May 2011), pp. 1012–1014.

[269] A. Le Donne et al. “Encapsulating Eu3+ Complex Doped Layers to Improve Si-based Solar Cell Efficiency”. In: *Prog. in Photovoltaics* 17 (Dec. 2009), pp. 519–525.

[270] W. B. Hung et al. “Enhanced conversion efficiency of crystalline Si solar cells via luminescent down-shifting using Ba2SiO4 : Eu2+ phosphor”. In: *J. Ceram. Process. Res.* 15 (2014), pp. 157–161.

[271] J. F. Liu, Q. H. Yao, and Y. D. Li. “Effects of downconversion luminescent film in dye-sensitized solar cells”. In: *Appl. Phys. Lett.* 88 (Apr. 2006).

[272] T. X. Wang et al. “Luminescent solar concentrator employing rare earth complex with zero self-absorption loss”. In: *Solar Energy* 85 (Nov. 2011), pp. 2571–2579.

[273] X. Wang et al. “Europium complex doped luminescent solar concentrators with extended absorption range from UV to visible region”. In: *Solar Energy* 85 (Sept. 2011), pp. 2179–2184.

[274] V. T. Freitas et al. “Role of the reactive atmosphere during the sol-gel synthesis on the enhancing of the emission quantum yield of urea cross-linked tripodal siloxane-based hybrids”. In: *J. Sol-Gel Sci. Technol.* 70 (May 2014), pp. 227–235.

[275] F. Uhlig and H. C. Marsmann. “29Si NMR Some practical aspects”. In: *Gelest Catalog* (2008).

[276] M. E. Smith and D. Holand. “Atomic scale structure of gel materials by solid state NMR”. In: *Handbook of Sol-Gel Science and Technology, Processing Characterization and Application, ed. S. Sakka, Characterization of the Sol-Gel materials and products* 2 (2005), pp. 35–63.

[277] L. S. Fu et al. "Optically functional nanocomposites with poly(oxyethylene)-based di-ureasils and mesoporous MCM-41". In: *Micropor. Mesopor. Mat.* 94 (Sept. 2006), pp. 185–192.

[278] L. D. Carlos et al. "Sol-gel derived urea cross-linked organically modified silicates. 2. Blue-light emission". In: *Chem. Mater.* 11 (Mar. 1999), pp. 581–588.

[279] D. J. Skrovanek et al. "Hydrogen-Bonding in Polymers - Infrared Temperature Studies of an Amorphous Polyamide". In: *Macromolecules* 18 (1985), pp. 1676–1683.

[280] L. D. Carlos et al. "Full-color phosphors from amine-functionalized crosslinked hybrids lacking metal activator ions". In: *Adv. Funct. Mater.* 11 (2001), pp. 111–115.

[281] Y. Sakakibara et al. "Photoluminescence properties of magnesium, chloroaluminum, bromoaluminum, and metal-free phthalocyanine solid films". In: *J. Phys. Chem. B* 105.8 (2001), pp. 1547–1553.

[282] S. R. Wilton et al. "Monte Carlo study of PbSe quantum dots as the fluorescent material in luminescent solar concentrators". In: *Opt. Express* 22 (Jan. 2014), pp. 35–43.

[283] X. M. Hu et al. "Ray-trace simulation of $CuInS(Se)_2$ quantum dot based luminescent solar concentrators". In: *Opt. Express* 23 (July 2015), A858–A867.

[284] K. E. Knowles et al. "Bright CuInS2/CdS nanocrystal phosphors for high-gain full-spectrum luminescent solar concentrators". In: *Chem. Comm.* 51 (2015), pp. 9129–9132.

[285] B. M. van der Ende, L. Aarts, and A. Meijerink. "Lanthanide ions as spectral converters for solar cells". In: *Phys. Chem. Chem. Phys.* 11 (2009), pp. 11081–11095.

[286] M. Kennedy et al. "Improving the optical efficiency and concentration of a single-plate quantum dot solar concentrator using near infra-red emitting quantum dots". In: *Solar Energy* 83 (July 2009), pp. 978–981.

[287] Y. M. Zhao et al. "Near-Infrared Harvesting Transparent Luminescent Solar Concentrators". In: *Adv. Opt. Mater.* 2 (July 2014), pp. 606–611.

[288] J. J. H. Videira, E. Bilotti, and A. J. Chatten. "Cylindrical and square fibre luminescent solar concentrators: experimental and simulation comparisons". In: *2014 IEEE 40th Photovoltaic Specialist Conference (PVSC)* (2014), pp. 2280–2285.

[289] E.-H. Banaei and A. F. Abouraddy. "Design of a polymer optical fiber luminescent solar concentrator". In: *Prog. Photovolt. Res. Appl.* 23 (2015), pp. 403–416.

[290] A. Alessi, M. Salvalaggio, and G. Ruzzon. "Rhodamine 800 as reference substance for fluorescence quantum yield measurements in deep red emission range". In: *J. Lumin.* 134 (Feb. 2013), pp. 385–389.

[291] S. C. Nunes et al. "Lamellar mono-amidosil hybrids incorporating monomethinecyanine dyes". In: *J. Mater. Chem. C* 1 (2013), pp. 2290–2301.

[292] A. Kaniyoor et al. "Design and response of high-efficiency, planar, doped luminescent solar concentrators using organic–inorganic di-Ureasil waveguides". In: *Adv. Opt. Mater.* 4 (2015), pp. 444–456.

[293] E. Pecoraro et al. "Photoluminescence of bulks and thin films of Eu3+-doped organic/inorganic hybrids". In: *J. Alloy. Comp.* 451.1-2 (2008), pp. 136–139.

[294] B. Demmig-Adams and W. W. Adams. "Photosynthesis - Harvesting sunlight safely". In: *Nature* 403 (Jan. 2000), pp. 371–374.

[295] A. Dey et al. "Fabrication ofsolar cell usingextracted biomolecules from tea leaves and hybrid perovskites". In: *Mater. Today* 3.10, Part A (2016). International Conference on Advances in Bioprocess Engineering and Technology 2016 (ICABET 2016), pp. 3498–3504.

[296] T. Han et al. "Theoretical realization of an ultra-efficient thermal-energy harvesting cell made of natural materials". In: *Energy Environ. Sci.* 6.12 (2013), pp. 3537–3541.

[297] V. Fattori et al. "Poly (lactic acid) as a transparent matrix for luminescent solar concentrators: a renewable material for a renewable energy technology". In: *Energy Environ. Sci.* 4.8 (2011), pp. 2849–2853.

[298] A. N. Glazer. "Phycobiliproteins". In: *Methods Enzymol.* Vol. 167. Elsevier, 1988, pp. 291–303.

[299] M. S. de Cardona et al. "Outdoor evaluation of luminescent solar concentratorprototypes". In: *Appl. Opt.* 24.13 (July 1985), pp. 2028–2032.

[300] R. Kondepudi and S. Srinivasan. "Optical studies on some dyes for liquid solar concentrators". In: *Sol. Energy Mater.* 20.3 (1990), pp. 257–263.

[301] Z. Krumer et al. "Tackling self-absorption in luminescent solar concentrators with type-II colloidal quantum dots". In: *Sol. Energy Mater. Sol. Cells* 111 (2013), pp. 57–65.

[302] G. Lifante et al. "Solar concentrators using total internal reflection". In: *Appl. Opt.* 22.24 (1983), pp. 3966–3970.

[303] A. F. Mansour. "Outdoor testing of luminescent solar concentrators in a liquid polymer and bulk plate of PMMA". In: *Polym. Test.* 17 (1998), pp. 153–162.

[304] M. Gajic et al. "Circular luminescent solar concentrators". In: *Solar Energy* 150 (July 2017), pp. 30–37.

[305] J. A. H. P. Sol et al. "Temperature-Responsive Luminescent Solar Concentrators: Tuning Energy Transfer in a Liquid Crystalline Matrix". In: *Angew. Chem.* 130.4 (2018), pp. 1042–1045.

[306] A. L. Rodarte et al. "Dye-integrated cholesteric photonic luminescent solar concentrator". In: *Liq. Cryst.* 41 (Oct. 2014), pp. 1442–1447.

[307] J. Niu et al. "Comprehensive extraction of agar and R-phycoerythrin from Gracilaria lemaneiformis (Bangiales, Rhodophyta)". In: (2013).

[308] J. A. Rivera and J. G. Eden. "Lasing at 602-620 nm from a red algae-derived phycobiliprotein". In: *APL Photonics* 2.12 (2017), p. 121301.

[309] L. D. Carlos et al. "Sol-gel derived nanocomposite hybrids for full colour displays". In: *J. Lumin.* 87-9 (May 2000), pp. 702–705.

[310] A. R. West. *Solid state chemistry and its applications.* John Wiley & Sons, 2007.

[311] C. Giacovazzo et al. *Fundamentals of Crystallography.* Oxford Science Publications: New York, 1995.

[312] A. S. Holt and E. E. Jacobs. "Infra-Red Absorption Spectra of Chlorophylls and Derivatives". In: *Plant Physiol.* 30 (1955), pp. 533–559.

[313] W. B. Person and G. Zerbi. *Vibrational intensities in infrared and Raman spectroscopy.* Vol. 20. Elsevier Science Ltd., 1982.

[314] N. Murata, Nishimur. M, and A. Takamiya. "Fluorescence of Chlorophyll in Photosynthetic Systems .3. Emission and Action Spectra of Fluorescence - 3 Emission Bands of Chlorophyll a and Energy Transfer between 2 Pigment Systems". In: *Biochim. Biophys. Acta* 126 (1966), pp. 234–243.

[315] H. K. Lichtenthaler. "Chlorophylls and Carotenoids - Pigments of Photosynthetic Biomembranes". In: *Methods Enzymol.* 148 (1987), pp. 350–382.

[316] A. P. J. Maestrin et al. "Extração e purificação de clorofila a, da alga Spirulina maxima: um experimento para os cursos de química". In: *Quim. Nova* 32 (2009), pp. 1670–1672.

[317] S. C. Nunes et al. "Lamellar mono-amidosil hybrids doped with Rhodamine (B) methyl ester perchlorate". In: *J. Sol-Gel Sci. Technol.* 72 (Nov. 2014), pp. 239–251.

[318] P. Mohanty, M. Srivastava, and K. B. Krishna. *Spirulina platensis arthrospira: physiology, cell-biology and biotechnology.* Ed. by Avigad Vonshak. CRC Press, 1997.

[319] G. Seely and J. Connolly. "Fluorescence of photosynthetic pigments in vitro". In: *Light emission by plants and bacteria.* Ed. by Elsevier. 2012, pp. 100–128.

[320] A. Pfarrherr et al. "Chlorophyll-B in Solution - Fluorescence Lifetimes, Absorption and Emission-Spectra as Criteria of Purity". In: *J. Photochem. Photobiol. B* 9 (Apr. 1991), pp. 35–41.

[321] C. S. French and V. K. Young. "The fluorescence spectra of red algae and the transfer of energy from phycoerythrin to phycocyanin and chlorophyll". In: *The Journal of general physiology* 35 (1952), pp. 873–890.

[322] M. Chen and R. E. Blankenship. "Expanding the solar spectrum used by photosynthesis". In: *Trends Plant Sci.* 16 (2011), pp. 427–431.

[323] V. V. Egorov. "Theory of the J-band: from the Frenkel exciton to charge transfer". In: *International Conference on Luminescence and Optical Spectroscopy of Condensed Matter* 2 (2009), pp. 223–326.

[324] S. S. Brody and M. Brody. "Fluorescence Properties of Aggregated Chlorophyll in Vivo and in Vitro". In: *J. Chem. Soc. Faraday Trans.* 58 (1962), pp. 416–428.

[325] L. O'Neill and H. J. Byrne. "Structure-property relationships for electron-vibrational coupling in conjugated organic oligomeric systems". In: *J. Phys. Chem. B* 109 (July 2005), pp. 12685–12690.

[326] K. D. Piatkevich et al. "Extended Stokes Shift in Fluorescent Proteins: Chromophore-Protein Interactions in a Near-Infrared TagRFP675 Variant". In: *Sci. Rep.* 3 (May 2013), p. 1847.

[327] L. S. Fu et al. "Photoluminescence and quantum yields of organic/inorganic hybrids prepared through formic solvolysis". In: *Opt. Mater.* 30 (Mar. 2008), pp. 1058–1064.

[328] Y. Q. Li et al. "Extinction coefficient for red-shifted chlorophylls: Chlorophyll d and chlorophyll f". In: *Biochim. Biophys. Acta* 1817 (Aug. 2012), pp. 1292–1298.

[329] R. Hein and R. Y. Tsien. "Engineering green fluorescent protein for improved brightness, longer wavelengths and fluorescence resonance energy transfer". In: *Curr. Biol.* 6 (Feb. 1996), pp. 178–182.

[330] A. N. Butkevich et al. "Hydroxylated Fluorescent Dyes for Live-Cell Labeling: Synthesis, Spectra and Super-Resolution STED Microscopy". In: *Chem. Eur. J.* 23 (Sept. 2017), pp. 12114–12119.

[331] M. Sottile et al. "Epoxy resin doped with Coumarin 6: Example of accessible luminescent collectors". In: *Eur. Polym. J.* 89 (Apr. 2017), pp. 23–33.

[332] D. L. Waldron et al. "PbSe quantum dot based luminescent solar concentrators". In: *Nanotechnology* 28 (Mar. 2017), pp. 1–6.

[333] Y. L. Li et al. "A structurally modified perylene dye for efficient luminescent solar concentrators". In: *Solar Energy* 136 (Oct. 2016), pp. 668–674.

[334] G. Griffini et al. "Anthracene/tetracene cocrystals as novel fluorophores in thin-film luminescent solar concentrators". In: *RSC Adv.* 4 (2014), pp. 9893–9897.

[335] L. Desmet et al. "Monocrystalline silicon photovoltaic luminescent solar concentrator with 4.2% power conversion efficiency". In: *Opt. Lett.* 37 (Aug. 2012), pp. 3087–3089.

[336] C. H. Chou, M. H. Hsu, and F. C. Chen. "Flexible luminescent waveguiding photovoltaics exhibiting strong scattering effects from the dye aggregation". In: *Nano Energy* 15 (July 2015), pp. 729–736.

[337] Y. El Mouedden et al. “A cost-effective, long-lifetime efficient organic luminescent solar concentrator”. In: *J. Appl. Phys.* 118 (July 2015).

[338] K. S. Rowan. *Photosynthetic pigments of algae*. CUP Archive, 1989.

[339] R. MacColl et al. “The discovery of a novel R-phycoerythrin from an Antarctic Red Alga”. In: *J. Biol. Chem.* 271 (July 1996), pp. 17157–17160.

[340] V. T. Oi, A. N. Glazer, and L. Stryer. “Fluorescent Phycobiliprotein Conjugates for Analyses of Cells and Molecules”. In: *J. Cell Biol.* 93 (1982), pp. 981–986.

[341] D. J. W. Barber and J. T. Richards. “Energy transfer in the accessory pigments R-phycoerythrin and C-phycocyanin”. In: *Photochem. Photobiol.* 25.6 (1977), pp. 565–569.

[342] Z. Krumer et al. “Compensation of self-absorption losses in luminescent solar concentrators by increasing luminophore concentration”. In: *Sol. Energy Mater. Sol. Cells* 167 (Aug. 2017), pp. 133–139.

[343] I. Parola et al. “High performance fluorescent fiber solar concentrators employing double-doped polymer optical fibers”. In: *Sol. Energy Mater. Sol. Cells* 178 (2018), pp. 20–28.

[344] K. Binnemans et al. “Recycling of rare earths: a critical review”. In: *J. Clean. Prod.* 51 (2013), pp. 1–22.

[345] J.-C. G. Bünzli and S. V. Eliseeva. “Intriguing aspects of lanthanide luminescence”. In: *Chem. Sci.* 4.5 (2013), pp. 1939–1949.

[346] S. V. Eliseeva and J.-C. G. Bünzli. “Rare earths: jewels for functional materials of the future”. In: *New J. Chem.* 35.6 (2011), pp. 1165–1176.

[347] M. A. De Boer and K. Lammertsma. “Scarcity of rare earth elements”. In: *ChemSusChem* 6.11 (2013), pp. 2045–2055.

[348] C. Storkey et al. “Preventing protein oxidation with sugars: scavenging of hypohalous acids by 5-selenopyranose and 4-selenofuranose derivatives”. In: *Chem. Res. Toxicol.* 25.11 (2012), pp. 2589–2599.

[349] A. Gaigalas et al. “A multistate model for the fluorescence response of R-phycoerythrin”. In: *Photochem. Photobiol.* 82.3 (2006), pp. 635–644.

[350] I. C. Anderson and D. S. Robertson. “Role of carotenoids in protecting chlorophyll from photodestruction”. In: *Plant Physiol.* 35.4 (1960), p. 531.

[351] D. S. Robertson, M. D. Bachmann, and I. C. Anderson. “Role of carotenoids in protecting chlorophyll from photodestruction - II. Studies on the effect of four modifiers of the albino cl1 mutant of maize”. In: *Photochem. Photobiol.* 5.10 (1966), pp. 797–805.